Development of Stud-SFRCC Connection and Its Application to Composite Beam-to-Column Connections

September 2013

Yunbiao LUO

TABLE OF CONTENTS

CHAPTER 1

Introduction

1.1 Motivation

Due to the development of modern seismic structures, a devastating sequence of earthquakes such as Christchurch earthquake in September 2010 and Chili earthquake in February 2010 fortunately claimed only a limited number of lives, but the economic and social consequences have been very significant. Therefore, in recent years, strong efforts within the earthquake engineering community have been directed toward the development of high-performance structural and non-structural systems, i.e. systems that for the same seismic action are less prone to damage.

In recent decades, many high performance construction materials have been developed (Shi 2008). High performance construction materials provide far greater strength, ductility, durability, and resistance to external elements than traditional construction materials. They can significantly increase the longevity of structures in the built environment and also reduce maintenance costs for these structures considerably. These most significant high performance construction materials include high performance concrete, high performance steel, fiber reinforced cement composites, FRP composites, and many others. These high performance construction materials provide great potential for the development of high performance structural and non-structural systems those are much damage-tolerant to seismic action.

Modern development and broad expansion of fiber reinforced cementitious and concrete composites (FRCCs) are marked in the past five decades (Brandt 2008). Today, it has already become an extensive application and market penetration worldwide. It is strongly believed that high performance and ultra-high performance fiber reinforced cementitious composite are emerging materials well suited for use in high performance structural systems. There is a real need to tailor design of composites to satisfy certain demands on strength, toughness, durability, ductility, and fracture energy. Figure 1.1 illustrates the types of applications where these materials can offer effective technical solutions for various structures. As illustrated in Figure 1.1, there are mainly four types of application of FRCCs in constructional engineering, which are standalone structural element, hybrid in combination with RC, PC or steel structures, hybrid in selected zones of structures where enhanced properties are needed, and repair and rehabilitation. In typical applications in RC or PC building structures, FRCCs are usually used either in stand-alone, or in combination with RC and PC structures, or in repair-strengthening situations, because the FRCCs can directly substitute the

concrete in the applications.

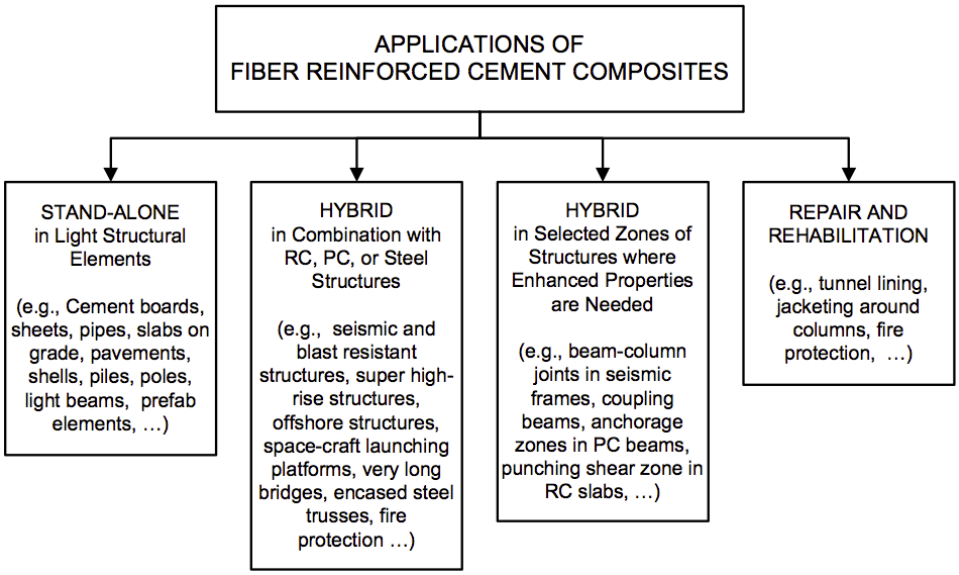

Figure 1.1 Classes of applications of fiber reinforced cement composites.

For the application of FRCCs in steel building structures, in which the main constructional material is steel, it is preferred to only apply FRCCs in a selected zone (a small part) of the steel building structure in need of strengthening or toughening. Applications in selected zones of steel structures may include: the punching shear zone around columns in composite floor slab systems; end blocks and anchorage zones in encased column bases (Cui and Nakashima 2011; Kaneko et al. 2006); beam-to-column connections in steel moment resistant frames (Kaneko et al. 2005); in-fill damping structural elements (Kesner and Billington 2003), etc. In most of these applications, FRCCs are used to take advantages of their toughness, ductility or high strength, to trigger a more preferable structural behavior (such as stronger, more ductile, or more damage tolerant) of the structural members. Usually, fracture of concrete is a dominant failure mechanism when steel and concrete interact mechanically. Due to the great difference on mechanical properties between steel and FRCCs, i.e. high stiffness and ductility of steel and relative brittleness of FRCCs, when applying FRCCs to the selected zone where steel and concrete are interacting, the most important mechanical properties of FRCCs are likely to be the toughness and strength.

Among various FRCCs, steel fiber reinforced cementitious composite (SFRCC hereafter) is remarkable for its high toughness and high tensile strength. SFRCC was developed based on CRC (compact reinforced composite), one of the ultra high performance fiber reinforced cementitious composite (UHPFRCC), which was invented by Bache (Bache 1981a) in Denmark. SFRCC is made with a very low water/binder ratio (0.16 or smaller), and contains a large amount of steel fiber range from 2 to 6%, and extreme densified small particles providing matrix strengths of 140 to 400 MPa. Comparing to conventional concrete, SFRCC has tensile strength approximately four times larger of that of conventional concrete (15MPa for SFRCC and 3MPa for conventional concrete). In addition, SFRCC is much stiffer than conventional concrete since its Young's modulus is about twice of that

of concrete. Because of the presence of steel fibers, the deformation and energy absorption capacities, i.e. the toughness, of SFRCC are significantly improved. Densely arranged steel rebar can be combined in SFRCC. Such distinguished mechanical properties of SFRCC make it very promising and suitable for the applications in the steel structures. In the applying SFRCC in steel structure, a key issue is the force transmission between steel components to SFRCC component. Such force transmission has to be achieved by connections, and headed stud shear connection is one of the most commonly used connections. In the past decades, much research has been conducted to the stud-connect/mortar connections, and mature design approach can be found in various design codes all over the world. However, research on the connection between headed stud shear connector and new developed FRCCs is very limited. Therefore, it deserves research on such stud-SFRCC connection to explore new possibilities for structural applications.

So far, research on SFRCC and its application on steel structures includes (1) experimental work on material properties with densified small particle cement (Bache 1981b) focusing on the fiber volume fraction and the water-binder ratio (Kirikoshi et al. 2000); (2) constitutive model formulated for both tension and compression to evaluate the performance of SFRCC in several kinds of structural applications based on material tests (Kaneko, et al. 2000), and (3) numerical evaluation on the performance of beam-to-column joint by using nonlinear finite element analysis for the two dimensional spliced element of the joints (Kaneko 2000); the structural performance of steel structures employing a beam-column joint system with steel fiber reinforced cementitious composites(Kaneko et al. 2005); and (4) shallowly embedded column based using SFRCC floor slab (Cui and Nakashima 2011) in which the seismic performance was evaluated by both experimental study and numerical investigation. Such research indicates that SFRCC exhibits great performance in high performance structural system in the steel structure, and it is promising for the development of other structural systems using SFRCC.

Steel moment-frame buildings are very popular in Japan. The open nature of moment-frame buildings is desirable for many owners and architects. Characteristically flexible behavior of steel moment-frame buildings have been seen as a benefit in withstanding large deformation demands and limiting forces imposed during the seismic excitation. However, recent earthquakes have shown that these large deformations can lead to premature, brittle fracture at the welded connections of steel moment-frame structural. In particular, after the 1994 Northridge earthquake and 1995 Hyogoken-Nanbu Kobe earthquakes, significant vulnerabilities in steel moment-frame buildings were discovered. Although considered as the best performing seismic structure previously, steel moment-frame buildings were observed to be susceptible to brittle fracture at beam-column connections. Retrofit to these structures have become more common in an effort to reduce the risk of connection failure, and rehabilitation of such damaged steel building structures for post-earthquake continuing use has also gaining wide attentions. Various practical solutions have been suggested to retrofit and rehabilitation of steel building structures. It includes reduced beam section approach (Uang et al. 2000), welded haunches, strengthening with cover plates (Kim et al. 2004; Engelhardt and Sabol 1998), and improved welding practice using high toughness material and geometrical modification on weld access hole details (Nakashima et al. 1998). It is noted that all of these solutions

are implemented by modifying the steel component by welding, flame cutting or drilling holes. Although satisfactory performance can be achieved by these modifications in the laboratory condition, there are still many issues to be resolved, such as the feasibility in practical in-site construction, difficulty in welding quality control, cost in fire proof, etc. To avoid the drawbacks of the methods mentioned above, it is better to develop strategies using other constructional materials to improve the performance of beam-to-column connections. For example, using high performance cementations composite to strengthen the beam-to-column connections or strengthen and toughen the concrete portion to trigger desirable performance of the existing steel members. Since some attempts have been proved successful in applications of SFRCC to the column case (Kaneko et al. 2006; Cui and Nakashima 2011), and beam-co-column joint (Kaneko et al. 2005) in steel building structures, development of alternative approach using SFRCC for the retrofit and rehabilitation of steel building structures would be promising and worthwhile, in particular when some of the drawbacks attached to the other approach can be avoided.

1.2 Objective

To promote the application of SFRCC in steel moment resistant frame building to improve their seismic performance, the following research goals are established.

The first goal is to develop a strong and compact shear connection to transfer the force between the steel and concrete components by taking advantage of the high toughness and high strength of SFRCC. A strong and compact steel-concrete shear connection has the benefit of providing a solution for high force concentration occasions and relaxing the spacing requirement for connection. In this study, a high strength steel-concrete connection with a stud cluster embedded in SFRCC is proposed to achieve larger shear capacity than the conventional connections. Unlike the conventional steel stud-concrete connections in which the studs spacing is limited to six times stud diameter in longitudinal and four times studs diameter in transverse respectively, the proposed steel studs-SFRCC connection features a very small stud spacing. In addition, in the conventional stud-concrete shear connection, steel reinforcement or steel mesh wire are used to reinforce the concrete slab and prevent the split failure. In the proposed stud-SFRCC shear connection, it is expected to eliminate the steel reinforcement due to the high toughness and tensile strength of SFRCC.

The proposed stud-SFRCC shear connection is featured with densely arranged studs and elimination of steel reinforcement, which are out of the scope in the current design codes. It is necessary to develop strength evaluation method for this shear connection. According to the possible failure modes of the stud-SFRCC shear, strength evaluation method should take into consideration various design parameters such as the dimension of studs, material properties of SFRCC, and number and arrangement of group-arranged studs.

For the beam-column connection, a new type beam-column connection with the feature of “weld-free” is proposed as illustrated in Fig. 1.2. The welding between the column face and beam

flange is removed. A portion of the floor slab around the column is cast by SFRCC. Through a group of headed studs, two SFRCC slabs (SFRCC diaphragms hereinafter) on both the top and bottom beam flange are adopted to connect the beam and column. The headed studs are closely welded on the beam flange to transfer the beam force to the SFRCC diaphragm. In this new beam-column connection, the beam hinge is expected to form at the edge of SFRCC diaphragm. Such a system is difficult to achieve by using conventional concrete, because the main steel reinforcement has to be densely placed in the slab, and also the small spacing of studs would cause trouble to cast concrete and bring high stress concentration in slab. All of these difficulties can be overcome by using SFRCC.

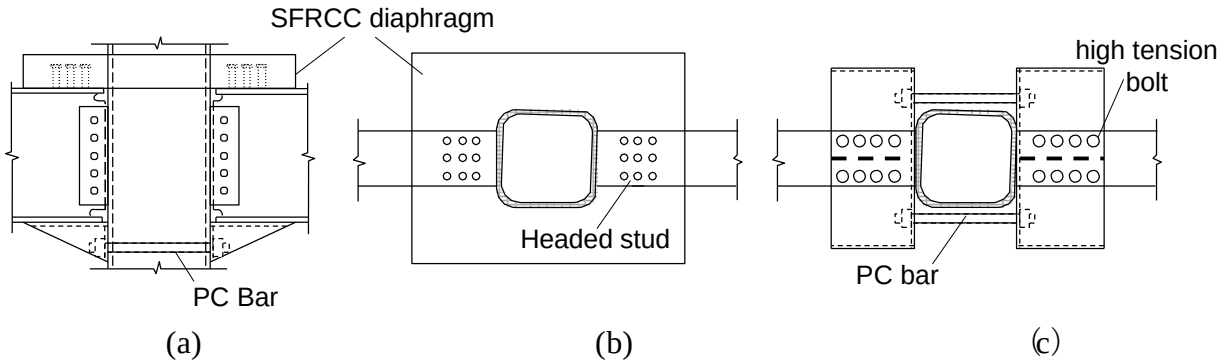

Figure 1.2 Proposed beam-to-column connection with floor slab functioning as exterior diaphragm: (a) Elevation, (b) Plan of top flange, (c) Plan of bottom flange

For rehabilitation of the damaged beam-column connection, a new method using SFRCC is proposed as illustrated in Figure 1.3. In the proposed method, widened steel plates are used to replace the fractured or buckled bottom flange and SFRCC replaces the damaged RC slab portion in the vicinity of column. The replaced SFRCC slab is to serve as a external diaphragm. SFRCC is high in both compressive and tensile strength, which make it possible to eliminate steel reinforcement in the slab and sustain the force transferred through headed studs. A gap between the SFRCC slab and existing RC slab is arranged intentionally to move the plastic hinge away from the column face. The proposed method aims at taking advantage of the high toughness of SFRCC to form the plastic hinge of the beam at the edge of the SFRCC slab, and taking advantage of the high tensile strength of SFRCC to transfer force without primary steel reinforcement.

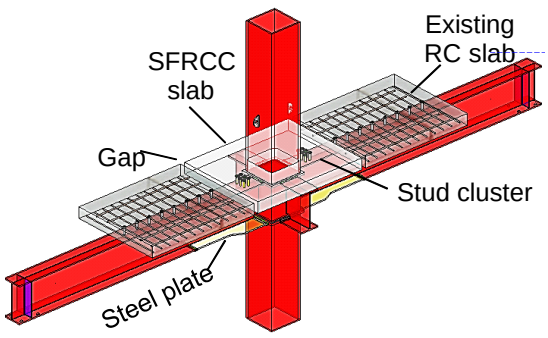

Figure 1.3 Proposed repair method to damaged beam-to-column connection

1.3 Organization

This dissertation consists of seven chapters. Chapter 1 presents the introduction of this study and Chapter 7 presents the conclusions. Chapters 2 to 6 constitute the main part of the dissertation.

Chapter 2 presents a brief review on the history, classifications of FRCCs and detailed introduction on background, history of development and mechanical properties of SFRCC. Special attention is given mechanical characteristic of SFRCC. Due to the tailored microstructure of the matrix and large amount of steel fiber added to the matrix, SFRCC is remarkable for its high strength and high toughness as well as the capacity to cooperate with densely placed main steel reinforcements. Several applications that using SFRCC on steel structural buildings are presented, and typical constitute models developed in the past research are introduced.

Chapter 3 presents a series of push-out tests for the proposed headed stud-SFRCC shear connection. Feasibility of the proposed stud-SFRCC shear connection, in which headed stud connectors are closely placed in SFRCC slab without reinforcement rebars, is validated by the pilot test. The effects of design parameters such as the stud number and stud arrangement and fiber volume ratio of SFRCC are investigated by the parametric tests. Finally, a supplemental test is conducted to check the effect of reserved cyclic loading on the strength and performance of the stud-SFRCC shear connection.

Chapter 4 presents an investigation on the strength evaluation of the stud-SFRCC shear connection. First, a FEM model is developed to reproduce the mechanical behavior of the stud-SFRCC shear connection and calibrated to the push-out tests. Strength evaluation methods on the two failure modes, the stud shear fracture and slab split, are discussed separately. For the failure mode of stud shear fracture, the strength for single stud and per stud strength for stud group is investigated. The effects of various design parameters, such as the stud dimension, material properties of studs and SFRCC, and the existence of the stud welded collar, on the strength of single stud are examined. For a group arranged studs, the relationship between the stud spacing and per stud strength is classified. As for the slab split failure mode, a strength evaluation method proposed in the past is adopted for stud-SFRCC shear connection. The derivation process of the evaluation formula is introduced. Necessary adjustments to the formula are given to make it suitable for application to the stud-SFRCC shear connection. The estimated per stud strengths given by the evaluation method based on the two failure modes are compared to avoid the slab failure of the stud-SFRCC shear connection.

Chapter 5 presents tests on the proposed beam-to-column connections with SFRCC floor slab diaphragms. First, two full-scale and three reduced-scale subassemblies are tested. The seismic performance and failure mechanism of the beam-to-column connection with SFRCC slab are examined based on a series of cyclic loading tests. The beam hinging mechanism is examined if it is achieved at the end of the SFRCC slab by the arrangement of a sufficient number of studs and rebar in the SFRCC slab. Finite element analysis associated with the tests is presented, and a few issues

regarding the design of the proposed connection are noted. Numerical models are developed to enhance the understanding the behavior of the proposed beam-to-column connection. A parametric study is also conducted to investigate the effect of the number of studs, slab size, and the amount of rebars on the elastic stiffness and strength of the proposed connection.

Chapter 6 presents a two-phase experimental program undertaken to evaluate the repaired performance of a new repair method using SFRCC for rehabilitation of the damaged beam-to-column connection with presence of the RC slab. The phase 1 test reproduces the damage pattern of steel moment beam-to-columns with the presence of RC floor slab. According to the damage pattern, a repair scheme using SFRCC is implemented. The design approach of proposed repair method is presented following the introduction to the practical repair scheme. The Phase 2 test was conducted to investigate the repaired performance. The repair performance is checked by comparison of both in terms of the strength and elastic stiffness. The bending behavior of the representative beam sections is compared for the repaired connection. The force resisting contributions of SFRCC and rebars is also discussed. The strain distribution on the critical failure faces is examined by both the test data and analysis results from the verified FEM model.

REFERENCES

Bache, H. H. (1981a). "Compact reinforced concrete composite, basic principles." *Aalborg Portland, Aalborg*.

Bache, H. H. (1981b). "Densified Cement/Ultra-Fine Particle-Based Materials." Portland, A, Ottawa, Ontario, Canada.

Brandt, A. M. (2008). "Fibre Reinforced Cement-Based (FRC) Composites After Over 40 Years of Development in Building and Civil Engineering." *Composite Structures*, 86(1-3), 3–9.

Cui, Y., and Nakashima, M. (2011). "Hysteretic Behavior and Strength Capacity of Shallowly Embedded Steel Column Bases with SFRCC Slab." *Earthquake Engineering & Structural Dynamics*, 40(13), 1495–1513.

Engelhardt, M. D., and Sabol, T. A. (1998). "Reinforcing of steel moment connections with cover plates: benefits and limitations." *Engineering Structures*, 20(4–6), 510–520.

Kaneko, Y., Mihashi, H., and Kirikoshi, K. (2000). "Mechanical Properties and Application of Steel Fiber Reinforced Cementitious Composite." *Cement Science and Concrete Technology*, 54, 723–730.

Kaneko, Y., Mihashi, H., and Kirikoshi, K. (2005). "Beam-Column Joint with Steel Fiber Reinforced Cementitious Composite in Steel Structures." *Journal of Advanced Concrete Technology*, 3(2), 321–330.

Kaneko, Y., Mihashi, H., Kirikoshi, K., and Abe, T. (2000). "Simplified uniaxial constitutive model of steel fiber reinforced cementitious composite." *AIJ Journal of Technology and Design*, 11, 5–8.

Kaneko, Y., Mihashi, H., and Osaku, R. (2006). "Column Base System of Steel Structures Employing

Steel Fiber Reinforced Cementitious Composite and Deformation Characteristics: Evaluation of Joint-Deformation Based on Mechanical Model for Shear Failure." *Journal of Structural and Construction Engineering. Transactions of AIJ*, (609), 181–188.

Kesner, K. E., and Billington, S. L. (2003). "Experimental Response of Precast Infill Panel Connections and Panels Made with DFRCC." *Journal of Advanced Concrete Technology*, 1(3), 327–333.

Kim, Y. J., Oh, S. H., and Moon, T. S. (2004). "Seismic behavior and retrofit of steel moment connections considering slab effects." *Engineering structures*, 26(13), 1993–2005.

Kirikoshi, K., Kaneko, Y., Mihashi, H., and Abe, T. (2000). "Material Properties of Steel Fiber Reinforced High Strength High Ductility Cementitious Composite." *Journal of Architecture and Building Science*, 115(1464), 1–4.

Nakashima, M., Inoue, K., and Tada, M. (1998). "Classification of damage to steel buildings observed in the 1995 Hyogoken-Nanbu earthquake." *Engineering Structures*, 20(4–6), 271–281.

Shi, C. (2008). "High-Performance Construction Materials Science and Applications." *Professional book*, (C. Shi and Y. L. Mo, eds.).

Uang, C. M., Yu, Q.-S. "Kent," Noel, S., and Gross, J. (2000). "Cyclic testing of steel moment connections rehabilitated with RBS or welded haunch." *Journal of Structural Engineering*, 126(1), 57–68.

LIST OF PUBLICATIONS

Refereed papers (full paper reviewed by multiple):

[1] Gang Wu, Zhishen Wu, **Yunbiao Luo**, Zeyang Sun, Xianqi Hu. "Mechanical Properties of steel-FRP Composite Bar under Uniaxial and Cyclic Tensile Loads." ***Journal of Materials in Civil Engineering, ASCE.*** Vol.22, pp.1056-1066, October, 2010.

[2] **Yunbiao Luo**, Kazuaki Hoki, Yao Cui, Masayoshi Nakashima, "Experimental Study on Strength of Composite Structural Connection with Steel Studs Closely Arranged in SFRCC Slab", 19th JSSC Annual Symposium, Tokyo, pp.215-220, November, 2011.

[3] Kazuaki Hoki, **Yunbiao Luo**, Masayoshi Nakashima, "Strength Evaluation of Composite Structural Connection with Steel Studs Embedded in SFRCC Slab." ***Journal of Structural and Construction Engineering***, ***AIJ***, Vol.77, No. 675, pp.975-984, June, 2012 (in Japanese).

[4] **Yunbiao Luo**, Kazuaki Hoki, Kazuhiro Hayashi, Masayoshi Nakashima, "Effects of Fiber Volume Ratio and Reversed Cyclic Loading on Behavior of Steel Stud-SFRCC Composite Connection", 20th JSSC Annual Symposium, Tokyo, pp.189-194, November, 2012.

[5] Yao Cui, **Yunbiao Luo**, Masayoshi Nakashima. "Development of steel beam-to-column connections using SFRCC slabs." Engineering Structures, 52, 545–557, 2013.

Conference Papers (Abstract reviewed):

[1] **Yunbiao Luo**, Kazuaki Hoki, Yao Cui, Masayoshi Nakashima, "Strength of Headed Studs in Composite Structural Connection with SFRCC," presented at the Behaviour of Steel Structures in Seismic Areas, STESSA 2012, Santiago, Chile, pp. 653–659, January, 2011.

[2] **Yunbiao Luo**, Gang Wu, Zhishen Wu, Ming Zhang, and Xianqi Hu. "Experimental study on flexural performance of RC beams strengthened with near surface mounted steel fiber composite bars (SFCB)". Proceedings of 9th international symposium on fiber reinforced polymer reinforcement for concrete structures, Sydney, Australia, July, 2009.

Domestic Conference Papers

[1] **Yunbiao Luo**, Yao Cui, Toru Tai, Shuhai Song, Masayoshi Nakashima. "Hysteretic Behavior for Steel Beam-to-column Connections Using SFRCC Floor Slabs : Part.4 Finite Element Analysis." Summaries of Technical Papers of Annual Meeting Architectural Institute of Japan. C-1, No. 787–788, 2010.

[2] Toru Tai, Shuhai Song, Yao Cui, **Yunbiao Luo**, Masayoshi Nakashima. "Hysteretic Behavior

for Steel Beam-to-column Connections Using SFRCC Floor Slabs: Part 3: Procedure to Estimate Maximum Strength." Summaries of Technical Papers of Annual Meeting Architectural Institute of Japan. C-1, No. 785–786, 2010.

[3] Shuhai Song, Toru Tai, Yao Cui, **Yunbiao Luo**, Masayoshi Nakashima. "Hysteretic Behavior for Steel Beam-to-column Connections Using SFRCC Floor Slabs: Part 1: Design of specimens and test setup." Summaries of Technical Papers of Annual Meeting Architectural Institute of Japan. C-1, No. 781–782, 2010.

[4] Yao Cui, Toru Tai, Shuhai Song, **Yunbiao Luo**, Masayoshi Nakashima. "Hysteretic Behavior for Steel Beam-to-column Connections Using SFRCC Floor Slabs: Part 2: Test Results." Summaries of Technical Papers of Annual Meeting Architectural Institute of Japan. C-1, No. 783–784, 2010.

[5] **Yunbiao Luo**, Kazuaki Hoki, Shuhai Song, Masayoshi Nakashima. "Strength Evaluation of Composite Structural Connection with Steel Studs Embedded in SFRCC Slab: Part 2 Numerical Study." Proceedings of Technical Papers of Kinki Branch, No. 51, pp.309–312, 2011.

[6] Kazuaki Hoki, **Yunbiao Luo**, Shuhai Song, Masayoshi Nakashima. "Strength Evaluation of Composite Structural Connection with Steel Studs Embedded in SFRCC Slab: Part 1 Push-out Test." Proceedings of Technical Papers of Kinki Branch, No. 51, pp.305–308, 2011.

[7] Shuhai Song, **Yunbiao Luo**, Kazuaki Hoki, Masayoshi Nakashima. "Strength Evaluation of Composite Structural Connection with Steel Studs Embedded in SFRCC Slab: Part 3 Proposal Equation for Strength Evaluation.." Proceedings of Technical Papers of Kinki Branch, No. 51, pp.313–316, 2011.

[8] Kazuaki Hoki, **Yunbiao Luo**, Shuhai Song, Masayoshi Nakashima. "Mechanical Behavior of Composite Structural Connection with Steel Studs Embedded in SFRCC Slab Part 1 Push-out Test." Summaries of Technical Papers of Annual Meeting Architectural Institute of Japan. C-1, No. 1149–1150, 2011.

[9] **Yunbiao Luo**, Kazuaki Hoki, Shuhai Song, Masayoshi Nakashima. "Mechanical Behavior of Composite Structural Connection with Steel Studs Embedded in SFRCC Slab Part 2 Numerical Analysis." Summaries of Technical Papers of Annual Meeting Architectural Institute of Japan. C-1, No. 1151–1152, 2011.

[10] **Yunbiao Luo**, Kazuaki Hoki, Kazuhiro Hayashi, Masayoshi Nakashima. "Performance of High Strength Connection with Steel Studs Embedded in SFRCC Slab: Part 1 Effect of Fiber Volume Fraction." Proceedings of Technical Papers of Kinki Branch, No. 52 pp.509–512, 2012.

[11] Kazuaki Hoki, **Yunbiao Luo**, Kazuhiro Hayashi, Masayoshi Nakashima. "Performance of High Strength Connection with Steel Studs Embedded in SFRCC Slab: Part 2 Effect of Cyclic

Loading." Proceedings of Technical Papers of Kinki Branch, No. 52 pp.513–516, 2012.

[12] **Yunbiao Luo**, Kazuaki Hoki, Kazuhiro Hayashi, Masayoshi Nakashima. "Study on Effects of Steel Fiber Volume and Cyclic Loading in High-Strength Composite Structural Connection with Steel Studs Embedded in SFRCC Slab : Part 1 : Effect of Steel Fiber Volume." Summaries of Technical Papers of Annual Meeting Architectural Institute of Japan. C-1, No. 1157–1158, 2012.

[13] Kazuaki Hoki, **Yunbiao Luo**, Kazuhiro Hayashi, Masayoshi Nakashima. "Study on Effects of Steel Fiber Volume and Cyclic Loading in High-Strength Composite Structural Connection with Steel Studs Embedded in SFRCC Slab : Part 1 : Comparison of Cyclic and Monotonic Loading Behavior." Summaries of Technical Papers of Annual Meeting Architectural Institute of Japan. C-1, No. 1159–1160, 2012.

Refereedpapers in Chinese

[1] **Yunbiao Luo**, Gang Wu, Zhishen Wu, Ming Zhang, and Xianqi. Hu. "Bearing Capacity Analysis of RC Beams Strengthened with Near Surface Mounted Steel FRP Composite Bar," ***Journal of Building Structures***, Vol.31, No. 8, pp.86–93, Aug, 2010 (in Chinese).

[2] Gang Wu, **Yunbiao Luo**, Zhishen Wu, Min Zhang, and Xianqi Hu "Experimental and Theoretical Studies on the Mechanical Properties of steel-FRP Composite Bars." ***China Civil Engineering Journal***,Vol.43, No.3, pp.53-61, March, 2010 (in Chinese)

[3] **Yunbiao Luo**, Gang Wu, Zhishen Wu, Xianqi Hu, and Ye Tian. "Study on Fabrication Technique of Steel Fiber Composite Bar (SFCB)." ***Earthquake Resistant Engineering and Retrofitting***, Vol.31, No. 1, pp.28–34, 2009 (in Chinese)

[4] **Yunbiao Luo**, Gang Wu, Zhishen Wu, Min Zhang, and Xianqi Hu, "Numerical Study on Seismic Performance of Steel Fiber Composite Bar (SFCB) Reinforced Concrete Column." ***Earthquake Resistant Engineering and Retrofitting***, Vol.31, No.1, pp.14–20, 2009 (in Chinese).

[5] Gang Wu, **Yunbiao Luo**, Zhishen Wu, Xianqi Hu, and Min Zhang. "Experimental Study on Mechanics Properties of Steel Fiber Composite Bar (SFCB) Under Uniaxial Load." ***Earthquake Resistant Engineering and Retrofitting***, Vol.31, No.1, pp.1–7, 2009 (in Chinese).

[6] Gang Wu, **Yunbiao Luo**, Zhishen Wu, Min Zhang, and Xianqi Hu. "Experimental Study on Flexural Performance of RC Beams Strengthened with Near Surface Mounted Steel Fiber Composite Bars (SFCB)." ***Earthquake Resistant Engineering and Retrofitting***, Vol.31, No.1, pp.8–13, 2009 (in Chinese).

CHAPTER 2

Material Properties and Applications of SFRCC

2.1 Introduction

Fiber reinforced cementitious composites (FRCCs) have brought striking advances and gained enormous momentum in recent years. Substantial progress on the development of FRCCs provides a unique opportunity for civil engineering and an enormous potential in exploiting excellent mechanical properties and in adopting them to engineering applications. This is especially true for the new subclasses of FRCCs, the High Performance Fiber Reinforced Cementitious Composites (HPFRCCs) and Ultra High Fiber Reinforced Cementitious Composites (UHPFRCCs), because their production and handling is similar to that of traditional construction materials and their introduction into engineering practice is straightforward.

Steel fiber reinforced cementitious composites (SFRCC) is one of the UHPFRCCs for use in structures. It was developed based on CRC (compact reinforced composite), one of UHPFRCCs, which was invented in Denmark in 1980s by (Bache 1987). This material is made with a very low water/binder ratio (0.18 or smaller), and contains from 2 to 6% steel fibers, providing matrix strengths of 140 to 400 MPa. The strength properties of SFRCC are comparable to those of conventional concrete, for example the tensile strength of SFRCC is approximately four times larger of that of conventional concrete (15MPa for SFRCC and 3MPa for conventional concrete). Because of the presence of steel fibers, the deformation and energy absorption capacities of SFRCC are significantly improved.

The objectives of this chapter are to present the SFRCC material properties of interest for advanced structural applications and to present the models for mechanical behavior needed for further structural analysis and design.

2.1.1 Overview and classification of FRCCs

Fiber Reinforced Cementitious Composites is a term commonly used for a broad class of materials. Every FRCC consists of two basic components: a cementitious base material called matrix, which is reinforced by steel or synthetic fibers. The most common reason why fibers are added to the material is to improve its tensile ductility or its tensile strength. In fact, the idea to use fibers in order to improve the tensile properties of brittle materials is old. The ancient Egyptians realized the efficiency of composite materials in reinforcing mud bricks with straw.

The development of modern FRCCs reaches back to early 1960s. In early days of fiber reinforced materials, straight steel fibers at relatively low volume contents were used to improve the mechanical properties of traditional concrete. The addition of larger volume contents of fibers was mainly prevented by workability problems.

In order to improve workability and restrict "balling" of fibers, the quantity of cement was increased and the amount of coarse aggregate was reduced. Further improvement of workability could be achieved by the introduction of high-range water-reducing admixtures. Hereby the possible volume content of fibers could be increased. Together with the use of improved cementitious matrices with fewer coarse aggregate and carefully adjusted properties, this finally leads to the high performance fiber reinforced materials we know today. Typical examples for modern high performance materials are: Engineered Cementitious Composites (ECC) (Li 2003) sometimes also called Ductile Fiber Reinforced Cementitious Composites (DFRCC), Hybrid Fiber Concretes (HFC) or Multi Scale Fiber Reinforced Cementitious Composites (MSFRCC), Compact Reinforced Composites (CRC) (Bache 1988) and Reactive Powder Concretes (RPC). A short overview and simple classification will be given to these high performance composites in the following sections.

Stang and Li (Stang and Li 2004) suggested a foundmental classification of FRCCs. Figure 2.1 gives an overview of different high performance composites discussed here and their classification.

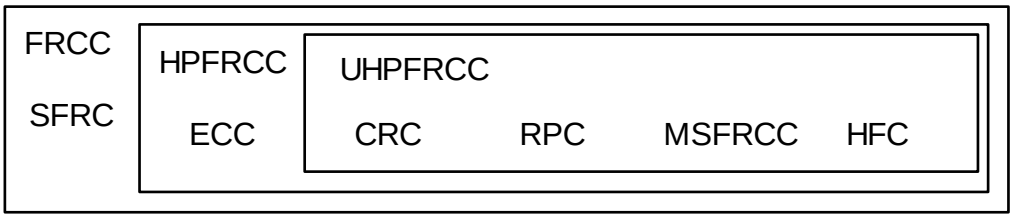

Figure 2.1 Overview of different FRCCs and their classification

Steel fiber reinforced concrete (SFRC) is the first FRCCs material that was developed in early 1960s. SFRC consists of a normal strength concrete matrix containing fine and coarse aggregate, which is reinforced by relatively long straight steel fibres at low volume contents. A good overview of the material and its applications is given in (ACI 544 1973; Balaguru and Shah 1992).

Although SFRC shows certain improvements compared to normal concrete, it was not considered to be a high performance material. The criterion which separates a High Performance Fibre Reinforced Cementitious Composite (HPFRCC) form a traditional FRCC, such as SFRC, is its response in tension. A FRCC can be considered to be a HPFRCC when the material which tension is stain hardening in the inelastic regime. Strain hardening of FRCCs can delay localization and lead to multiple cracking and structural ductility even without the addition of structural reinforcing bars. For this reason they are called high performance fibre reinforced cementitious composites. A typical HPFRCC is ECC (Engineering Cementitious Composite) (Li 2003).

On the other hand, another class of FRCCs was developed with focus on the mechanical characteristics of very high compressive strength rather than the tensile strain hardening behavior.

This type of FRCCs with extremely high compressive strength is called Ultra High Performance Cementitious Composite (UHPFRCC). The developement of UHPFRCC was launched by the invention of Densified Small Particle (DSP) concrete (Bache 1981b) in 1970's, which was later commercialized under the name Densit®. By targeting a very dense packing of particles in the concrete matrix, Bache (Bache 1981b) presented a concept to creat a concrete with an extremely high compressive strength, in which a large amount of cement and fine particles such as silica fume is used. The application of superplasticizers ensured effective dense packing and sufficient workability even at low w/b-ratios from 0.14 to 0.20. Coarse aggregate are eliminated and small-sized but extremely strong aggregate are used instead. Using these procedures, considerable compressive strengths, typically between 120 and 250 MPa can be obtained. However, DSP concrete has a significant drawback that with increasing compressive strength the brittleness increases as well. Later, it was found that this problem can be solved by adding steel fibres to the cementitious matrix, which increases the fracture energy and thereby reduces the brittleness. UHPFRCCs were developed based on this idea. UHPFRCCs are a sub group of HPFRCCs combining the ductility of strain hardening cementitious composites with the high compressive strength of DSP concrete. Originating from this concept, research continued following slightly different paths which lead to the development of Compact Reinforced Concrete (CRC), Reactive Powder Concrete (RPC), Multi Scale Fibre Reinforced Cementitious Composite (MSFRCC) and Hybrid Fibre Concrete (HFC). The following Table 2.1 summarizes the high performance FRCCs. Although DSP concrete and SFRC are not high performance FRCCs, they are still included in the above summary because they represent essential stages in the development of the other FRCCs.

Table 2.1 Summary of Typical High Performance FRCCs (Trub 2011)

	Abbr.	Name	Commercial Product	Period of Development
	SFRC	Steel Fiber Reinforced Concrete	-	1960s
	DSP	Densified Small Particle Concrete	Densit®	1970s
UHPFRCCs	CRC	Compact Reinforced Composite	CRC TECH®	1990s
	RPC	Reactive Powder Concrete	DUCTAL®	1990s
	MSFRCC	Multi-Scale Fiber Reinforced Cementitious Composite	CEMTECH®	1990s
	HFC	Hybrid Fiber Concrete	-	2000s
HPFRCCs	SIFCON	Slurry Infiltrated Fiber Concrete	-	1980s
	ECC	Engineered Cementitious Composite	-	1990s
	HPFRC	High Performance Fiber Reinforced Concrete	-	2000s

Although these FRCCs seem to be quite similar in compositions, the individual material may show a completely different mechanical behavior and performance. Among the Typical FRCCs listed in Table 2.1, Compact Reinforced Composite (CRC) is remarkable for its high tensile

strength, compressive strength and shear strength, while ECC has excellent performance on tensile ductility due to its strain hardening and high tensile strain. Trub (Trub 2011) conducted comprehensive comparison to typical FRCCs on mechanical performances for the field of structural applications. If an application requires a structural element of conventional strength but that has an extremely high inherent ability to maintain its integrity and prevent any premature and non-ductile failure mechanism, then ECC is the most suitable option. If on the other hand an application requires a slender structural element consisting of a high performance composite that has a very high compressive, tensile and shear strength, then CRC is the optimal choice.

CRC is characterized by a high tensile and compressive strength accompanied by outstanding cooperation with steel reinforcement due to its excellent bonding properties. Due to these excellent mechanical properties, it is believed that the use of CRCs instead of conventional concrete can be very beneficial to structural elements subjected to seismic action, significantly simplifying the construction of plastic hinges zones, improving their serviceability and ensuring at least equivalent structural safety. In this thesis, since the goal is to develop and promote the application of CRCs in steel moment resistant frame building structures, a better understanding on the mechanical properties and characteristics of CRCs is essential. For this reason, more detailed information on CRCs is presented in this chapter.

It should be noted that, when referring to the literature, not all authors use the same terminology for the same type of FRCCs, e.g., in Japan CRCs is called SFRCC. To keep consistence on terminology in this thesis, the term SFRCC is used to refer to the compact reinforced composite (CRC) throughout this thesis.

2.1.2 Organization

The chapter consists of four parts. In Section 2.2, the development of advanced cementitious materials is briefly reviewed, a basic insight into the microstructure of SFRCC is provided, and an example for the preparation of SFRCC is presented. Also, the main advances of UHPFRC composition with respect to other concrete materials are briefly discussed. Section 2.3 focuses on the material properties of SFRCC. The material properties, relevant for the structural application, are divided into mechanical characteristics, mechanical properties, and other material properties. The structural application of SFRCC is introduced in section 2.4, with a particular emphasis on applications in improving the seismic performance of building structures and applications in practical engineering. Finally, Section 2.4 focuses on the material's behavior in uniaxial compression and in uniaxial tension. Several constitutive material models are presented for the description of both compressive and tensile behavior.

2.2 Basic Principles of SFRCC

2.2.1 Background of development of SFRCC

In early 1980s, Bache from Portland Cement and Concrete Laboratory in Aalborg discovered that the

density of the cementitious matrix can be increased significantly by adding a large amounts of small fillers (like fly-ash and silica fume). Base on this discovery, Bache presented a concept to create a concrete with extremely high compressive strength by making very dense packing of the particles in the concrete matrix. The application of supper plasticizers ensured effective dense packing and sufficient workability even at a low water-to-binder ratio. The coarse aggregates were also eliminated by substituting with extremely strong aggregates such as quarts sand. Such procedure leads to a concrete with an extremely high compressive strength, which Bache called Densified Small Particle (DSP) concrete (Bache 1981b, 1988). The DSP concrete was later commercialized under the name Densit®. However, DSP concrete has a significant drawback that with high compressive strength typically from 120 MPa to 250 MPa its brittleness is magnified as well.

To solve this problem, Bache added short steel fibers to the cementitious matrix, which has increased the fracture energy and thereby reduced the brittleness. This idea gave birth to an UHPFRCCs that he called Compact Reinforced Composite (CRC) (Bache 1981a, 1990, 1995), which is the origin of the SFRCC studied in this thesis.

Since the birth of CRC, much research on CRC has been conducted. Many researcher adopted different terminologies for this type of UHPFRCCs, such as Ultra High-strength Steel Fiber Reinforced Concrete (UHSFRC) (Nielsen 1995, 1996), Steel Fiber Reinforced Cementitious Composite (SFRCC) (Kaneko et al. 2000, 2001), among others. To keep consistence on terminology in this thesis, only the term SFRCC is used to refer to this type of UHPFRCC.

Comparison of mechanical properties obtained so far for different cementitious material, such as normal concrete, HSC, FRC, ECC, and SFRCC, is given in Table 2.2 (Bache 1981 and Li 1998). The SFRCC material has excellent mechanical properties, including improvement in all strength properties, fracture toughness, and exhibit strain-hardening behavior beyond first cracking in tension. Moreover, the tensile strains at which the SFRCC matrix cracks would increase exceed 3 mm/m, whereas ordinary reinforced concrete typically cracks at strains of about 0.1 to 0.2 mm/m. Such properties promised SFRCC matrix is able to follow the tensile deformations of the rebar as a coherent, crack-free, load-bearing body right up to yielding of the rebar. Because of the significant improvement in mechanical properties, SFRCC is recommended to work with the main reinforcements, even over-reinforced, in a given structural member. The bending behavior of SFRCC-beam and conventional concrete beam are compared in Fig.2.2 (b). For the SFRCC beam, the strains correspond to the maximum strains with ideal linear elastic behavior. The load capacity is extremely high, which is about 5to 10 times that of the normal reinforced concrete. However, the very high load capacities of the SFRCC beam are primarily secured by the densely arranged main reinforcement, which transmits about 70to 80% of the load at the start of yielding (Bache 1987, Kaneko et al. 2001).

Table 2.2 Comparison on mechanical properties

	Compressive strength (MPa)	Tensile strength (MPa)	Tensile strain (mm/m)	Elastic Modulus (GPa)	Fracture Energy (N/m)
Concrete	30	3.0	0.2	29.6	40
HSC	>60	3.0	0.2	29.6	120
FRC	55	4.3	0.35	32.5	4900
SFRCC	128	27.2	3.0	50	8130
ECC	33	4.3	22.5	24.1	35 kJ/m^2

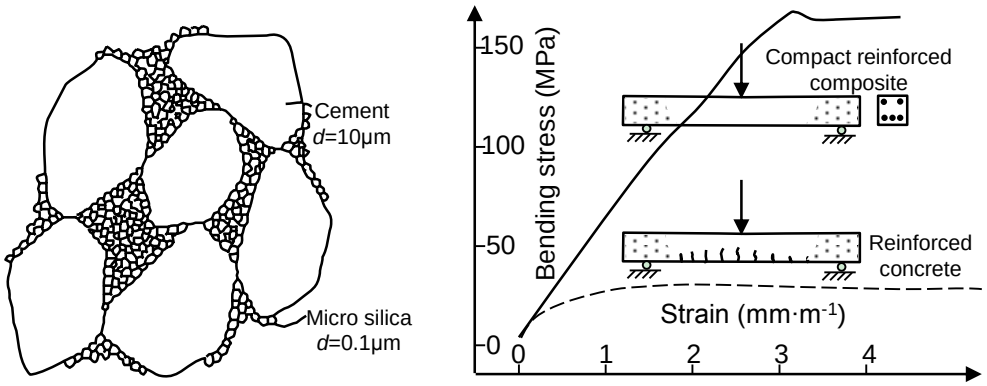

Figure 2.2 Characteristic of SFRCC

2.2.2 Microstructure of SFRCC

The mechanical performances of SFRCC are determined by the properties of its principal constituents: the cementitious matrix, and the fibers, and their interaction. The conceptual bases of the advanced UHPFRCCs matrix are discussed in this section. It aims to examine the relationship between the mechanical performance and microstructure of the material, but no in depth explanation on concrete chemistry and formation of the microstructure are provided. Types of fibers used in SFRCC and the role of matrix-fibers interaction are also discussed.

Cementitious matrix

The cementitious matrix of SFRCC has all the characteristics of the DSP concrete, which have already been mentioned. More specifically, these is an extremely dense packing of particles, which is achieved by adding a large amounts of ultra-fine silica fume (up to 10 to 50% by volume), a low w/b-ratio of 0.16 to 0.18 thanks to the use of superplasticizers, and a distinct gap grading (large diameter ratio). The structure of the fresh paste is shown in Figure 2.3, in which it is compared with that of ordinary cement paste and superplasticized cement paste. In the conventional cement paste, the dense packing is prevented by surface forces. But with the advent of effective dispersants that eliminate the locking effect of surface forces, it became possible to pack fine particle systems densely on the basis of purely geometrical principles, as illustrated in Figure 2.3 (b). The cement particles (particle size 5-10μm) were very densely packed and secured by an efficient dispersing agent. The

space between them was additionally filled with a high concentration of silica fume (particle size 0.1-0.2μm) (Figure 2.3 (c)). This results in very dense, extremely high-strength concrete.

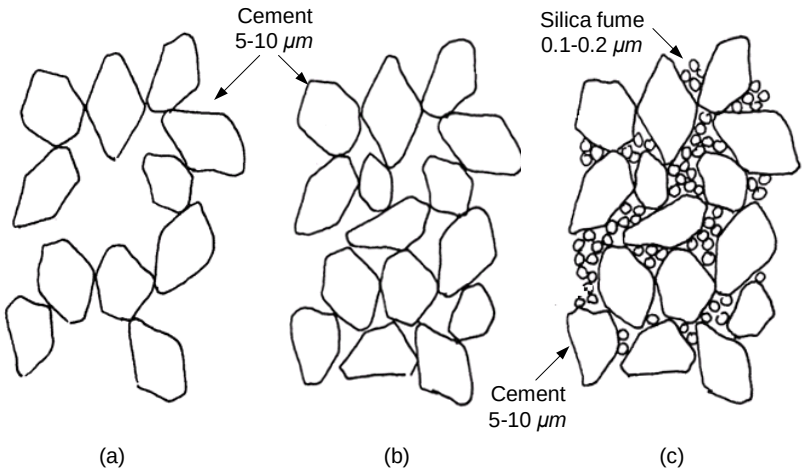

Figure 2.3 The structural of the matrix:
(a) Normal concrete; (b) High strength concrete; and (c) SFRCC (CBL No.41)

Due to the addition of 10 to 50% of ultra-fine silica fume particles that occupy the space between the cement particles in the densely packed matrix, the water requirement is considerably reduced. The amount of water required to achieve an easily castable fluid densely packed matrix is thus considerably lower than that used in ordinary superplasticized concrete mortar (typically between 0.12 and 0.18 by weight in comparison with 0.3 by weight for ordinary concrete mortar).

The much densified hardened structure results in much improved anchorage to steel fiber besides the strength and durability. Figure 2.4 illustrates the difference on mechanical anchorage of straight steel fiber when it is embedded in conventional cement paste and densely packed cement paste. While steel fiber is not fixed firmly in conventional cement matrix, the mechanical fixation of the fine fibers is greatly increased by incorporating the silica fume particles in the spaces between the densely packed cements, because the dimensions of roughness and wave configuration on the reinforcement that are necessary for "mechanical locking" of the reinforcement in the matrix are thereby strongly reduced.

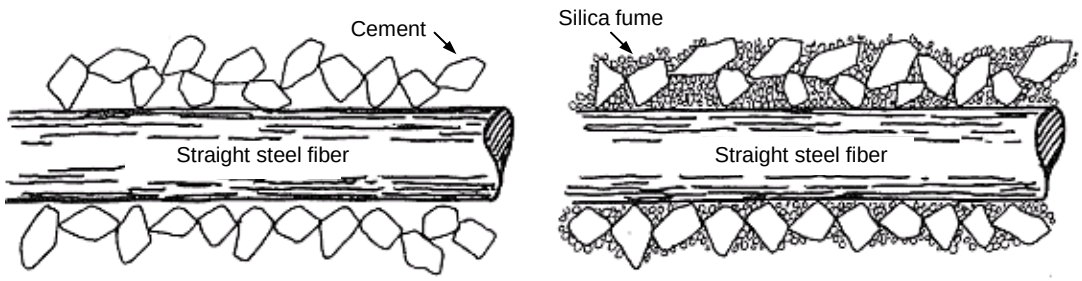

Figure 2.4 Straight fibers embedded in different paste:
(a) cement paste; (b) densely packed cement paste (CBL No.40)

Fine aggregates

The aggregates used in SFRCC need to be strong and small. If the strength of the aggregates is not sufficient, fracture surfaces will pass through them, which would mean that the high strength of the cementitious binder is not exploited to its maximal extent. The reason for not using large particles is that they are the major source of inhomogeneity, which in turn are responsible for defects in the matrix and crack initiation. Smaller the aggregate grains are, the better is the homogeneity of the matrix. Those are why hard and small aggregates such as quartz sand or calcined bauxite are usually used.

Fibers in SFRCC

The densely packed cement matrix exhibits ultra strong compressive strength. However, the material has proved to be extremely brittle. Steel fibers were therefore adopted to conquer the serious brittleness problem. Fibers work with the matrix utilizing two mechanisms: the spacing mechanism and the crack bridging mechanism. Based on the spacing mechanism, a large number of fibers are required to be distributed uniformly within the concrete matrix to arrest any existing micro-crack that could potentially expand and create a macro-crack. The second mechanism, termed crack bridging, requires stronger fibers with adequate bond to the cement matrix, in which most fibers are pull out at a load close to that required to break the fibers. As mentioned, a high content of fine, strong and stiff fibers in SFRCC are well fixed to the matrix due to the densely packed material structure. In addition, because of the special rheological properties of the fresh matrix, it is possible to mix far more fibers in the densely packed cement matrix than in conventional concrete.

2.2.3 Preparation of SFRCC

Figure 2.5 shows the mixing components of SFRCC in this study. Compositions for per m^3 SFRCC were summarized in Table 2.3. High strength steel straight fiber (diameter of 0.4mm, length of 12.0mm, and tensile strength of 1350MPa) was used in SFRCC at 6% of the mix by volume. The binder used was Densit cement, from Aalborg Portland Company. The mix had a water-to-binder ratio of 0.17. The fine aggregate was refined sand of uniform size distribution and with the maximum size of 0.4 mm in diameter. The SFRCC is mixed in a planetary mixer in the following manner:

- Mix Densit® cement (binder, micro silica fume) and sand dry for 180 seconds.
- Add water-reducing agent to water.
- Add water incrementally, mixing for 300 seconds between additions.
- Stop mixer to scrape sides as necessary.
- Add fiber, mix for 120 seconds.

The mass has a dry appearance for the first few minutes of mixing after water had been added. It then undergoes a rather sudden change into a doughy mass, which is gradually changed into a softer, glossy, viscous mass, indicating complete saturation of the system.

Table 2.3 Compositions for 1 m^3 SFRCC

Densit cement	Fine aggregate	Steel fiber	Water	Water/binder ratio
871	1179	444	152	0.17

Figure 2.5 Mixing components of SFRCC

2.3 Material Properties of SFRCC

2.3.1 Mechanical characteristic of SFRCC

There are three characteristics for SFRCC distinguished with other cement materials.

High strength

Probably the most interesting mechanical property which distinguishes SFRCC form other FRCCs is their relatively high direct tensile strength. Depending on the fiber content the maximum tensile strength can range from 6 MPa to 15 MPa. Crack initiation will usually start at a tensile stress of about 6 MPa to 7 MPa. The use of short fibers leads to a high tensile strength of the SFRCC because the fibers have a similar size and spatial distribution as microcracks which enable them to effectively arrest microcrack propagation.

As expected, SFRCC have the high compressive strength of Ultra High Strength Concretes such as DSP concrete. Depending on the quality of the aggregates and on the thermal curing conditions the compressive strength reaches from 120 MPa to 300 MPa. A compressive strength of 150 MPa is achieved with quartz aggregates whereas the 400 MPa are reached when using calcined bauxite and heat curing. The typical module of elasticity of SFRCC is about 45 GPa.

Because of the high tensile strength SFRCC also have high shear strength. In fact, in many structural applications the shear reinforcement can be omitted and the shear stresses are carried by the fiber reinforced matrix alone (Bache 1990).

Dense main rebar

The most important mechanism in SFRCC is a further, more remarkable increase in the tensile strain capacity of the ductile, fiber-reinforced matrix material, which is achieved by very effective fixation to very dense main reinforcement. As already mentioned, an extremely high quantity of short stiff steel fibers is employed in SFRCC. The fibers mainly have an influence on the tensile strength and ductility of SFRCC on a material level. However, the fibers are not able to improve the ductility on a structural level significantly.

One of the reasons why the combination of SFRCC and high reinforcement contents is so successful are the good bond characteristics between the fiber reinforced matrix and the

reinforcement bars.

There are several reasons for this. The first is the high density of the matrix. The significant content of silica fume results in large contact surfaces and by consequence large frictional forces. Secondly, the short steel fibers provide ductility and control crack formation in the anchorage zone of the reinforcement bars. In fact, when using a high volume content of fibers (6 %) the material ductility of CRCs is sufficient to give the matrix approximately the same strain capacity before crack localization as mild steel has at yielding. This means that up to yielding of the longitudinal reinforcement there is no visible cracking. The good bond characteristics result in shorter rebar anchorage lengths which are typically between 5 and 10 bar diameters (Aarup et al. 2000). It is also due to these good bond properties that the high reinforcement ratios used in CRCs are possible.

In reinforced SFRCC, the main rebar act as the stiff frame that divides the matrix into many small volumes. The crack zone deformations are thereby distributed over the body when the material is forced, during tensile deformation, to follow closely the elongations of the main reinforcement.

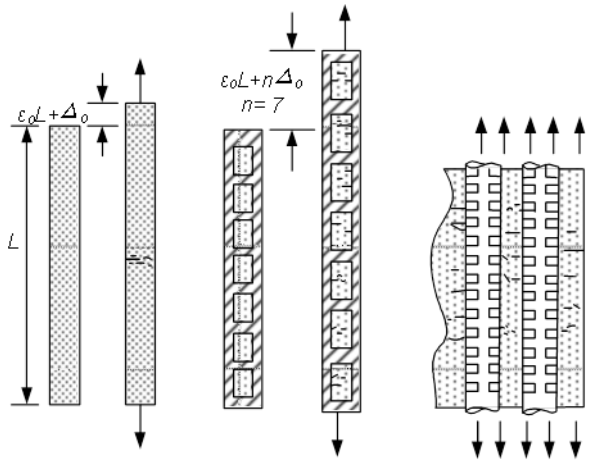

(a) (b) (c)

Figure 2.6 Tensile deformation of bar of different material: (a) cement bar; (b) cement fixed by a stiff frame; and (c) SFRCC with densely arranged rebar (Elfgren, 1989)

The difference between reinforced SFRCC and ordinary reinforced concrete is that SFRCC is able to ensure effective utilization of a very large amount of reinforcement while remaining substantially free of cracks. In normal reinforced concrete (with a moderate amount of reinforcement), the concrete cracks past the reinforcement, which resists the tensile stresses but retains acceptable inner coherence. If we attempt to use more reinforcement, the concrete cracks and splits, and the inner coherence is lost. With SFRCC we are now able to achieve an extremely large amount of reinforcement without losing inner coherence and without cracking for loads right up to yield limit of steel.

2.3.2 Mechanical properties of SFRCC

SFRCC with such a large amount of fiber (6% in volume) while maintaining an acceptable workability is manufactured using a large content of water reducing agent composed of much micro silica and with water/binder ratios, e.g. 0.2 or lower. Compared to conventional concrete,

SFRCC has a remarkably large compressive strength and a better tensile behavior in terms of the strength and the ductility, as shown in Fig.2.11. Because of the large content of steel fibers, the matrix becomes very ductile. It is made possible to utilize reinforcing bars much more effectively, since the development of large cracks is effectively prevented by the bridging of steel fibers. Furthermore, the distance between reinforcing bars and the cover layer to the reinforcement can be as small as 15mm, because relatively small sizes of the fibers and fine aggregate are used. Because of the highly compacted material structures of SFRCC, durability and resistance to corrosion are also to be good so that such a small cover to reinforcement is still sufficient.

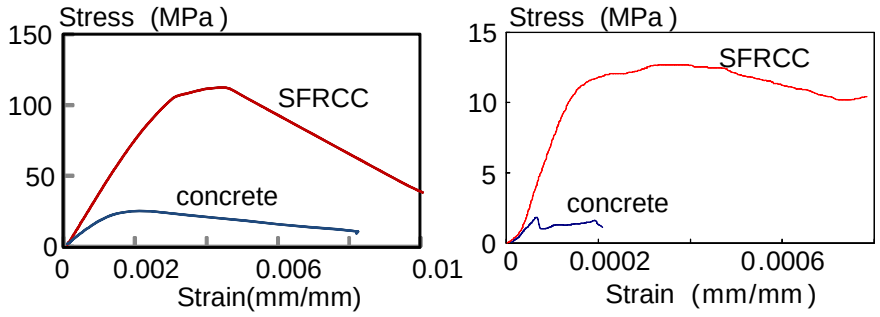

Figure 2.7 Stress-strain behavior of concrete and SFRCC: (a) in compression; (b) in tension

Table 2.4 summaries the mean values of a number of properties of SFRCC from the material tests conducted by the CRC TECH Company. In the tests, the standard composition of SFRCC with quarts sand and 6 % volume ratio of steel fibers typically has a compressive strength of 140 MPa measured on cylinders at 28 days. The flexural strength is approximately 25 MPa. In design calculations a characteristic compressive strength of 115 MPa is used, and the Young's modulus of SFRCC is about 45 GPa.

Table 2.4 Material properties for SFRCC with different fiber volume ratio

Steel fiber content	**2%**	**4%**	**6%**
Compressive strength (MPa)	125	135	140
Flexural strength (MPa)	16	20	25
Uniaxial tensile strength (MPa)	6	10	14
Splitting strength (MPa)	10	15	20
Shear strength (MPa)	6	9	12
Young's modulus (GPa)	42	44	46

The fiber content of the matrix was selected as one of the test parameters. From Table 2.4 the material properties are indicated as a function of the fiber content of the matrix. Interpolation between the values can be used to assess the properties of other fiber contents. The uniaxial tensile strength corresponds to the maximum stress that can be transferred in a cracked section.

2.3.3 Other properties of SFRCC

The exceptional durability is another important property of SFRCC. The very dense matrix and the lack of capillarity lead to an extremely low permeability. This means that there is practically no corrosive agent transport and freezing–thawing problems can be eliminated. As a result, SFRCC elements rarely have a concrete cover of more than 10 mm even if they are exposed to an aggressive environment.

SFRCC structural members have a problem with respect to their fire resistance. Because the matrix is so dense the water inside the pores cannot escape and high vapor pressures might build up. This can lead to spalling or explosive failure of SFRCC elements if they are exposed to high temperatures.

2.4 Application of SFRCC

In this section, a literature survey will be carried out to given an overview on the applications of SFRCC, including those being proceeding in fundamental research and those already applied in practical engineering constructions. Before that, a short overview will be given to the general FRCCs to generalize the typical classes of applications and the advantages of using FRCCs in these structural applications.

FRCCs have been used in numerous applications, either as stand-alone or in combination with reinforcing bars and prestressing tendons; they have also been used as support materials in repair and rehabilitation work. Naaman (Naaman and Reinhardt 2006) summarized the main classes of application of FRCCs as shown in Figure 2.8. Examples of the applications include impact and seismic resistant structures, jacketing for repair and strengthening of beams and columns, and, in the case of steel, encased beams and trusses to improve ductility and fire resistance. Particular applications of high performance fiber reinforced cement composites include bridge decks and special structures such as offshore platforms, space-craft launching platforms, super high rise structures, blast resistant structures, bank vaults, and other high-end structures. The particular design property or properties that would call for the use FRCCs in a particular application is illustrated in Figure 2.9.

When the use the FRCCs is considered as an alternative in design, it is generally not necessary throughout the structure. Commonly, only a small part (a selected zone) of the structure may be in need of strengthening or toughening. In such a case their use is often competitive and economically justifiable.

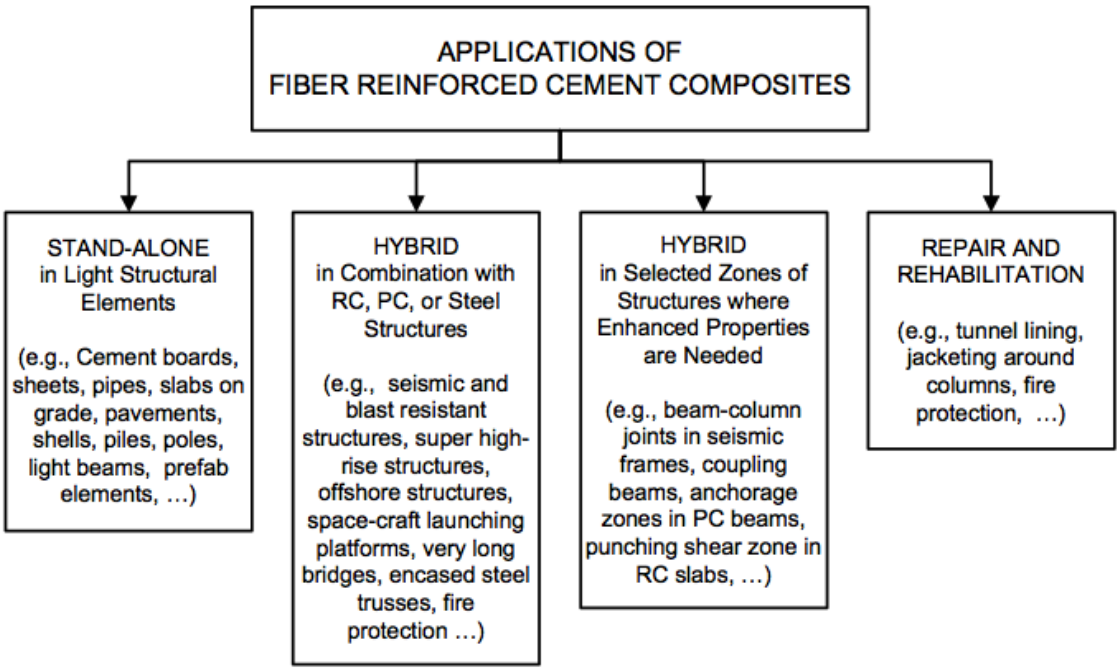

Figure 2.8 Classes of applications of fiber reinforced cement composites (Naaman and Reinhardt 2006)

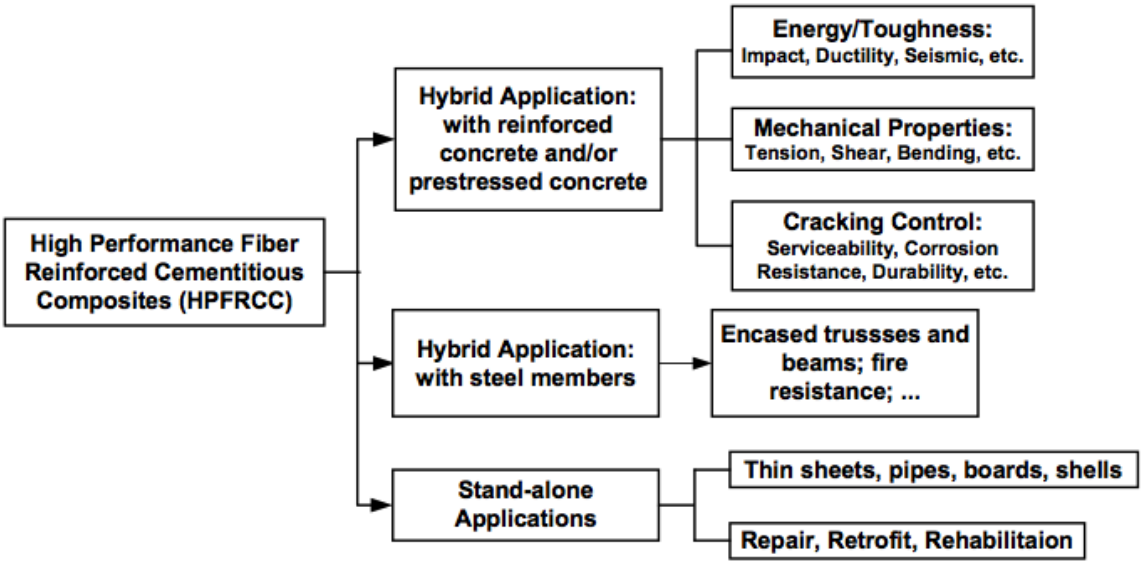

Figure 2.9 Advantages of using HPFRC composites in structural applications (Naaman and Reinhardt 2006)

After a broad view on the applications of FRCCs and their respective advantages on specific structural applications, the applications of SFRCC both in practical use and under fundamental research are introduced with more detail below.

2.4.1 Application of SFRCC in practical engineering

A commercial application of SFRCC is JointCast (Aarup et al. 2000; Aarup 2004). The concept of JointCast is to exploit the good bond characteristics and the high strength of SFRCC for in-situ cast

joints between precast elements. JointCast is used for the assembly of moment resisting frames from precast elements and for joining precast slabs. Figure 2.10 shows two images of such a joint between precast floor slabs. Although the SFRCC joints appear promising, the major field of SFRCC applications is limited to thin, precast structural elements such as staircases, balconies or bridge deck panels (Kaptijn and Blom 2005). These elements make use of the very high flexural strength of SFRCC, which allows them to be extremely thin and architecturally elegant. Another application of SFRCC is their use for impact resistant structures such as defense shelters, gas tanks, nuclear reactor containment shields and crash barriers (Bindiganavile et al. 2002).

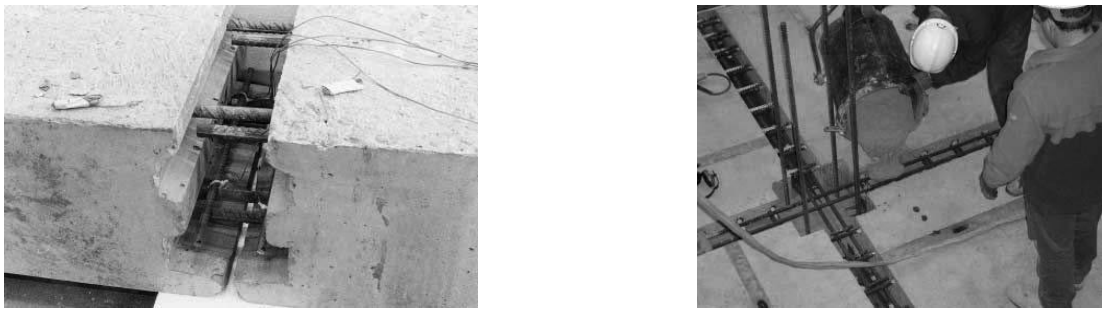

(a) (b)

Figure 2.10 Precast column and floor slabs are joined in-situ by JointCast (CRC)

2.4.2 Research on application of SFRCC

The application of UHPFRCCs in building structure is mainly focused on the beam-to-column connection and concrete-encased steel column base in steel building structure, and RC beam, RC column and beam-to-column connection in RC structures. In addition, some research was conducted to application on steel beam-to-RC column connection.

An overview of the applications of UHPFRCCs to improve the seismic performance of building structures is introduced in Table 2.5. The target applications of SFRCC are mainly on the steel structural members, such as steel beam-to-column connection and steel concrete encased column base.

Table 2.5 Reference on seismic application of UHPFRCCs

UHPFRCCs	Target applications	Purpose and merit of utilization	References
SFRCC	Steel beam-to-column connection	Labor-saving construction	(Kaneko et al. 2002, 2003)
	Steel concrete-encased column base	Labor-saving construction	(Kaneko et al. 2006, 2007)
RPC	RC beam	Improve shear, bending strength and ductility	(Shirai et al. 2003; Ujiie et al.2005)
	RC column	Damage mitigation; improve shear, bending strength and ductility	(Ueda et al. 2004; Ukai et al. 2009)
	RC beam-to-column connection	Improve shear, bending strength and ductility	(Shoko et al. 2004;Suzuki et al. 2008;Takatsu et al. 2009)
	Steel beam-to-RC column connection	Improve seismic performance; Damage mitigation.	(Kubo et al. 2009)

In the research by Kaneko (Kaneko et al. 2002; Kaneko, Mihashi, and Osaku 2006), as an alternative to conventional welded or bolted connection commonly used in steel beam-to-column connection, Kaneko et al. proposed a simple beam-to-column connection using steel fiber reinforced cementitious composites (SFRCC) with fiber volume ratio of 6%.

In the research by Kaneko et al. (Kaneko et al. 2007; Kaneko, Mihashi, and Osaku 2006; Kaneko, Mihashi, Kirikoshi, et al. 2006), a simple junction column base was proposed. The high strength high ductility steel fiber reinforced cementitious composite (SFRCC) with fiber volume ratio of 6% was applied to the encased part of the junction column base. Also, by taking advantage of the high strength, high ductility of SFRCC and high adhesive capacity between SFRCC and steel rebar, the height of the encased part was reduced to below the level of floor slab, therefore the constructability was improved and the building space occupied by the encased part was effectively utilized.

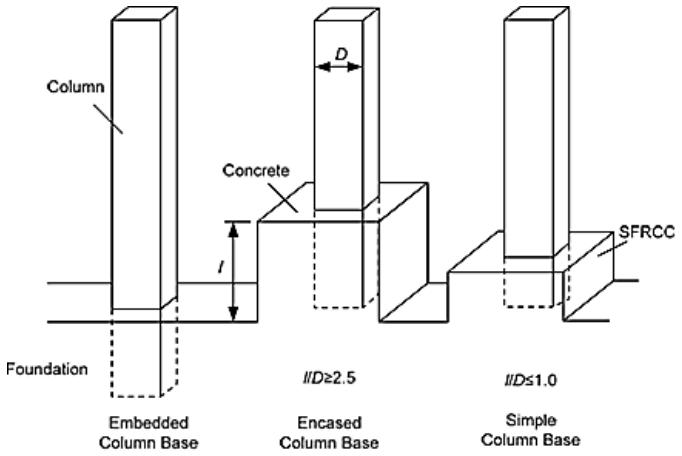

(a)

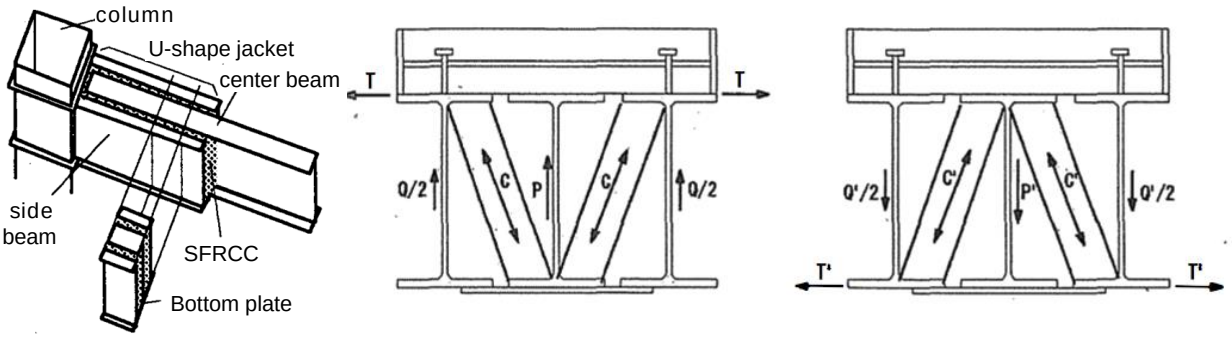

(b)

Figure 2.11 Application of SFRCC steel moment resistant frame building: (a) Steel column base; (b) Steel beam-to-column connection with U-shape bracket

In Table 2.5, along with SFRCC, the applications of another type of typical UHPFRCC, Reactive Powder Concrete (RPC), were presented. RPC has many similarities with SFRCC because both materials share the basic principles of using DSP (Densified Small Particle) concrete. However, from the common starting point of DSP concrete, SFRCC and RPC devolved in two different directions. In SFRCC, the main improvement compared to DSP concrete is a higher tensile strength by adding a

large amount of short steel fiber, whereas in RPC the main improvement is a higher ductility improved by adding medium sized straight steel fibers. From Table 2.5, it is noted that the main application fields of RPC is on RC members and RC-to-Steel connections. The difference in the application field indicated the different advantages of SFRCC and RPC. In steel structures, since steel is ductile material, SFRCC part is used to help triggering the ductile behavior of the steel members, thus strength and toughness are required. On the other hand, in RC structure members made of RPC itself are expected to behavior ductile, thus the ductile performance is more desirable.

2.5 Constitutive Model for SFRCC

As introduced in the previous section, SFRCC exhibits material behavior significantly different from that of normal concrete. Therefore, a different uniaxial strain-stress (σ-ε) relation model is needed for SFRCC. The damage plasticity model, a material model commonly used for the analysis using ABAQUS, can be adopted to represent the material characteristics of SFRCC. This model considers the failure mechanism of tensile cracking and compressive crushing independently.

To accurately predict the structural performance of SFRCC components under different loading conditions, a good constitutive material model is needed for structural scale simulations. Since SFRCC is a relatively new material, research on its constitutive model is very limited, especially on the tensile behavior, which is more difficult to measure than compressive behavior. (Nielsen 1995) did a series of basic material research on SFRCC. According to the test results, the uniaxial tensile and compressive strengths increase with the fiber parameters. A satisfactory linear relationship is found, depending on the fiber reinforcement index $V_f(L_f/d_f)$, where V_f is the fiber content by volume, L_f is the length of fiber, and d_f is the diameter of fiber, as follows.

Tensile strength:

$$f_t = 6V_f\frac{L_f}{d_f}, \quad 1 \le V_f\frac{L_f}{d_f} \le 4 \tag{2.1}$$

Compressive strength and peak compressive strain:

$$\left.\begin{aligned} f_c &= \left(145 + 25V_f\frac{L_f}{d_f}\right)\ \text{MPa} \\ \varepsilon_c &= \left(0.24 + 0.18V_f\frac{L_f}{d_f}\right)\ \% \end{aligned}\right\} \quad 0 \le V_f\frac{L_f}{d_f} \le 5 \tag{2.2}$$

Fracture energy:

$$G_F = (0.1 + V_f\frac{{L_f}^2}{d_f}) \tag{2.3}$$

If W/B =0.20 and V_f =6% is adopted and the fiber is taken to be 12.0 mm in length and 0.4 mm in diameter, the basic material properties of SFRCC adopted in this analysis are as shown in Table 2.6.

Table 2.6 Basic material properties of SFRCC in analysis

Tensile strength f_t (Mpa)	Fracture energy G_f (Mpa)	Compressive strength f_c (Mpa)	Compressive strain ε_c (%)
10.8	121.6	190	0.564

In uniaxial compression SFRCC exhibits a rather ductile failure. From a qualitative point of view, the compressive behavior of SFRCC does not differ substantially from the behavior of ordinary concrete, and it is possible to model it with a slight adaptation of material laws used for ordinary concretes. According to the research of Nielsen (1995), the compressive stress-strain relationship of the model is defined by the following equation,

$$\frac{\sigma}{f_c} = \frac{\beta(\frac{\varepsilon}{\varepsilon_c})}{\beta - 1 + (\frac{\varepsilon}{\varepsilon_c})^{\beta}}, \qquad \beta \geq 1 \tag{2.4}$$

where ε_c and f_c are the compressive strain and stress at the peak point; the σ-ε relation is graphically shown in Figure 2.12 (a).

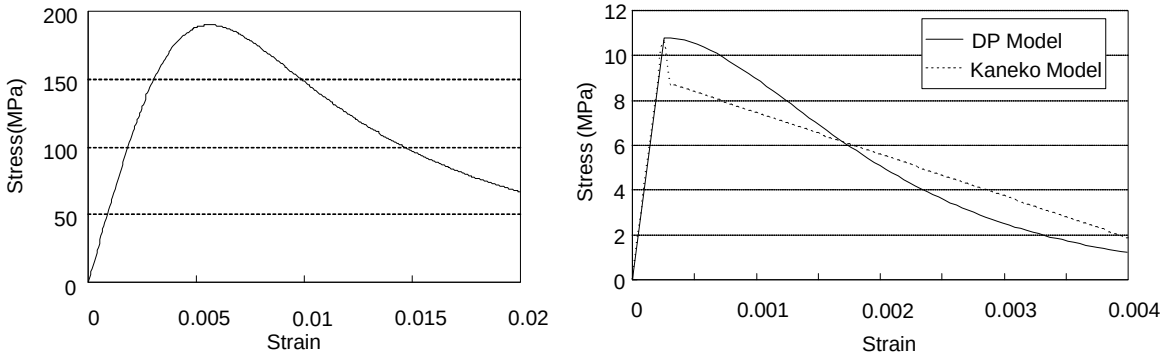

Figure 2.12 Material Property: (a) compression; (b) tension

However, the tensile constitutive model of SFRCC was not described in the report of Nielsen (1995). Here, the tensile constitutive model of SFRCC proposed by Kaneko (2000can be used for the basic tensile behavior of SFRCC. Then, the equations associated with the tensile behavior proposed by Lee and Fenves (1998) can be adopted to describe the tensile behavior of SFRCC in the damaged plasticity model.

The tensile constitutive model of SFRCC proposed by Kaneko (2000) is introduced as follows. The behavior of SFRCC in tension is described by the linear stress-strain relation (σt-εt) before cracking, and thereafter by the bilinear stress-strain relation as shown in Eq. (2.5) and (2.6).

Before cracking:

$$\sigma_t = E_0 \varepsilon_t \,, \quad \varepsilon_t \leq \varepsilon_{cr} \tag{2.5}$$

After cracking:

$$\sigma_t = \alpha f_t \left(\frac{\varepsilon_{tu} - \varepsilon_t}{\varepsilon_{ut} - \varepsilon_{cr}} \right), \quad \varepsilon_{cr} \leq \varepsilon_{tu} \tag{2.6}$$

$$\alpha = \frac{2G_f}{1.5 f_t w_{tcr\,1}} \tag{2.7}$$

$$W_{tcr2}=2W_{tcr1}=2.0 \text{ mm} \tag{2.8}$$

Where E_0 is an initial elastic modulus, f_t is a tensile strength; w_t is a crack opening displacement, w_{tcr1} is the critical crack opening displacement, $w_{tcr,2}$ is the crack opening displacement at the complete release of stress, G_f is the fracture energy, and α and β are the strength reduction coefficient. In this model, β=0.5α and w_{tcr1}=1.0 mm are adopted.

2.6 Summary

In this chapter, a brief look at the history and classifications of FRCCs is noted. The background and history of development of SFRCC is introduced. The SFRCC material properties important for structural applications are presented.

SFRCC is a new, advanced fiber reinforced cementitious material of elaborated composition, with remarkably superior mechanical strengths and toughness in comparison to concrete. The compressive strength of SFRCC is higher than 120 MPa; tensile strength, in the range of 20 MPa, is characterized by significant ultimate strain (more than 3 %), and the excellent corporation with dense main reinforcements due to the much improved bonding performance.

The combination of these properties postulates more advanced structural application:

(1) The high tensile strengths and high shear strength, suggest that in many structural applications the reinforcement can be omitted and the tensile or shear stresses are carried by the fiber reinforced matrix alone.

(2) The good bond characteristics between the SFRCC and the reinforcement bars and the toughness of SFRCC, suggest that main reinforcement can be embedded in SFRCC to transfer forces through compact structural elements.

REFERENCES

ACI 544. (1973). "State-of-the-Art Report on Fiber Reinforced Concrete." *ACI Journal Proceedings*.

Aarup, B. (2004). "CRC- A Special Fibre Reinforced High Performance Concrete." 8, RILEM Publications SARL.

Aarup, B., Karlsen, J., and Lindström, G. (2000). "Fiber Reinforced High Performance Concrete for in-Situ Cast Joints." *Proceedings from International Symposium on High Performance Concrete*, 25–27.

Bache, H. H. (1981a). "Compact reinforced concrete composite, basic principles." *Aalborg Portland, Aalborg*.

Bache, H. H. (1981b). "Densified Cement/Ultra-Fine Particle-Based Materials." Portland, A, Ottawa, Ontario, Canada.

Bache, H. H. (1987). "High-Strength Concrete Development Through 25 Years."

Bache, H. H. (1988). "The New Strong Cements: Their Use in Structures." *Physics in Technology*, 43.

Bache, H. H. (1990). "Compact Reinforced Composite."

Bache, H. H. (1995). "Concrete and Concrete Technology in a Broad Perspective." *In Nordic Symposium on Modern Design of Concrete Structures*, Aalborg University, Denmark.

Balaguru, P. N., and Shah, S. P. (1992). *Fiber Reinforced Cement Composites*. McGraw Hill, Inc., New York.

Bindiganavile, V., Banthia, N., and Aarup, B. (2002). "Impact Response of Ultra-High-Strength Fiber-Reinforced Cement Composite." *ACI Materials journal*, 99(6).

CRC. (n.d.). "Introduction to fibre reinforced UHPC." <http://www.crc-tech.com/> (May. 22, 2013).

Kaneko, Y., Mihashi, H., and Kirikoshi, K. (2007). "Column Base System of Steel Structures Employing Steel Fiber Reinforced Cementitious Composite: Fracture Mode and Deformation Characteristics of Applied Model with Joint-Height Ratio of 0.75 and 0.65." *Journal of structural and construction engineering. Transactions of AIJ*, (619), 179–185.

Kaneko, Y., Mihashi, H., Kirikoshi, K., and Abe, T. (2000). "Simplified uniaxial constitutive model of steel fiber reinforced cementitious composite." *AIJ Journal of Technology and Design*, 11, 5–8.

Kaneko, Y., Mihashi, H., Kirikoshi, K., and Abe, T. (2001). "New Application Field of Steel Fiber Reinforced Cementitious Composites: Experiment on Column-Beam Joint in Steel Structures." *Journal of architecture and building science*, (14), 119–122.

Kaneko, Y., Mihashi, H., Kirikoshi, K., and Abe, T. (2002). "Simple Column-Beam Joint of Steel Structures Employing Steel Fiber Reinforced Cementitious Composite: Experimental Verification on Structural Performance of Joint." *Journal of Structural and Construction Engineering. Transactions of AIJ*, (558), 219–225.

Kaneko, Y., Mihashi, H., Kirikoshi, K., and Suwanai, Y. (2006). "Simple Column Base System of Steel Structures Employing Steel Fiber Reinforced Cementitious Composite: Experiment on Structural Performance of Basic Model and Applied Model." *Journal of Structural and*

Construction Engineering. Transactions of AIJ, (600), 179–186.

Kaneko, Y., Mihashi, H., and Osaku, R. (2006). "Column Base System of Steel Structures Employing Steel Fiber Reinforced Cementitious Composite and Deformation Characteristics: Evaluation of Joint-Deformation Based on Mechanical Model for Shear Failure." *Journal of Structural and Construction Engineering. Transactions of AIJ*, (609), 181–188.

Kaneko, Y., Mihashi, H., and Sasaki, T. (2003). "Column-Beam Joint of Steel Structures Employing Steel Fiber Reinforced Cementitious Composite and Deformation Characteristics: Joint-Spring Evaluation Based on Mechanical Model for Shear Failure." *Journal of Structural and Construction Engineering. Transactions of AIJ*, (573), 169–176.

Kaptijn, N., and Blom, J. (2005). "A New CRC (Compact Reinforced Composite) Bridge Deck." Amsterdam, The Netherlands.

Li, V. C. (2003). "On Engineered Cementitious Composites (ECC): A Review of the Material and Its Applications." *Journal of Advanced Concrete Technology*, 1(3), 215–230.

Naaman, A. E., and Reinhardt, H. W. (2006). "Proposed Classification of HPFRC Composites Based on Their Tensile Response." *Materials and Structures*, 39(5), 547–555.

Nielsen, C. V. (1995). "Ultra High-Strength Steel Fibre Reinforced Concrete, Part I, Basic Strength Properties of Compresit Matrix." *Technical University of Denmark. Series R*, 323.

Nielsen, C. V. (1996). "Tensile Postcrack Behavior of Steel Fiber Reinforced Ultra-High-Strength Concrete." *ACI SPECIAL PUBLICATIONS*, 159, 231–246.

Stang, H., and Li, V. C. (2004). "Classification of Fiber Reinforced Cementitious Materials for Structural Applications." *6th RILEM Symposium on Fiber-Reinforced Concretes (FRC) - BEFIB 2004*, 197–218.

Trub, M. (2011). "Numerical Modeling of High Performance Fiber Reinforced Cementitious Composites." Institute of Structural Engineering Swiss Federal Institute of Technology.

CHAPTER 3

Push-out Test of Stud-SFRCC Shear Connection

3.1 Introduction

3.1.1 Background

Steel-concrete composite structures make use of the advantages of both the concrete and steel, it has been widely used in the world. In steel-concrete composite structural components, the transfer of shear forces at the interface between steel and concrete is commonly achieved by shear connectors. Headed stud shear connectors are the most widely used shear connectors in many types of steel-concrete composite elements such as composite girders (Figure 3.1(a)), composite column bases (Figure 3.1(b)), and boundary elements of steel frame-infill wall systems (Figure 3.1(c)).

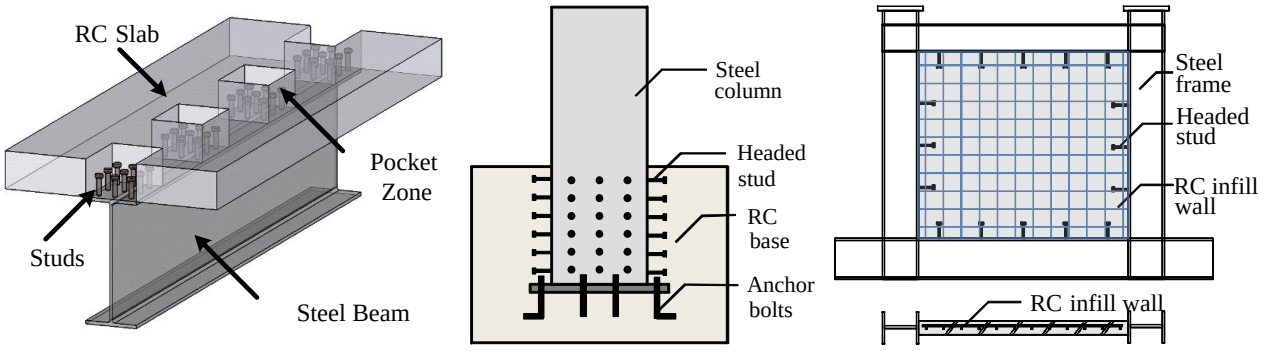

(a) (b) (c)

Figure 3.1 Applications of steel-concrete composite elements with headed studs: (a) Composite girder; (b) Composite column base; (c) Steel frame with infill RC wall.

Behavior and design of stud shear connectors has been investigated extensively for many years. Many studies, for example (Viest 1956; Ollgaard et al. 1971; Oehlers and Coughlan 1986; An and Cederwall 1996; Okada et al. 2006), indicated that the performance of stud shear connectors is controlled primarily by the shank diameter, height, and tensile strength of the stud, compressive strength and elastic modulus of concrete, and reinforcement detailing. Based on extensive push-out tests, Ollgaard et al. (Ollgaard et al. 1971) developed design formulas to predict the stud bearing capacity, and many codes, for example (ANSI/AISC 360 2010; Architectural Institute of Japan (AIJ) 2010; Eurocode 4. EN 1994 2004; Oehlers 1995), adopted the formulas. Until now, most research on

stud connections focused on steel studs embedded in normal concrete or mortar. In steel-concrete connections whose force transfer is achieved by shear studs, a combination of large stiffness and toughness of steel and high brittleness of concrete typically results in a brittle fracture of the concrete such as the pry out failure (Anderson and Meinheit 2005) or the splitting failure (Oehlers 1989). To avoid this, steel reinforcement is always required (Oehlers 1995). Minimum spacing between the connectors is stipulated in design codes (ANSI/AISC 360 2010; Architectural Institute of Japan (AIJ) 2010; Eurocode 4. EN 1994 2004) to make the connectors fully develop the respective strengths.

In some studies (Oehlers and Coughlan 1986; An and Cederwall 1996; Okada et al. 2006; Doinghaus et al. 2003), the behavior and strength of headed stud connectors embedded in other materials, such as the high strength concrete and fiber reinforced cementitious composite. Oehlers conducted a number of push-out tests and found that studs embedded in strong concrete were stiffer than those in weaker concrete, since stronger concrete can provide larger restraining effect on the studs. An et al. (An and Cederwall 1996) conducted push-out tests in normal and high strength concrete indicated that the studs embedded in high strength concrete had larger shear strengths than those in normal strength concrete. Okada et al. (Okada et al. 2006) conducted a study on the stud shear strength in which stud spacing and concrete strength were adopted as the test parameters. They indicated that the strength reduction caused by small stud spacing can become less notable when stronger concrete is applied. Li et al. (Qian and Li 2009) carried out push-out tests of headed studs in ECC (engineering cementitious composite, a type of tension ductile cementitious composite), plane concrete, reinforced concrete, and reinforced SFRC (steel fiber reinforced concrete). Their results showed that the tensile ductility of ECC relaxed the high stress concentration at the stud-concrete interface and prevented the connection from brittle concrete failure. These studies suggest that using stronger and more ductile concrete would lead us to improved performance (in terms of both the strength and ductility) of steel-concrete connections using steel studs.

Recently, a high performance material called fiber reinforced cementitious composites (FRCC hereafter) was developed and has shown its superiority to conventional concrete and mortar in terms of the strength and ductility. The FRCC consists of two basic components: the cementitious base material called “matrix” and the steel or synthetic fibers used to reinforce the matrix and improve the tensile strength and/or the tensile ductility. Various fibers have been applied for FRCC, for examples, steel fibers and glass fibers among others.

Among the types of FRCC, a newly developed steel fiber reinforced cement composites (SFRCC hereafter) (An and Cederwall 1996; Nielsen 1995; Buzzini and Dazio 2006) is most remarkable for its high tensile strength. SFRCC consists of densified small particles (An and Cederwall 1996) and a relative large volume fraction (2%~6%) of short steel fibers. Depending on the fiber content, the maximum tensile strength can reach 20 MPa, while the tensile strength of other FRCCs range typically from 2 to 8 MPa (Stang and Li 2004). Because of its high tensile strength, SFRCC also has high shear strength. This advantage makes it possible to reduce or even omit steel reinforcement in its structural applications (An and Cederwall 1996; Buzzini and Dazio 2006). It is also notable that a high compressive strength of 120 to 150 MPa and a high modulus of elasticity of 45 GPa is achieved by quartz aggregates (Kaneko et al. 2000; Nielsen 1995).

In summary of the introduction, steel headed studs are most commonly adopted in the shear connections between the concrete and steel components; the stud shear connection can be strengthened when high strength concrete is adopted; and a new material named SFRCC, which is characterized by large strength in both tension and compression relative to conventional concrete, has been made available.

In reference to these situations, the aim of this study is to explore the possibility of achieving strong and compact shear connections in steel-concrete composite components using SFRCC and steel headed studs. Here, "compact" means the connection in which the transfer of forces is achieved in a small region. Specific subjects to examine are as follows:

(1) The feasibility to arrange studs densely within a small region in the shear connection.

(2) The feasibility to cast slabs in the shear connections without reinforcing bars.

After the pilot study to check the feasibility of the proposed stud-SFRCC shear connection, parametric study is conducted to examine the influence of various parameters as below"

(3) The number and arrangement of studs.

(4) The variation of fiber volume ratio of SFRCC.

Followed by the above experimental investigations, a supplemental test is conducted to check the effect of reserved cyclic loading on strength and performance of the stud-SFRCC shear connection.

3.1.2 Organization

To investigate the specific issues mentioned above, several series of push-out tests are conducted in this chapter. First, the design of the test specimens, test parameters was introduced. Then, the test results including the different failure modes, shear-slip behavior, and shear strength will be presented. Based on the test results, the influences of the stud number, stud arrangement including pitch spacing and gauge spacing, and SFRCC fiber volume ratio are discussed. In the end, a supplemental test to check the effect of reversed cyclic loading comparing to monotonic loading is introduced.

3.2 Solid SFRCC Slab Push-out Tests

3.2.1 Overview of the tests and specimens

A total of 16 solid slab push-out specimens were tested to gain a better understanding of the behavior and performance of the stud-SFRCC shear connections. The specimens were divided into two series. First, a pilot test was conducted to verify the feasibility of the proposed shear connection. This was following by a parametric test in which effects of the details of the shear connection, such as the stud spacing, number of stud, and fiber volume ratio of SFRCC, on the connection performance. The basic properties of the specimens and test parameters are summarized in Table 3.1. Two kinds of studs, stud with diameter of 22 mm and stud with diameter of 13 mm, were used for the pilot test and the parametric tests, respectively. The 22 mm diameter stud used in the first series is the most commonly size in the practical applications. The 13 mm diameter stud was used due primarily to the limitation of

the loading apparatus, when many studs were placed in the parametric test. Corresponding to reduced size on stud diameter, all the other dimensions was fabricated adopting reduced scale of 0.6 (13/22) in these specimens. The stud had a diameter of 13 mm (instead of 22 mm) and a height of 47 mm (instead of 80 mm), and the minimum spacing was set at 30 mm instead of 50 mm.

The global dimensions of specimens are as shown in Figure 3.2. Figure 3.2(a) shows the dimension and specimen details for specimens with 22 mm diameter studs, the specimen consists of two halves with a SFRCC slab connected by studs to a 500 mm long structural steel tee. The SFRCC slabs were placed against the steel tees such that the center of the stud group would meet the center of the slab. Each SFRCC slab was cast horizontally, locating the studs in a vertical position. Material test cylinders were prepared together with the specimens and cured simultaneously. After the SFRCC slabs hardened in 28 days of curing, the two specimen halves were bolted together through the webs by steel plates to form a solid slab push-out specimen. The configuration of specimens with 13 mm diameters studs is same to those with 22 mm diameter studs, the dimension is shown in Figure 3.2(b). The layouts of stud arranged in slabs for each specimen are referred to column 'stud layout' in Table 3.1 and as shown in Figure 3.3.

Each specimen was denominated in the following format. e.g., in 'SP4G2', 'S' means scaled specimen using stud with diameter of 13 mm; 'P4' means 4 studs placed in the pitch direction (parallel to the shear direction) and 'G2' means 2 studs placed in the gauge direction (perpendicular to shear direction). For the specimens in which the slabs cast with SFRCC, each specimen is identified with "2%", "4%" or "6%", indicating the corresponding fiber volume fraction used for the specimen. Nonetheless, "P2G1-C" and "P2G1-M" represent the specimens with slabs cast with concrete and mortar respectively.

Table 3.1 Specimen details and material properties

No.	Spec.	V_f	Stud layout	Stud		D_p	D_g	D_p/d	D_g/d	n	f_c	f_{st}	f_u
				d	L								
Pilot test													
1	P2G1-CON	Concrete	(b)	22	80	50	2.3	-	-	2	23.5	2.3	475.0
2	P2G1-HSM	Mortar	(b)			50	2.3	-	-	2	65.2	4.6	
3	P1G1-6%	6%	(a)			-	-	-	-	1	118.5	18.4	
4	P2G1-6%		(b)			50	-	2.3	-	2	132.4	20.1	
5	P2G2-6%		(c)				50		2.3	4	126.3	17.3	
6	P4G1-6%		(d)				-		-		129.0	17.9	
Parametric test													
7	SP1G1-6%	6%	(e)	13	47	-	-	-	-	1	119.1	17.1	471.3
8	SP2G2-6%		(f)			90	60	6.9	4.6	4			
9	SP3G2-6%		(g)			45		3.5		6			
10	SP3G3-6%		(h)				30		2.3	9			
11	SP4G2-6%		(i)			30	60	2.3	4.6	8			
12	SP4G1-2%	2%	(j)			30	-	2.3	-	4	119.5	10	471.3
13	SP4G1-4%	4%	(j)								104.0	12.5	
14	SP4G1-6%	6%	(j)								113.2	19.7	
15	SP2G2-2%	2%	(k)				30	2.3	2.3		119.5	10	
16	SP2G2-4%	4%	(k)								104.0	12.5	

d: Stud diameter; L: Stud length; D_p: Stud pitch length (center-to-center spacing along loading direction); D_g: Stud gauge length (center-to-center spacing perpendicular to loading direction); n: number of studs embedded in each slab; f_c: compressive strength of SFRCC; f_{st}: split tensile strength of SFRCC; f_u: tensile strength of stud.

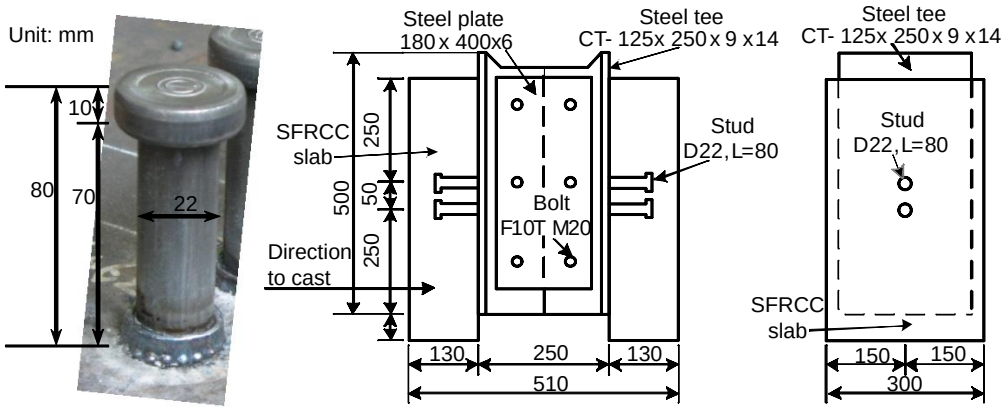

(a)

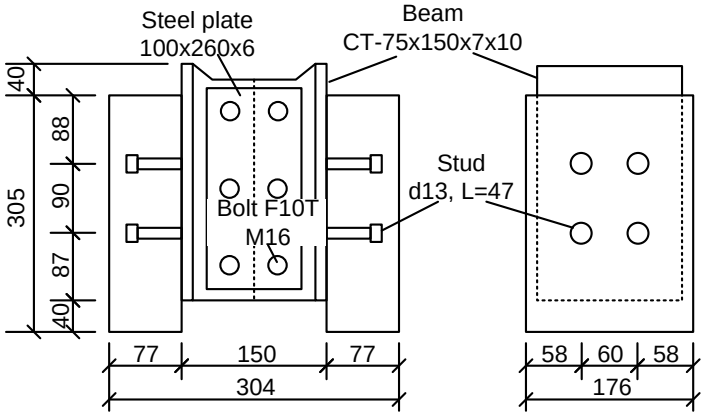

(b)

Figure 3.2 Dimension of specimens: (a) specimens with 22 mm diameter stud; (b) specimens with 13 mm diameter stud.

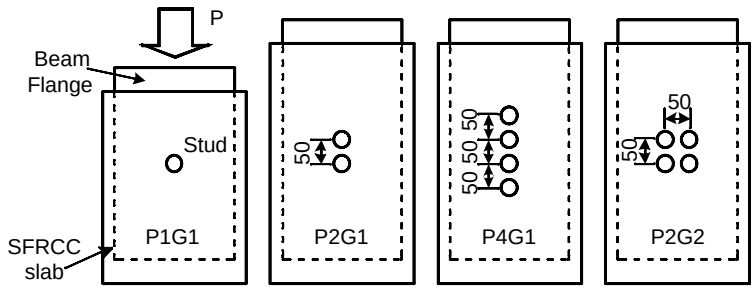

(a) (b) (c) (d)

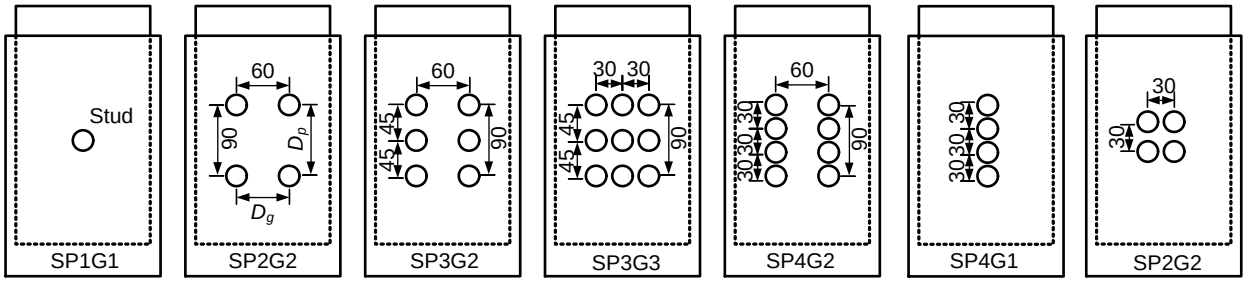

(e) (f) (g) (h) (i) (j) (k)

Figure 3.3 Layout of studs in slabs

Specimens P2G1-CON, P2G1-HSM and P2G1-6% are identical in dimensions and specimen details except for the material used to cast slab. Specimens P2G1-CON, P2G1-HSM used the common plain concrete and high strength mortar to cast slabs respectively, while SFRCC was applied for Specimen P2G1-6%. Noted that densified cement was used as the binder for both SFRCC and high strength mortar. In SFRCC, a rather high 6% fiber volume fraction of straight steel fiber (diameter of 0.4 mm, length of 12 mm, tensile strength of 1350 N/mm^2 and density of 7.85 g/cm^3) was adopted. The three specimens were design to compare the strength and performance of the connections when high performance material-SFRCC and commonly used concrete and mortar are used. Pair of studs is placed to each beam flange as shown in Figure 3.3(b). In order to compare the effect of different slab materials, no steel reinforcement was used to reinforce the slabs.

Specimens No.3 ~ No.6 are the specimens using 22 mm diameter headed studs. For these four specimens, the number and layout of studs were designed as the test parameters as illustrated in Figure 3.3(a) ~ (d). Specimen 'P1G1-6%', which is with one stud for each side beam flange, was designed as the baseline specimen to investigate the basic behavior of the stud in SFRCC slab. Other specimens were designed to investigate the group effect, i.e., the longitudinal spacing, transverse spacing and the number of studs. A stud spacing of 50 mm, which is the minimum space required to install 22 mm diameter studs using a stud gun, was adopted for the three specimens with multiple studs. Specimen 'P2G1' was designed to investigate the effect of longitudinal spacing, and Specimen P2G2 was designed to investigate the effect of transverse spacing. Four studs arranged in a line (Specimens P4G1-6%) and two by two studs (Specimens P2G2-6%) were to examine the performance of a 'densely arranged stud group'.

As introduced above, beside the specimens with 22 mm diameter headed studs, specimens with 13 mm diameter headed studs were also made for parametric study.

Specimens No.7 ~ No.11 are specimen with 13 mm diameter studs. The focus of these five specimens was to investigate how to arrange a stud arrangement to obtain the largest transmittable shear force in a certain area. According to AISC 2005, the permitted minimum pitch length and gauge length are 6 times and 4 times the stud diameter, i.e. 78 mm and 52 mm for D13 studs. Since the minimum stud spacing to install D13 studs was 30 mm, by slightly enlarging the minimum studs spacing of 78 mm × 52 mm, a 90 mm × 60 mm area (as shown in Figure 3.3) was determined that it is possible to array four and three studs in the longitudinal and transverse directions, respectively. The longitudinal spacing ('pitch length' hereafter, D_p), transverse spacing ('gauge length' hereafter, D_g),

and the number of studs *n* were chosen as the test parameters and the studs were arrayed in various patterns within this area. Specimen 'SP2G2-6%' was designed as the specimen with the 'standard' stud spacing, in which the pitch and gauge lengths of the studs were 90 mm and 60 mm. Specimen 'SP2G2-6%', 'SP3G2-6%', and 'SP4G2-6%' were designed to investigate the effect of longitudinal spacing by reducing the pitch length from 90 mm to 45 mm and 30 mm, respectively. Specimen 'SP3G2-6%' and 'SP3G3-6%' were designed to investigate the effect of transverse spacing by reducing the gauge length from 60 mm to 30 mm, while Specimen 'SP1G1-6%' with only one stud in each slab was designed as the baseline specimen.

In order to determine the effect of SFRCC fiber volume ratio on the stud-SFRCC shear connection, push out tests were carried out to verify the load-slip and shear capacity behavior. Specimens No.12 ~ No.16 and No.5, which are of different SFRCC fiber volume ratio and stud layout, were tested. For these specimens, three fiber volume ratio of SFRCC, 2%, 4% and 6%, were used to cast the slabs. Two stud arrangements were designed based on the following considerations: the four studs arranged in two by two (as shown in Figure 3.3(j)) is the basic unit of the "densely arranged studs group", while the four studs arranged in a line, as shown in Figure 3.3(k), is the most arranged unfavorably for slab shear capacity. It is notable that in these specimens the transversal and longitudinal studs spacing is set at the smallest interval of 30 mm, which is the smallest spacing for the stud installation with 13 mm diameter headed stud.

To examine the basic properties of the connection with steel stud embedded in SFRCC slab, and also to exploit the possibility to eliminate the steel reinforcement, the SFRCC slabs were cast without any rebar unlike conventional push-out test specimens.

3.2.2 Test setup and instrumentation

Figure 3.4 shows the test setup used for the test. The test specimen was placed on a steel base and in the loading frame shown in Figure 3.4(a). The load capacity of the loading system was 2 MN. The load was applied to a 40mm thick steel plate that was placed on the upper end of the test specimen's steel tees. Four restraining beams were used to ensure the loading in the exact vertical direction. The specimen was placed on a layer of mortar, and thin steel strips were inserted into the gap between the steel plate and the flanges to achieve the uniform load distribution both in the slab and steel. A total of eight linear variable displacement transducers (LVDTs), four attached in each slab, were used to measure the slip between the beam and slabs as indicated in Figure 3.4(b). The average taken from the eight measured values (numbered 1 to 8 in Figure 3.4(b)) was adopted as the slip between the slab and steel flange. Two LVTDs (numbered 9 to 10 in Figure 3.4(b)) were used to measure the displacement of the loading steel plate in the vertical direction.

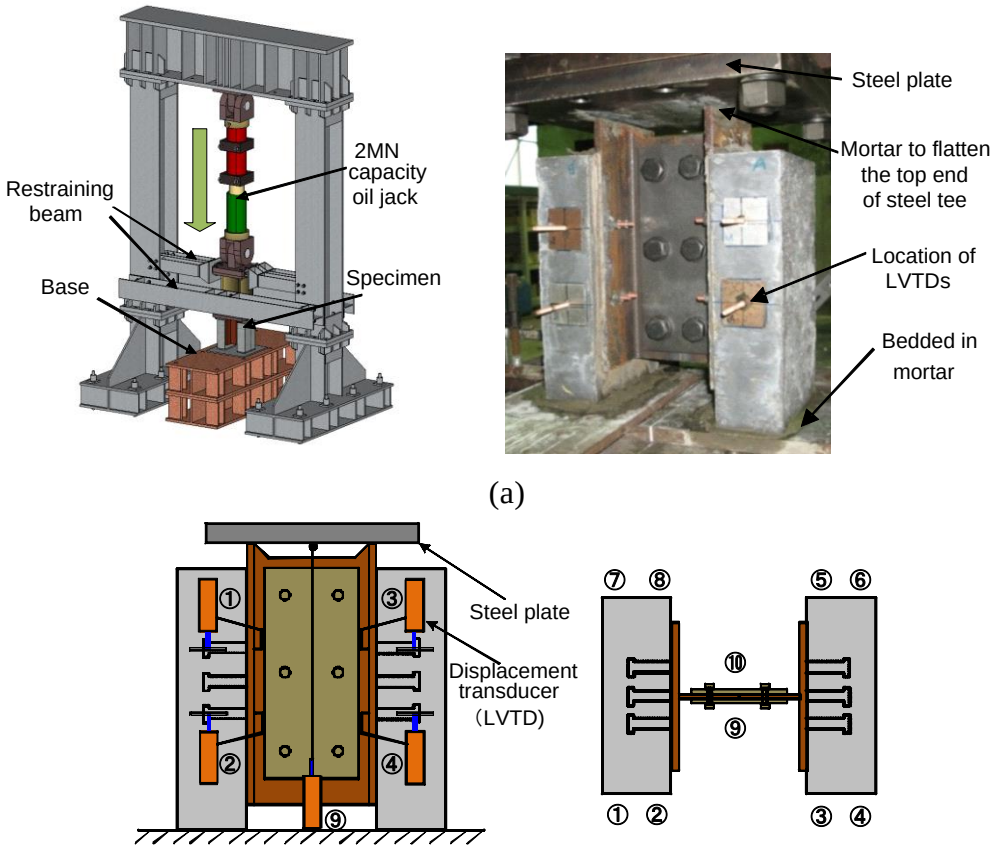

Figure 3.4 Setup for push-out tests (a) Loading frame and specimen; (b) Measurement of slips and displacements

3.3 Test results and discussion

The results for the solid slab tests are shown in Table 3.2. For comparison purposes, the strength calculated by the AISC specifications (ANSI/AISC 360 2010) is also shown in the table. P_{stud}, is the average shear force induced per stud, which was obtained as the maximum applied force divided by the number of studs embedded in the specimen. P_{max} is the maximum shear force transferred to each beam flange. P_{AISC} is the per stud strength obtained from the AISC design equation. S_{max} is the slip displacement when the load reached its peak, and S_u is the slip distance when the stud fractured for the first time or the applied load was reduced to 90 % of the maximum strength. α is the strength reduction factor, defined as the ratio of the per stud strength to the strength for the single study, which was obtained from the test for the baseline specimen. Note that Specimens 'P1G1' and 'SP1G1' were chosen as the baseline specimens for specimens adopting 22 mm diameter studs in the pilot test and 13 mm diameter stud in the parametric test, respectively.

Table 3.2 Summary of test results

No.	Specimens	D_p/d	D_g/d	P_{max} (kN)	P_{stud} (kN)	α	P_{AISC} (kN)	P_{stud}/P_{AISC}	S_{max}	S_u	Failure mode
Pilot test											
1	P2G1-CON	2.3	-	82.4	41.2	-	-	-	1.46	-	Slab split
2	P2G1-HSM	2.3	-	130.4	65.2	-	-	-	1.43	-	Slab split
3	P1G1-6%	-	-	217	217	100%	181	1.20	4.85	6.16	Stud fracture
4	P2G1-6%	2.3	-	391	196	90.2%		1.08	4.81	6.30	
5	P2G2-6%	2.3	2.3	384	192	88.5%		1.06	4.62	9.29	
6	P4G1-6%	2.3	-	684	171	78.9%		0.95	1.44	-	Slab split
Parametric test											
7	SP1G1-6%	-	-	110	110	100%	62.6	1.76	2.64	3.98	Stud fracture
8	SP2G2-6%	6.9	4.6	418	104	94.7%		1.69	3.23	4.55	
9	SP3G2-6%	3.5	4.6	562	93.1	84.5%		1.49	2.07	3.51	
10	SP3G3-6%	3.5	2.3	842	93.6	84.9%		1.50	3.59	3.59	
11	SP4G2-6%	2.3	4.6	612	76.6	69.5%		1.22	0.35	-	Slab split
12	SP4G1-2%	2.3	-	279	69.7	63.4%		1.11	0.95	-	Slab split
13	SP4G1-4%	2.3	-	305	76.3	69.4%		1.22	3.23	-	Slab split
14	SP4G1-6%	2.3	-	295	73.7	67.0%		1.18	3.22	5.30	Stud fracture
15	SP2G2-2%	2.3	2.3	340	85.0	77.3%		1.36	3.49	5.20	Stud fracture
16	SP2G2-4%	2.3	2.3	355	88.7	80.6%		1.42	3.92	4.88	Stud fracture

3.3.1 Failure modes

The test specimens were loaded until one or both slabs separated from the steel beam by one of the two failure modes, the stud fracture and the SFRCC slab split. The failure mode of each specimen is indicated in Table 3.2.

The failure of stud shear off is presented in Figure 3.5. The arrows with load P in Figure 3.5 represent the direction of push-out loading. In the specimens failed by the stud fracture, the studs were separated at the stud shank near the roots as shown in Figure 3.5(a). The failure surface was located in the stud shank directly adjacent to the weld flush. On the SRFCC side, local crushes with a powdery appearance occurred on the slab bearing surface in front of the studs, as shown in Figure 3.5(b). The local deformation of the stud root creates a void pocket behind the stud. The specimens that failed by studs fracture were sawed along the centerline after testing, Figure 3.5(c) shows the cutting surface. It can be seen that the fractured studs remained upright in the slab.

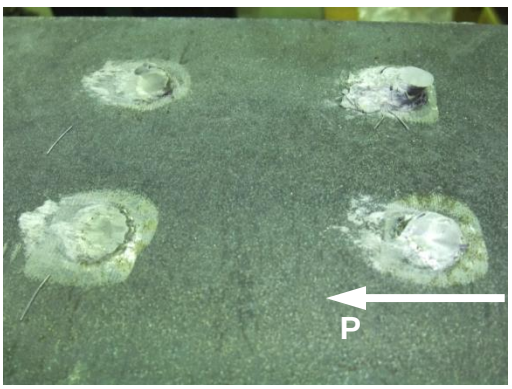

(a)

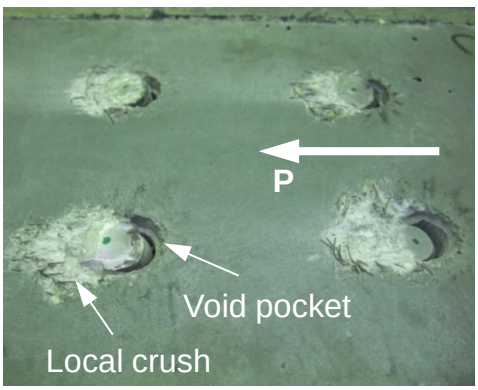

(b)

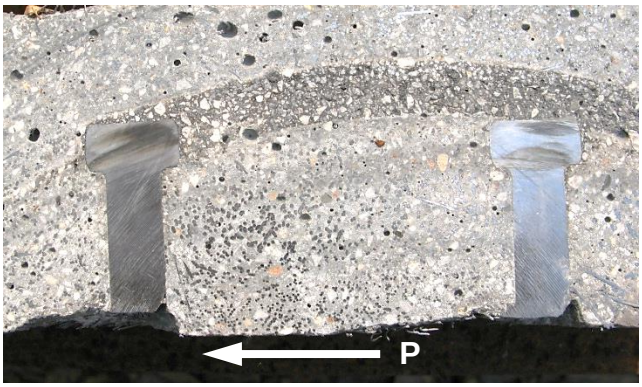

(c)

Figure 3.5 Detail of specimens failed in stud shearing:
(a) beam flange; (b) slab side; (c) sawed section

As indicated inTable 3.2, four specimens failed by the slab split among the specimens with SFRCC slabs. Figure 3.6(a) presents the slab failure of Specimen SP4G1-6%, in which eight studs were arranged into two lines at a pitch length of 2.3*d*. Initial crack occurred at the location indicated by an arrow in Figure 3.6(a), i.e., the lower end of the slab right under the arranged studs. With further loading, the crack was extended to a complete split of the SFRCC slab along the studs. Figure 3.6(b) shows photo of the steel beam part token after the test. SFRCC still remained between the studs, and the studs tilted significantly. Bending deformation of the most front stud was most significant among the studs arranged in the line. The fracture failure mode of the most front stud, in fact, is a secondary failure after considerable SFRCC crushing and stud deformation has occurred.

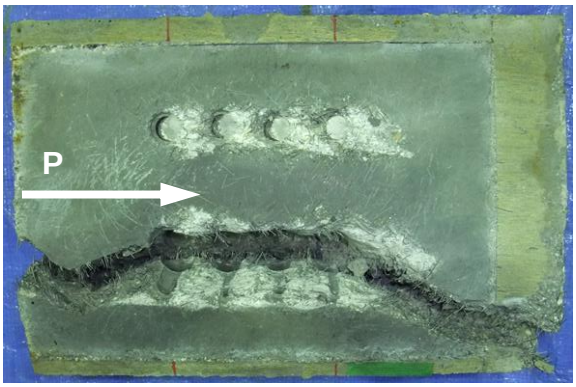

(a) (b)

Figure 3.6 Detail of specimen failed in slab: (a) Slab: (b) Beam and studs

When the specimen was loaded, slip occurred and grew between the steel beam and the SFRCC slab. Selected load-slip curves for specimens with 22 mm diameter stud and 13 mm diameter are presented in Figure 3.7. The slip was the average of four transducers attached to each specimen. The loads are the obtained by dividing the total load applied to the push-out specimen by the total number of studs.

For the specimens failed by the stud fracture, the load-slip curves show ductile plastic plateau before the stud fracture. They reached the maximum strength at a slip about 6 mm for 22 mm diameter studs, and about 2.3 mm to 3.7 mm for 13 mm diameter, which are about 0.2 to 0.3 of the stud diameter for D13 studs. For the specimens failed by the slab split, the load decreased continuously after reaching the maximum strength.

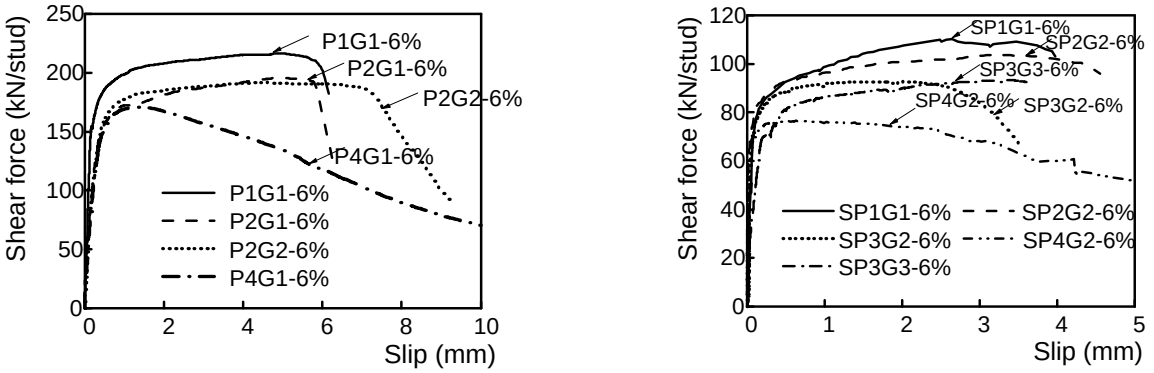

(a) (b)

Figure 3.7 The shear-slip relation curves: (a) D22 stud specimens; (b) D13 stud specimen

3.3.2 Effect of fiber reinforcement in slab

The first parameter evaluated was the effect of fiber reinforcement on strength and shear-slip behavior of shear connection. The shear-slip relationship curves from Specimens P2G1-6% (SFRCC slab), P2G1-CON (plain concrete slab) and P2G1-HSM (high-strength mortar slab) are compared in Figure 3.8. Because of the inherent deficiency of tensile strength, the specimen with the slab of high-strength mortar and the specimen with the slab of concrete experienced a similar process of slab split failure and developed very low shear strength. In Specimen P2G1-6%, because the discrete steel fiber provides reinforcement to the matrix in SFRCC slab, the specimen shows large strength and appear much ductile shear-slip behavior. The damage pattern at slab (see Figure 3.9) shows that, the slab in Specimen P2G1-CON and P2G1-HSM both split along the centerline under downward loading, while there was no observation on the damage of slab except a few fine cracks on the slab in P2G1-6% specimen.

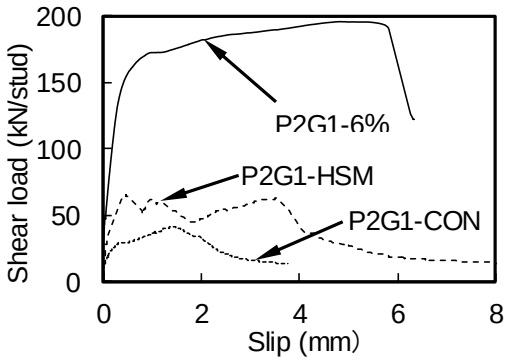

Figure 3.8 Load-slip relationship curves for specimens using different material for slab

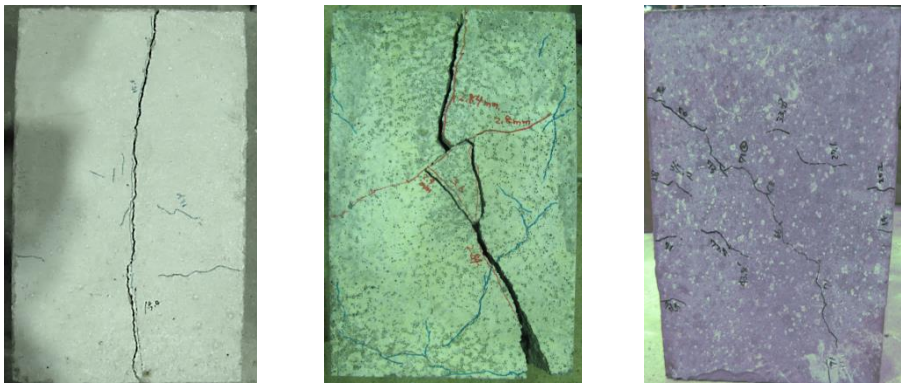

(a) (b) (c)

Figure 3.9 Damage pattern at slab after testing:
(a) Specimen P2G1-CON; (b) Specimen P2G1-HSM; (c) Specimen P2G1-6%

3.3.3 Effect of stud spacing

The second parameter evaluated is the effect of stud spacing on strength of stud-SFRCC connection. It is investigated by the comparison among specimens No.3 to No.6, and No.7 to No.11.

Effect of pitch length

Specimens 'SP2G2-6%', 'SP3G2-6%', and 'SP4G2-6%' had the same gauge length of 4.6*d*, and the corresponding pitch length, were 6.9*d*, 3.5*d*, and 2.3*d*. Compared with the baseline specimen 'SP1G1', the per stud strength was reduced to 95%, 85%, and 70%, as shown in Figure 3.10 (a).

In the series, a test purpose is to compare the strength reduction between Specimens with studs arranged in small stud spacing to that with studs in normal stud spacing. Therefore, Specimens with small stud spacing also compared with Specimens 'SP2G2-6%', which is considered to place studs with normal spacing in both pitch direction and gauge direction.

When compared to Specimen 'SP2G2-6%' (a pitch length of 6.9*d*), Specimens 'SP3G2' (a pitch length of 3.5*d*) show about 10 % reduction on the maximum per stud strength P_{stud}, while Specimen 'SP4G2-6%' (a pitch length of 2.3*d*) failed by slab split was reduced in strength by 27%.

It is proven that when embedded in SFRCC, the studs arranged densely with a pitch length of 3.5*d*, can still possess the shear strength (per stud) not smaller than 90% of the shear strength expected when studs are arranged in a normal pitch length (6.9*d*).

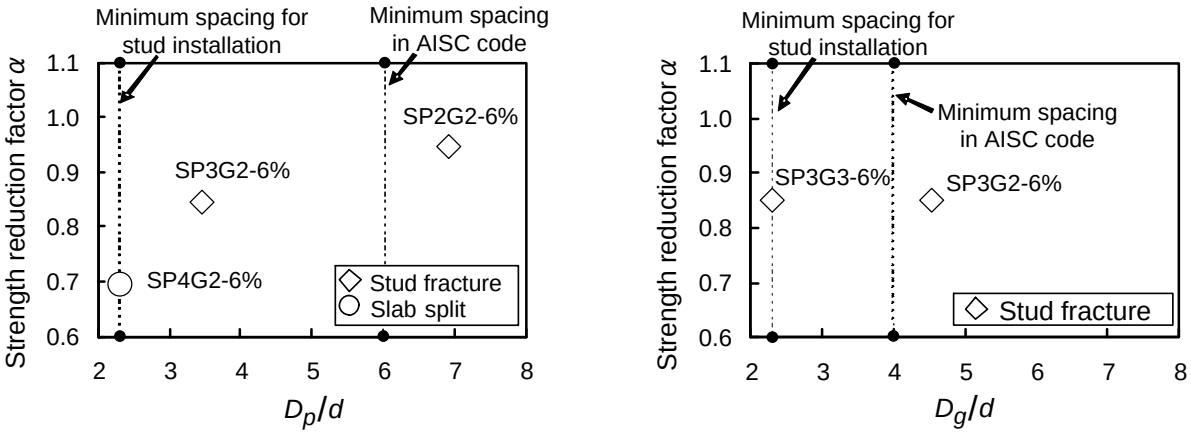

(a) (b)

Figure 3.10 Effect of stud spacing: (a) Effect of pitch length; (b) effect of gauge length.

The comparison on damaged regions in the SFRCC slab is shown in Figure 3.5(a). The locally crushed area in front each stud root remain separated from each other in the specimen with normal stud spacing ('SP2G2-6%'), but in the specimen with small stud spacing ('SP3G3-6%'), the damage areas were nearly overlapped. It is notable that although no reinforcing bar was used in the SFRCC slab, no cracks were detected on both the inner and outer side surfaces of the slabs for the specimens failed by the stud fracture.

To observe the details such as deformation of the studs and stud-SFRCC interactions, the specimens failed in stud fracture were sawed longitudinally through the slab and stud connectors along the centerline. As shown in Figure 3.5(c) and (d), no cracks were observed on the sawed slab section, and the deformation of studs was found concentrating at the very lower part. Accompanied with the concentrated stud deformation, the portion of SFRCC was crushed in front of the stud root and a gap between stud root and its rear SFRCC portion was created. It is notable that in Specimen 'SP2G2-6%', the crushed SFRCC portion in front of the rear stud was far away from the gap behind the front stud; while in Specimen 'SP3G2-6%', the crushed SFRCC portion in front of the rear stud was very close to the gap behind the front studs. Due to the presences of the crushed SFRCC portion and the gap, the restraining effect on the studs is likely to decrease and thus causes reduction on stud strength. Research about this will be discussed at a later section.

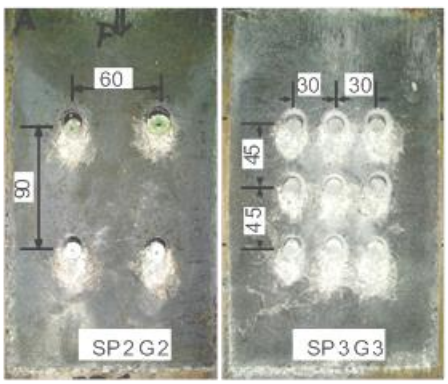

(a)

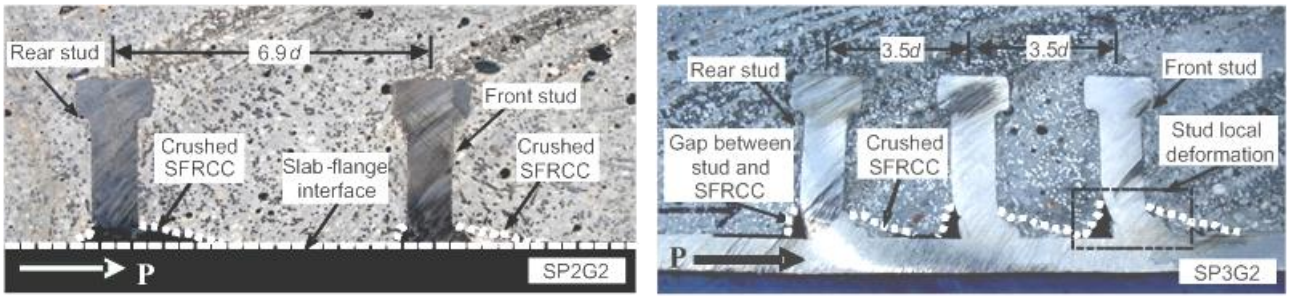

(b) (c)

Figure 3.11 Sawed section for specimens with different stud spacing

Effect of gauge length

Specimens 'SP3G2-6%' and 'SP3G3-6%' had the same pitch length of 3.5*d*, and the respective gauge lengths were 4.6*d* and 2.3*d*. The per stud strength was 93.1 kN for Specimens 'SP3G2' and 93.6 kN for Specimens 'SP3G3-6%' as shown in Figure 3.10(b). Again, the difference in per stud strength was minimal and not affected by the gauge length.

To summarize, the effect of gauge length on the per stud strength would be minimal as long as the length is not smaller than 2.3*d*, which is the minimum length tolerated in the stud installation.

3.3.4 Effect of the *number* of studs

The effect of the number of studs are evaluated in two ways, the variation of per stud strength due to the changes of number of studs, and the total transferable shear force within given area for stud installation.

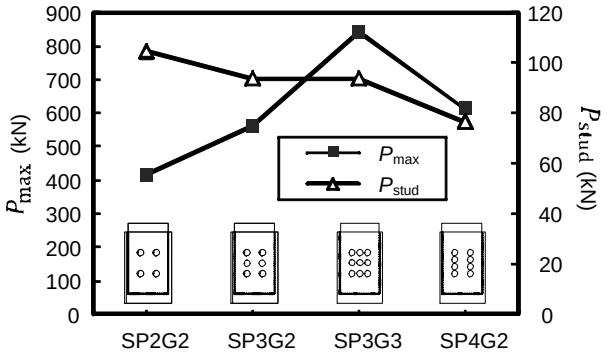

Figure 3.12 Comparison of P_{max} and P_{stud}

Figure 3.12 plots the ultimate transferred shear force by each side of the beam (P_{max}) and the per stud strength (P_{stud}) for the specimens in which studs were arranged for the area of 90 mm by 60 mm. In Specimen 'SP2G2-6%', four studs were placed for each slab with the stud spacing according to current design code. In Specimen 'SP3G3-6%', nine studs are placed for each slab, in which the stud spacing was half that adopted in Specimen 'SP2G2-6%'. The per stud strength P_{stud} of was reduced to

90% in Specimen 'SP3G3-6%' relative to Specimen 'SP2G2-6%', but the total transferred shear force P_{max} was more than twice in Specimen 'SP3G3-6%' than in Specimen 'SP2G2-6%'.

3.3.5 Effect of fiber volume ratio

The normalized shear-slip relationship curves are shown in Figure 3.13, where the vertical axis is the shear force normalized by the respective per stud strength P_{stud} and the horizontal axis is the slip normalized by the stud diameter. The mark on each curve indicates the moment when the specimen initiated its failure.

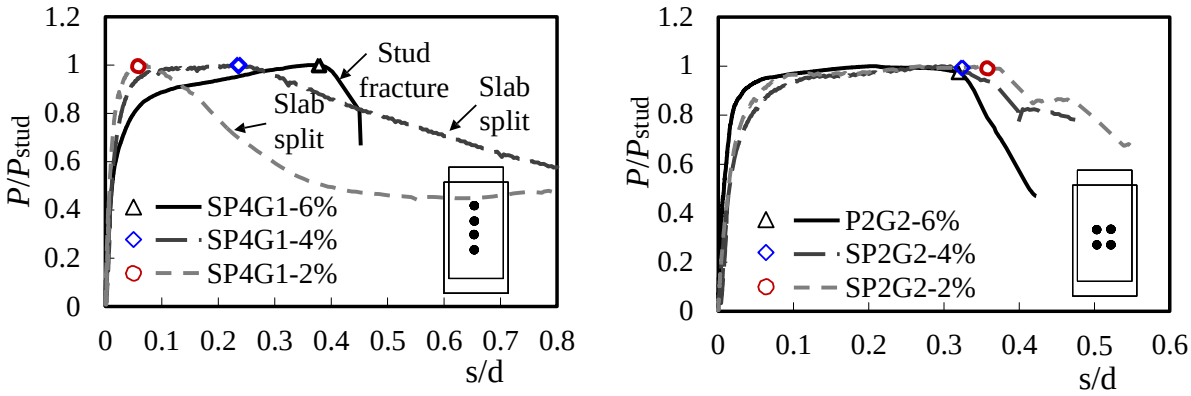

(a) (b)

Figure 3.13 Normalized shear-slip response.

As shown in Figure 3.13(a), for the specimens with four studs in a line, Specimens SP4G1-6% failed by stud fracture shows a most ductile shear-slip response; specimen "SP4G1-4%" shows a ductile plateau after yielding and a much gently decreasing branch after reaching the maximum strength at a slip about 0.24 times stud diameter; and Specimen "SP4G1-2%" loses its strength rapidly after reaching the maximum strength at a small slip.

Figure 3.13(b) shows the shear-slip response of specimens with studs arranged in two by two. Since all the specimens failed in the failure mode of stud fracture, the normalized shear-slip curves and the ultimate slippage (indicates by marks) are very similar.

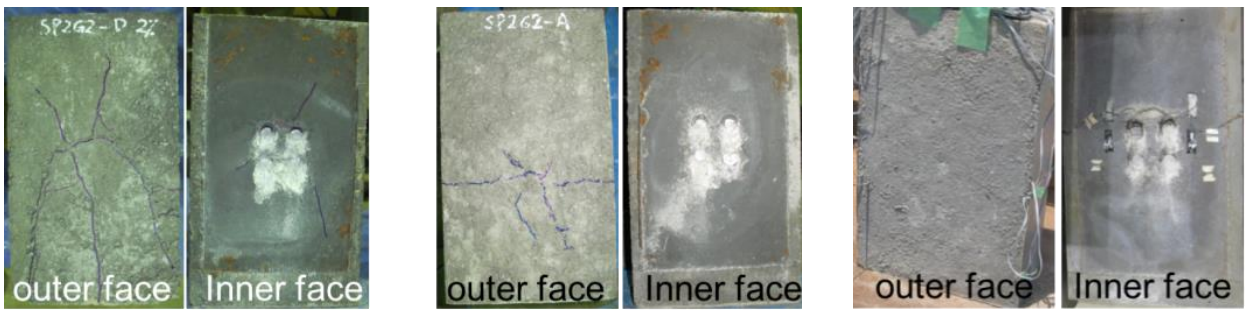

(a) SP2G2-2% (b) SP2G2-4% (c) P2G2-6%

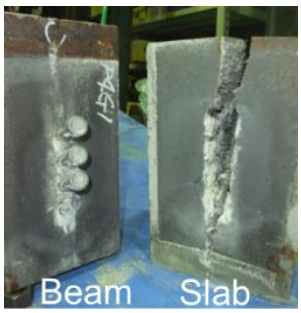

(d) SP4G1-2%

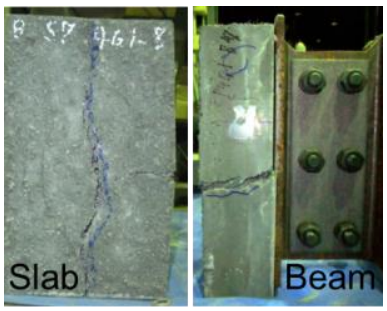

(e) SP4G1-4%

(f) SP4G1-6%

Figure 3.14 Failure mode of specimens with different fiber volume

The failure modes of specimens with four studs arranged in a line are shown in Figure 3.3(j). Specimen SP4G1-6%, in which the fiber volume ratio was 6%, was failed by stud fracture as shown in Figure 3.14(f). When the fiber volume ratio was 4%, the specimen failed by slab split but slab was not separated from the beam flange (Figure 3.14(e)). In the case of 2%, the slab even split into two pieces (Figure 3.14(d)).

All specimens with four studs arranged in two by two pattern failed by stud fracture. Nonetheless, when the fiber volume ratio was reduced, the slabs developed more cracks. As shown in Figure 3.14(a), cracks were found on both the inner and outer faces of the slab in Specimen SP2G2-2%; while in Specimen P2G2-6%, no visible crack was found on the slab as shown in Figure 3.14(c).

3.3.6 Evaluation of test results

Load-slip relationship

Empirical formulas were proposed by An et al (An and Cederwall 1996). for the shear-slip relationship of a stud embedded in normal strength concrete and high strength concrete (whose compressive strength was about 90 MPa). The expressions are given by:

$$\frac{P}{P_u} = \frac{2.24(s - 0.058)}{1 + 1.98(s - 0.058)} \qquad \text{For normal strength concrete} \qquad (3.1)$$

$$\frac{P}{P_u} = \frac{4.44(s - 0.031)}{1 + 4.24(s - 0.031)} \qquad \text{For high strength concrete} \qquad (3.2)$$

Where P is the shear force, and s is the slip in mm. P_u is the maximum strength per stud. In Figure 3.15, the above empirical curves are compared with the measured shear-slip curves for the specimens in the test. From Figure 3.15, we find that the empirical relationships give a larger stiffness for the high strength concrete than for the normal strength concrete. If such trend is further extrapolated to SFRCC, the stiffness associated with SFRCC should be even larger than what was estimated for high strength concrete. Figure 3.15 indeed shows a significantly larger stiffness for the SFRCC specimens. This comparison confirms the past research such that stud connection was stiffer when the studs are embedded in stronger concrete.

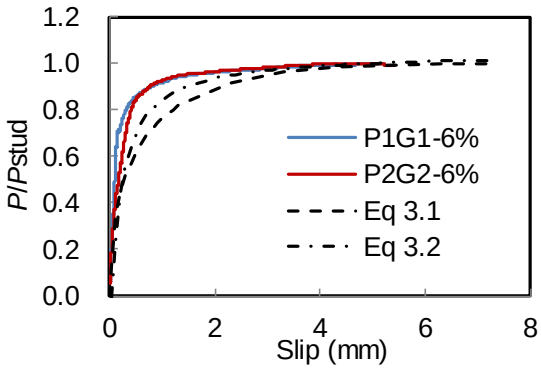

Figure 3.15 Test results and regression curves

Shear strength of studs

For the strength of shear studs embedded in solid concrete slabs, design equations are available in AISC 2010 (ANSI/AISC 360 2010) and other design specifications such as Eurocode 4 (Eurocode 4. EN 1994 2004), and AIJ design code (Architectural Institute of Japan (AIJ) 2010).

The design equations of AISC 2005 are based on the tests by Ollgaard et al. (Ollgaard et al. 1971) and are given as:

$$P_{\text{AISC}} = 0.5A_s\sqrt{E_c f_c'} \leq A_s f_u \tag{3.3}$$

where A_s is the cross-sectional area of the stud; f_u is specified minimum tensile strength of a stud shear connector (MPa); E_c is modulus of elasticity of concrete (MPa); and f_c' is compressive strength of concrete cylinders (MPa). Noted that the equation is applicable only when the value of $\sqrt{E_c f_c'}$ ranges from 490 MPa to 882 MPa. Since the corresponding value of SFRCC is larger than 2,000 MPa, the upper limit $A_s f_u$ was adopted as the estimated shear strength of studs embedded in SFRCC slab. The per strength P_{AISC} calculated by the Eq. (3.3) is listed in Table.2.

In the test, P_{stud} was significantly larger than P_{AISC}, by 49% to 76% for specimens failed in the stud fracture. This notable difference in over-strength (relative to P_{AISC}) was attributed to the difference in the scale adopted in the two test series. Detail on this will be explicated at a later section.

The test data clearly indicate that the current design equation for the strength of the shear connectors may be too conservative when it is applied to SFRCC.

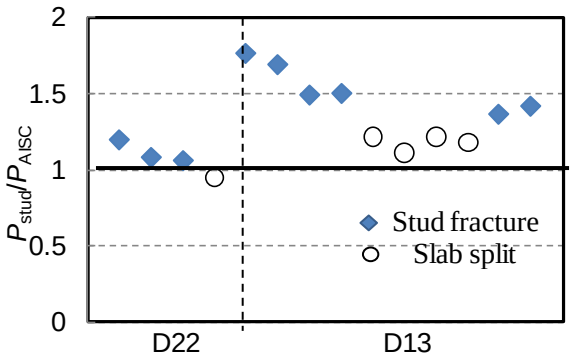

Figure 3.16 The comparison between tested per stud strength to predicted stud strength

3.4 Supplementary push-out tests

In the current design codes, the shear stud capacity is examined based on the static loading of shear studs. An understanding of shear stud behavior under seismic loading is significantly for several situations. First, designing a building for a consistent factor of safety against collapse and for performance-based design requires accurate measures of structural stresses, displacements, and story drifts at various levels of loading. Composite action in the structure may significantly influence these calculations and therefore should be considered. In addition, many of the newer hybrid structural systems being developed are being investigated for applicability in seismic regions. Recent experimental studies also show that the design provisions for calculating the capacity of shear studs may be inadequate under inelastic cyclic loading.

As for the stud-SFRCC shear connection, if it is applied to structures in seismic region, the shear-slip behavior under reverse cyclic loading need to be characterized. Since the previous study is limited to one-way, monotonic loading, effects of load reversals and cyclic loading on the strength and performance of the stud-SFRCC shear connections will be investigated.

3.4.1 Push-out tests for studs in solid SFRCC slab

Overviews of the tests and specimens

Four specimens were tested with the global dimensions as shown in Figure 3.17. The fabrication of the specimens is similar to those specimens tested in the previous sections. To achieve the reverse cyclic loading condition, the specimens were modified by extending the end flanges to expose from the slabs.

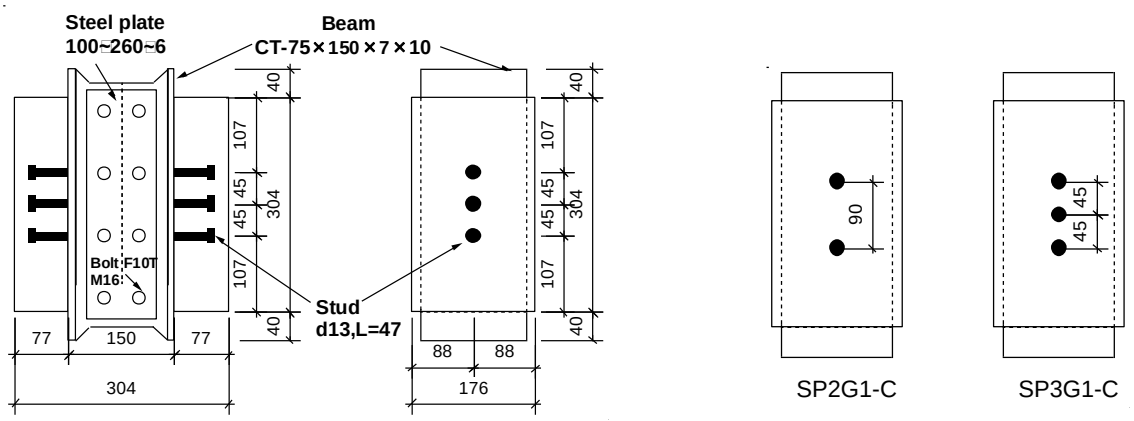

(a) (b)

Figure 3.17 Details of specimens

All specimens are summarized in Table 3.3. The stud layout in the SFRCC slab of specimens are as shown in Figure 3.17.

In the test, each specimen is identified either with "M", indicating a monotonically loaded specimen or with "C", indicating a reversed cyclically loaded specimen. For each reversed cyclically loaded specimen, there was a counterpart specimen tested monotonically. Besides the loading type, the specimens in this series also can be divided into two groups according to the stud spacing: Specimens "SP2G2"-M" and "SP2G2-C" are with a stud spacing of 90 mm, while Specimens "SP3G1"-M" and "SP3G1-C" are with a stud spacing of 45 mm.

Table 3.3 Specimen details and material properties

Spec.	Stud layout	V_f	Loading type	f'_c (MPa)	f'_{st} (MPa)
SP2G1-M	2x1	6%	Monotonic	113.2	19.7
SP3G1-M	3x1				
SP2G1-C	2x1		Reversed cyclic		
SP3G1-C	3x1				

Material properties

The compressive strength of SFRCC was obtained from the associated cylinder compressive tests. The tensile strength of SFRCC was obtained from the cylinder splitting tests. Both the compressive strength and tensile strength were determined by taking average of the measured values from three corresponding test pieces. The cylinder was 50 mm in diameter and 100 mm in height. Material properties of SFRCC cast with different fiber volumes are listed along with the material properties of stud in Table 3.3 Specimen details and material properties. Material tests on studs were not conducted; the tensile strength of the stud in its inspection certificate was 473N/mm^2.

Test Setup and Loading Program

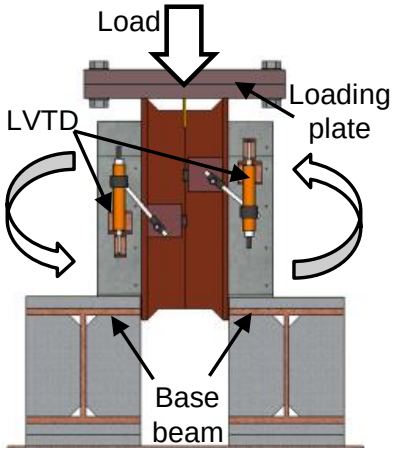

Figure 3.18 Setup of push-out test.

The test setup for the push-out test involving the specimens for investigation of the effect of fiber volume ratio are the same systems as described in the previous section.

For the specimens in second series, the test setup used in the previous push-out test has to be modified to achieve the reserved cyclic loading. Figure 3.18 shows schemata of the test setup. During the test, specimens were reset by making the specimen "upside down" prior to each half cycle of loading, placing the loading plate and loading on the reversed upper flange, as shown in Figure 3.18.

Due to the unidirectional nature of the loading system, some error was therefore introduced in the continuity of deflection measurements for cyclic loading. However, testing was consistent for all specimens and the ultimate capacities were unaffected.

Four linear variable displacement transducers (LVDTs) are used to measure the slip between the beam and slabs as indicated in Figure 3.18. The average taken from the four values measured by LVDTs was defined as the slip between the slab and steel flange.

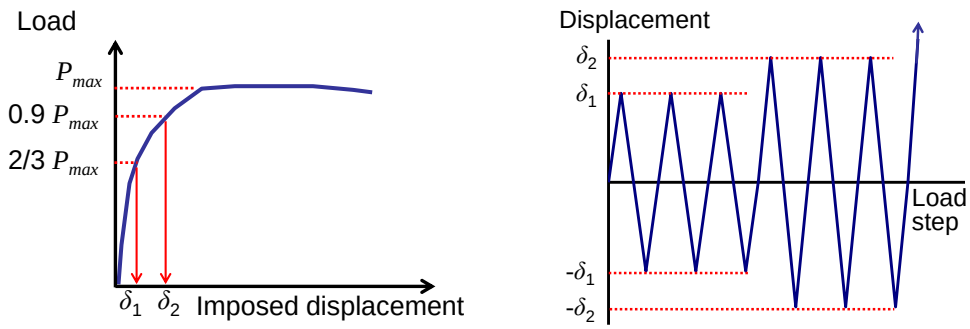

Figure 3.19 Loading regime for reverse cyclic loading

Static loading consisted of steadily increasing the load up until failure. Reverse cyclic loading consisted of three full cycles at the slippage corresponding to the load of ±2/3 P_{max}, ±0.9 P_{max}, and then unidirectional increasing loading. Here, two third of the monotonic load was determined basing on the consideration that the short term strength of headed stud shear connector in AIJ

design code is 2/3 of its design strength. 90% of monotonic strength was adopted because of P_{max} is the static yield capacity of the control specimen as determined from the load-slip plot obtained from the corresponding monotonic loaded specimens. Displacement control was adopted for the loading. The loading regime for reserve cyclic loading is illustrated as shown in Figure 3.19.

3.4.2 Tests Results

Failure modes

All specimens in the test are failed by stud fracture, which is typically shown in Error! Reference ource not found.(a). Error! Reference source not found.(b) shows comparison of local SFRCC crush adjacent to the base of the studs between specimens subjected to monotonic loading and reserved loading. When subjected to reverse cyclical loading, a more severe local SFRCC crush occurred, and they overlap each other.

(a) (b)

Figure 3.20 Failure modes of second series: (a) Stud fracture; (b) SFRCC local crushes on slab.

Maximum strength

The force and slip were measured for all the specimens. The shear capacity and failure modes of the tested specimens are summarized in Table 3.4. The shear force, P_{stud}, is the average shear force induced per stud, and defined as the measured applied force divided by the number of studs. $P_{\max}$ is the ultimate transferred shear load by each side beam flange. α is the ratio of the tested per stud strength P_{stud} to the predict strength of 62.9 kN obtained from Equation (3.3). S_{max} is the slip between beam flange and slab when the specimen reaches its maximum strength, while S_u is the slip when the specimen failed and the corresponding load was reduced to 90 % of the maximum strength.

Table 3.4 Push-out test results

Spec.	P_{stud} (kN)	a	S_{max}/d	Failure mode
SP2G1-M	94.4	1.5	0.47	Stud fracture
SP3G1-M	74.6	1.2	0.14	Stud fracture
SP2G1-C	79.3	1.3	0.16	Stud fracture
SP3G1-C	69.4	1.1	0.18	Stud fracture

Effect of reverse cyclic loading

Figure 3.21(a) compares the monotonic shear slip behavior of Specimen "SP2G1-M" with the reversed cyclic loading behavior of Specimen "SP2G1-C". Specimen "SP2G1-C" was subjected to four cycles of reversed loading and reached the peak loads equal to 84% of the capacity of specimen "SP2G1-M". The point of the peak load is indicated with the 'triangle mark' in the Fig. 8a. Failure occurred at the first positive peak for the fifth cycle of reversed loading with a load equal to 64% of the monotonic capacity of "SP2G1-M". Both specimens failed by shearing of the studs at the level just above the welds.

Figure 3.21(b) compares the monotonic and reverse cyclic loading behavior of Specimens "SP3G1-M" and "SP3G1-C". The properties of the two specimens were identical. They had three 13 mm studs arranged in a line with a 45 mm longitudinal spacing placed within 77 mm high solid slab. Interaction of the densely arranged studs led to obvious slab damage in both specimens. Both the monotonic and reverse cyclic loaded specimens reach their maximum strength at very small slips. Failure of Specimen "SP3G1-C" occurred at a load corresponding to 93% of the monotonic capacity in Specimen "SP3G1-M".

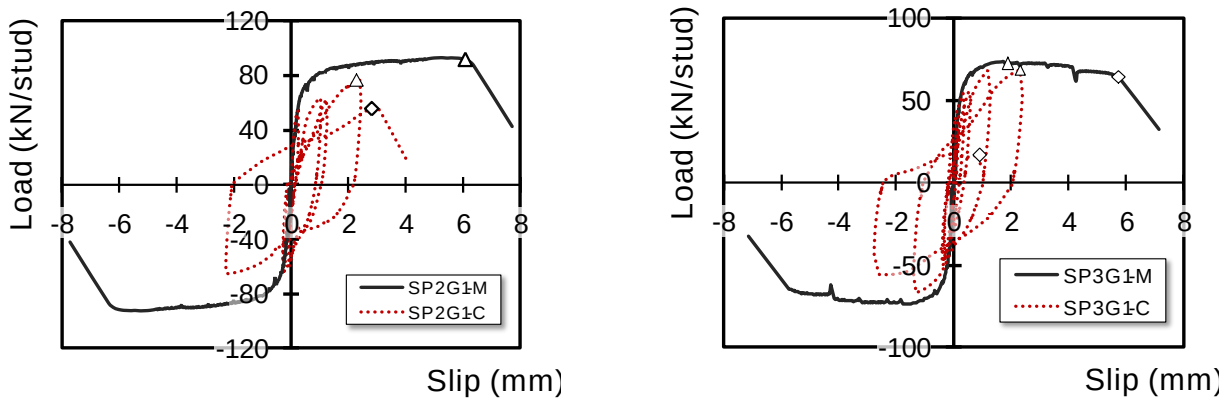

(a) (b)

Figure 3.21 Specimens responses when subject to monotonic and reversed cyclic loading

The cause of this strength degradation in cyclic loading can be attributed to several phenomena. Most importantly is the crushing the SFRCC adjacent to the base of the studs in the compressive face of slabs. The crushing of the SFRCC may not be very crucial for the monotonic load application; however, if the shear force applied to the SFRCC cyclicly, due to the separation of the damaged SFRCC from the stud in the folllowing cycles, the cyclic behavior may not be as ductile as disered. Also, tests indicate that large deformation and plastic yielding occure at the base of the stud shank. The high strain concentration, in the very short length zone affectd by the weld heat, cannot help to make the stud shear connector to behave better under reversed cyclic load. These phenomena have been nearly reported about the stud shear connectors in concrete component previously and we think that they also true with stud in SFRCC.

As Viest (Viest et al. 1997) has pointed out, for the case of cyclic loading, the behavior is highly dependent on the load history. If unloading at low loads, the behaivor is essentially linear and the systems shakes down with a stiffness very close to original stiffness. If unloading occures after the

stud enters athe grossly nonlinear range, the unloading occurs occurs initially at original stiffness. However, because the concrete in front of the connector has undergone permanent deformations, the unloading is not perferctly elastic and large residual displacements occur. If the load is reapplied, large slips take place with little increase of the load because of the void that formed in the concrete behind the stud at higher loads. Upon continued reloading the stud may not reach the monotonic envelop, and a decrease in strength and stiffness may be observed.

Effect of stud spacing

Figure 3.22(a) shows comparison on the monotonic shear-slip behavior before Specimen "SP2G1-M", which had two studs with a 90 mm longitudinal spacing, and Specimen "SP3G1-M", which had three studs with a 45 mm longitudinal spacing. Specimen "SP2G1-M" exhibits a typical shear-slip curve of stud fracture failure so that it reached the maximum strength right before a drastically drop due to stud fracturing. Specimen "SP3G1-M" reached its maximum strength at a small slip due to the onset of the splitting cracks in the slab. As shown in Figure 3.22a, after reaching the maximum strength, Specimen "SP3G1-M" showed a gently decreasing shear slip behavior until the studs fractured at the slip about 6 mm. The per stud strength of Specimen "SP3G1-M" is 74.6 kN, which is about 79% of the per stud capacity of specimen "SP2G1-M".

Figure 3.22(b) shows the comparison on the reverse cyclic shear-slip behavior of specimens "SP2G1-C" and "SP3G1-C". As indicated with the 'triangle mark', Specimens "SP2G1-C" and "SP3G1-C" reached their maximum strengths at a similar slip about 2 mm. After reaching the maximum strength, both specimens failed by stud fracture in the first half of the next cyclic. The per stud strength of Specimen "SP3G1-C" is 69.4 kN, which is about 88% of that of the per stud capacity of specimen "SP2G1-C".

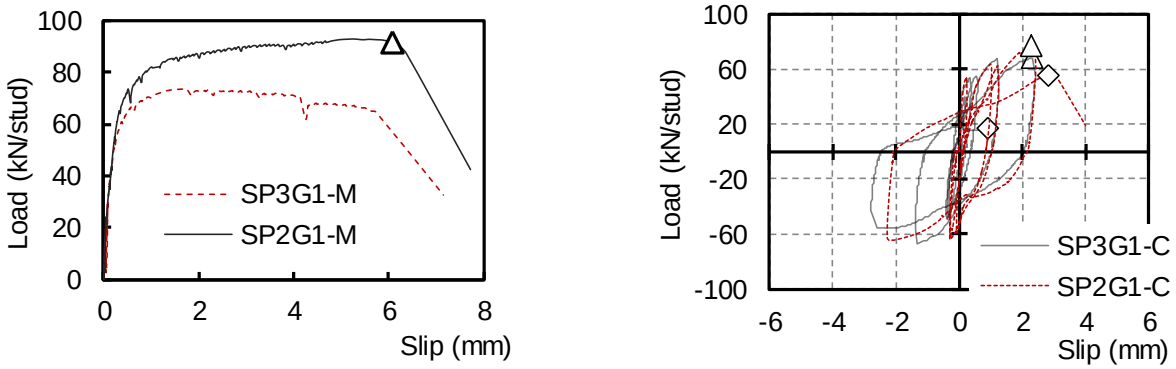

(a) (b)

Figure 3.22 Comparison on response of specimens with different stud spacing: (a) Monotonic loaded specimens; (b) Cyclic loaded specimens

Comparing the difference on per strength between the specimens with different stud spacing, it is notable that the difference between Specimens "SP2G1-M" and "SP3G1-M" is larger than the difference between Specimens "SP2G1-C" and "SP3G1-C". This implies that when the specimens subjected to reverse cyclic loading, the strength reduction caused by smaller stud spacing is released.

3.5 Conclusions

This research examines the possibility of achieving strong and compact connections in steel-concrete composite components using SFRCC and steel headed studs. As the initial step of this research, sixteen push-out tests were conducted for studs embedded in SFRCC. The diameter of studs, number of studs, pitch length, gauge length, and the fiber volume ratio of SFRCC were chosen as the test variables. Major findings obtained from this study are summarized below.

(1) Without reinforcing steel bars, the slab cast with SFRCC can achieve the failure mode of stud fracture with a shear capacity not smaller than that stipulated in design codes for reinforced concrete. This shows that using SFRCC is possible to avoid the cumbersome placement of shear and confinement reinforcement.

(2) When embedded in SFRCC, the studs arranged densely with a pitch length of 3.5 times the stud diameter can still possess a shear strength (per-stud) not smaller than 90% of the shear strength of a single stud, while in conventional concrete, a pitch length of 6 times the stud diameter is required to achieve the same strength.

(3) Even if the gauge length is reduced from 6.9 times the stud diameter (a code specified minimum) to 2.3 times the stud diameter (the minimum spacing allowed for stud installation), no reduction was found in the shear strength carried by the stud.

(4) Within an area of 6.9 d x 4.6 d, which is close to the minimum area stipulated in current design codes, only four studs are permitted to place for reinforced concrete, but for SFRCC, it is possible to place nine studs. Although the per-stud strength decreases as the pitch length decreases, but as the number of studs in the limited area increases, the total of transferred shear force increases to more than twice what can be achieved in reinforced concrete.

(5) The test results indicate that when the fiber volume fraction was reduced from 6% to 2%, the fiber volume does not affect shear strength but did have a significant impact mainly on the ductility and damage tolerance of the connection.

Supplemental push-out tests were conducted to investigate the effect cyclic loading on the strength and behavior of stud-SFRCC shear connection.

(1) Comparison on the specimens subjected to reverse cyclic loading and monotonic loading show that, the reverse cyclic shear reduced the maximum strength by 16% and ultimate slippage to one third of those subjected to monotonic shear.

(2) Under reserved cyclic loading, specimens showed 7% to 16% strength degradation from corresponding monotonic cases with changing the failure mode. In this type of loading, none of the specimens could withstand more than two cycles at 90% of its monotonic capacity.

REFERENCES

An, L., and Cederwall, K. (1996). “Push-Out Tests on Studs in High Strength and Normal Strength Concrete.” *Journal of Constructional Steel Research*, 36(1), 15–29.

Anderson, N. S., and Meinheit, D. F. (2005). "Pryout Capacity of Cast-In Headed Stud Anchors." *PCI journal*, 50(2), 90–112.

ANSI/AISC 360. (2010). *Specification for Structural Steel Buildings*. American Institute of Steel Construction, Chicago, Illinois.

Architectural Institute of Japan (AIJ). (2010). *Design Recommendations for Composite Constructions*. Tokyo.

Buzzini, D., and Dazio, A. (2006). *Quasi-Static Cyclic Tests on Three Hybrid Fibre Concrete Structural Walls*. Institute of Structural Engineering Swiss Federal Institute of Technology.

Doinghaus, P., Goralski, C., and Will, N. (2003). "Design Rules for Composite Structures with High Performance Steel and High Performance Concrete." American Society of Civil Engineers, 139–149.

Eurocode 4. EN 1994. (2004). *Design of composite steel and concrete structures. Part 1 General rules and rules for buildings*.

Kaneko, Y., Mihashi, H., Kirikoshi, K., and Abe, T. (2000). "Simplified uniaxial constitutive model of steel fiber reinforced cementitious composite." *AIJ Journal of Technology and Design*, 11, 5–8.

Nielsen, C. V. (1995). "Ultra High-Strength Steel Fibre Reinforced Concrete, Part I, Basic Strength Properties of Compresit Matrix." *Technical University of Denmark. Series R*, 323.

Oehlers, D. J. (1989). "Splitting Induced by Shear Connectors in Composite Beams." *Journal of Structural Engineering*, 115(2), 341–362.

Oehlers, D. J. (1995). "Design and Assessment of Shear Connectors in Composite Bridge Beams." *Journal of Structural Engineering*, 121(2), 214–224.

Oehlers, D. J., and Coughlan, C. G. (1986). "The Shear Stiffness of Stud Shear Connections in Composite Beams." *Journal of Constructional Steel Research*, 6(4), 273–284.

Okada, J., Yoda, T., and Lebet, J.-P. (2006). "A Study of the Grouped Arrangements of Stud Connectors on Shear Strength Behavior." *Struct Eng Earthqu Eng*, 23(1), 75S–89S.

Ollgaard, J. G., Slutter, R. G., and Fisher, J. W. (1971). "Shear strength of stud connectors in lightweight and normal-weight concrete." *AISC Engineering Journal*, 8(2), 55–64.

Qian, S., and Li, V. C. (2009). "Influence of concrete material ductility on headed anchor pullout performance." *ACI Materials Journal*, 106(1), 72.

Stang, H., and Li, V. C. (2004). "Classification of Fiber Reinforced Cementitious Materials for Structural Applications." *6th RILEM Symposium on Fiber-Reinforced Concretes (FRC) - BEFIB 2004*, 197–218.

Viest, I. M. (1956). "Investigation of Stud Shear Connectors for Composite Concrete and Steel T-Beams." *ACI Journal Proceedings*.

Viest, I. M., Colaco, J. P., Furlong, R. W., Griffis, L. G., Leon, R. T., and Wyllie, L. A. (1997). "Composite Construction Design for Buildings."

CHAPTER 4

Strength Evaluation of Stud-SFRCC Shear Connection

4.1 Introduction

4.1.1 Background

Headed stud shear connectors are the most widely used shear connectors in steel-concrete composite construction. Past research reveals that the ability of shear connection to transfer shear load depends on the steel-flange-concrete-slab interaction, named the dowel action. The strength of the dowel action depends on the stud details (height, diameter and strength), as well as on the surrounding concrete environment, such as concrete properties and reinforcement detailing. (Oehlers and Johnson 1981)

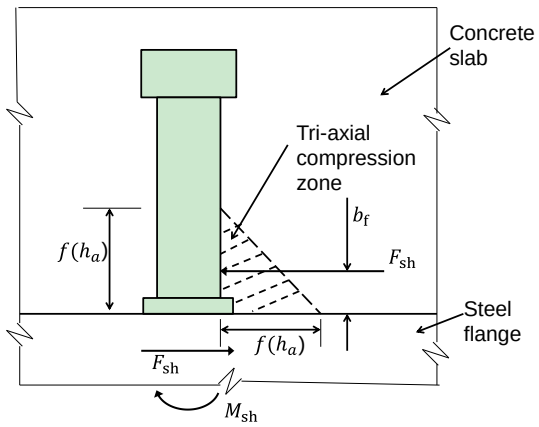

Figure 4.1 Dowel action (Johnson and Oehlers 1981)

The mechanism (Johnson and Oehlers 1981) by which the dowel action transfers the shear forces is illustrated in Figure 4.1 for the case of a stud shear connector. This shear force (F_{sh}) and flexural forces (M_{sh}) are induced in the shank of the stud. These forces are in equilibrium with an eccentric normal force across the stud-shank-concrete-slab interface acting at a distance b_f from the steel-flange-concrete-slab interface. The shank of the stud is, therefore, subjected to shear and flexural stresses, and the concrete zone immediately in front of the stud is subjected to high compressive stresses. The magnitude of these stresses depends not only on the shear force but on the position b_f of the resultant normal force, which is a function of the stiffness of the concrete relative to that of the steel. For example, if the stiffness of the concrete E_c tended to infinity, then the eccentricity

b_f would tend to zero, and similarly, if E_c tended to zero, then b_f would tend to half the height of the stud, i.e., the normal stress across the shank-concrete interface would be uniformly distributed. The dowel strength of the shear connection, therefore, depends on the strength and stiffness of the stud material and, also, on the compressive strength and stiffness of the concrete in the zone directly in front of the stud. Depending on the material properties of concrete and stud, two different failure mechanisms were reported in the previous research. One of the two failure mechanisms is defined by the shear fracture in the shank of stud close to the welded collar; the other is a failure in the concrete slab by pull out of the concrete adjacent to the stud.

Headed stud connections in precast concrete members can be found in column corbels, spandrel beams, dapped end members, wall panels, tee beams, and other component. Commonly, studs in precast members are 80 mm to 200 mm long and form a multi-stud group connection. The load capacities by these connections are generally affected by stud spacing, edge distances, and member depth or thickness. The headed stud anchorage group is a type of connection commonly used by the precast concrete industry.

The design standards for shear studs in solid concrete slabs are available in AISC-LRFD (2005), and other design specifications, such as Eurocode 4 (Eurocode 4 2004), and AASHTO (AASHTO 1998). AISC-LRFD prescribes the nominal strength of one stud shear connector embedded in solid concrete or in a composite slab is follows:

$$P_u = 0.5\mathrm{A_s}\sqrt{E_c f_c'} \le A_s f_{su} \tag{4.1}$$

where A_s: the cross-sectional area of the stud; f_{su}=specified minimum tensile strength of a stud shear connector (MPa); E_c=modulus of elasticity of concrete (MPa); and f_c'=compressive strength of concrete cylinders (MPa).

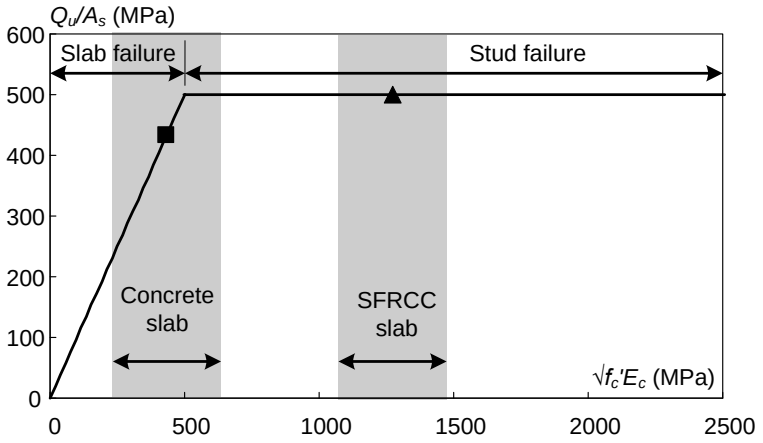

Figure 4.2 Nominal shear strength of one stud embedded in solid slab

However, it should be noted that the design Eq. (4.1) are only applicable when the tri-axial compression zones (as defined previously in Figure 4.1), do not overlap. This can be prevented by

placing limitations to the minimum lateral and longitudinal shear connector spacing. For example, with regard to the design Eq. (4.1), AISC (2005) restricts the lateral spacing to 6d and transverse spacing to 4d, where d is the diameter of the shank of the stud. These lower bound values were based on the smaller pitch and gage length applied on a substantial number of test specimens.

With regard to the Equation (4.1), here, we define q_{su1} and q_{su2} as follows,

$$q_{su1} = 0.5\mathrm{A_s}\sqrt{E_c f_c'} \tag{4.2}$$

$$q_{su2} = A_s f_{su} \tag{4.3}$$

Of these two variables, q_{su1} is the shear capacity of a stud failing for shear fracture, while q_{su2} is for the failure in the slab. To study Eq. 4.2, q_{su2} is equal to the product of the ultimate tensile strength and the section area of a stud, and this indicates that one shear connector provides large shear capacity for the given material volume and strength.

Shear strength capacity, Q_u, of a stud connector with 22mm diameter and 500N/mm^2 of f_{su}, with concrete of variable compression strength is shown in Figure 4.2. Note that the following equation was used to estimate E_c.

$$E_c = 2.1 \times 10^5 \times (\gamma/2.3) \times \sqrt{f_c'/20} \tag{4.4}$$

where γ is the density of the concrete. Figure 4.2 was obtained assuming γ=2.7g/cm^3. Hence, stud connectors can possess the shear capacity of q_{su2}, the larger of the two strengths, using readily available concrete.

However, it is not easy to further improve the shear strength of the stud connectors, namely, as Figure 4.2 suggests, q_{su2}. It can be achieved either by using studs of a large diameter or a high ultimate strength, but the former option requires the usage of a heavy welding machine and a huge weld heat input, and for the latter, manufacturing high-strength (e.g. 800N/mm^2) studs has been proved too costly (Inoue at 2002). On the other hand, if, in a connection using multiple studs allocated with pitch and gauge lengths significantly smaller than the aforementioned lower bound values, each stud could develop a shear strength comparable to q_{su2}, and a large shear force would be transferred through a small connection area.

When the studs are applied to the shear connection between the steel girder and the shear holes of precast slabs, to the connection between the main girders and the piers, as well as to the connection between the steel cells of the pier and the covering concrete, the studs are often arranged longitudinally and transversally with smaller spacing between two adjacent studs. Such arrangement is referred to hereafter as 'grouped arrangement'. If the studs are grouped very closely together in the connection, the required performance may not be satisfied.

According to the Architecture Institute of Japanese Design Specifications (Architectural Institute

of Japan 2001) or the AISC-LRFD (AISC 1999) etc., the design shear strength of studs is based on standard push-out tests where the studs are arranged in larger spacing. Such arrangement is referred to hereafter as 'standard arrangement'. Therefore, whether or not the strength of the grouped arrangement of studs equals the sum of the strengths of single stud.

Studies on the shear strength of the grouped arrangement of studs were also become a concern based on push-out tests. Okada carried out push-out tests at EPFL in Switzerland. Later Okubo et al. (Okubo and Kurita 2005) did push-out tests using the same parameters of test specimens as Okada did. It was recognized from these tests that no obvious reduction in shear strength can be found if the specimen size, the amount of reinforcement, and the strength of concrete are sufficiently large. Some investigation, however, depending on experimental parameters that a possible reduction in shear strength may occur due the highly concentrated forces in the grouped arrangement. Accordingly, the test results lack in consistency.

Generally, the stud spacing smaller than that stipulated in the specifications is not allowed. However, to achieve better rationalization of application of headed stud connectors, it is necessary to arranged studs to a narrow space in the connection. Therefore, the dowel strength of closely spaced connectors should be reduced to allow for the lateral overlap of the tri-axial compression zone. Many studies (Davies in 1967, Roik & Hanswille in 1975, Hiragi in 1995) were conducted to this issue. An example for this reduction (Johnson and Oehlers 1982) is given in Eq. (4.5) as follow:

$$P_{pr} = P_{cb} + 0.2P_{cb}(d_g/d) \tag{4.5}$$

where $P_{pr} \leq 2P_{cb}$, P_{cb} is the shear strength of per stud; d_g = transverse spacing of stud connectors; P_{pr} is the strength of a pair of stud.

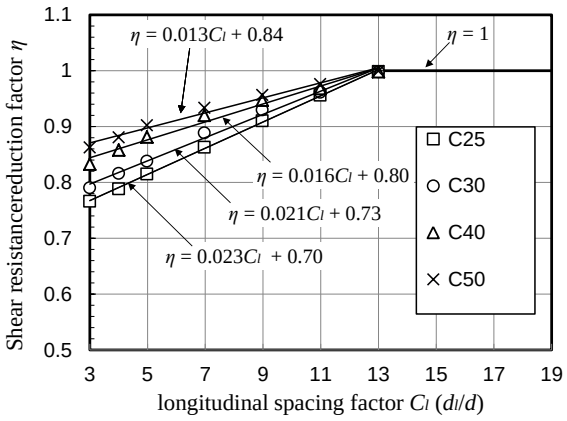

Figure 4.3 Strength reduction factor versus stud longitudinal spacing (Okada et al. 2006)

Okada et al. (2006) investigated headed stud shear connectors in the group arrangement both experimentally and analytically. In their study, the effect of group arrangement on the strength of stud shear connectors was investigated by using the longitudinal spacing of studs as the parameter and the

reduction factor related to longitudinal spacing-stud diameter ratio is proposed for concrete with different compressive strengths ranging from 25 MPa to 50 MPa, as shown in Figure 4.3. Okada (Okada et al. 2006) pointed out that when the studs are placed closely, the static strength of the connection would decrease because of the damage overlapping in the concrete portion around the bottom parts of the stud shank. Their research also indicates that the strength reduction caused by small longitudinal stud spacing will loosen when stronger concrete is used.

In order to allow for the particular design situation of close stud spacing than the design requirement, it is necessary to provide an empirical equation for the shear connector with headed studs embedded in the solid SFRCC slab.

4.1.2 Objectives

The main objective of this chapter is to quantify the strength of stud-SFRCC shear connection. To evaluate the strength of the stud-SFRCC shear connection, two failure mode, the stud shear failure and slab split failure are considered based on the experiment observation and analysis investigation.

For the failure mode of stud fracture, the strength for single stud connector embedded in SFRCC slab should be estimated first. In the proposed stud-SFRCC shear connection, stud connectors are closely placed in SFRCC slab. The reduction for per stud strength will be considered in view of the reduction mechanism.

For the failure modes of slab split, past research on the slab split strength evaluation for stud-concrete connection was referred. Since SFRCC is much different to convention concrete, adjustment will be employed to take into account the different material properties of SFRCC.

The strength evaluation for stud-SFRCC shear connection is established by generalizing the strength estimation formulas for the two failures. Effects of various design parameters on strength of the stud-SFRCC shear connection are illustrated through a given example.

4.1.3 Organization

A reliable nonlinear three-dimensional finite element model is developed to reproduce the experimental behavior of stud-SFRCC connection specimens presented in the Chapter 3. Using the verified FEM model, a comprehensive parametric study is carried out to investigate various effects on the strength and performance of headed stud connectors embedded in solid SFRCC slab. Finally, information for the strength evaluation and design is proposed by generalizing the analytical and experimental results.

4.2 FEM modeling and verification on stud-SFRCC connection

In Chapter 3, a series of push-out test for stud-SFRCC shear connection was conducted to investigate its strength and behavior. To supplement the results obtained from the experimental study, finite element method was adopted to further study the interaction mechanism and effect of design parameters on the strength and behavior of the stud-SFRCC shear connection. In this section, the

push-out test specimens are modeled to reproduce the experimental behavior of the stud-SFRCC shear connections. The calibrated FEM model will be used for the following parametric study.

4.2.1 Finite element model

A finite-element model for the specimens tested in the push-out test was constructed using a standard finite-element package ABAQUS 6.10.1 (Systèmes 2010). The model was developed to reproduce the push-out tests and then performs a parametric study on the influence of the weld collar and stud pitch length on the shear capacity of a group of studs.

A three-dimensional eight-node (C3D8R) with reduced integration with an hourglass control was used to model the push-out specimens for improving the rate of convergence. Components including the SFRCC slab, beam flange, beam web and studs were modeled with solid C3D8R elements. Due to the symmetrical nature of the specimen, only a quarter of the push-out test specimen was modeled. An overview of the finite element model is shown in Figure 4.4(a) and (b).

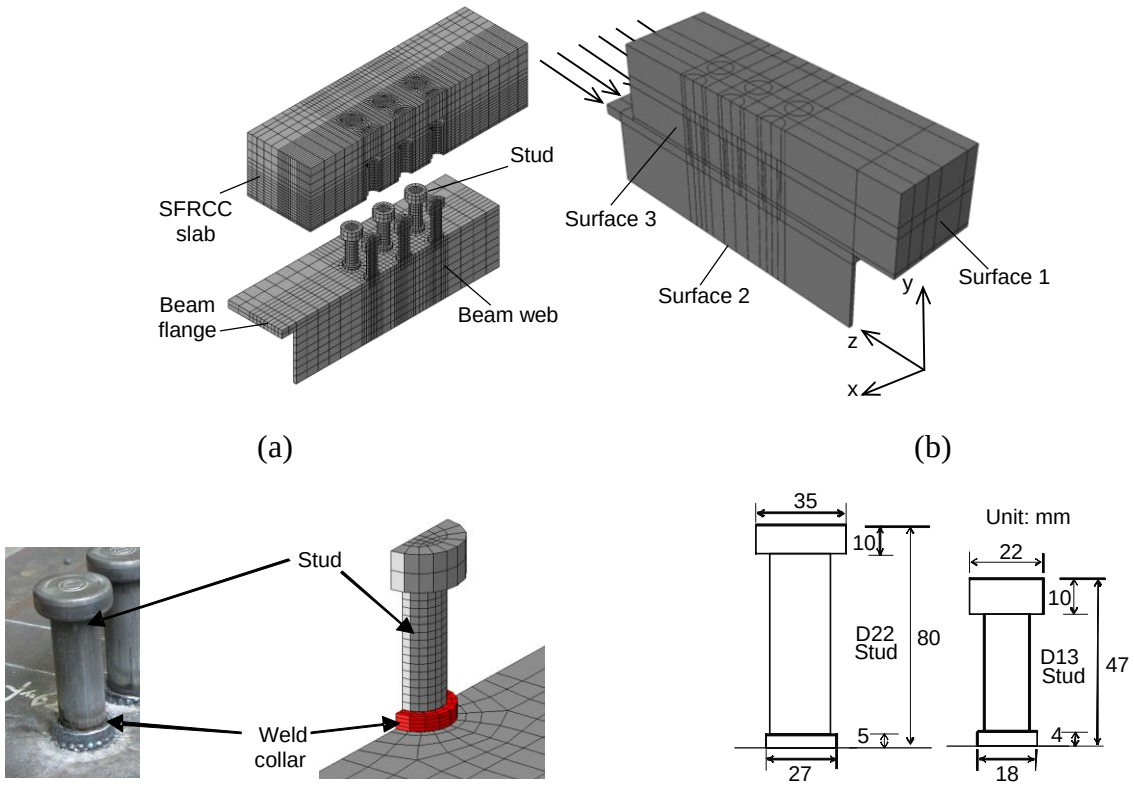

Figure 4.4 Analysis Model: (a) Model; (b) Boundary conditions; (c) Model for stud; (d) Dimensions of stud

As for the modeling of studs, a previous study (Doinghaus 2001; Doinghaus et al. 2003; Hegger et al. 2006) pointed out that the presence of a weld collar can significantly affect the strength of the stud shear connector and its effect increases for higher strength concrete. To reflect those observations as well as the high strength of SFRCC, the collar portion was also modeled in the analysis. Figure 4.4(c) and (d) shows the model mesh and the dimension detail of the studs.

4.2.2 Contact interaction and boundary conditions

Contact interaction between the slab and beam flange surface was defined with a friction coefficient of 0.4 (PCI Industry Handbook Committee 2004). Contact interaction between the stud and slab surface was defined without friction.

Load was applied on the nodes on the end surface of the beam flange and web as shown in Figure 4.4(b). The load was controlled by the displacement in the longitudinal (Z) direction up to a displacement of 6 mm, which was close to the slip corresponding to the stud fracture (4 to 5 mm) observed in the test. The displacements of all nodes in the slab (Surface 1 in Figure 4.4(b)) were restrained. Considering the symmetry, the displacements of all nodes in the vertical (Y) direction were restrained along the web end (Surface 2); likewise, the displacements of all nodes in the transverse (X) direction were restrained for the slab, stud, and steel web (Surface 3).

4.2.3 Material models and properties

A classical metal plasticity based on von Mises yield surface with associated plastic flow was adopted to define the material properties of the elements that represented the stud and steel beam. A bilinear and tri-linear stress-strain models as adopted to simulate the beam and the studs, respectively (Figure 4.5(a) and (b)).

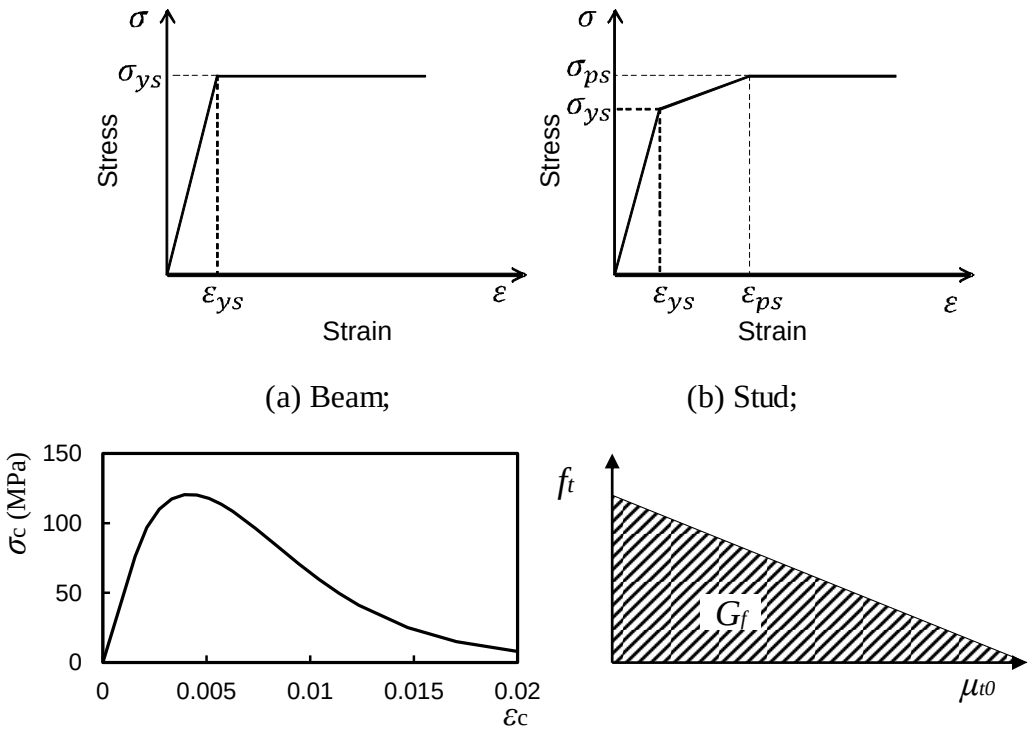

(a) Beam; (b) Stud;

(c) Compression/SFRCC; (d) Tension/ SFRCC

Figure 4.5 Stress-strain relationship curves: (a) Beam; (b) Stud; (c) Compression/SFRCC; (d) Tension/SFRCC

The shear connector would sustain significant yielding; hence the material was modeled by a tri-linear stress-strain curve as shown in Figure 4.5(b). The material behavior is initially elastic,

followed by strain hardening and then plastic flow. Young's modulus E_s, the yield stress σ_{ys}, and the ultimate stress σ_{us} were taken to be 205 GPa, 394 MPa and 475 MPa in reference to the associated material tests. A simpler bilinear model was adopted for the beam, but it remained elastic in the analysis.

The damage plasticity model was adopted to represent the material characteristics of SFRCC. According to (Nielsen 1995), the compressive stress-strain relationship of SFRCC is defined by the following equation,

$$\frac{\sigma}{f_c'} = \frac{2.5\frac{\varepsilon}{\varepsilon_c}}{1.5 + \left(\frac{\varepsilon}{\varepsilon_c}\right)^{2.5}} \tag{4.6}$$

Where ε_c and f_c' are the compressive strain and stress at the peak point, the strain-stress relationship is schematically shown in Figure 4.5. On the tension side, the model was defined independently in two strain levels. Up to cracking, the stress-strain relation was linear; and post-cracking behavior was represented by a linear stress-crack opening displacement relationship as shown in Figure 4.5(d).

The cracking displacement, at which the tensile strength is reduced to zero, was calculated by Equation 5, which was based on the fracture energy. The compressive stress at the peak point f_c' was determined by the associated material test; the tensile stress at the peak point f_t was calculated by the model developed in the past (Kaneko et al. 2000) and using the split strength obtained from the material test. Young's modulus of E_0=45GPa and a fracture energy of G_f= 6.6 N/mm were adopted in reference to (Kaneko et al. 2000).

4.2.4 FEM analysis and verification

By use of the ABAQUS post processor, the overall load-slip relationships as well as the stress distribution across the stud and SFRCC slabs were obtained.

Figure 4.6 shows comparison between the experimental and analytical load-displacement relation curves for Specimens P1G1-6% and P2G1-6%, which was arranged with studs of a diameter of 22 mm, and Specimen SP2G2-4% and SP2G2-2%. Table 4.1 tabulates the comparison in the per stud strength between the test and FEM analysis. Good agreement between the test and analysis was observed in both Figure 4.6 and Table 4.1, and the difference in maximum strength ranged from 2% to 14 %.

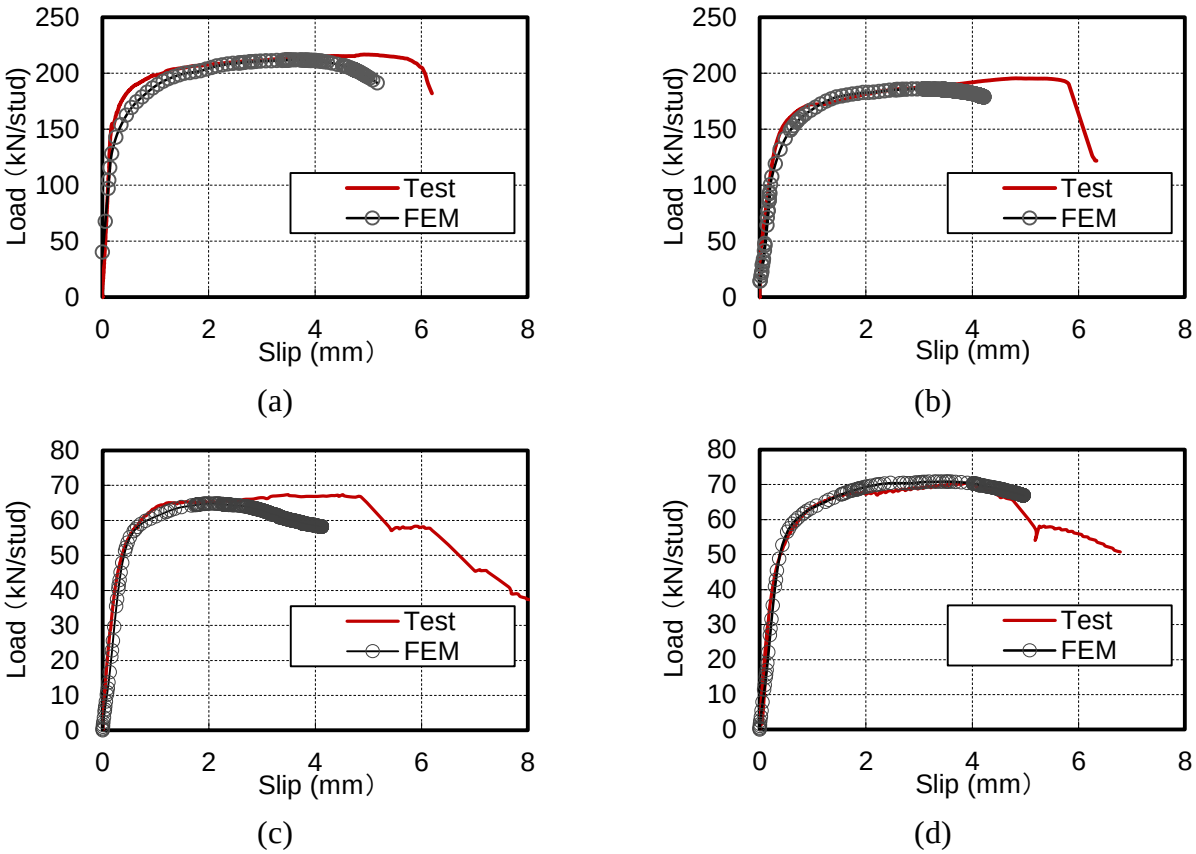

Figure 4.6 Load-displacement curves of specimens:
(a) P1G1-6%; (b) P2G1-6%; (c) SP2G2-2%; (d) SP2G2-4%

Table 4.1 Comparison on per stud strength between FEM results and test results

No.	Specimens	D_p/d	D_g/d	P_{stud} (kN)	P_{FEM} (kN)	P_{FEM}/P_{stud}
Pilot test						
1	P1G1-6%	-	-	217	212	0.98
2	P2G1-6%	2.3	-	196	189	0.96
3	P2G2-6%	2.3	2.3	192	186	0.97
4	P4G1-6%	2.3	-	171	171	1.00
Parametric test						
5	SP1G1-6%	-	-	110	105.1	0.96
6	SP2G2-6%	6.9	4.6	104	101.4	0.98
7	SP3G2-6%	3.5	4.6	93.1	90.6	0.97
8	SP3G3-6%	3.5	2.3	93.6	80.3	0.86
9	SP4G2-6%	2.3	4.6	76.6	73.7	0.96
10	SP4G1-2%	2.3	-	69.7	66.8	0.96
11	SP4G1-4%	2.3	-	76.3	73.8	0.97
12	SP4G1-6%	2.3	-	73.7	75.5	1.02
13	SP2G2-2%	2.3	2.3	85.0	81.0	0.95
14	SP2G2-4%	2.3	2.3	88.7	88.5	1.00

The two failure modes, i.e., the stud fracture and slab split, observed from the analysis, are shown in Figure 4.7. The white regions encircled by thin black bordering regions are where the strain reached a very large level; for the studs, it was defined where the equivalent plastic strain was greater

than 20%; and for the SFRCC slab, it was defined where the equivalent plastic strain was greater than 3%. When reaching these strain levels, SFRCC was considered to crush.

For the specimens failed in the stud fracture, the local equivalent plastic strain was far larger than 20% at the lower end of the shank (close to the weld collar) as shown in Figure 4.7(a). This suggests that the fracture failure section would coincide what was observed in the test. As for the slab, the local region directly in front of each stud reached 3% in the strain, which means that that region would crush along the loading direction as shown in Figure 4.7(b).

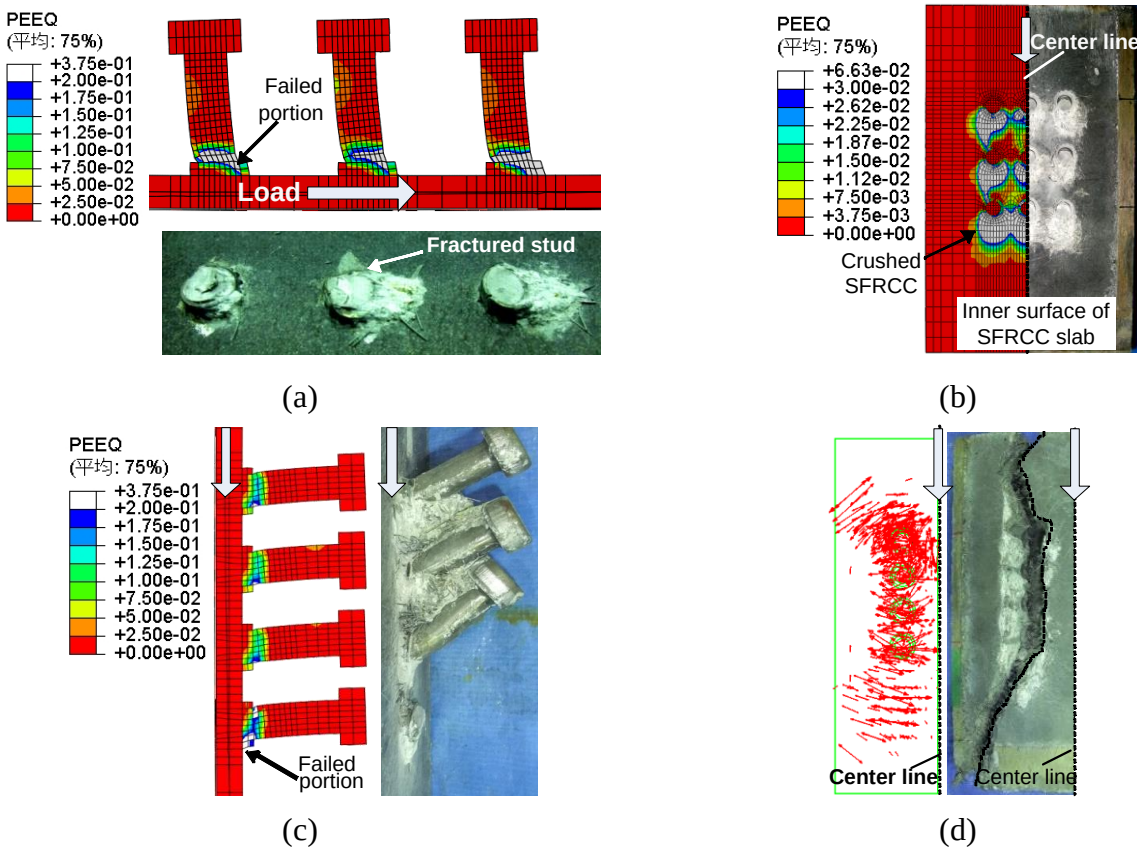

Figure 4.7 Failure modes obtained from analysis: (a) Studs in specimen failed in stud fracture; (b) Slab in specimen failed by stud fracture; (c) Studs in specimen failed by slab split; (d) Slab in specimen failed by slab split

For the specimen failed in the slab split (SP4G2), the stud's equivalent plastic strain exceeding 20% was observed only in a small region at the root of the most front stud as shown in Figure 4.7(c), and the maximum strain in the other studs were substantially smaller (5% to 15%). It suggests that the studs had not reached their shear capacity at the instant of slab split. On the other hand, the tensor plots of maximum principal strain in SFRCC slab (Figure 4.7(d)) shows the crack pattern, where the crack is presented as a line and the length of the line represents amount of the maximum principal strain. It can be seen that the region around the studs are completely occupied by cracks, and the cracks even extend to the side free edge of the slab. Those evidences suggest that the failure of this specimen was caused by splitting cracks formed in the slab.

The simulated ultimate state was very similar to what was observed in the physical test as shown

in Figure 4.7, indicating that the finite element model can reproduce the behavior of steel-stud embedded in SFRCC slab with reasonable accuracy. Using the calibrated FEM models, a future study focusing on the strength evaluation for the stud-SFRCC shear connection will be carried out in the following sections.

4.3 Strength evaluation for single headed stud embedded in SFRCC

4.3.1 Effect of welded collar portion

(Doinghaus et al. 2003) pointed out that the load-bearing behavior of headed stud shear connectors in high-strength concrete is different from that in normal-strength concrete. To investigate the influence of welded collar on the strength of headed stud connector embedded on SFRCC, a parametric analysis focusing on the dimension of weld color and SFRCC compression strength was carried out.

To investigate the effect of stud welded collar on the stud shear strength in SFRCC slab, and an FEM model without the collar portion was created for each of Specimens 'P1G1-6%' and 'SP1G1-6%' and compared to those modeled with the collar portion.

Table 4.2 summaries the analysis results. P_{FEM} is a per stud strength obtained from the analysis. The model with postfix of 'NWC' did not consider the weld collar portion, whilst the model with postfix of 'WC' did. As for the maximum strength P_{FEM}, the difference between the two models, i.e., 'NWC' and 'WC', was 29 % and 58 % for Specimens P1G1 and SP1G1, respectively. When the weld collar was considered, P_{FEM} shows little difference from the corresponding experimental strength P_{stud} (from 4% to 8%).

Table 4.2 Analysis results

Model	P_{FEM} (kN)	P_{stud} (kN)	P_{AISC} (kN)	$P_{\mathrm{FEM}}/P_{\mathrm{stud}}$	$P_{\mathrm{FEM}}/P_{\mathrm{AISC}}$
P1G1-NWC	180.6	216.7	180.2	0.83	1.00
P1G1-WC	233.5			1.08	1.30
SP1G1-NWC	66.7	110.2	62.9	0.61	1.06
SP1G1-WC	105.4			0.96	1.68

Figure 4.8 shows the shear bearing force distribution along the stud height when the maximum load was attained. In the figure, the vertical axis is the height of the stud section, and the horizontal axis is the shear bearing force at the corresponding stud section. The shear force distribution is almost same for the two models in the upper half of the stud, while in the lower part, the model that considered the weld collar shows larger shear bearing force by about 25 % for Specimen 'P1G1' and 41 % for Specimen 'SP1G1'. This concentration was a plausible source that had caused larger shear bearing capacity obtained in the test than the code specified strength. It is notable that the increase in

strength by the presence of collar portion was more conspicuous in SP1G1 (the scaled specimen with D13 studs) than P1G1 (the full-scale specimen with D22 studs). It occurred primarily because of the difference in the rate of increase in the cross sectional area by the addition of collar portion. The cross sectional area increased to 1.51 for P1G1 (with D22 studs) and to 1.91 for SP1G1 (with D13 studs). This is another evidence that the weld collar portion would be responsible for the increase in stud strength (relative to the code specified strength).

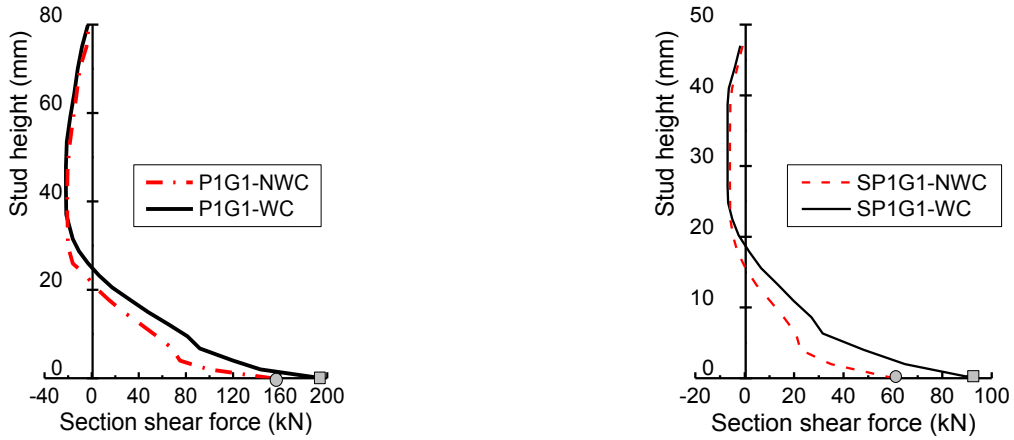

(a) (b)

Figure 4.8 Comparison on section shear force along stud height: (a) P1G1; (b) SP1G1

(Doinghaus et al. 2003) pointed out that the load-bearing behavior of headed stud shear connectors in high-strength concrete is different from that in normal-strength concrete. They proposed a formula specifically for headed stud shear connector in high-strength concrete. By considering the load bearing contribution of the weld collar, the formula is given by

$$P_u = A_{sc} f_{su} + \eta f_{cu} d_{\mathrm{wc}} l_{\mathrm{wc}} \tag{4.7}$$

Where A_{sc}=cross-sectional area of a stud shear connector;

f_{su}=ultimate tensile strength of stud;

η is the empirical correction value to determine the load-bearing action of the concrete in front of a shear connector ($\eta = 1.5$ for concrete was suggested by Doinghaus);

f_{cu}: Concrete cylinder compressive strength; $f_{\mathrm{cu}} d_{\mathrm{wc}} l_{\mathrm{wc}}$

d_{wc}: Equivalent diameter of weld collar;

l_{wc}: Equivalent height of weld collar.

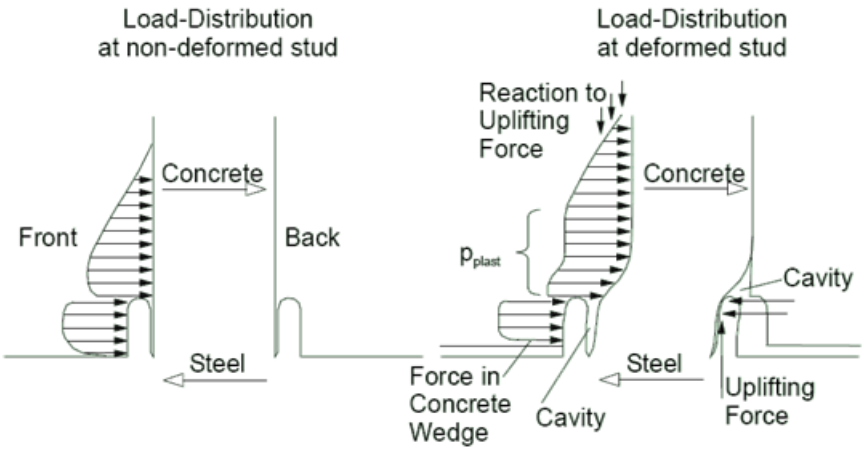

Figure 4.9 Load distribution and deformation of the connector shaft (Hegger et al. 2001)

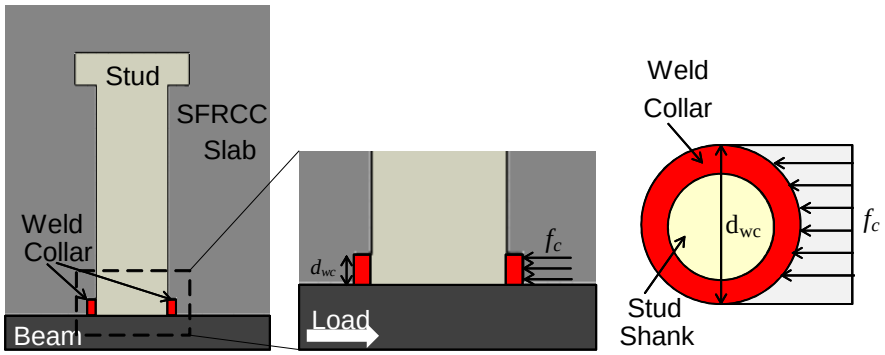

Figure 4.10 Modeling for the force acting on the concrete wedge

The FEM analysis and the past research (Hegger et al. 2001) both indicate that the existence of the weld collar can affect the strength of the headed stud shear connection. In Eq. (4.7), an empirical factor $\eta = 1.5$ is suggested for a headed stud embedded in concrete slab. Because SFRCC is much stronger (higher compression strength and higher Young's Modulus) and much stiffer (two times elastic modulus) than conventional concrete, it is necessary to quantify the value of η to make it applicable for SFRCC. In order to quantify the η for SFRCC, a series of numerical studies were carried out using specimens P1G1 and SP1G1 as the prototype specimens. The dimensions of the weld collar and the compression strength of SFRCC were selected as the main variable. The details of the FEM models are summarized in Table 4.3.

Table 4.3 List of analysis cases

FEM models	d (mm)	h (mm)	h_{wc} (mm)	d_{wc} (mm)	f_c' (MPa)
D13H80_WC1	13	80	4	18	120
D13H80_WC2			4	16	
D13H80_WC3			7	18	
D13H47_C120	13	47	4	18	
D13H100_C120	13	100	4	18	
D16H80_C120	16	80	5	21	

D19H80_C120	19	80	5	25	
D22H80_C120	22	80	5	27	
D25H80_C120	25	80	5	32	
D22H80_WC1	22	80	5	27	
D22H80_WC2			5	25	
D22H80_WC3			7	27	
D13H100_WC1	22	100	5	27	
D13H100_WC2			5	25	
D13H100_WC3			7	27	
D13H47_C90	13	47	4	18	90
D13H47_C105					105
D13H47_C120					120
D13H47_C135					135
D13H47_C150					150
D22H80_C90	22	80	5	27	90
D22H80_C105					105
D22H80_C120					120
D22H80_C135					135
D22H80_C150					150

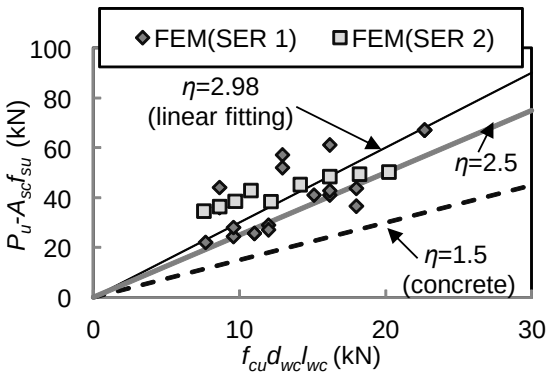

Figure 4.11 Comparison on different empirical factor, η

Summarizing the obtained FEM analysis results of the cases listed in Table 4.3, the relationship between the strength contributions of weld collar P_u-$A_{sc}f_{su}$ and the product of the terms related to stud dimensions $f_{cu}d_{wc}l_{wc}$ is plotted in Figure 4.11. Tendency lines using different values of η are also plotted and compare to the scatting data points, including η =1.5 for concrete, η =2.98 obtained by linear fitting to the scatters, and η =2.5 conservatively modified from the linear fitting value. From Figure 4.11, it can be seen that the empirical factor η =1.5 is too conservative for the obtained results. Although η =2.98 is obtained from the best linear fitting to the scatter of data points, because the data from the two series of FEM analysis show relative large discreteness, a modified

value η =2.5 is found shown a good balance between conservative and accuracy as shown in Figure 4.11.

The modified η =2.5 is verified with experimental results and finite element analyses results. The test data includes that from the previous test introduced in the Chapter 3 and push-out test on stud shear connector in high strength concrete slab from other researchers (An and Cederwall 1996). The verification data from finite element analyses consist of two series of analyses that focus on different variables. The first series focus on the dimension of welded collar, while the second series focus on the compressive strength of the SFRCC slab. Figure 4.12 shows a comparison of the predicted shear strength calculated using the modified empirical factor η=2.5 and the shear strength determined experimentally and by numerical analysis. It is found that the proposed equation can estimate the shear bearing capacity of the headed stud connector embedded in solid high strength concrete slab properly.

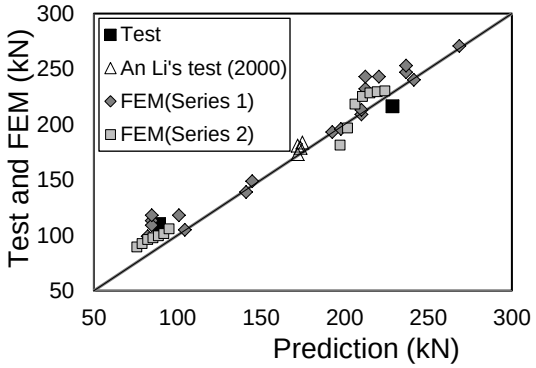

Figure 4.12 Verification on predicted strength for single stud in SFRCC

4.4 Strength evaluation for headed stud cluster embedded in SFRCC

4.4.1 Strength reduction mechanism for close arranged studs

Based on the test observation in Chapter 3 and the understanding from the past research, two reasons were presumed responsible to the reduction of per stud strength of group arranged studs.

The first reason is the stiffness deterioration caused by the damage of the slab in the vicinity of the stud. As a result, the confining effect from the surrounding SFRCC on the headed stud will decrease. Past research (Johnson and Oehlers 1981) indicates that the strength of headed stud connector depends on the interaction between steel stud and surrounding concrete, and therefore reduction of the confining effect from slab on stud can cause the reduction of shear strength. A bending coupled shear deformation is more likely to happen. In the analysis by Anderson and Meinheit (Anderson and Meinheit 2005), higher bending deformation combined with shear deformation reduces the capacity of the headed stud to a lower value than the A_sF_{ut}. Furthermore, there are two sources for the stiffness deterioration of the surrounding SFRCC of the stud connector. First, when the slab portion in the vicinity of the stud root is crushed by the compression from the stud, the stiffness of this portion decreases. When reducing the stud spacing, the front stud is included

within the bearing zone of the rear stud. Secondly, as the front stud deforms during the shear loading, a cavity occurred between the stud root and the slab. The presence of such cavity reduced the confining effect on the rear stud.

The second reason is that the studs do not reach their ultimate strength simultaneously due to the difference of the confining conditions on each stud. Along the loading direction, the most front stud connector subjects to largest confining effect and thus reach its ultimate strength earliest and fracture first. When the most front stud fracture, the remaining studs cannot sustain the applied load and fracture accordingly. Since the rest studs do not reach their respective maximum strength, the per stud strength is made smaller than the strength of a single stud.

To examine the above interpretation of the mechanism of the strength reduction in closely arranged stud group, various models with different D_p values were analyzed. The pitch length ranged from 90 mm, the length close to the minimum specified spacing (78 mm) allowed for D13 stud embedded in concrete slab, to 30 mm, the minimum spacing allowed for stud installation. Following notation was adopted, e.g., in 'Dp30', 'Dp' represents the distance in the pitch direction; '30' means the center-to-center distance between two adjacent studs is 30mm. Figure 4.13 shows the shear-slip curves and the corresponding per stud strengths obtained from the analysis. Both the maximum strength and initial stiffness decreased for a smaller stud pitch length; when the pitch length was reduced from 90 mm to 30mm, the maximum strength dropped by about 10% (Figure 4.13(a)).

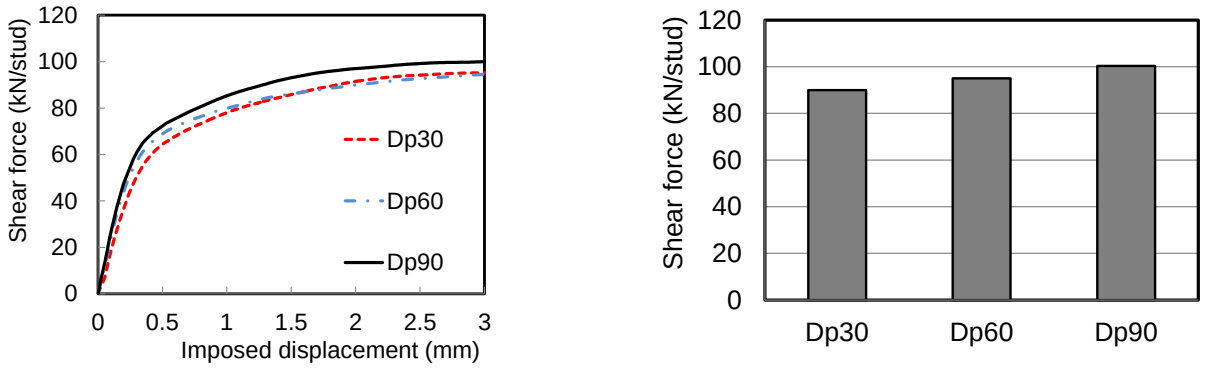

(a) (b)

Figure 4.13 Per stud strength for various pitch lengths: (a) Load-displacement relationship curves; (b) Shear strength.

Figure 4.14 shows the equivalent plastic strain contours of the SFRCC slab and studs for'Dp30' and 'Dp90' at the instant when the applied load reached its maximum. In the contours, regions in white represent where the equivalent plastic strain exceeds 20% for the stud and exceeds 3% for SFRCC slab. These values were considered to indicate failure. As shown in Figure 4.14(a), the SFRCC failed portions that appear in front of the two studs merged together in 'Dp30', while the SFRCC failed portions remained relatively independent in 'Dp90'. The overlap of SFRCC failed portions in 'Dp30' was believed to have lessened the confinement of the rear stud, which in turn have reduced the read stud's shear strength.

On the other hand, the stud failed portions in the front and rear studs are very similar in 'Dp90' (Figure 4.14(b)). In 'Dp30', the front stud develops a larger stud failure portion, meaning that the front stud sustains a larger force than the rear stud. In addition, the two studs in 'Dp30' are arranged so close to each other that the gap behind the front stud is filled with the SFRCC portion pushed by the rear stud as shown in Figure 4.14(b). This indicates that the SFRCC portion between the roots of the front and rear studs deformed substantially and therefore promoted the reduction in confinement of the rear stud.

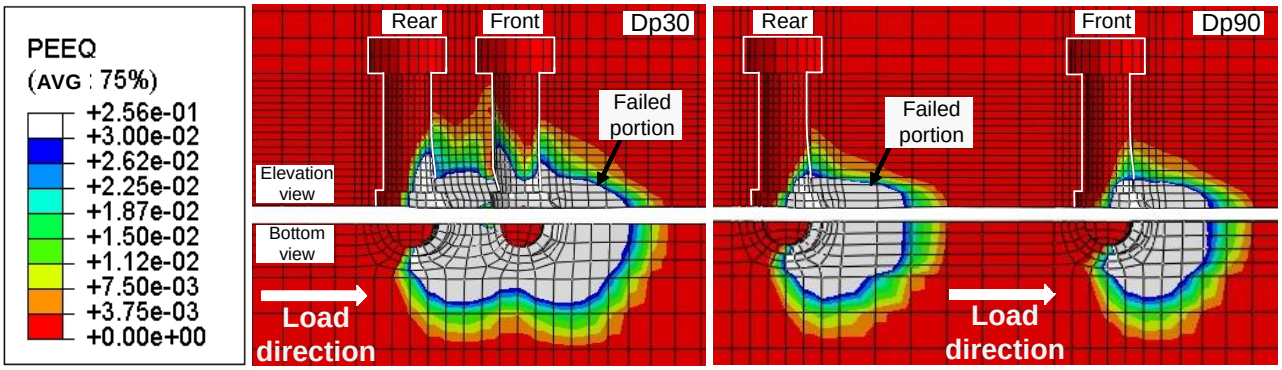

(a)

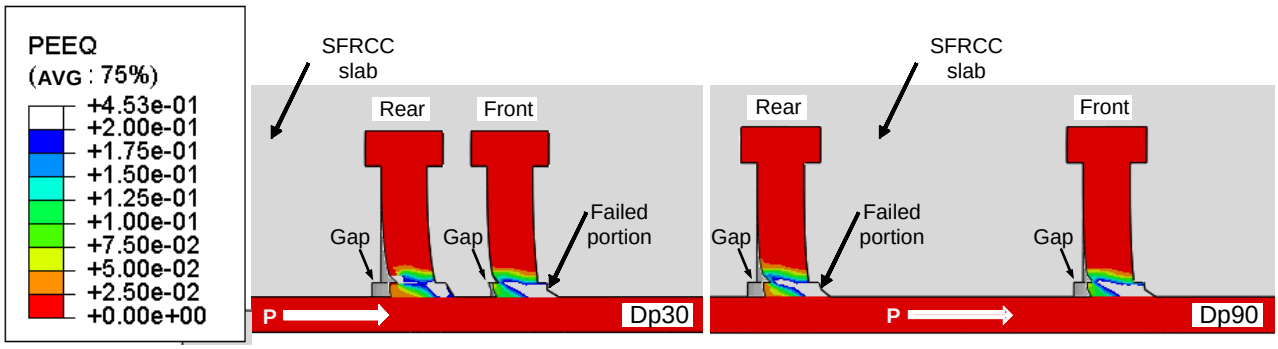

(b)

Figure 4.14 Comparison on plastic strain contour: (a) SFRCC slab; (b) Stud.

The shear bearing force at the instant when the maximum load was attained was estimated for respective studs. The shear force-slip curves of the front stud and rear stud are shown in Figure 4.15 for both 'Dp30' and 'Dp90'. In the beginning, the shear bearing force is similar in the front and rear studs, but when the studs began to yield, a notable difference on the shear bearing force is observed. The front stud showed a 21% larger shear force than the rear stud at the slip of 0.5 mm in 'Dp30', while the two studs showed the same shear bearing load in 'Dp90'. Those evidences obtained from the test and analysis suggest that the shear bearing capacity of the rear stud would decrease by the overlap of crushed SFRCC portion between the studs as well as the gap induced by local deformations of the front stud. Therefore, the mean strength of a group of studs would be made smaller for a smaller pitch length.

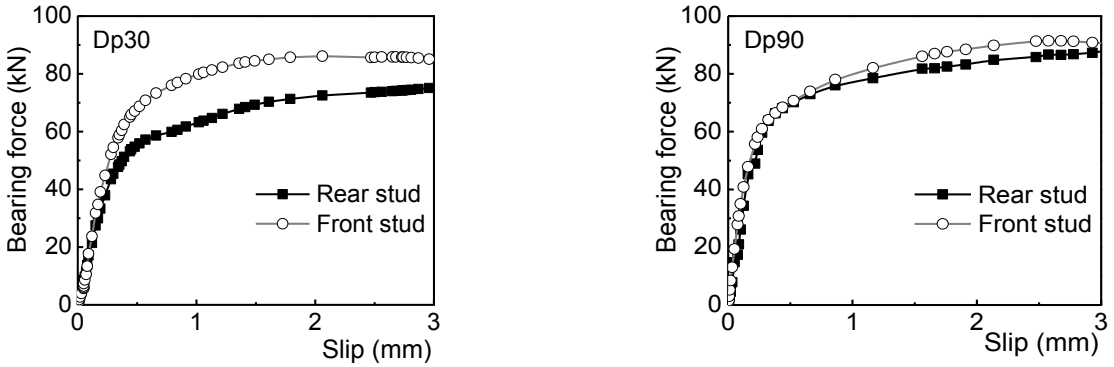

(a) (b)

Figure 4.15 Bearing force-slip curves for front and rear studs: (a) Model 'Dp30'; (b) Model 'Dp90'

4.4.2 Shear contribution among studs arranged in a line

A preliminary investigation on the shear force sustained by each stud was carried out for the case of pair stud arranged in a line by means of the FEM analysis, the following understanding on the mechanism of closely arranged stud group was obtained: (1) In the headed stud connection cluster, the stud subjected to largest confining reached its ultimate strength and fracture earlier, rather than all the studs reach the ultimate strength and fracture at the same instance; (2) Small stud spacing caused overlap of the bearing zone and led to the reduction of the confining effect on studs and the reduction of the stud strength.

To generalize the interpretation on behavior of group arranged studs under more extensive conditions, e.g. multiple studs more than two, a comprehensive parametric study is carried out using finite element analysis.

Analysis cases and parameters

The analysis parameters were the stud pitch length and the number of studs. The stud dimension, the material properties of headed stud and SFRCC, the dimension of the steel beam, the distance from the center of the most rear stud (Stud_D in Figure 4.16) to the free edge of the slab, the distance from the center of the most front stud (Stud_A in Figure 4.16) near the fixed end of the slab, and the thickness of the slab are set to be constant. The stud pitch length (Dp) ranged from 150 mm, the length close to the minimum specified spacing in the design code (132 mm) allowed for D22 stud embedded in concrete slab, to 50 mm, the minimum spacing allowed for stud installation. The number of stud varies as two, three, and four. Among the multiple studs, the most front stud (close to the fixed end) was named as 'Stud_A', other studs were accordingly named following the alphabetical order. Sketches of stud arrangement in the models are indicated in Table 4.4.

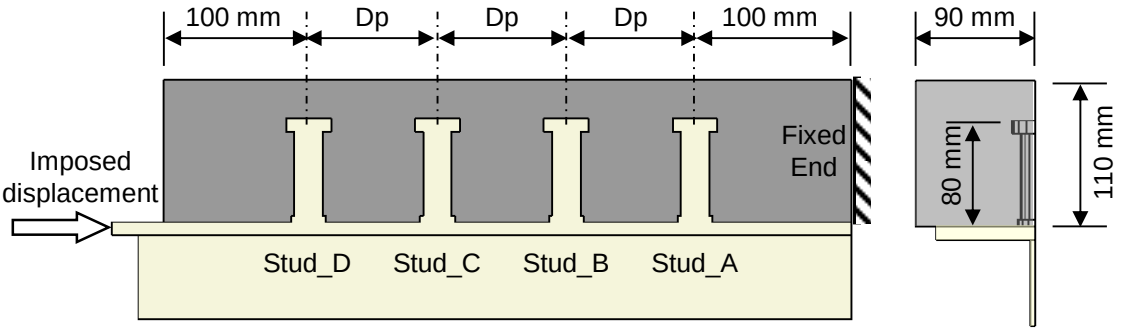

Figure 4.16 Analysis model

Table 4.4 Sketch of analysis models

Sketch of model	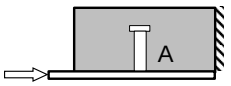 *n*=1	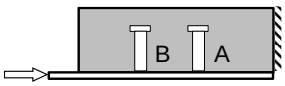 *n*=2
	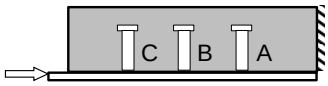 *n*=3	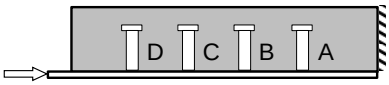 *n*=4

The list of analysis cases is shown in Table 4.5 along with the common constant parameters for the analysis and the material properties adopted for these analyses. Twelve analysis cases were modeled including a baseline specimen with single stud named 'Dp0_n1'. It is noted that the case for four studs with a pitch length of 50 mm is not included, because it is found in the previous analysis that its failure mode was slab failure.

Table 4.5 List of analysis cases

Nomenclature of analysis model: **Dp**(stud pitch length)**_n**(stud number)			
Dp0-n1	Dp75-n2	Dp100-n2	Dp150-n2
Dp50-n2	Dp75-n3	Dp100-n3	Dp150-n3
Dp50-n3	Dp75-n4	Dp100-n4	Dp150-n4

Constant parameter

Slab dimension: Thickness × Width = 110 mm × 180 mm; Stud-slab free edge distance and stud-slab fixed end distance: 100 mm; Stud: D22/80; Steel bean: flange thickness 10 mm, web thickness 7 mm.

Material properties for analysis		
SFRCC (MPa)	f_c	120
	f_t	15
	E_c	45000
Stud (MPa)	f_{yst}	390
	f_{ust}	474
	E_s	205000
Steel beam (MPa)	E_s	205000

Analysis results

The bearing force of each stud in the multi-stud models are shown in Figure 4.17. The horizontal axis is the slab-beam flange slip caused by the imposed displacement at the steel beam. The vertical axis is the bearing force that each stud sustaining during the loading in the analysis. For general comparison, the bearing force of ecah stud is defined as the bearing force at the instance when the Stud_A reaches its maximum strength, at which the multi-studs shear connection are considered to be reaching its ultimate bearing force. From Figure 4.17, the following observations are notable: (1) the most front stud (Stud_A) always develops larger bearing force than other rear studs; (2) The sustained shear force of the Stud_A decreases as the stud number increases and the stud spacing decreases; (3) the rear studs sustain substaintial smaller shear force than the most front stud, but the sustained shear force of the rear sutds are similar for each other, even when the stud number is changed.

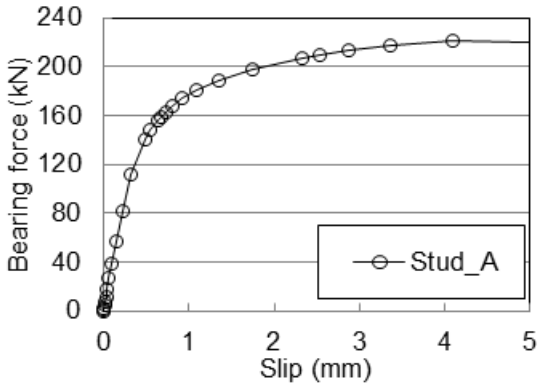

(a)

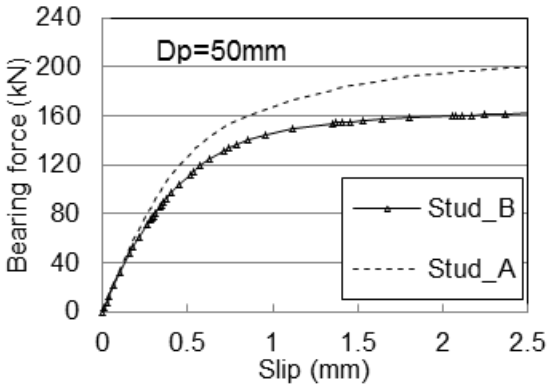

(b)

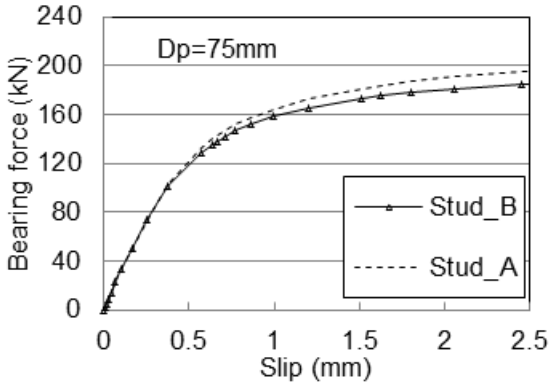

(c)

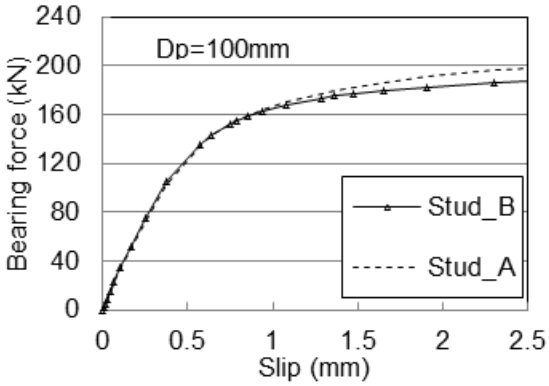

(d)

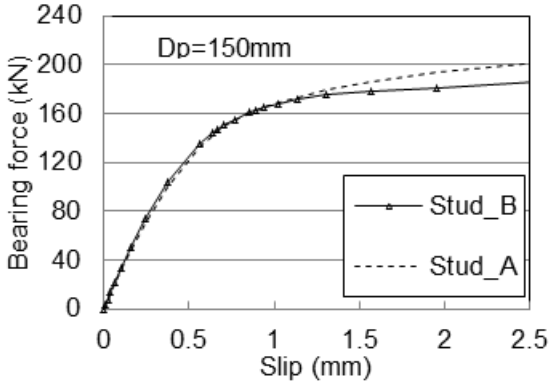
Dp=150mm
Bearing force (kN)
Slip (mm)
Stud_B
Stud_A

(e)

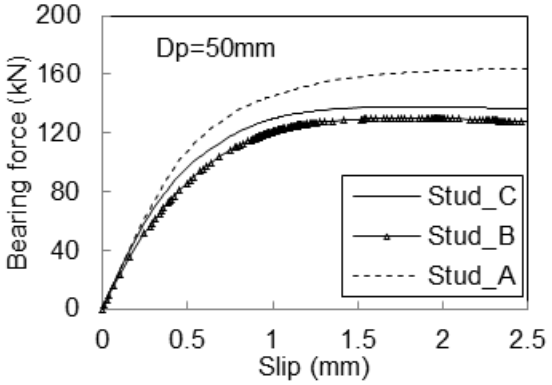
Dp=50mm
Bearing force (kN)
Slip (mm)
Stud_C
Stud_B
Stud_A

(f)

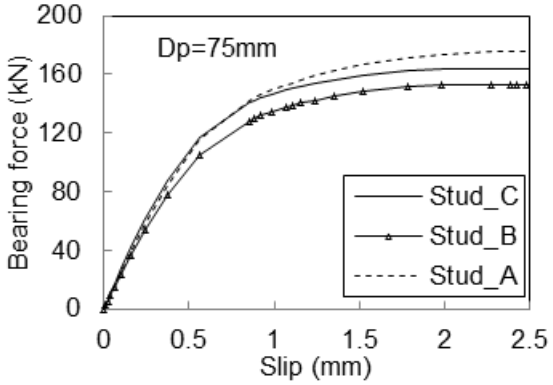
Dp=75mm
Bearing force (kN)
Slip (mm)
Stud_C
Stud_B
Stud_A

(g)

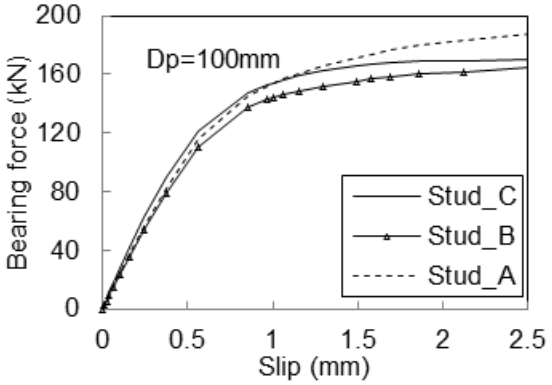
Dp=100mm
Bearing force (kN)
Slip (mm)
Stud_C
Stud_B
Stud_A

(h)

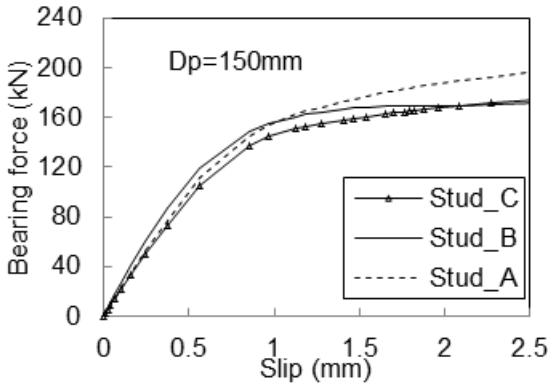
Dp=150mm
Bearing force (kN)
Slip (mm)
Stud_C
Stud_B
Stud_A

(i)

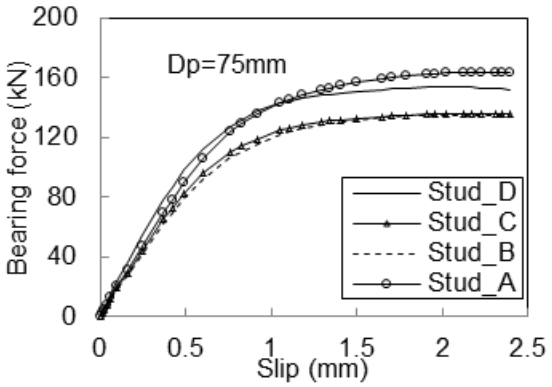
Dp=75mm
Bearing force (kN)
Slip (mm)
Stud_D
Stud_C
Stud_B
Stud_A

(j)

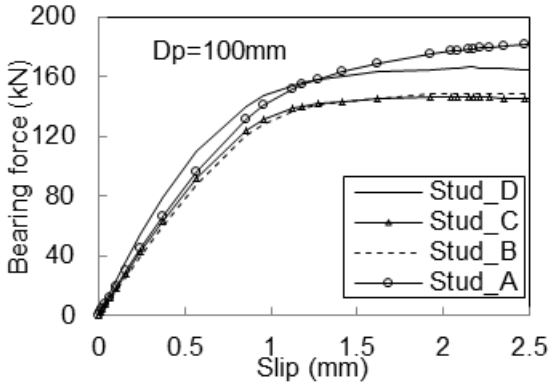
Dp=100mm
Bearing force (kN)
Slip (mm)
Stud_D
Stud_C
Stud_B
Stud_A

(k)

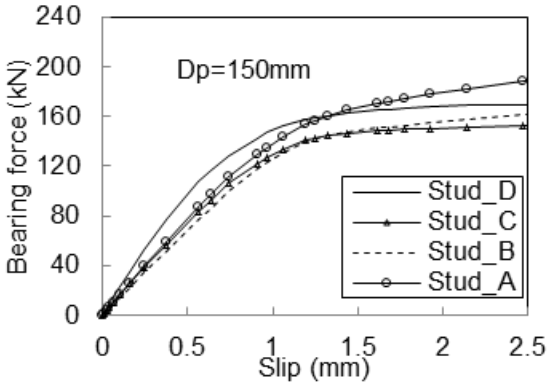
Dp=150mm
Bearing force (kN)
Slip (mm)
Stud_D
Stud_C
Stud_B
Stud_A

(l)

Figure 4.17 Comparison on shear force sustained by each stud:
(a) Dp0-n1; (b) Dp50-n2; (c) Dp75-n2; (d) Dp100-n2; (d) Dp150-n2; (e) Dp50-n3; (f) Dp75-n3; (g) Dp100-n3; (h) Dp150-n3; (i) Dp50-n4; (j) Dp75-n4; (k) Dp100-n4; (l) Dp150-n4

The analysis results shown in Figure 4.17 indicates that the per stud strength of stud-SFRCC shear connection is affected by both the stud spacing and the stud number. To quantified the strength reduction for stud-SFRCC connection with multiple studs, the precedures to deduce the strength reduction are based on the following strategies: (1) The most front stud sustains the largest shear force and the ratio of the sustained shear force to the single stud strength is affected by stud number and stud spacing; (2) the sustained shear force of rear stud is summaried by comparing to the sustained shear force of the most front stud rather than by comparing to the single stud strength, so the variable of stud number on strength reduction of rear stud may be decoupled.

The reduction ratio of Stud_A of each analysis case, which is defined as the ratio of sustained shear force of Stud_A to shear force of single stud model (Dp0-n1), is summaried in Figure 4.18. In Figure 4.18, the X-axis and the Y-axis are variable of the stud number and D_p/d ratio respectively, while the Z-axis is the reduction ratio of Stud_A. Tendencies of the reduction ratio of Stud_A can be figured out from Figure 4.18, they are: the reduction ratio of Stud_A decreases as the the stud number increase and the the reduction ratio of Stud_A increases as the D_p/d ratio decreases. The reduction ratio of Stud_A was calculated by binary linear regression as shown in Figure 4.9 and the expression of the reduction ratio of Stud_A is given by the folowing equation:

$$\alpha_A = 0.9 - 0.067n + 0.027C_p \tag{4.8}$$

Where, n is the stud number, $n \geq 2$; C_p is the ratio of stud spacing D_p and stud diameter d, $C_p > 2.3$.

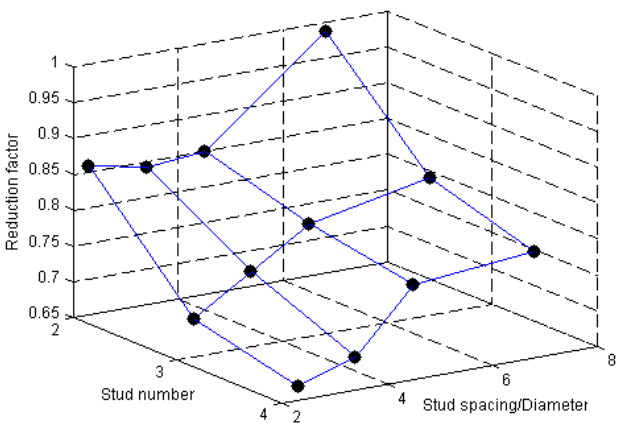

Figure 4.18 Reduction ratio of Stud_A

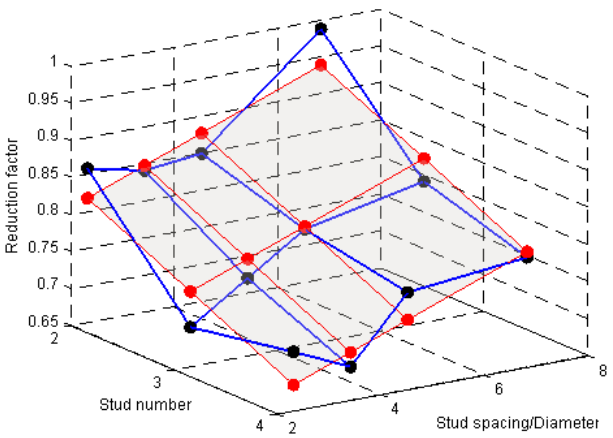

Figure 4.19 Regression on reduction ratio

The normalized bearing force of each studs in each analysis models are summaried in Figure 4.20, in which the vertical axis is the normalized per stud strength, which is calculated by dividing the

bearing force of each stud to that of Stud_A. Analysis cases having the same stud pitch length (D_p) are plotted in the same chart. It can be seen from Figure 4.20 that, 'stud A' bears biggest force than the rest of studs because it locates most close to the fix end thus under largest confining, while the other studs sustained nearly same bearing force as indicated by the plotted fitting lines. The fitting lines for different analysis series classified by 'D_p' are summarized in Figure 4.20(d). It can be seen that, bear force ratio of rear stud to most front stud decreases when the stud pitch length decreases. When normalized by the shear force of Stud_A, α_B shows independency to the parameter of stud number n, and only depend on the stud spacing.

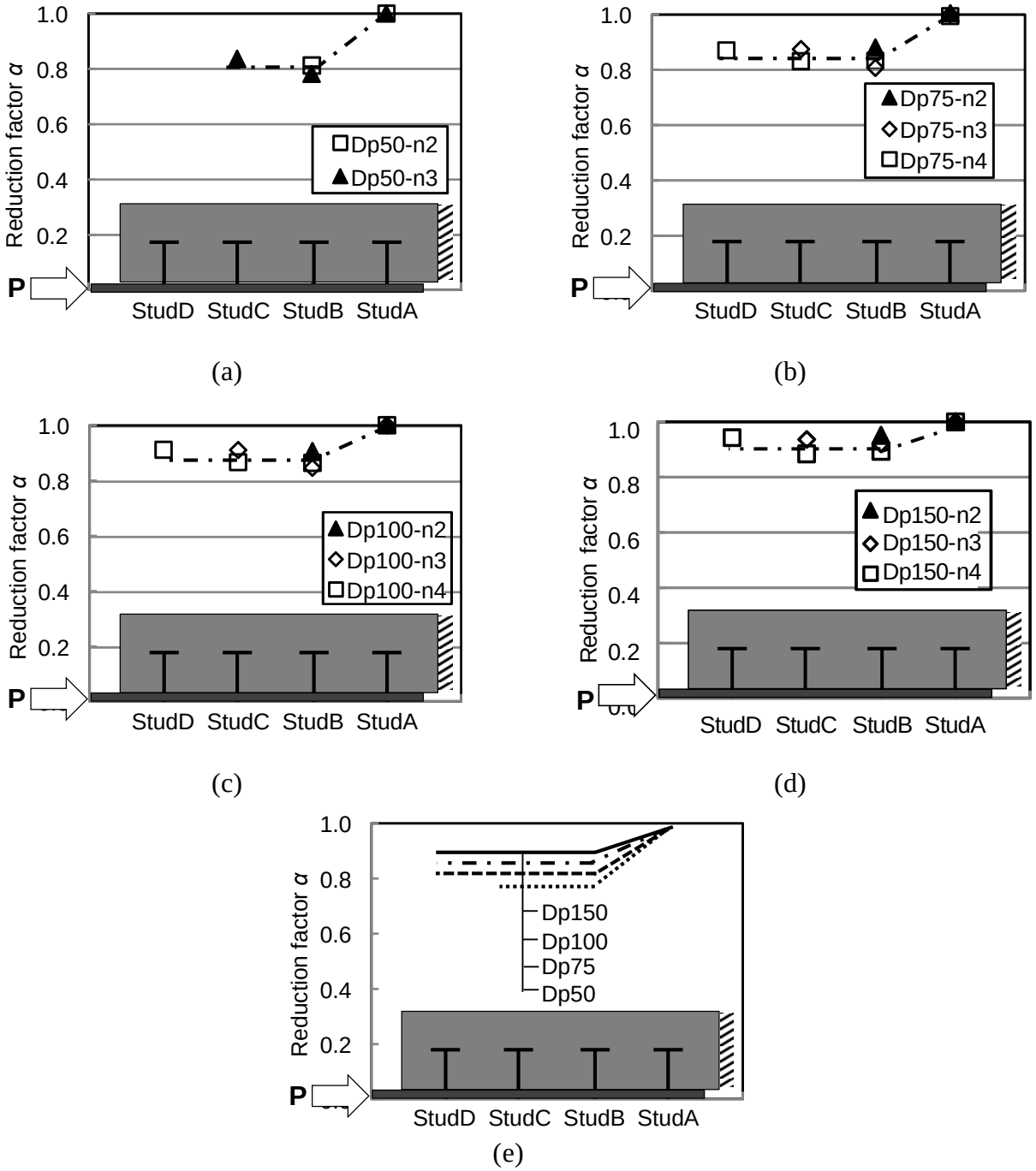

Figure 4.20 Analysis results of α_B: (a) pitch length 50 mm; (b) pitch length 75 mm; (c) pitch length 100 mm; (d) pitch length 150 mm; (e) Summary of the fitting lines

Calculated by linear fitting, α_B which is the reduction ratio of strength of rear stud to that of most front stud, is given by the following equation.

$$\alpha_B = 0.02C_p + 0.74 \tag{4.9}$$

For the case when the stud number is *n*, because the strength of most front stud is assumed to be $\alpha_A P_u$, and strength of the other (*n*-1) studs are assumed to be $\alpha_A \alpha_B P_u$, thus the reduction factor for per stud strength α_n is given by.

$$\alpha_n = \frac{\alpha_A + \alpha_A \alpha_B (n-1)}{n} \tag{4.10}$$

Therefore, the per stud strength of stud-SFRCC connection with multiple studs, $P_{u,n}$, is obtained as the product of the single stud strength P_u and the strength reduction factor α_n, and given by.

$$P_{u,n} = P_u \alpha_n = (A_{sc} f_{su} + 2.5 f_{cu} d_{\mathrm{wc}} l_{\mathrm{wc}}) \frac{\alpha_A + \alpha_A \alpha_B (n-1)}{n} \tag{4.11}$$

The predicted strength calculated by Eq. (4.11) is compared to the results from the FEM analysis and tests as shown in Figure 4.21, and the results show a good agreement.

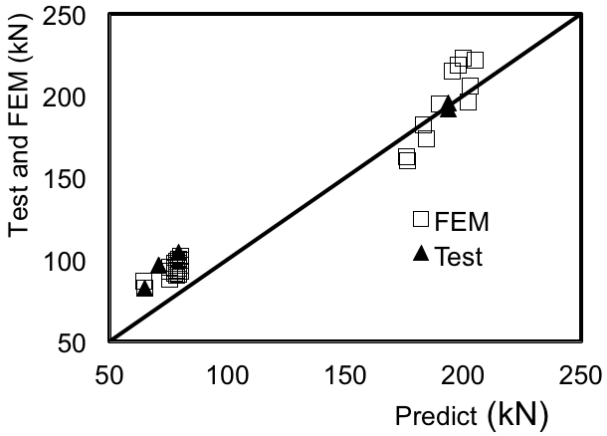

Figure 4.21 Verification on predicted per stud strength for stud-SFRCC connection

4.5 Slab bearing capacity of headed stud-SFRCC shear connection

The equations proposed in Section 4.4 are naturally valid when the failure mode of the stud-SFRCC shear connection is stud fracture. Therefore, for the group arrangement of stud connectors, it is necessary to conduct strength checking for SFRCC slab to prevent the slab failure. If the slab failure is prior to the stud failure, the slab should be strengthened by reinforcement. According to the

research conducted by Oehlers (Oehlers 1989) developed a method to determine the characteristic splitting resistance of concrete slab, in which local concentrations of load applied by individual studs, line of studs, and groups of studs were examined. The evaluation method proposed in the past is introduced in this section, and some adjustment was made to the equation to make it suitable for the strength evaluation for stud-SFRCC shear connection.

4.5.1 Strength estimation based on the longitudinal splitting failure model

Split strength for slab with single stud

Oehlers (Johnson and Oehlers 1981) carried out a series of analytical investigation on the splitting strength of concrete slab subjected to a concentrated force. In their research, the longitudinal split crack caused by stud shear was analogous to local compression in a concrete block subjected to a strip load. A model of split crack caused by shear stud is illustrated in Figure 4.22. Figure 4.22(a) shows the prototype condition that a stud with a diameter of b_a is placed in the slab with a lateral free edge distance of $b_c/2$. The lateral tensile stress induced by a concentric shear force P applying on the stud causes a longitudinal split crack along the shear direction. To simplify the problem, an effective region with a lateral width of two times the free edge distance and the longitudinal height of two times the lateral width is assumed as shown in Figure 4.22(b). Here, all mentioned were considered linear. The problem is represented by local compression caused by strip local bearing on a prism as shown in Figure 4.22(c). A uniform strip patch load with width of b_a and height of h_a compresses on a prism, and the induced lateral tensile stress would cause a split crack at the critical face beneath the center of the strip patch. The split strength P is defined as the shear force when the lateral tensile stress would reach the tensile strength of the prism material.

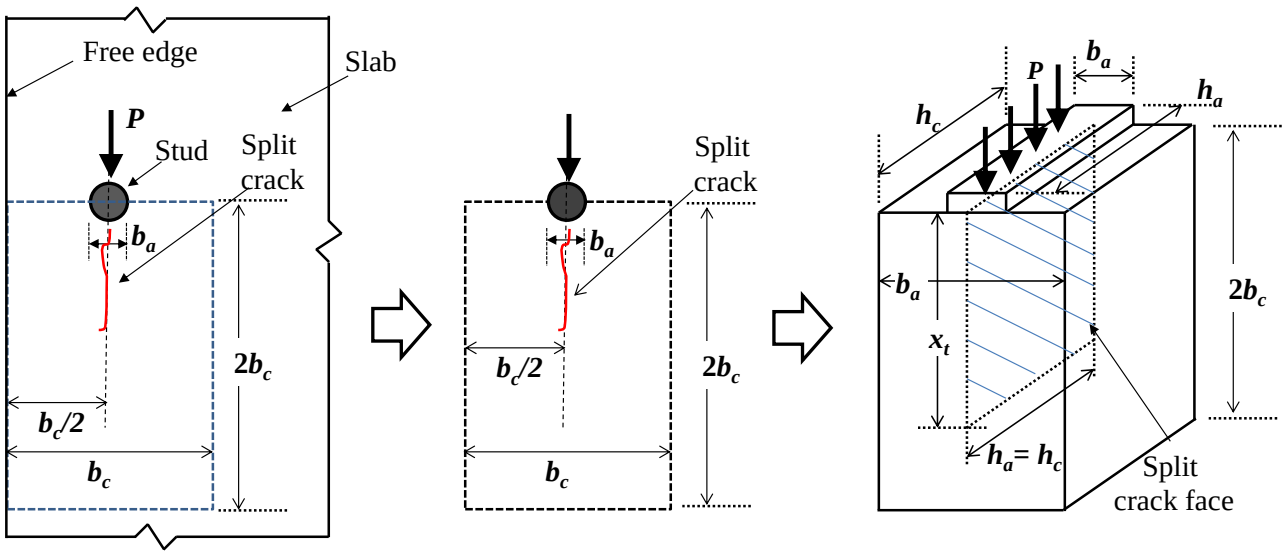

(a) (b) (c)

Figure 4.22 Modeling of split crack in slab caused by single shear stud: (a) prototype split crack problem; (b) effective region for split crack problem; (c) strip load local compression problem

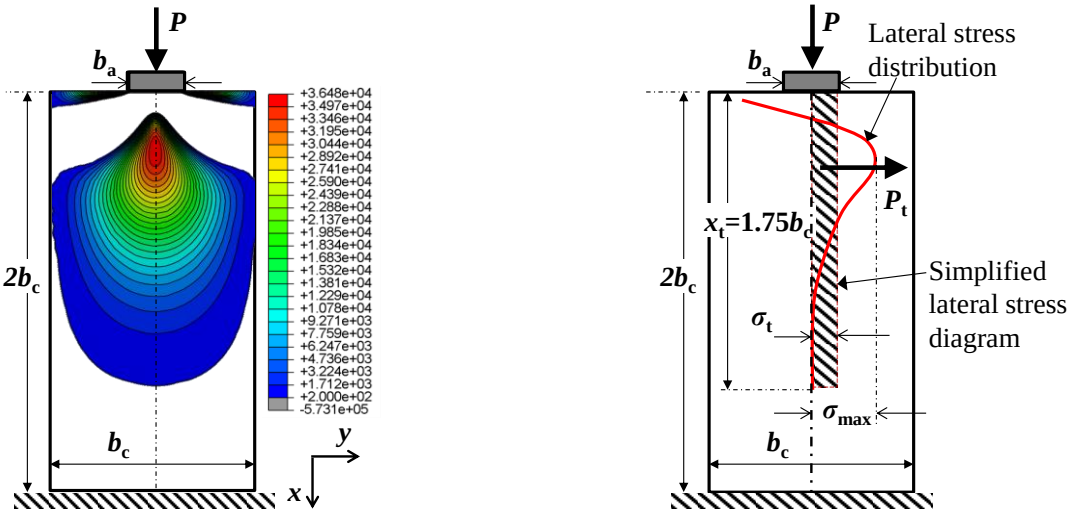

Figure 4.23 Lateral stress zones distribution

The characteristics of the induced lateral tensile stress are the key issue for this problem. Figure 4.23(a) plots the lateral tensile stress contour of the prism obtained from elastic FEM analysis. Based on the stress contour, the lateral tensile stress along the centerline of the prism (where the critical face locates) is as shown in Figure 4.23(b). The lateral tensile stress shows a nonlinear distribution with an effective influence range (x_t) about 1.75b_c. P_t is defined as the resultant tensile force of the lateral tensile stress. The induced lateral tensile force P_t and the imposed local compression force P have the relationship as follows:

$$P_t = k_d P \tag{4.12}$$

Where, k_d is a transformation factor, which depends on the width of strip patch load (b_a) and effective width of the slab (b_c), it is determined according to the following formula.

$$k_d = \frac{1}{\pi}\left(1 - \frac{b_a}{b_c}\right)^2 \tag{4.13}$$

To derive a single relationship between the induced resultant tensile force P_t and peak tensile stress σ_{max}, the nonlinear tensile stress distribution is simplified to be a rectangular stress diagram as shown in Figure 4.23(b). The simplified rectangular stress diagram has the same effective influence range $x_t = 1.75b_c$ as the nonlinear tensile stress distribution, and the average tensile stress $\sigma_t = 0.34\sigma_{max}$ is determined by elastic finite element analysis (Leonhardt 1964). Therefore, the induced resultant tensile force P_t is given as below,

$$P_t = x_t \sigma_t h_a = (1.75b_c)(0.34\sigma_{\max})h_a = 0.6 b_c h_a \sigma_{\max} \tag{4.14}$$

Substitute P_t and k_d in Equation (4.12) by Equation (4.13) and Equation (4.14), the imposed force

P is given by,

$$P = \frac{0.6\pi b_c h_a \sigma_{\max}}{\left(1 - \frac{b_a}{b_c}\right)^2} \tag{4.15}$$

When $\sigma_{\max}$ equals to the tensile strength f_t of the prism material, P_{split} is taken as it reach the split strength of the prism as presented in Figure 4.22(c).

$$P_{split} = \frac{0.6\pi b_c h_a f_t}{\left(1 - \frac{b_a}{b_c}\right)^2} \tag{4.16}$$

From two-dimension splitting to three dimensional splitting

The two-dimensional analysis introduced above underestimate the resistance to splitting, as it assumed that the concentrated load is only dispersed in two dimensions. Hence the connector in Figure 4.22(c) is assumed to be acting on Prism 1 of cross-sectional area $h_a b_c$, so that the concentrated load is only dispersed in the x-y plane. In reality, the dispersal of the concentrated load has vertical component as well, that distributes the concentrated load to the remaining volume of the slab. This vertical component will relieve the lateral stresses in the x-y plane and hence increase the concentrated load to cause splitting. A theoretical solution to this three-dimensional problem is difficult to find, so recourse is made to adapting two dimensional solutions for use in this three-dimensional problem.

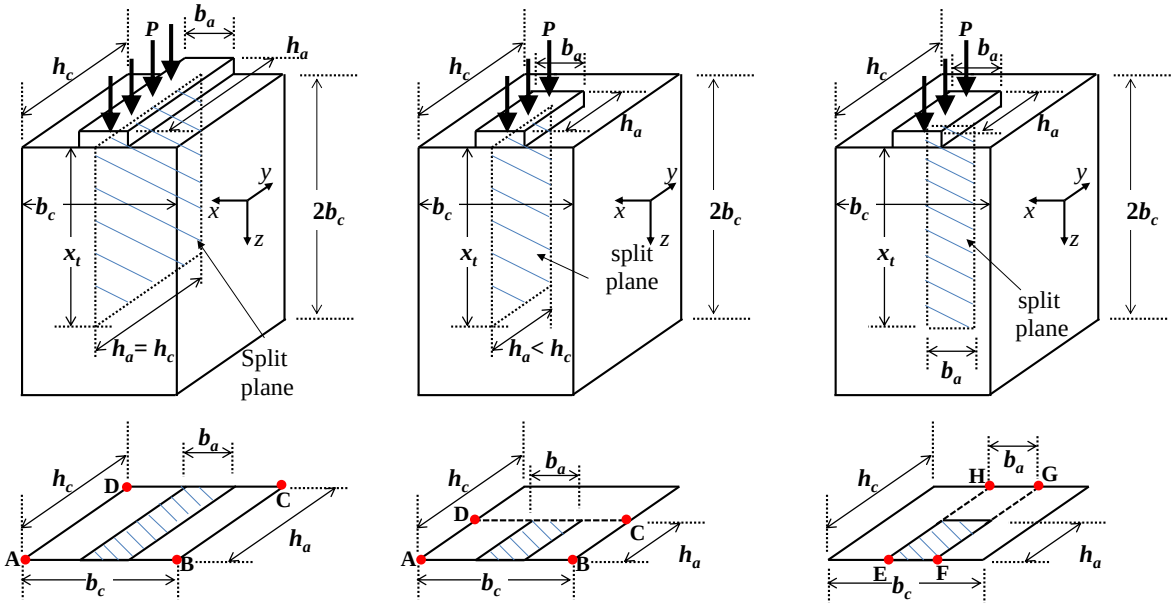

Figure 4.24 From two-dimensional split to three-dimensional split

Firstly, consider a concentric patch load acting on a prism as shown in Figure 4.22 (c), since this is the simplest form of three-dimensional splitting. Experimental research has shown that the splitting resistance of this concentric patch load prism, in which the load is dispersed in three dimensions, can be predicated from the splitting resistance of the prism to strip loads in which only two-dimensional dispersal of the load occurs.

Let P_x be the strip load to cause the prism in Figure 4.24(c) to split when subjected to a strip load over area A-B-C-D. The strength P_x can be derived from Eq.(4.15), where b_a is the width of the strip measured in the x-direction, b_c is the width of the prism measured in the x-direction, and h_a is the height of both the strip load and the prism measured in the y-direction which is this case is equal to h_c. Similarly, let P_y be the strip load to cause the prism to split when subjected to a strip load over the area E-F-G-H. The strength P_y can also be determined from Eq.(4.15). In this case b_a and b_c in Eq.(4.15) are the width of the strip load and prism measured in the y-direction, which is this case is equal to ha and h_a and h_c, and h_a in Eq.(4.15) is the height of both the strip load and the prism measured in the x-direction that is h_c.

One way to allow for three-dimensional dispersal is to follow the technique that is often used in the anchorage zone design of post-tensioned members (Leonhardt 1964). The anchorage zone or patch load area $b_a h_a$ in Figure 4.24 is assumed to be supported by both prism A-B-C-D and E-F-G-H, so that the resistance to the patch is the sum of the resistances of each of these prisms. Oehlers suggested that (Oehlers 1989) the similar approach can be applied to the splitting resistances of the patch on A-B-C-D and E-F-G-H, both of which can be determined from Eq.(4.15). It is important to note that it is assumed that the splitting resistance of both prisms can be achieved simultaneously before failure. Hence, the three-dimensional splitting resistance P_{split} is given by

$$P_{\text{split}} = P_x + P_y = \frac{0.6\pi b_c h_a f_t}{(1-\frac{b_a}{b_c})^2} + \frac{0.6\pi b_a h_c f_t}{(1-\frac{h_a}{h_c})^2} \tag{4.17}$$

The first term and the second term on the right hand side of Eq. (4.17) is the splitting strength of Prism A-B-C-D and Prism E-F-G-H in Figure 4.24, respectively. To simplified the form of Eq. (4.17), dividing Eq. (4.17) by the first term gives the proportional increase in strength due to vertical dispersal Q as

$$Q=1+V \tag{4.18}$$

Where V is the percentage increase of the two-dimensional strength due to the vertical dispersal of the load, and is given by

$$V = K_d \rho \frac{b_a}{b_c} K_s \tag{4.19}$$

Where K_s is given by

$$K_s = \left(\left(1 - \frac{h_a}{h_c} \right)^2 \frac{h_a}{h_c} \right)^{-1} \tag{4.20}$$

The simplest method of allowing for the beneficial effects of vertical dispersal is to use an effective height of the shear connector *h*, instead of the actual height ha in all the two-dimensional splitting equations (From Eq. (4.14) to Eq. (4.17)), where

$$h_v = h_a Q \tag{4.21}$$

Equivalent height of connector

It should be noted that, in the patch local compression, the load is uniformly applied to the prism. This assumption is only valid when the shear stud is completely rigid, while the actual shear stud is of flexibility, by which the bearing force concentrates mostly at the lower part of the stud. To make the evaluation approach applicable for shear stud in slab, further adjustment is needed. The effective height of the shear stud connector h_e was adopted to substitute h_a is Eq. (4.22). The effective height h_e was determined based on the fact that the shear action between the shear connector to the concrete slab varies along the height direction of the shear stud. Past research and tests shows that the root of the shear connector bears almost all the shear transferred by the whole connector. It is the reason why the crack always initiates at the concrete near the stud connector root and propagates up from the slab bottom to the top surface along the slab thickness direction. Only the splitting resistance contribution of a certain thickness of slab was considered, and was named the effective concrete slab thickness. According to Johnson (Johnson and Oehlers 1981), the effective slab thickness is dependent to diameter of the stud shear connector and can be approximated as 1.8*d*, where *d* is the diameter of the stud shear connector.

$$h_e = 1.8d \tag{4.22}$$

Split strength for slab with studs arranged closely in a line

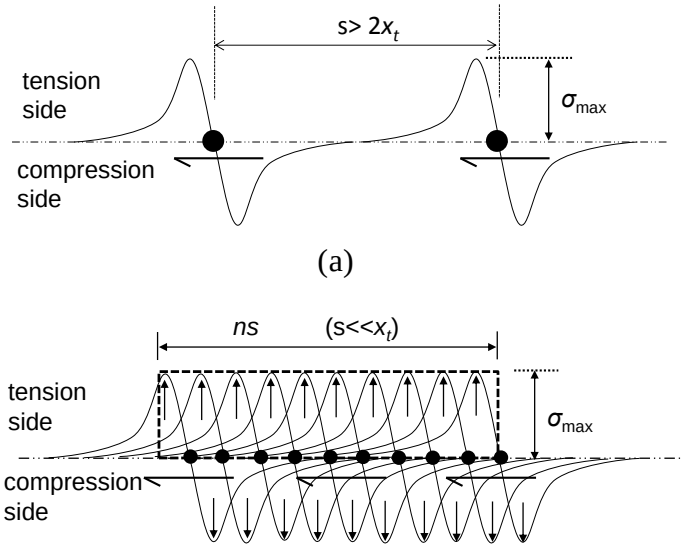

Figure 4.25 Lateral tensile stress overlap for a line of closely placed stud connector: (a) Studs

arranged in large spacing; (b) Studs arranged in small spacing

In the analyses of longitudinal splitting of concrete slab in composite beam, the stud shear connectors are usually arranged in a line. In this condition, interaction between adjacent stud connectors needs to be considered. Moreover, the effective length of the lateral tensile stress caused by the imposed load P to the shear connectors is x_t=1.75b_c (b_c are the effective width of slab), when spacing between adjacent studs s is larger than two times of x_t, there is no overlap of lateral stress as indicated in Figure 4.25(a). Since in the steel-concrete composite beam in practical applications, spacing between adjacent studs s is usually much smaller than x_t, lateral tensile stress induced by each stud overlaps along the line of multiple shear stud connectors as indicated in Figure 4.25(b). Considering such overlap of lateral stresses, and for the case of stud connectors placed closely in a line, the lateral tensile stress on concrete slab between the adjacent stud connectors is simplified to be uniformly distributed as depicted in Figure 4.25(b). In the past research (Oehlers 1995), it is suggested that mean distributed lateral tensile stress σ_t of the simplified stress diagram is equal to σ_t, and the average resultant tensile force between the two shear connectors is assumed as $P_t = \sigma_t h_e s$, where P_t is equal to the resultant tensile force induced by the single stud as defined in Eq. (4.12). The relationship described in Eq. (4.12) is still valid, thus the split force P between two adjacent studs is given as

$$P = \frac{P_t}{k_d} = \frac{\sigma_t h_v s}{k_d} \tag{4.23}$$

When the number of the studs arranged in a line is n (n>2), the total shear force of the stud line P_n is given by the formula below

$$P_n = n\frac{\pi h_v s}{\left(1-\frac{b_a}{b_c}\right)^2}\sigma_t \tag{4.24}$$

When σ_t reaches the tensile strength f_t of the slab material, the per stud reaches the split strength of the slab with a line of shear stud.

$$q_u = \frac{\pi h_v s}{\left(1-\frac{b_a}{b_c}\right)^2} f_t \tag{4.25}$$

4.6 Example of strength checking for stud-SFRCC shear connection

Summarizing the studies in Section 4.4 and 4.5, the strength evaluation procedures are generalized as

below:

The per stud strength for stud shear failure is estimated by

$$P_{u,1} = (A_{sc} f_{su} + \eta f_{cu} d_{\mathrm{wc}} l_{\mathrm{wc}}) \frac{\alpha_A + \alpha_A \alpha_B (n-1)}{n} \tag{4.26}$$

The per stud strength for slab split failure is estimated by

$$P_{u,2} = \frac{\pi h_v s}{\left(1 - \frac{b_a}{b_c}\right)^2} f_t \tag{4.27}$$

The per stud strength of the group stud-SFRCC shear connection is determined as the smaller of the $P_{u,1}$ and $P_{u,2}$ and expected failure mode is correspondingly determined.

An example is given below to illustrate the effects of various design parameters on the per stud strength determined by two types of failure modes.

Given a stud-SFRCC shear connection having a line of studs placed in solid flat SFRCC slab, the strength checking based on the prescribed two failure modes will be illustrated using this example. Basic data from the tested specimen P4G1-6% is listed in Figure 4.26.

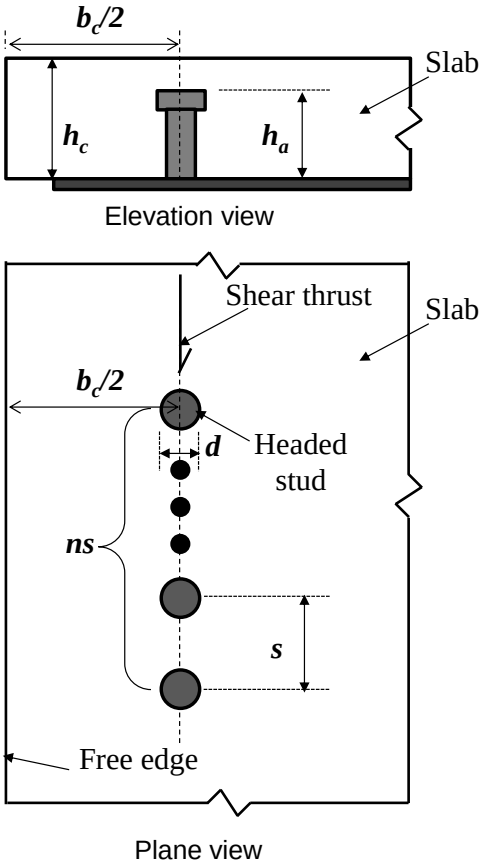

Basic data:
<stud>
n=4,
s=50 mm,
d= 22 mm,
f_{su} = 472 MPa,

<slab>
f_t = 15 MPa,
f_c = 120 MPa,
b_c= 170 mm,
h_a=80 mm
h_c=130 mm
……

Parameters:
f_t
s
n
……

Figure 4.26 Prototype of design example

The variable parameters considered in this example are the tensile strength of SFRCC, stud spacing and the number of studs. When one of the design parameters is considered as the variable, the other parameters are kept constant following the basic data. The per stud strength is calculated according to Eq. (4.26) and (4.27), respectively. The results from two formulas indicting two different failure modes are compared in Figure 4.27.

Figure 4.27 shows the effects of design parameters, such as SFRCC tensile strength, stud spacing, and number of studs, on the estimated per stud strength. It can be seen that the per stud strength for slab failure increases linearly with the increasing tensile strength of SFRCC and stud spacing. This indicates that using SFRCC with larger tensile strength (higher fiber volume ratio) and enlarging stud spacing are most effective to improve the slab failure strength. In other words, when a fiber volume ratio is enough to ensure the stud failure, adding fiber do not help to improve the maximum shear strength of the connection. It is consistence with the test results of the push-out test on effect of fiber volume ratio. From calculation results shown in Figure 4.27(c), since the slab strength is independent of stud number, increasing number of stud do not intense the tendency for slab failure but only causes the strength reduction for stud failure. The strength for stud failure reduces as the stud number increase and gradually convergent to a certain value.

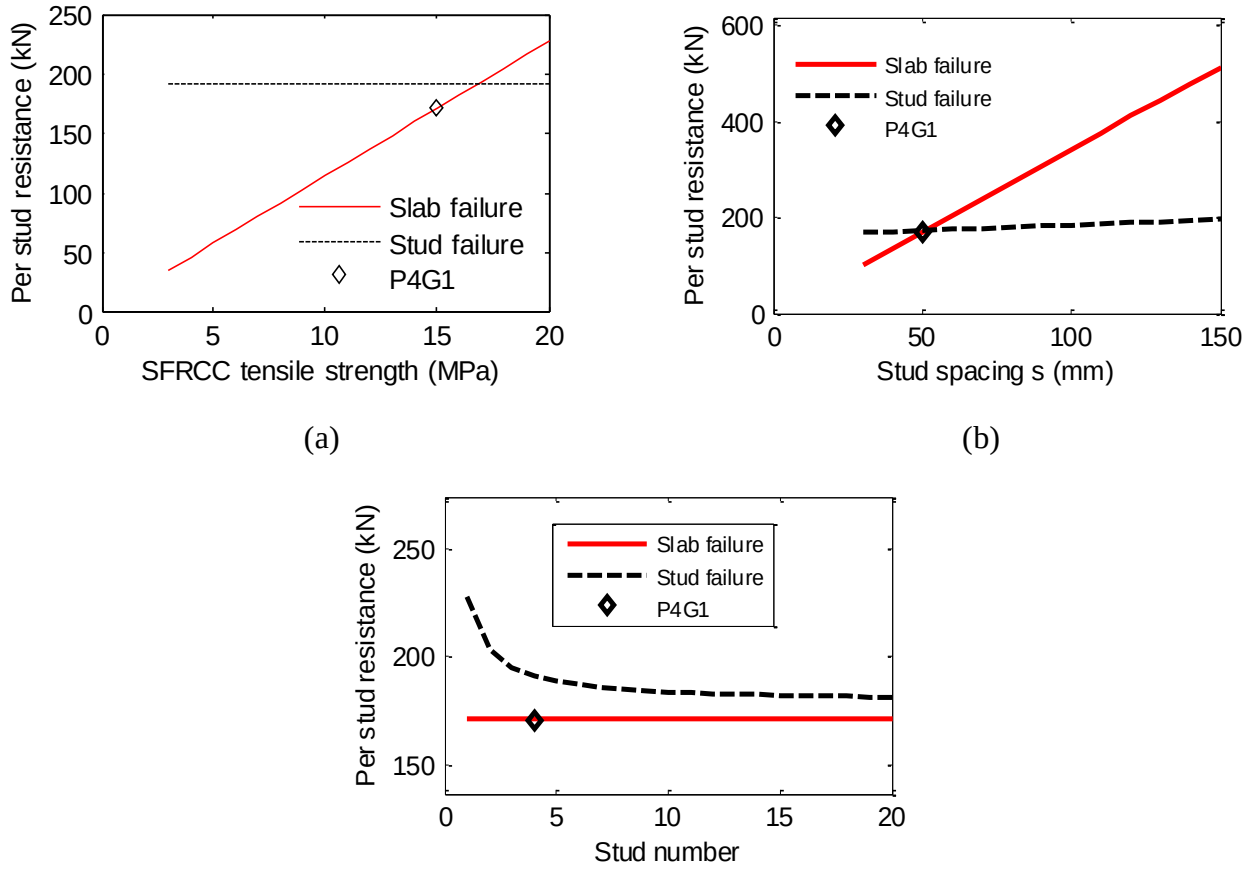

Figure 4.27 Effects of parameters on per stud strength: (a) SFRCC tensile strength; (b) stud spacing; (c) number of studs.

4.7 Summary and conclusions

In this Chapter, comprehensive investigations on strength of stud-SFRCC shear connection were conducted. The nonlinear three-dimensional finite element model was developed to reproduce the experimental behavior of stud-SFRCC connection specimens presented in the chapter 3.

(1) By adopting the contact interaction between the headed stud and surrounding slab, the FEM models are found to be able to trace the experimental behavior of the push-out test specimens well, in terms of strength and failure modes.

(2) The numerical analysis indicated that the presence of welded collar has substantial contribution to shear strength of the headed stud when it is embedded in SFRCC. The contribution of welded collar was found relating to the dimension of welded collar and compression strength of SFRCC. Parametric study was conducted to generalize the relationship between strength contribution of welded collar and the influencing factors. An empirical equation to evaluate the welded collar contribution was adopted and updated by modifying an empirical factor based on the parametric analysis results to make to suitable for headed stud embedded in SFRCC.

(3) The strength reduction mechanism due to small spacing between studs was studied. Using the FEM models, investigation into the shear force of each stud in the group arranged studs revealed that, the interaction between closely arranged studs weakens the confining effect on studs thus studs sustained less shear force comparing to those with large stud spacing. In additions, studs placed in different position sustain different shear force. Such difference becomes more significant when the stud spacing becomes smaller.

(4) Formulas to evaluate the reduction for per stud strength of a group arranged studs is derived by generalizing the parametric numerical analysis results. The stud spacing in loading direction and the number of studs are considered as the two primary parameters affecting the per stud strength reduction.

(5) The resistance for slab failure of the stud-SFRCC connection needs to be checked to avoid the slab failure. The evaluation method for strength of slab proposed in the past was introduced and the derivation process was illustrated.

REFERENCES

AASHTO, L. (1998). *Bridge Design Specifications*. American Association of State Highway and Transportation Officials, Washington, DC.

AISC, L. (1999). “Resistance Factor Design Specification for Structural Steel Buildings, American Institute of Steel Construction.” *Inc., Chicago (IL)*.

An, L., and Cederwall, K. (1996). “Push-Out Tests on Studs in High Strength and Normal Strength Concrete.” *Journal of Constructional Steel Research*, 36(1), 15–29.

Anderson, N. S., and Meinheit, D. F. (2005). “Pryout Capacity of Cast-In Headed Stud Anchors.” *PCI journal*, 50(2), 90–112.

Architectural Institute of Japan. (2001). *Recommendations for Design of Connections in Steel Structures*. Tokyo.

Doinghaus, P. (2001). *Zum Zusammenwirken hochfester Baustoffe in Verbundtragern*. Universitätsbibliothek.

Doinghaus, P., Goralski, C., and Will, N. (2003). "Design Rules for Composite Structures with High Performance Steel and High Performance Concrete." American Society of Civil Engineers, 139–149.

Eurocode 4, C. (2004). *Design of composite steel and concrete structures*. Part.

Hegger, J., Feldmann, M., Rauscher, S., and Hechler, O. (2006). "Load-Deformation Behavior of Shear Connectors in High Strength Concrete subjected to Static and Fatigue Loading." *IABSE Symposium Report*, 17–24.

Hegger, J., Sedlacek, G., Döinghaus, P., Trumpf, H., and Eligehausen, R. (2001). "Studies on the Ductility of Shear Connectors When Using High-Strength Steel and High-Strength Concrete." *International Symposium on Connections between Steel and Concrete*, 1025–1045.

Johnson, R. P., and Oehlers, D. J. (1981). "Analysis and Design for Longitudinal Shear in Composite T-Beams."

Kaneko, Y., Mihashi, H., Kirikoshi, K., and Abe, T. (2000). "Simplified uniaxial constitutive model of steel fiber reinforced cementitious composite." *AIJ Journal of Technology and Design*, 11, 5–8.

Leonhardt, F. (1964). *Prestressed concrete;: Design and construction*. W. Ernst.

Nielsen, C. V. (1995). "Ultra High-Strength Steel Fibre Reinforced Concrete, Part I, Basic Strength Properties of Compresit Matrix." *Technical University of Denmark. Series R*, 323.

Oehlers, D. J. (1989). "Splitting Induced by Shear Connectors in Composite Beams." *Journal of Structural Engineering*, 115(2), 341–362.

Oehlers, D. J. (1995). "Design and Assessment of Shear Connectors in Composite Bridge Beams." *Journal of Structural Engineering*, 121(2), 214–224.

Okubo, N., and Kurita, A. (2005). "Application of Grouped Studs to Continuous Composite Girder Bridges." *Proceedings of JSCE (Japan Society of Civil Engineers)*, 780(133-143).

PCI Industry Handbook Committee. (2004). *PCI Design Handbook: Precast and Prestressed Concrete*. Chicago, IL: PCI.

Systèmes, D. (2010). "Abaqus 6.10: Analysis User's Manual." *Providence, RI: Dassault Systèmes Simulia Corp*.

CHAPTER 5

Beam-Column Connection using SFRCC Slab as External Diaphragm

5.1 Introduction

5.1.1 Background

Steel moment frames are widely used in seismic regions. During the 1994 Northridge earthquake and the 1995 Hyogoken-Nanbu (Kobe) earthquake, a large number of steel building structures sustained severe damage including collapse (for example (Architectural Institute of Japan (AIJ) 1995), (Nakashima et al. 1998)) . A form of most serious damage was appearance of cracks and succeeding brittle fracture at welded beam-to-column connections (Youssef et al. 1995). Strength and ductility of the welded connections were seriously lessened accordingly.

In Japan, box columns welded with wide-flange beams are commonly used for building construction. As illustrated in Figure 5.1(a), through plate diaphragms are most commonly used to connect the column and beam. The through diaphragm connection requires four full penetration column welds at each column-story intersection in addition to the beam web and flange welds. Learning from the 1995 Kobe earthquake that welds would be the source of damage. Connections that can avoid welds at the most stressed portion had been sought. The exterior diaphragm connection is regarded as a reasonable option in Japan (Matsuo et al. 2006). With the exterior diaphragm, the beams are connected using high tension bolts to the continuous box column via a wider plate placed around the column (Figure 5.1(b)). As compared to the through diaphragm connection, the exterior diaphragm connection require a significantly smaller volume of weld.

In steel moment resisting frame buildings, steel beams are typically used together with concrete floor slabs. As a variation of exterior diaphragm, a floor slab may serve as an exterior diaphragm instead of adding an extra steel diaphragm plate. Figure 5.2 shows an example image of such a beam-to-column connection using the floor slab as an exterior diaphragm. A group of headed studs, which are commonly used to connect steel beam and concrete floor slab, are welded on the top flange of beam to transfer the beam flange load to the floor slab that functions as an exterior diaphragm (Figure 5.2(b)). In the example of Figure 5.2(b), the beam bottom flange is bolted to a seat angle using high-strength bolts, while a pair of posttensioned steel bars is used to connect the seat angles located at both sides of the column. To achieve such a connection, the key is to make the floor slab diaphragm

strong enough to transfer the required forces.

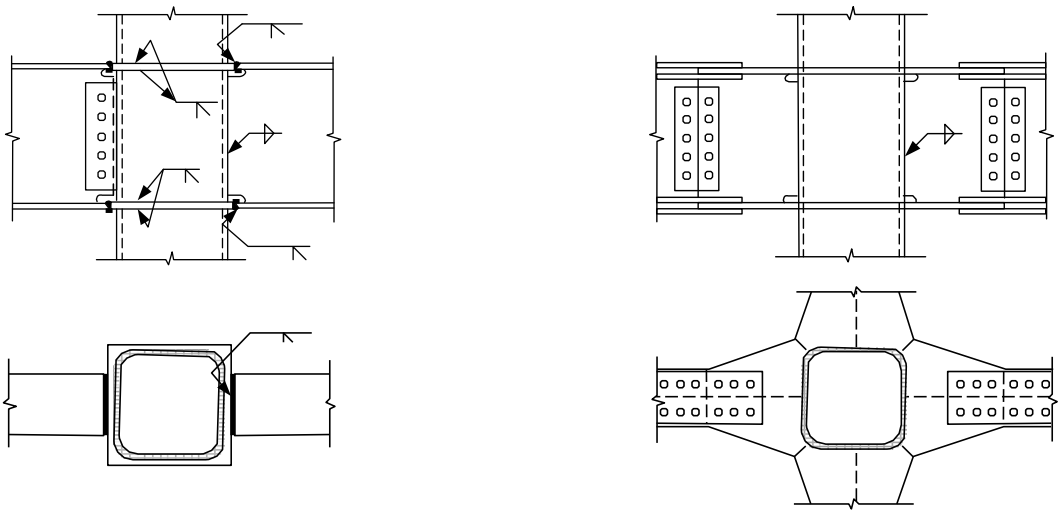

(a) (b)

Figure 5.1 Beam-to-column connections: (a) Through diaphragm, (b) Exterior diaphragm

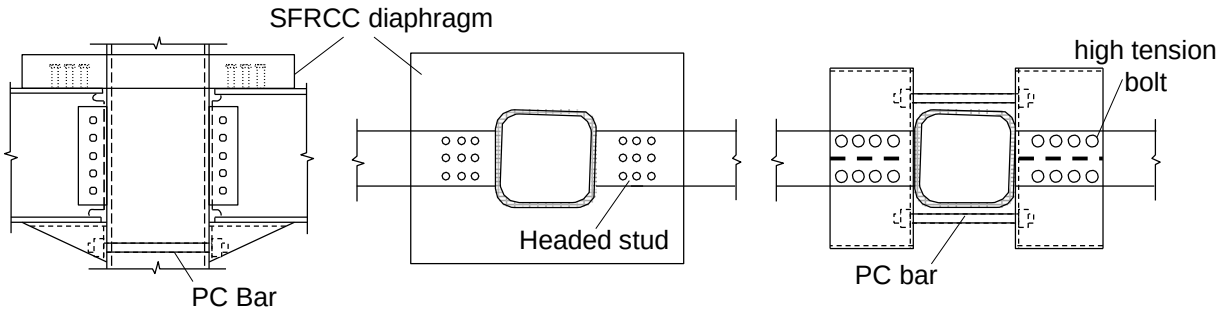

(a) (b) (c)

Figure 5.2 Proposed beam-to-column connection with floor slab functioning as exterior diaphragm: (a) Elevation, (b) Plan of top flange, (c) Plan of bottom flange

Recently, much development has been made for advanced materials. Steel fiber reinforced cementitious composites (SFRCC) is one of the advanced concrete for use in structures. It was developed based on CRC (compact reinforced composite) (Bache 1981), a kind of ultra-high performance fiber reinforced concrete (UHPFRC). SFRCC is made with a very low water/binder ratio W/B (0.2 or smaller) and a large amount of silica fume, and contains from 2 to 6% steel fibers. The strength properties of SFRCC are better than those of conventional concrete. For example, the tensile strength of SFRCC is approximately four times larger of that of conventional concrete (15MPa for SFRCC and 3MPa for conventional concrete). By using a large amount of steel fibers, ductility under tension is also larger than that of conventional concrete. This also leads to a possibility of dense arrangement of steel rebars.

Thus far, SFRCC has been applied primarily to precast elements, such as cantilevered balcony slabs and stair-cases (Aarup 2004). In Japan, applications of SFRCC to column bases (Cui and

Nakashima 2011; Kaneko et al. 2006) and beam-to-column connections (Kaneko et al. 2001, 2002) were also explored. The associated test results promised the possibility of making high-strength and compact structural components using SFRCC. In this study, SFRCC was adopted as the material to make the floor slab diaphragm.

5.1.2 Organization

In this Chapter, tests on the proposed beam-to-column connections with SFRCC floor slab diaphragms are presented. Two full-scale and three reduced-scale subassemblies were tested. Last, finite element analysis associated with the tests is presented, and a few issues regarding the design of the proposed connection are noted.

5.2 Test Program

5.2.1 Specimen design

Two series tests were conducted for the proposed beam-to-column connection using SFRCC slabs. First, a pilot test was conducted to verify the feasibility of the proposed connection. This was followed by a parametric test in which effects of the details of the proposed connection, such as the slab size, number of studs, and rebar arrangement, on the connection performance. The test specimens shown in Figure 5.3 were designed to simulate interior moment-resisting connections of a low-rise steel structure with a story height of 3 m and a span length of 6 m. As noted in Figure 5.2, the SFRCC slab are intended to be placed on top of the beam, and the beam bottom flanges are connected by seat angles and bolts. In the tests presented in this paper, however, the SFRCC slabs were applied symmetrically on both the top and bottom flange. This treatment was adopted with a belief that the behavior and characteristics of the proposed connection could be identified more clearly.

In the pilot test, two full-scaled specimens were tested. Specimen ‘C4’ were designed to fail by the stud fracture and ‘C9’ to fail by the beam yielding at the SFRCC slab edge. Details of the two specimens were the same expect for the number of the studs, four studs for Specimen ‘C4’ and nine studs for Specimen ‘C9’. A relatively strong column was arranged with the column-to- beam strength ratio was 2.2. This design was adopted to ensure beam yielding, which was a preferred mode of failure in this study and was expected in Specimen ‘C9’. Both specimens comprised a cold-formed, square-tube cross section column (300 mm in width, with a thickness of 19 mm), two H-shaped steel beams (400 mm in height and 200 mm in width, with a thickness of 8 mm and 13 mm for the web and flange, respectively). The size of the SFRCC slab was 1,150 mm along the beam, which was approximately one-tenth of the beam span, and 700 mm orthogonal to the beam. The thickness of the SFRCC slab was 150 mm, which was the same as a commonly used thickness for concrete floor slab. The beam web was designed to resist the shear load by using slotted bolt holes of the shear plate. The global dimensions of the specimens are shown in Figure 5.3.

The number of studs was determined in reference to the push-out test results. To achieve the beam yielding before the stud fracture, Eq. ((**5.1**) must be satisfied.

$$M_p \leq n \cdot A_{sc} \cdot F_u \cdot d_f \tag{5.1}$$

Where, M_p is the full plastic moment of the beam, n is the number of studs, $A_{sc}F_u$ is the shear resistance of one stud, d_f is the depth of the beam section. According to the push-out test results, the shear resistance per stud with the diameter of 22 mm was 190 kN when the studs are arranged with 50 mm spacing along the loading direction. Four and nine studs were used for Specimen 'C4' and 'C9', respectively. The bending moment transferred by the stud was therefore 0.68 times and 1.54 times of the full-plastic moment M_p of the beam (458 kNm) for Specimen 'C4' and 'C9', respectively.

The SFRCC slab was reinforced with rebars. Two types of rebars were used. The rebars arranged in the longitudinal direction, i.e., along the beam direction (x-direction in Figure 5.3(b)), were taken to resist the tensile force induced in the SFRCC slab. The amount of longitudinal rebars was designed to transfer the flange force when the full-plastic moment of beam was achieved. In this case, Eq. (5.2) is applied.

$$A_f \cdot \sigma_{u,f} \leq n \cdot A_{sb} \cdot \sigma_{u,r} \tag{5.2}$$

Where, A_f is beam flange's cross-sectional area; A_{sb} is the cross-sectional area of a rebar; n is the number of rebars; $\sigma_{u,f}$ is the ultimate strength of beam flange; and $\sigma_{y,r}$ is the yield strength of the rebar.

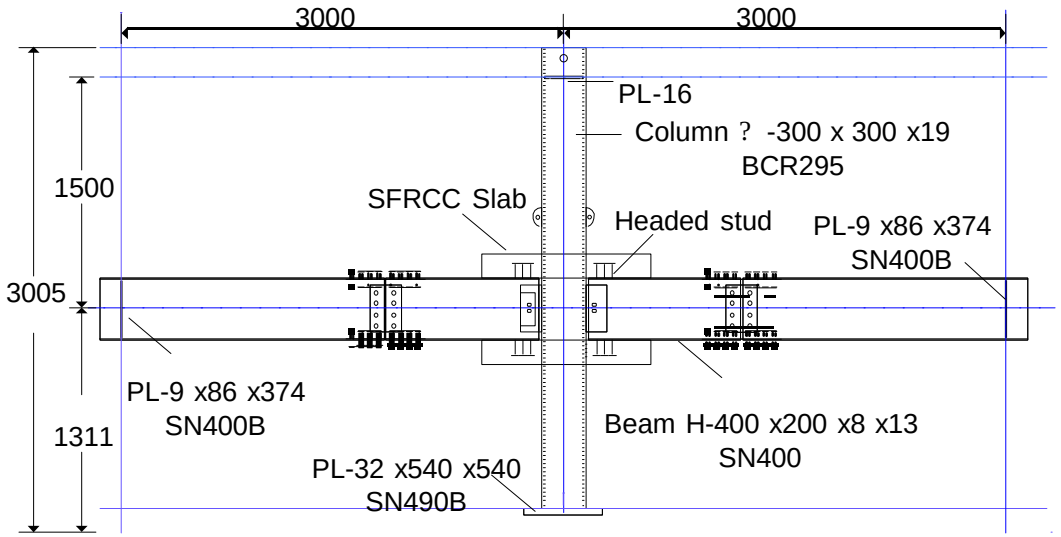

(a)

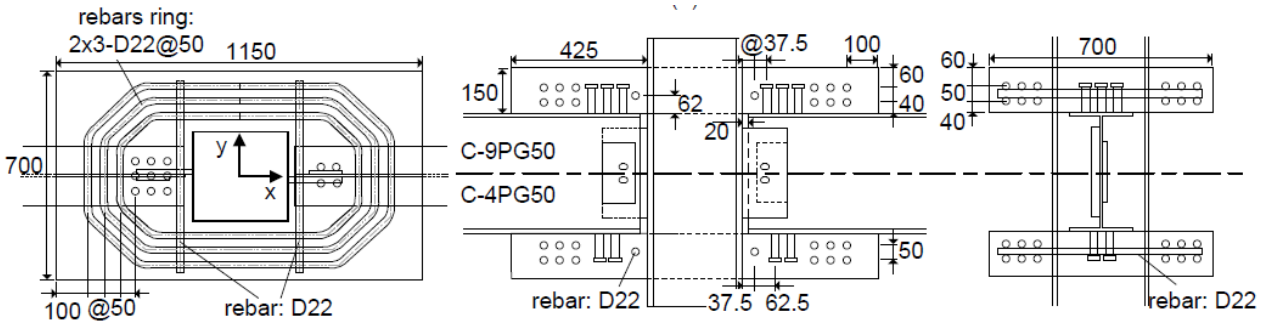

(b) (c) (d)

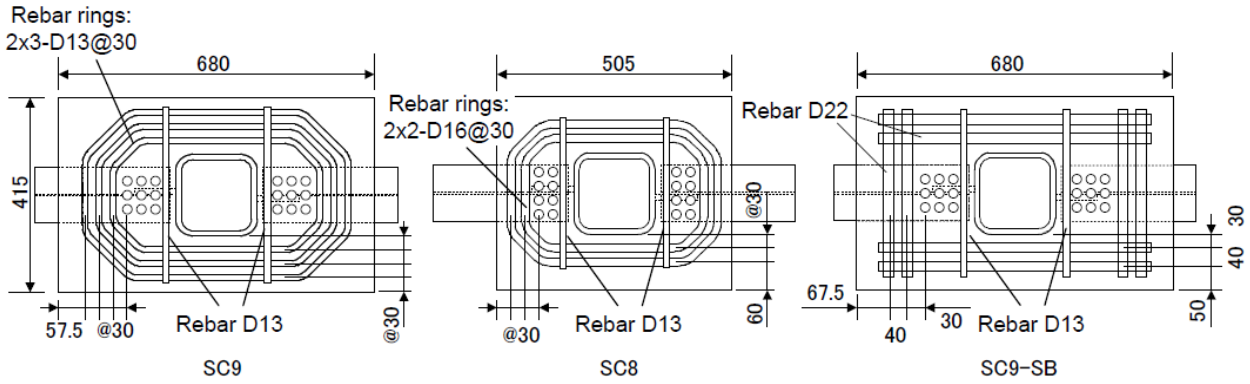

(e)

Figure 5.3 Test specimen: (a) Global view, (b) Plan of slab, (c) Front view of slab, (d) Side view of slab, (e) Details of parametric test specimens (unit: mm)

The rebars arranged in the transverse direction, i.e., the direction perpendicular to the beam direction (y-direction in Figure 5.3(b)), were taken to prevent the split cracks induced by the studs as observed in the push-out test (Specimen '4P50'). Rebar rings were adopted considering the space and cover layer limitations. The rebars were bent by 45° at the corner to directly transfer the force along and perpendicular to the beam axis (x and y direction in Figure 5.3(b)). As illustrated in Figure 5.3(b) to (d), two layers of three rebar rings are placed around the studs group with a 50 mm space in both the horizontal and vertical directions. The rebar rings placed at the upper layer was located 60 mm below the top surface of the slab.

Table 5.1 Basic dimensions of specimens

Spec.	Column	Beam
Pilot test		
C4 C9	□-300×300×19	H-400×200×8×13
Parametric test		
SC9 SC8 SC9-SB	□-175×175×12	BH-220×120×4.5×9

Spec.	Scale	Stud		Slab length (mm)	Rebar	
		Arrangement	Diameter (mm)		Design	Diameter (mm)
Pilot test						
C4	1.0	2×2	22	1150	Rebar ring: 2×2	22
C9	1.0	3×3	22	1150	Rebar ring: 2×3	22
Parametric test						
SC9	0.6	3×3	13	680	Rebar ring: 2×3	13
SC8	0.6	4×2	13	505	Rebar ring: 2×2	16
SC9-SB	0.6	3×3	13	680	Straight rebar	22

Considering the difficulties in fabrication and operation of the test with full-scaled specimens, the specimens used for the parametric test were scaled down to 0.6. This scaled factor was determined in reference to the stud diameter. The smallest stud available in Japan is 13 mm, which is 0.6 times of the studs used in the pilot test (22 mm). Three reduced-scaled specimens,

'SC9', 'SC8', and 'SC9-SB', were designed to investigate the effect of slab size, stud arrangement, and rebar design on the behavior of the proposed beam-to-column connection. The basic dimensions of the specimens are also summarized in Table 1. The details of the SFRCC slab, stud arrangement, and rebar arrangement are shown in Figure 5.3.

Specimen 'SC9' is the reduced scale specimen of Specimen'C9'. It was designed as a specimen to bridge the behavior of specimens in the pilot and parametric tests. Compact slabs were adopted for Specimen 'SC8'. The length of SFRCC slab of Specimen 'SC8' was 0.75 times of that of Specimen 'SC9'. Considering the requirement for the covering thickness of rebars, arrangement of both the studs and rebars was changed in Specimen 'SC8'. As shown in Figure 5.3(e), eight studs were used instead of nine, while stud spacing was the same as that of Specimen 'SC9'. According to the aforementioned design procedure, the bending moment governed by the stud fracture was still 1.50 times the full-plastic moment M_p of the beam. The rebars were changed to two layers of two rebar rings with the diameter of 16 mm from the two layers of three rebar rings with the diameter of 13 mm. Note that the total cross sectional area of rebars were the same between the two specimens. Since fabrication of the rebar rings is rather cumbersome, straight steel rebars were adopted for Specimen 'SC9-SB' to investigate the effect of rebar arrangement.

Specimen 'SC9-SB' had the same stud arrangement as Specimen 'SC9'. To lessen the congestion of rebars at the corners of SFRCC slab, the rebars were changed from two layers of three rebar rings to one layer of two straight rebars. Here, the rebar diameter was increased from 13 mm to 22mm to keep the same cross-sectional area of rebars of Specimen 'SC9'.

In all specimens, the web was not connected to the column, and it was to ensure clear examination into the load transferring capacity of the proposed connection. The material properties of the steel and SFRCC used for the specimens were obtained from associated material tests and are summarized in Table 5.2.

Table 5.2 Material properties (steel and SFRCC) (unit: MPa)

		Yield strength σ_y	Tensile strength σ_u
Column (BCR295)		430	439
Beam (SN400)	Pilot test	340	472
	Parametric test	284	430
Rebar (SD295)		396	566

		Compressive strength f_c'	Split strength f_{sp}'
SFRCC	Pilot test	115	18.1
	Parametric test	122	18.1

5.2.2 Test setup and loading program

Two types of test setup were used for the experimental study, as illustrated in Figure 5.4. The test specimen in the pilot test was placed in the loading frame shown in Figure 5.4(a). The top and bottom of the column and free ends of the beams were considered to be pin-supported. The beams were supported vertically by pin-ended struts. The lateral load was applied as a cyclic drift displacement at the top of the column. Different from the test setup of the pilot test, the specimen in the parametric test was placed horizontally (parallel to the laboratory floor), as shown in Figure 5.4(b). The ends of column were pin-supported. A pair of horizontal jacks enforced cyclic load to each end of the beams. A series of steel assemblies fitted with lubricated nylon sliding provided out-of-plane restraint with minimal frictional resistance for both test setups.

For each specimen, the drift angle was measured as the displacement at the top of the column divided by the height of the column. Drift angles of 0.005, 0.01, 0.02, 0.03, 0.04, and 0.06 rad were adopted, and two cycles were performed for each drift angle. Loading of specimens was terminated till the specimen lost the resisting capacity completely.

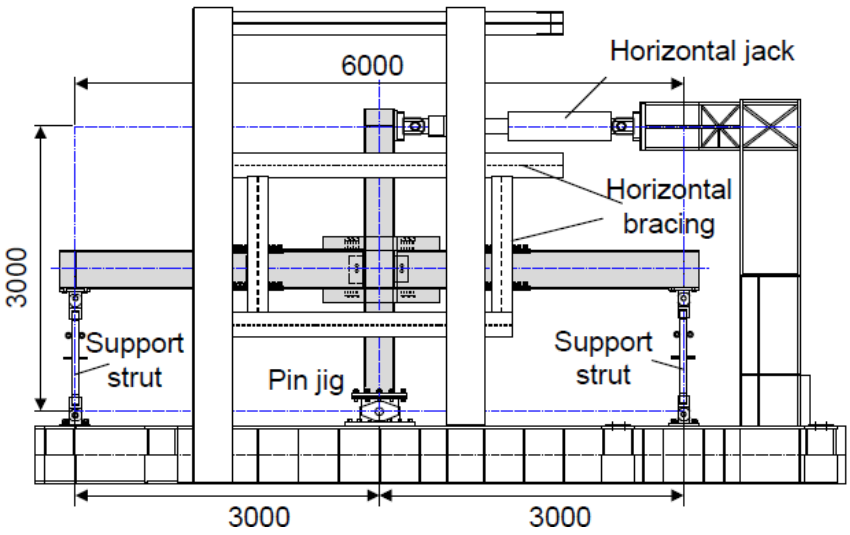

(a)

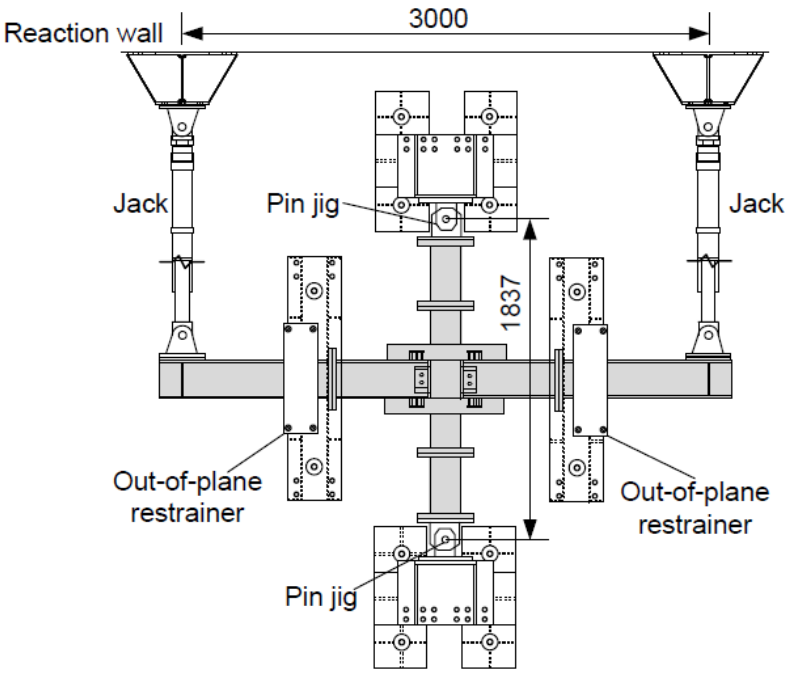

(b)

Figure 5.4 Test setup: (a) Pilot test, (b) Parametric test (unit: mm)

5.2.3 Test Results

The moment–rotation curves of the five specimens are shown in Figure 5.5 in terms of the normalized beam end moment versus beam-to-column rotation. The beam moment was estimated at the face of the column, and was normalized by the full plastic moment of the beam M_p. The failure pattern of each specimen is shown in Figure 5.6.

Specimen 'C4', with four studs, showed the smallest moment resistance, since it failed by stud fracture (Figure 5.6(a)) as expected. The specimen lost its strength during the story drift of 0.03 rad. A plastic hinge was formed in the location near the edge of the SFRCC slab diaphragm in Specimens 'C9' and 'SC9', the two specimens with nine studs. The two specimens showed stable hysteretic behavior till the 0.06 rad story drift. The damage on the slab was relatively small, although some cracks in the SFRCC slab was observed. At the final stage of loading, the strength of the specimens was reduced due to the growth of cracks in the SFRCC slab. Specimen 'SC8', the one with a shorter slab and eight studs, exhibited pinched hysteretic loops. This specimen failed by the bending failure of the slab. As illustrated in Figure 5.6(d), the transverse cracks formed from the root of studs at the loading cycle of 0.02 rad and connected into the main crack at the loading cycle of 0.03 rad. The end of the slab was pushed by the studs and rotated around Point A as shown in Figure 5.6(d). Strength deterioration and pinching of hysteretic curves became more notable as the transverse cracks grew. Specimen 'SC9-SB', the one with straight rebars, showed similar stable hysteresis behavior as Specimen 'SC9' till 0.03 rad story drift. However, the anchorage of rebars was broken in the loading cycle of 0.04 rad. As illustrated in Figure 5.6(e), the diagonal cracks developed from the root of studs to the corner of the SFRCC slab end where the longitudinal and transverse rebars overlapped. The longitudinal rebars was not able to transfer the full load induced in the SFRCC Slab. The specimen lost its resistance dramatically once the rebars were debonded.

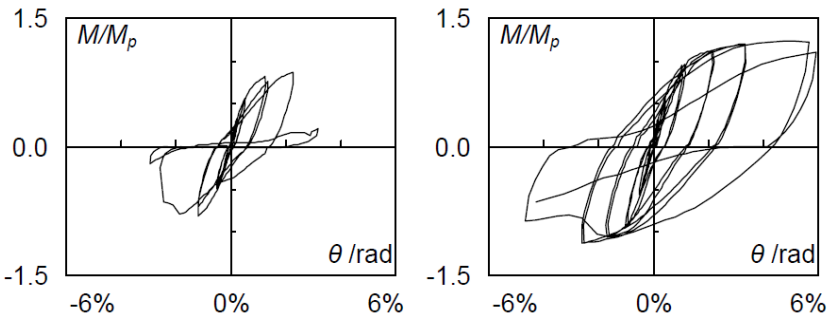

(a) (b)

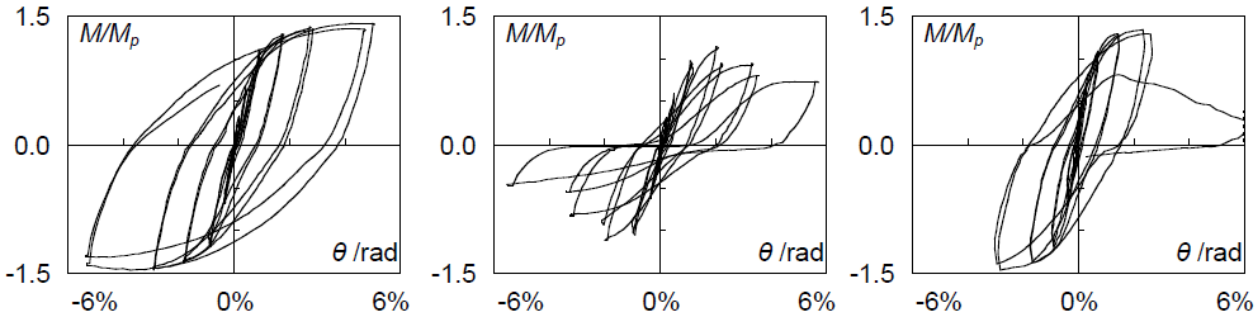

(c) (d) (e)

Figure 5.5 Beam moment versus beam-to-column rotation curves:
(a) 'C4', (b) 'C9', (c) 'SC9', (d) 'SC8', (e) 'SC9-SB'

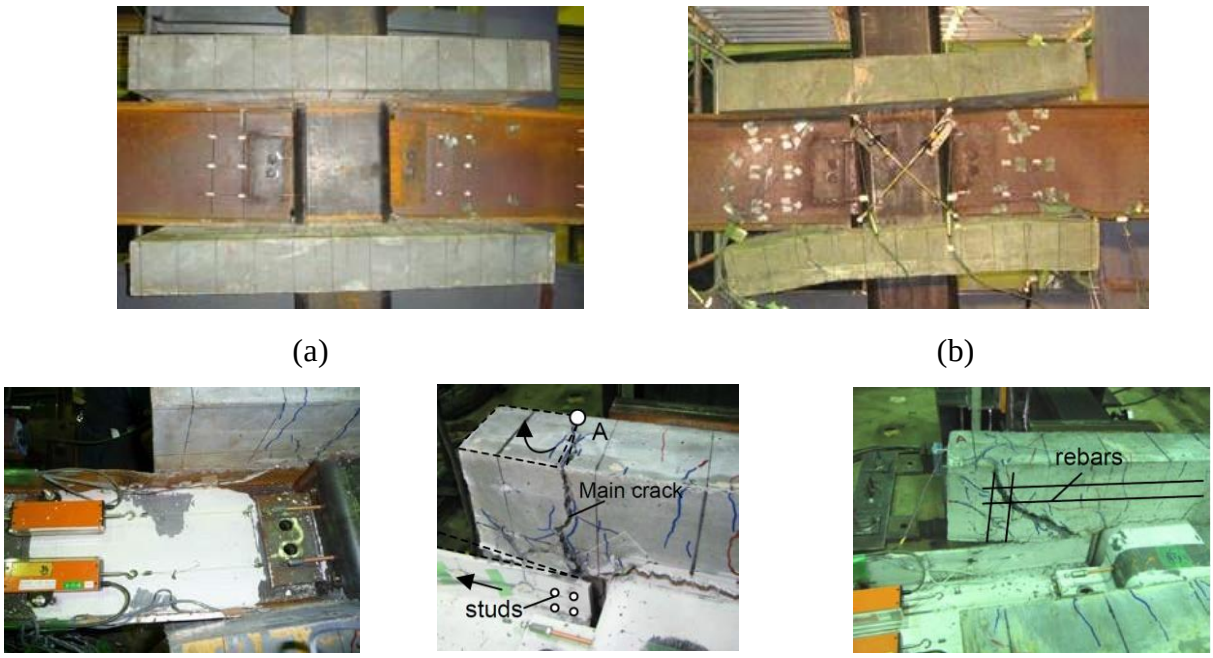

(a) (b)

(c) (d) (e)

Figure 5.6 Experimental observations on failure pattern:
(a) 'C4', (b) 'C9', (c) 'SC9', (d) 'SC8', (e) 'SC9-SB'

The elastic stiffness of the specimen is defined as the secant stiffness between the points at ±0.5% rad of the hysteretic curves (Figure 5.5). Figure 5.7 showed the elastic stiffness of the specimens normalized by the theoretical elastic stiffness, which was calculated based on basic statics. The elastic stiffness of the specimens was smaller than the theoretical one by 20 to 30%. A major factor of the difference was the separation of the beam web from the column (the beam web not connected to the column intentionally). According to a numerical analysis (whose detail will be described later), the web separation would reduce the elastic stiffness by about 10%. Other factors were those associated with fabrication of the specimens such as micro cracks of the slab, small gaps between the column and SFRCC slab, stud slip, among others. In fact, the test showed that the moment-rotation curves exhibited slight hysteresis (energy dissipation) even for the amplitude of ±0.5%.

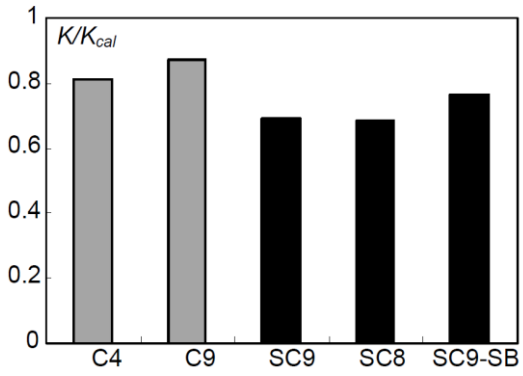

Figure 5.7 Elastic stiffness

In the pilot test in which the specimens were in the full-scale, Specimen 'C4' with four studs was slightly smaller in the elastic stiffness than Specimen 'C9' with nine studs. Specimen 'SC9' in the parametric test, unfortunately, did receive an accidental large force prior to the loading; hence the elastic stiffness was reduced from the beginning. Considering the configuration of the specimens, its elastic stiffness should have been as large as that obtained from Specimen 'SC9- SB'. Specimen 'SC8' was 5% smaller in the elastic stiffness than Specimen 'SC9-SB'. A smaller number of studs and a shorter slab (505 mm instead of 680 mm) were responsible for the difference. Those observations reveal that the stiffness of the specimens was affected by the size and number of studs as well as the slab size.

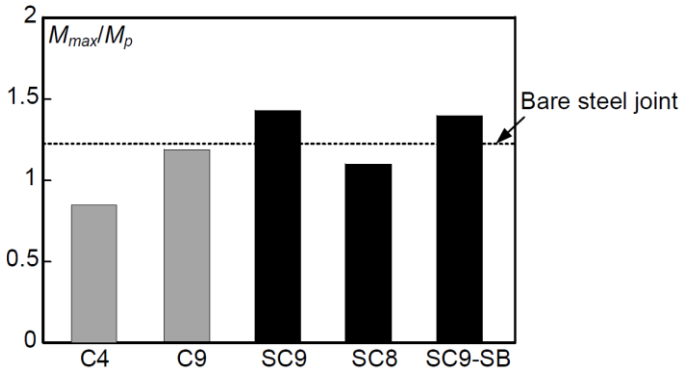

Figure 5.8 Normalized maximum moment

As shown in Figure 5.8, the maximum beam moments are normalized by the full plastic moment of the corresponding beam, M_p. The maximum moment of the beam (M_{max}) was estimated at the column face and taken as the average of the maximum moments achieved at the right and left beams. The strength of a conventional bare steel beam-to-column connection (Suita et al. 2009), in which a through diaphragm beam-to-column connection was tested, is shown in Figure 5.8 as an example for comparison. The maximum beam moment of Specimen 'C4' was about $0.8M_p$, since it failed by stud fracture. The maximum strength of Specimen 'C9' was $1.2M_p$, which was similar to the moment resistance of the bare steel beam-to-column connection. The reduced-scaled Specimen 'SC9' showed the maximum strength of $1.4M_p$, which was 17% larger than the strength of the corresponding full-scaled Specimen 'C9'. It occurred primarily because the yield strength (f_y) of the beam used in

Specimen ‘SC9’ (284 MPa) was significantly smaller than that of the beam used in Specimen ‘C9’ (340 MPa). The full-plastic moment of beams, M_p, in the parametric test (Specimen ‘SC9’) is 20% smaller than that of the beams in the pilot test (Specimen ‘C9’). The specimen having a shorter slab, Specimen ‘SC8’, showed the maximum strength of 1.1Mp. It was about 80% of the maximum strength of Specimen ‘SC9’. It was due to the bending failure of slab (Figure 5.6(d)) as mentioned in the previous section. Specimen ‘SC9-SB’ showed a similar maximum strength with Specimen ‘SC9’, but the strength deterioration caused by the loss of anchorage of rebars was more serious in the succeeding loading cycles.

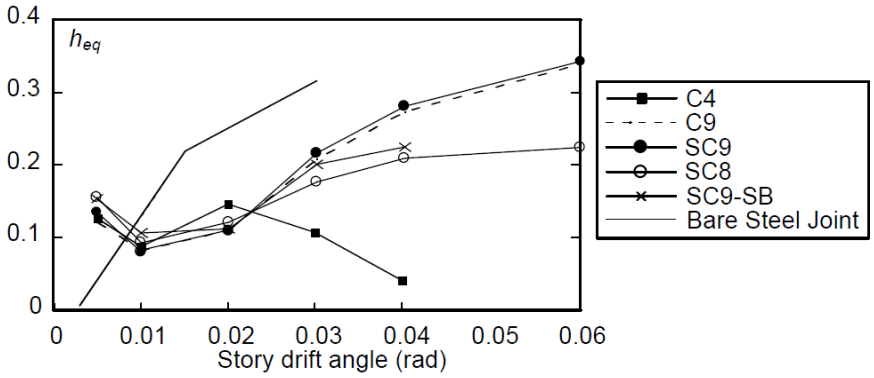

Figure 5.9 Equivalent viscous damping coefficient

In Figure 5.9, the equivalent viscous damping coefficients of the tested specimens are compared with that of the aforementioned bare steel beam-to-column connection (Suita et al. 2009). At the beam rotation of 0.005 rad, the dissipated energy of the specimens was about 1.2 times larger than the energy dissipated by the conventional bare steel beam-to-column connection. It was likely to be because of some local failure of the SFRCC slab around the root of studs. The equivalent viscous damping coefficient of Specimen ‘C4’ was reduced at 3% rad story drift because of the stud fracture. The other four specimens dissipated nearly the same amount of energy till the beam rotation of 0.03 rad. The difference of energy dissipation between Specimens ‘C9’ and ‘SC9’ was minimal. In comparison with Specimen ‘SC9’, Specimen ‘SC8’ and ‘SC9-SB’ dissipated less energy for story drift not smaller than 3%. It was due primarily to development of more cracks in the slab in Specimen ‘SC8’ and ‘SC9-SB’. In comparison with the bare steel beam-to- column connection, all the specimens with SFRCC slab exhibited similar energy dissipation up to 0.01 rad. For loading in larger amplitudes up to 0.03 rad, the specimens with SFRCC slab dissipated significantly smaller energy. Local failure of SFRCC slab particularly around the studs naturally promoted pinching of the hysteretic curves.

5.3 Numerical study

5.3.1 Analysis Model

To further understand the contribution of SFRCC slab and studs on the behavior of the beam-to-

column connection with SFRCC slab, numerical analysis was conducted. The specimens adopted in the parametric test were used for the study. The general-purpose finite element program ABAQUS version 6.10 (Systèmes 2010) was used. Half of the specimen was modeled by taking an advantage of symmetry and the geometry and boundary conditions of the model conformed to the experimental conditions. As shown in Figure 5.10, the following Cartesian coordinate system was chosen: the axis perpendicular to the beam was denoted as Ox, the axis along the bean was denoted as Oy, and the axis Oz ran from the top to bottom along the column.

Figure 5.10(a) shows the boundary condition of the models. The boundary conditions of the model were the same as the test and reflected the symmetric properties of the model. The standard symmetric boundary conditions were introduced at plane x=0. The 'Pin' constraints were applied to the top and bottom end of the column. The models were loaded at the end of the two beams along the Oy axis, but in the opposite direction. The loading history adopted in the test was applied by imposing displacement.

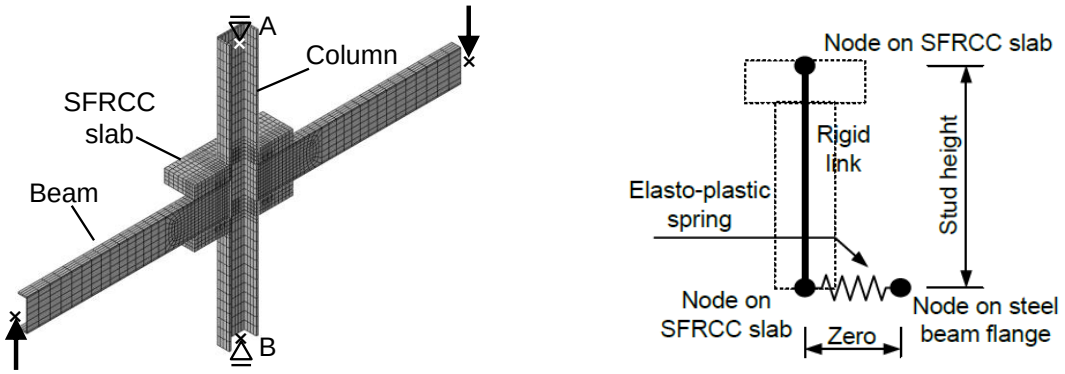

(a) (b)

Figure 5.10 Modeling of specimen: (a) Boundary condition, (b) Modeling of stud

A four-node linear reduced integration with an hourglass control shell element (S4R) was used for the column and beams. The SFRCC slab was meshed by an 8-node hexahedral element with reduced integration (C3D8R). The rebars were modeled using the truss element (T3D2). They were treated as an equivalent uniaxial material embedded in the SFRCC slab solid elements, and the bond-slip effect between the slab and rebars was not considered. Contact interaction without friction behavior was adopted for the interfaces between the slab and beam flange/column face. Contact and detachment at the interfaces therefore was considered.

The studs were modeled using the combination of two spring elements and one rigid link. In the model, rigid links were introduced between the nodes at the stud head and the note at the stud root in the SFRCC. Since the stud's deformation was represented by a shear-slip relationship, a horizontal spring was assigned for each stud and in each of the two horizontal directions as shown in Figure 5.10(b). An elastic and perfectly plastic material model was assigned to the spring element. The elastic shear stiffness and maximum shear force of each stud were determined based on the push-out test results.

The multi-linear kinematic hardening option was adopted to simulate the material behavior of

steel, with the parameter values provided from the associated material tests. For the column, beams, and rebars, the stress-strain curve was assumed to be bilinear with a strain hardening ratio of $E_s/100$, where E_s was Young's modulus of steel.

The damage plasticity model, which provides a general capability for the analysis of concrete structures under cyclic loading, was adopted to model the behavior of SFRCC. According to the research by Nielsen (Nielsen 1995), the compressive stress-strain relationship of SFRCC was defined by the following Equation,

$$\frac{\sigma}{f_c'} = 2.5\frac{\varepsilon}{\varepsilon_c}\cdot\left[1.5+\left(\frac{\varepsilon}{\varepsilon_c}\right)^{2.5}\right]^{-1} \tag{5.3}$$

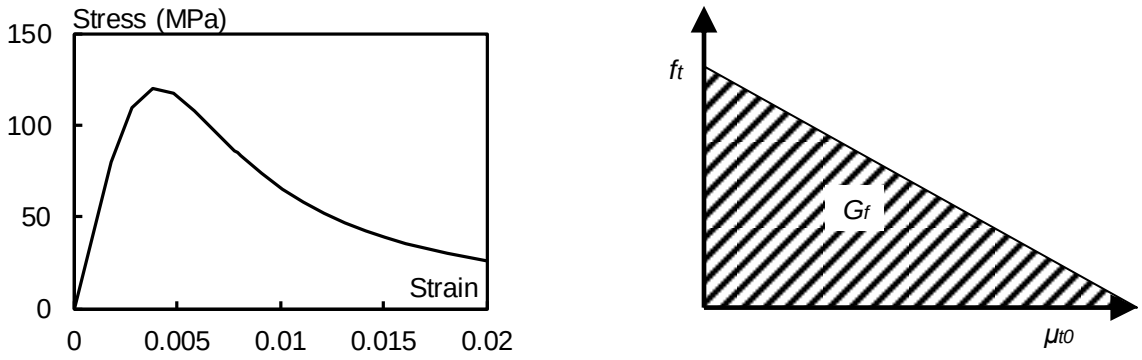

(a) (b)

Figure 5.11 Material model for SFRCC: (a) Compression, (b) Tension

Where ε_c and f_c' are the compressive strain and stress at the peak point; and the strain-stress relation is graphically shown in Figure 5.11(a). The tensile behavior of the applied material model was defined independently in two strain levels. Up to the initiation of cracks, the stress-strain relation is linear; and post-cracking behavior is defined by a linear stress-crack opening displacement relationship shown in Figure 5.11(b).The cracking displacement, at which the tensile strength is reduced to zero, is calculated by Eq. (5.4), which is based on the fracture energy. In this test, the water binder ratio (W/B) and volume fraction of steel fibers (V_f) were adopted as 0.20 and 6% for SFRCC. Based on the material test results, E_0=50GPa, f_c' =120MPa, f_t=15MPa, and G_f= 1.3kN/m were used.

$$\mu_{t0} = 2G_f/f_t \tag{5.4}$$

5.3.2 Analysis Results

Figure 5.12(a) shows the relationship between the bending moment at the column face and story drift, plotting the curves from the amplitudes of 0.005 to 0.04 rad. The black and gray lines are the analytical and experimental curves, respectively. The stiffness was defined as the secant stiffness between the origin and the point at 0.005 rad in the story drift angle. The experimental stiffness were somewhat larger than the analytical stiffness, with differences within 10%. The experimental

maximum strengths were consistently smaller than the analytical maximum strengths, with differences not greater than 5%.

The crack distributions observed from the test and analysis are compared in Figure 5.12(b). The failure regions are marked in dark gray, where the tensile equivalent plastic strain of SFRCC slab reached larger than 0.2%. This was the strain level where cracks in tension could be formed in SFRCC. Reasonable agreement between the test and analysis is observed. The analysis was able to predict the experimental failure mode. Specimen 'SC9' sustained beam yielding, and slight pinching of hysteretic curves caused by local crushes of SFRCC around studs was traced reasonable, too. Pinching of hysteretic curves, which was caused by the slab fracture, was successfully traced in the analysis for Specimen 'SC8'. Transverse cracks associated with the bending failure of slab in Specimen 'SC8' were also noticed in the analytical tensile strain contours of the slab shown in Figure 5.12 (b). In the test of Specimen 'SC9-SB' failed by the loss of the anchorage of rebars. As shown in the tensile strain contours of the slab of 'SC9-SB' (Figure 5.12 (b)), analytical cracks are developed to the corners of the slab, where rebars arranged in two horizontal directions crossed. This suggests anchorage failure of the straight rebars, which also corresponds to the test. Both the test and analysis indicated serious loss in resistance after the anchorage failure.

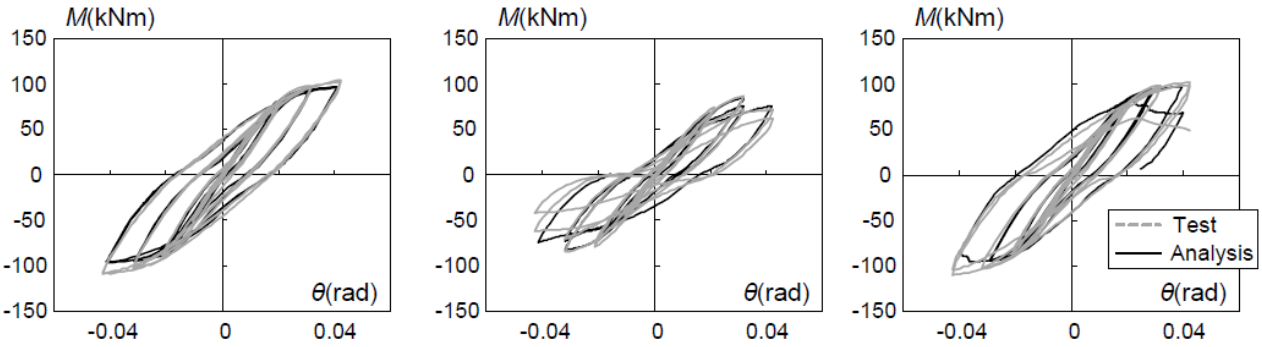

(a)

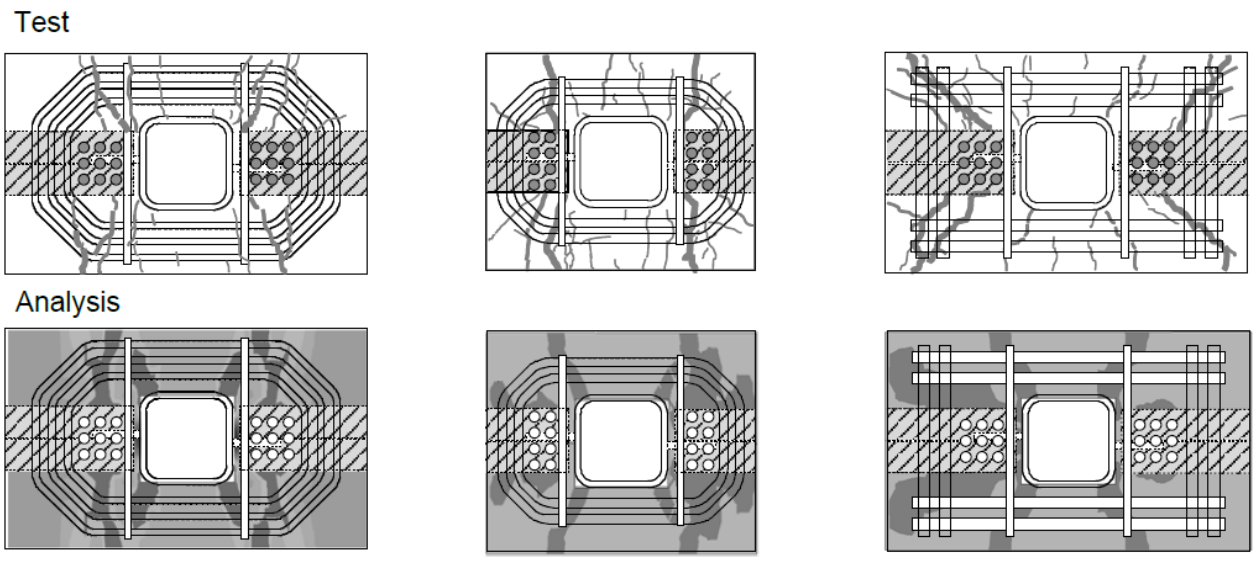

(b)

Figure 5.12 Comparison of test and analysis: (a) Moment – rotation curves, (b) Crack distribution

5.4 Parametric study

The failure modes of the proposed beam-to-column connection with SFRCC slab are summarized in Figure 5.13. The beam yielding (Figure 5.13(a)) is the preferred failure mode in design, since the beam would behave in a most ductile manner and the moment-rotation curve is made stable as observed in Specimen 'C9'. The stud fracture (Figure 5.13(b)) is an undesirable failure mode, since the connection would sustain brittle failure as observed in Specimen 'C4'. The strengths corresponding to the two failure modes form the strength boundaries of the proposed beam-to-column connection.

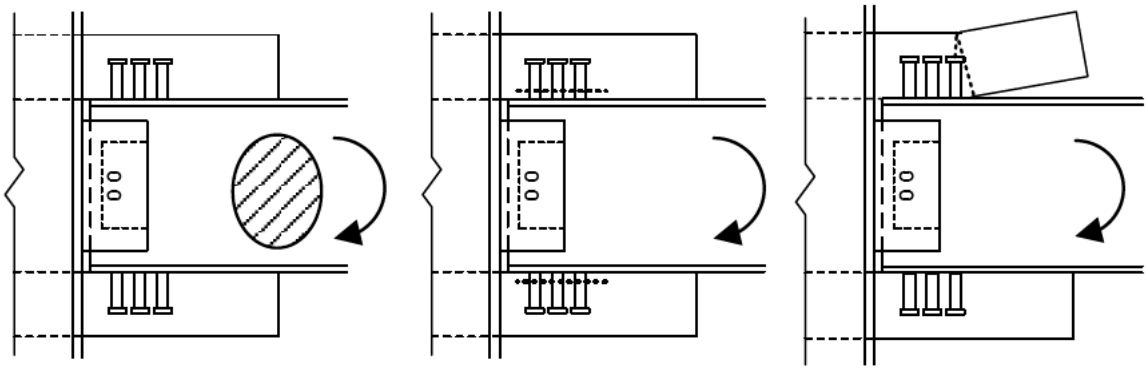

(a) (b) (c)

Figure 5.13 Failure mode: (a) Beam yielding, (b) Stud fracture, (c) Slab bending failure

Another design factor that would control the strength is the strength and stiffness of the SFRCC slab. In the test, cracks were observed in the SFRCC slab, and Specimen 'SC8' failed by the slab bending failure (Figure 5.13(c)) before the beam formed a significant plastic rotation. In what follows, effects of a few design parameters associated with the SFRCC slab on the strength of the proposed connection are examined using the numerical model developed in the previous section. Here, Specimen 'SC9' was used as the baseline specimen, and the number of studs, the SFRCC slab thickness, and the amount of rebars were chosen as variables.

In Figure 5.14, the maximum strengths obtained for respective analysis cases are compared with respect to the baseline Specimen 'SC9'. The abscissa indicates the name of each analysis case, i.e., the number of studs (Figure 5.14(a)), slab thickness (Figure 5.14(b)), and rebar size (Figure 5.14(c)). The ordinate denotes the ratio of the maximum strength of each case to that of the baseline Specimen 'SC9'.

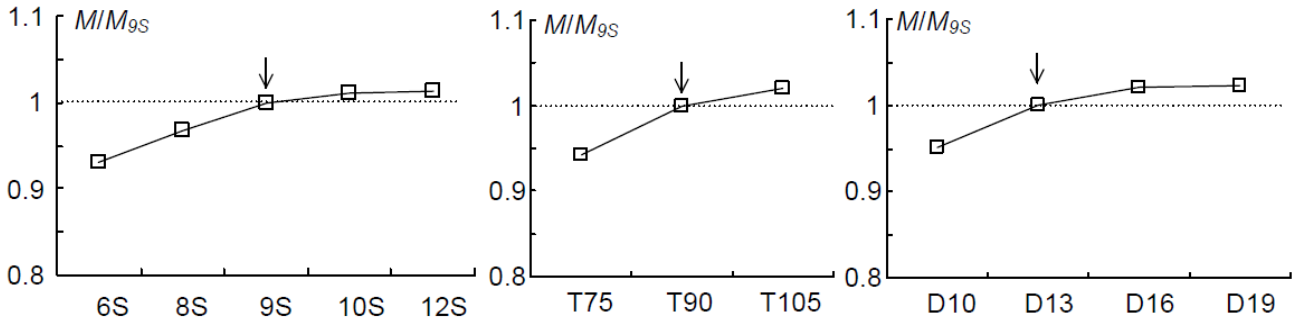

Figure 5.14 Effect of (a) number of studs, (b) slab thickness, (c) rebar size

As for the effect of number of studs (Figure 5.14(a)), five models were considered, in which six, eight, nine, ten and twelve studs were arranged. The region to arrange studs and the slab and rebar arrangement of the five models were the same as those adopted in the baseline Specimen 'SC9'. According to Eq. (5.1), six studs were sufficient to avoid the stud fracture before the formation of beam hinging. It was also disclosed from the push-out tests that studs can be arranged without losing per stud strength for an interval of not smaller than two times the diameter of studs. With this interval, twelve studs in maximum can be arranged within the specified region. As shown in Figure 5.14(a), the maximum strength was reduced by 5% when the number of studs was reduced from nine to six. As the number of studs increase, the maximum strength increases slightly. The change in strength is primarily the result of the stiffness reduction of the SFRCC slab when the number of studs is smaller. For a fewer studs, the SFRCC slab sustains more damage around the studs, which lessens the slab stiffness (both in-plane and bending). In the meantime, the stiffness loss reduces the plastic rotation of the beam and accordingly the beam bending moment for the given story drift.

Three cases were considered to examine the effect of the SFRCC slab thickness. The SFRCC slab thickness was set as 75 mm for a thinner slab case considering the required covering depth of rebars to the slab surface. For comparison, the SFRCC slab was set 105 mm for a thicker slab case. In Fig. 19(b), the maximum strength was reduced by 5% for the thinner slab and increased by 2% for the thicker slab. In all three cases, the slab sustained cracks, with more cracks for thinner slabs. Decrease in the strength for the thinner slab case is associated with the reduced slab stiffness as discussed for the effect of number of studs.

As observed from the test, the proposed rebar ring solved the anchorage problem associated with the rebars embedded in the SFRCC slab. To investigate the effect of the amount of rebars, considered were four cases, in which the rebars with nominal diameters of 10 mm, 13 mm, 16 mm and 19 mm were adopted. The maximum strength of the four cases are compared with that of the baseline Specimen 'SC9' ('D13') in Figure 5.14(c). According to Eq. (5.2), the rebars with the nominal diameter of 10 mm were not sufficient to transfer the required tensile force induced in the longitudinal direction of the SFRCC slab. Indeed, for the case with 10 mm diameters, the slab sustained failure. Although the strength reduction was by 6%, serious pinching behavior was observed in the hysteresis. As the nominal diameter of rebars increases from 13 mm to 16 mm and 19 mm, the SFRCC slab is further stiffened and strengthened, and the beam plastic rotation was secured and promoted. As noted in those examples, the stiffness and strength of the proposed connection are affected by the design

details of SFRCC slab such as the number of studs, dimensions of the slab, and rebar arrangement, among others. A further study, both experimental and numerical, is underway to identify the design variables to control the SFRCC slab behavior and develop design procedures of these variables. As mentioned in the introduction, the SFRCC slab was proposed to work as an exterior diaphragm to transfer the beam flange load. A further study is underway to investigate the behavior of the proposed connection only with the top SFRCC slab, such as the connection shown in Figure 5.2.

5.5 Conclusions

Considering the high strength of SFRCC, a SFRCC slab was proposed to serve as an exterior diaphragm instead of adding an extra steel diaphragm plate for the beam-to-column connection. Series of tests were conducted for the proposed beam-to-column connection. A numerical study was also carried out to reproduce the experimental results and to examine the effects of design parameters such as the number of studs, SFRCC slab size, and amount of rebars, on the elastic stiffness and maximum strength. Major findings obtained from this study are summarized as follows.

(1) The beam-to-column connection using SFRCC slab was found to be a promising alternative for the design of ductile steel moment frames. Beam plastic rotations appeared at the end of SFRCC slab for specimens with proper arrangements of studs and rebars. The specimens showed stable hysteresis till 0.06 rad story drift angle and had the moment resistance capacity similar to that of the corresponding bare steel beam-to-column connection. The energy dissipation of the specimen was notably smaller than what can be achieved by traditional beam-to-column connections. This was primarily because of local damage of the SFRCC around the root of studs. Anchorage of rebars was found to control the strength, and it was secured by the use of rebar rings.

(2) The elastic stiffness of the proposed beam-to-column connection is controlled by the steel beam, SFRCC slab, and studs. The stiffness increases with the increase of the number of studs, length or thickness of SFRCC slab. The rebars have a minimal effect on the elastic stiffness.

(3) Among the various failure modes that characterize the maximum strength of the proposed beam-to-column connection, the beam yielding at the end of SFRCC slab is considered as the preferred failure mode. A preliminary numerical analysis was conducted to examine the effect of design variables associated with the SFRCC slab on the strength of the proposed connection. The number of studs, slab thickness, and amount of rebars were chosen as variables, and their effects on the strength were found rather minimal within the ranges considered in the analysis.

As observed from the experimental and numerical studies, the proposed beam-to-column connection with SFRCC slab has a potential to attain the structural performance that can be expected for conventional beam-to-column connections using welds. Dimensions of the SFRCC slab and the arrangement of studs and rebars in the slab are the primary factors that control the performance of this connection. Further studies are underway to lead the proposed connection to actual implementation, and their results will be reported later.

REFERENCES

Aarup, B. (2004). "CRC- A Special Fibre Reinforced High Performance Concrete." 8, RILEM Publications SARL.

Architectural Institute of Japan (AIJ) (Ed.). (1995). *Reconnaissance Report on Damage to Steel Building Structures Observed from the 1995 Hyogoken Nanbu Earthquake*. Kinki Branch, Osaka.

Bache, H. H. (1981). "Compact reinforced concrete composite, basic principles." *Aalborg Portland, Aalborg*.

Cui, Y., and Nakashima, M. (2011). "Hysteretic Behavior and Strength Capacity of Shallowly Embedded Steel Column Bases with Sfrcc Slab." *Earthquake Engineering & Structural Dynamics*, 40(13), 1495–1513.

Kaneko, Y., Mihashi, H., Kirikoshi, K., and Abe, T. (2001). "New Application Field of Steel Fiber Reinforced Cementitious Composites: Experiment on Column-Beam Joint in Steel Structures." *Journal of architecture and building science*, (14), 119–122.

Kaneko, Y., Mihashi, H., Kirikoshi, K., and Abe, T. (2002). "Simple Column-Beam Joint of Steel Structures Employing Steel Fiber Reinforced Cementitious Composite: Experimental Verification on Structural Performance of Joint." *Journal of Structural and Construction Engineering. Transactions of AIJ*, (558), 219–225.

Kaneko, Y., Mihashi, H., Kirikoshi, K., and Suwanai, Y. (2006). "Simple Column Base System of Steel Structures Employing Steel Fiber Reinforced Cementitious Composite: Experiment on Structural Performance of Basic Model and Applied Model." *Journal of Structural and Construction Engineering. Transactions of AIJ*, (600), 179–186.

Matsuo, S., Tanaka, T., and Inoue, K. (2006). "Theoretical and Experimental Study on Strength of RHS-Column to Beam Connections with Exterior Diaphragm." *Journal of structural and construction engineering. Transactions of AIJ*, (606), 225–232.

Nakashima, M., Inoue, K., and Tada, M. (1998). "Classification of damage to steel buildings observed in the 1995 Hyogoken-Nanbu earthquake." *Engineering Structures*, 20(4–6), 271–281.

Nielsen, C. V. (1995). "Ultra High-Strength Steel Fibre Reinforced Concrete, Part I, Basic Strength Properties of Compresit Matrix." *Technical University of Denmark. Series R*, 323.

Suita, K., Kitamura, Y., and Hashida, I. (2009). "Seismic performance and retrofit of beam-to-column connection for early high-rise buildings." *Journal of Structural and Construction Engineering, Transactions of AIJ*, 636(74), 367–374.

Systèmes, D. (2010). "Abaqus 6.10: Analysis User's Manual." *Providence, RI: Dassault Systèmes Simulia Corp*.

Youssef, N. F. G., Bonowitz, D., and Gross, J. L. (1995). *A Survey of Steel Moment-Resisting Frame Buildings Affected by the 1994 Northridge Earthquake*. US National Institute of Standards and Technology.

CHAPTER 6

Preliminary Member Tests on SFRCC Repaired Connections

6.1 Introduction

During the severe earthquakes, such as 1994 Northridge and 1995 Hyogoken-Nanbu (Kobe) earthquakes, a large number of steel-frame buildings is likely sustain severely damage such as cracks and brittle fracture at welded beam-to-column connections. Figure 6.1 shows the typical seismic damage patterns of beam-to-column connection, such as the bottom and top flange fracture, flange and wed buckling, and slab crush or crack. Although experienced such substantial structural damage, many of such steel-frame buildings did not collapse. Therefore, to restore such damaged steel-frame buildings to their normal state for post-earthquake continuing use, it is important to repair and strengthen the damaged beam-to-column connections.

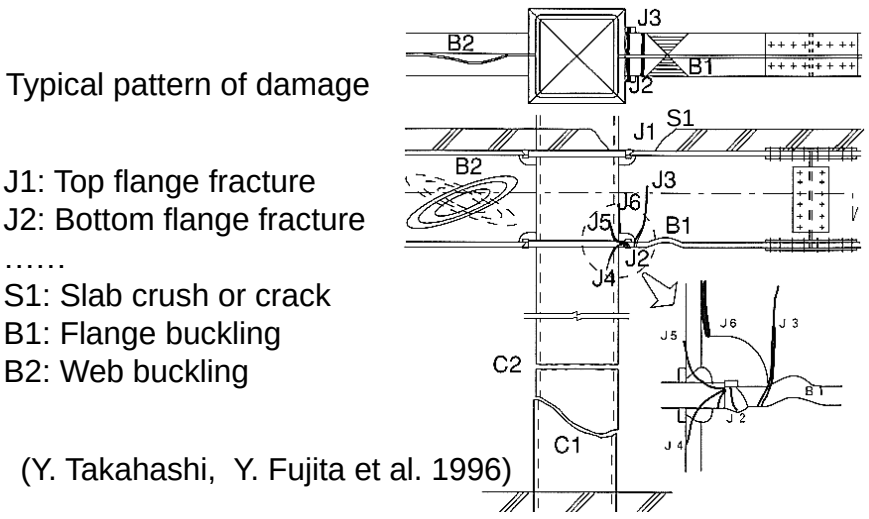

Figure 6.1 Typical damage pattern for the beam-to-column connection in the earthquake (Takahashi et al. 1996)

Various repair and strengthening methods (Anderson and Duan 1998; FEMA 351 2000; Uang et al. 1998) have been developed and proposed for the rehabilitation of the damaged steel beam-to-column connections. For example, as shown in Figure 6.2, partial replacement to the damaged flange and web and replacement of the entire beam segment have been applied to the post-Kobe earthquake beam-to-column rehabilitation (Takahashi et al. 1996). However, for the

rehabilitation, these methods seem to have difficulty in applications because of the presence of RC floor slab. In the practical applications, the removal of the RC slabs is always required (FEMA 547 2006). For the seismic rehabilitation for steel moment frame, the existing slabs and metal decks must be chipped and cut away before the repair. It not only requires the removal of the floor slab but also consideration for how to replace the removal portion of slab.

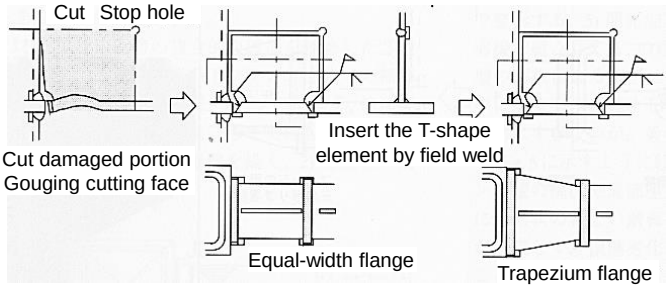

(a)

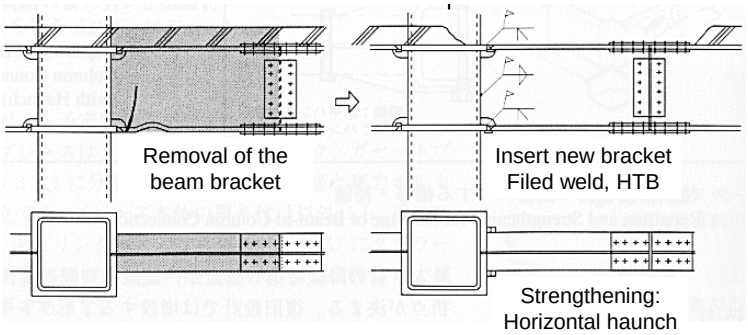

(b)

Figure 6.2 Some repair methods to connection: (a) Cut and replace the damaged web and beam flange; (b) Replace beam segment

To provide an alternative to repair the damaged beam-to-column connection, a repair method is proposed by replacing the damaged slab portion with SFRCC rather than by repairing the damaged slab portion with new concrete,. As shown in Figure 6.3(a), widened steel plates are used to replace the fractured and buckled bottom flange, and SFRCC slab without steel reinforcement is used to replace the damaged concrete floor slab portion in the vicinity of the column. A stud cluster is welded to the top flange and embedded in the SFRCC slab. SFRCC slab serves as an external diaphragm to transfer the force from the top flange through the stud cluster. Clearances are made between the SFRCC slab and the remained RC slab; consequently, a plastic hinge develops at the edge of the SFRCC slab, and thus the potential fracture location is moved away from the column face as shown in Figure 6.3(b). Moreover, because the headed stud can be welded conveniently with the stud gun, and elimination of steel reinforcement due to the high tensile strength of SFRCC, the constructional difficulty and labor time are expected to be reduced.

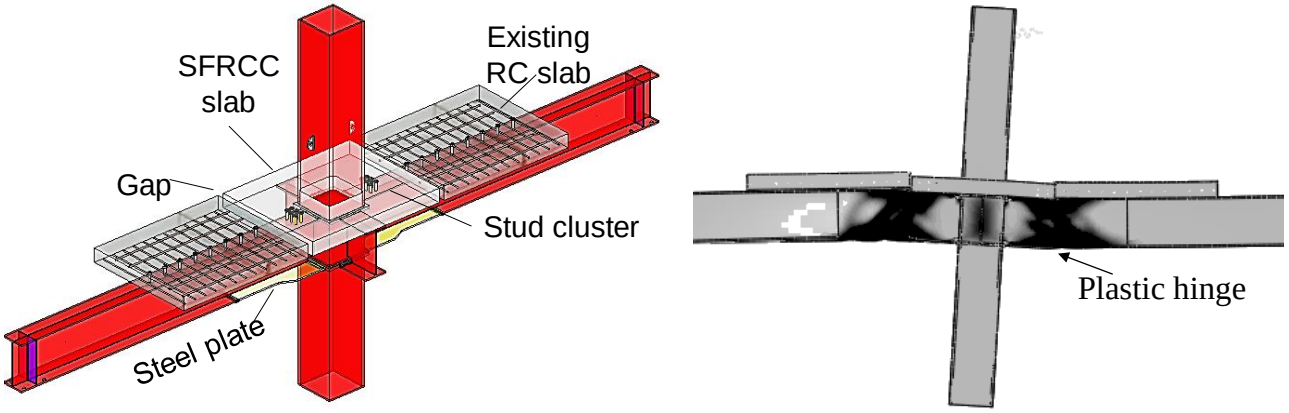

(a) (b)

Figure 6.3 Illustration of the proposed repair method: (a) Schematic of the proposed repair method; (b) Expected failure mode

A design method using SFRCC and steel plates to repair the damaged composite beam-column connection is proposed, and corresponding full-scale member tests were conducted to verify the feasibility of the proposed methods and examine the performance of the repaired connection. The tests were divided into two phases. Phase 1 was the quasi-static cyclic loading test to two identical full-scale composite beam-column connection, two connections were tested to fail under specified loading pattern. In phase 2, the proposed repair methods were applied to the damaged original connections. The repaired connections were tested under identical loading history used in the phase 1 test. Based on the test results, the repaired performance such as the elastic stiffness, maximum strength and energy dissipate capacity are examined. The mechanism of force transfer in SFRCC slab and the stud cluster are also investigated.

6.1.1 *Organization*

In this chapter, a two-phase experimental program was undertaken to evaluate the proposed. The damage pattern of the steel moment beam-to-column with the presence of the RC floor slab is reproduced by the Phase 1 test. The repair scheme is introduced according to the damage pattern. The design approach of proposed repair method is presented following by the introduction to the practical repair scheme. The Phase 2 test was conducted to investigate the repaired performance. Test results are given as summaries of the behavior and the test data for repaired connections and original connections. The repair performance is checked by comparison of both in the terms of strength and elastic stiffness. The bending behavior of the representative beam sections is compared for the repaired connection. The force resisting contributions of SFRCC and rebar is also discussed. The strain distribution on the critical failure faces is examined by both the test data and analysis results from the verified FEM model.

6.2 Test on original beam-to-column connection

6.2.1 *Introduction*

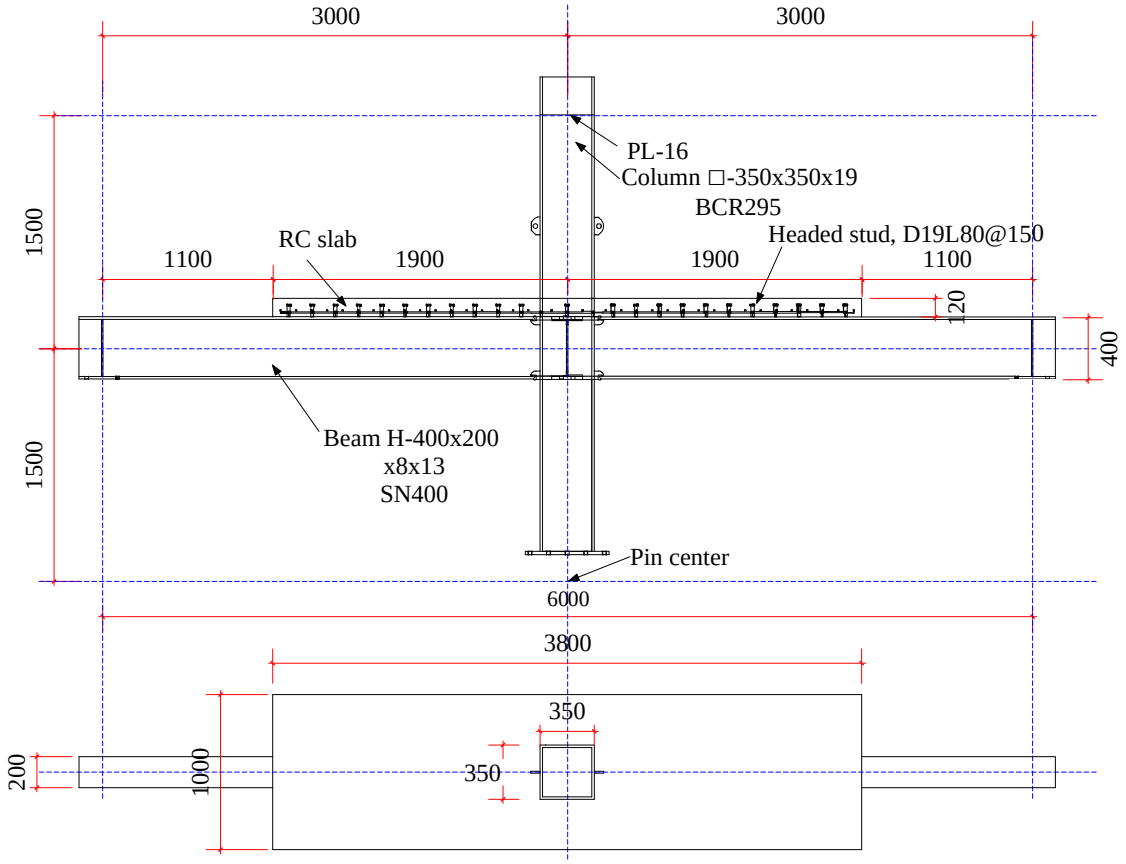

Figure 6.4 Test specimens: (a) Front elevation; (b) Plane view.

Two identical composite beam-to-column connection specimens, named 'OC-1' and 'OC-2', are conducted for the Phase 1 test. Figure 6.4 shows the global dimension of the specimen. The specimen was designed to represent the interior connection of a typical low- to middle- rise building designed following the post-Kobe Japanese seismic design method. The columns were made of cold-formed square tubes (350 mm in the width, with a thickness of 19 mm), beams were made of hot-rolled wide-flanges (H-400x200x8x13), and through-diaphragm connection details were adopted in which beams are shop-welded to the columns. A relatively strong column was used to ensure that the beams could initiate the development of a plastic hinge mechanism during cyclic loading before damage would develop in the column.

Figure 6.5 shows details of the through-diaphragm connection adopted. The top and bottom square tube columns were welded to each other using a 25 mm thick complete penetration diaphragm. The beam flanges were welded to the diaphragms instead of the column flange, and an improved web access hole was used. CJP (complete joint penetration) single bevel groove welds were used to connect the beam flanges to the diaphragm plates, and fillet-welds were used to connect the beam web to the column. The root of the CJP groove welds was located on the interior side of both the top and the bottom flange. To simulate the actual steel building, two side beams were design on each side of the column web and connected to the through-diaphragm with the same connection details adopted for the main beam.

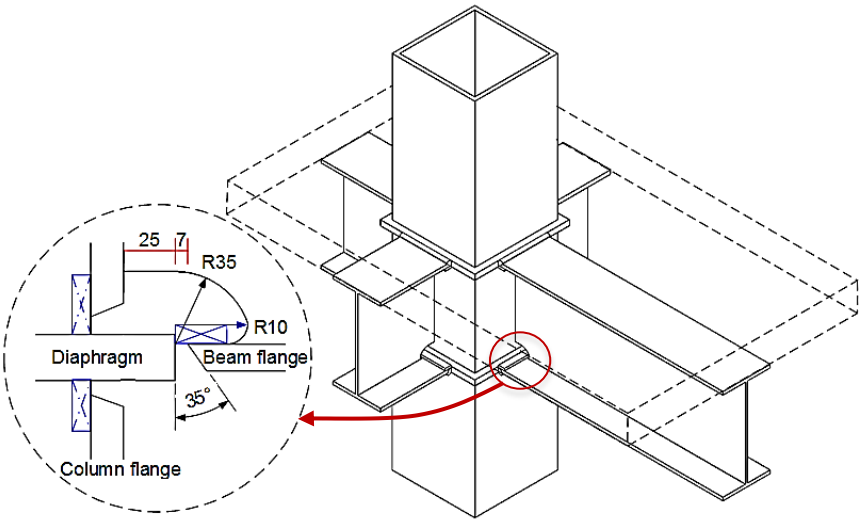

Figure 6.5 The through-diaphragm connection details

A solid RC floor slab with a thickness of 120 mm was placed on top of the beams and connection to the upper flange through headed studs. The number and location of shear studs was chosen to be representative of existing buildings. These shear studs provide fully composite action as defined by AIJ code (Architectural Institute of Japan (AIJ) 2010). A layer of D10 (10 mm diameter) reinforcing bars were placed perpendicular to the beams to prevent longitudinal temperature and shrinkage cracking.

The material properties of the steel and concrete used for the specimens were obtained from the associated material tests and are summarized in Table 6.1

Table 6.1 Material properties (steel and concrete)

		Yield strength σ_y	Tensile strength σ_u
Column □-350×350×19 (BCR295)		400	406
H-400×200×8×13 (SN400)	Flange	295	458
	Web	331	467
Rebar (SD295)		396	566
Concrete		23.9 MPa	

6.2.2 *Loading system, loading program and measurement*

Loading system

The test setup and test specimen are shown in Figure 6.6. The specimen consists of one column and two beams with respective beam-to-column connections. The top and bottom of the column and the two ends of the beams are pin supported. The column is 3 m long from the jack to the pin support. The beam was 3 m from the center of the column to the pin support. The entire specimen is 3 m in height and 6 m in width, which are the commonly used span length and story height for low- to middle- rise steel moment resistant frame built in Japan. The horizontal load was applied at the top of the column by 1,500 kN oil jack. A RC slab with the thickness of 120 mm was placed on top of the

beams. The RC slab was 1 m in width and 1.9 m in length on each side.

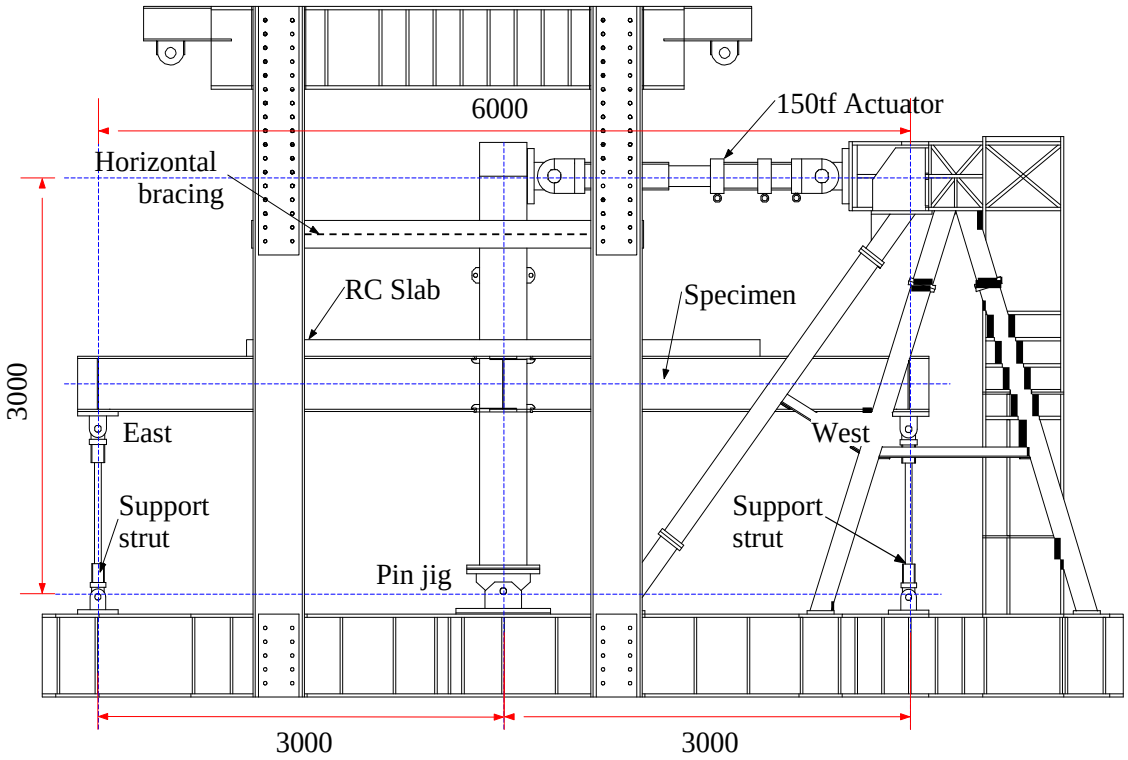

Figure 6.6 Quasi-static loading test setup (unit: mm)

Loading protocol

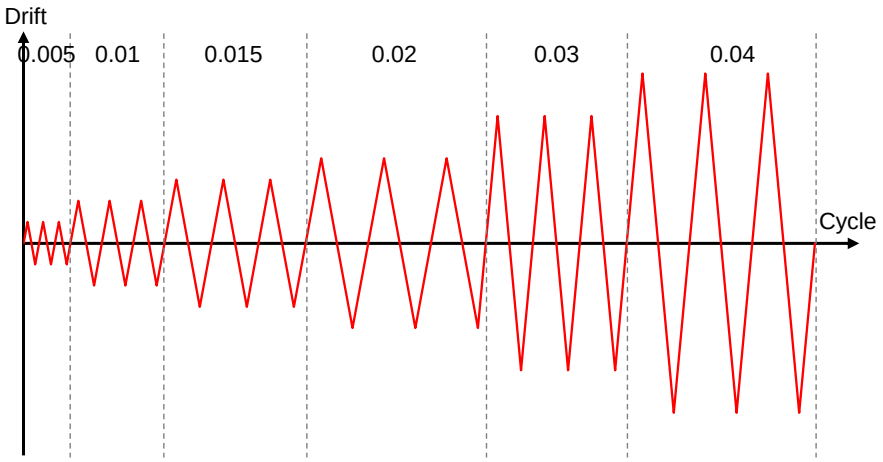

Figure 6.7 Loading history

The loading history adopted in the test was determined in reference to the loading program adopted in the full-scale test of a composite frame examined by Nakashima et al (Nakashima et al. 2007). Quasi-static cyclic loading with increasing displacement amplitudes was adopted as shown in Figure 6.7. In the figure, the displacement is expressed in terms of the overall story drift ratio (SDR hereafter), defined as the horizontal displacement at the loading point relative to the loading height

i.e., 3 m. The overall SDR of 0.005, 0.01, 0.015, 0.02, and 0.03 rad are adopted. Three cycles were repeated for each amplitude. Beyond that displacement, the cyclic loading with the drift amplitude of 0.04 rad was imposed and continued until the specimen's final failure. The failure was defined as the instant when the specimens strength was deteriorated to 80% of its maximum strength.

6.2.3 *Measurement*

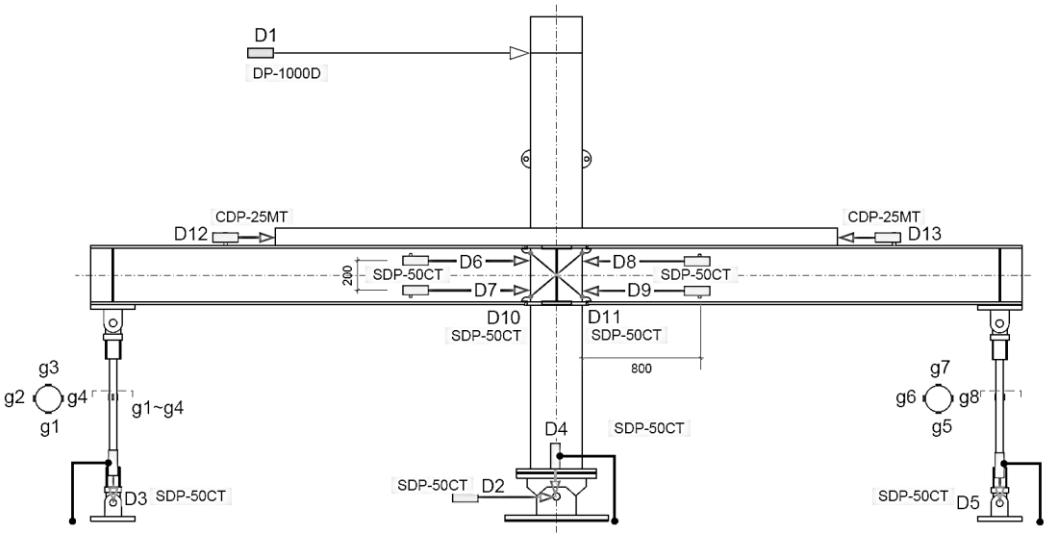

Figure 6.8 Layout of LVDT

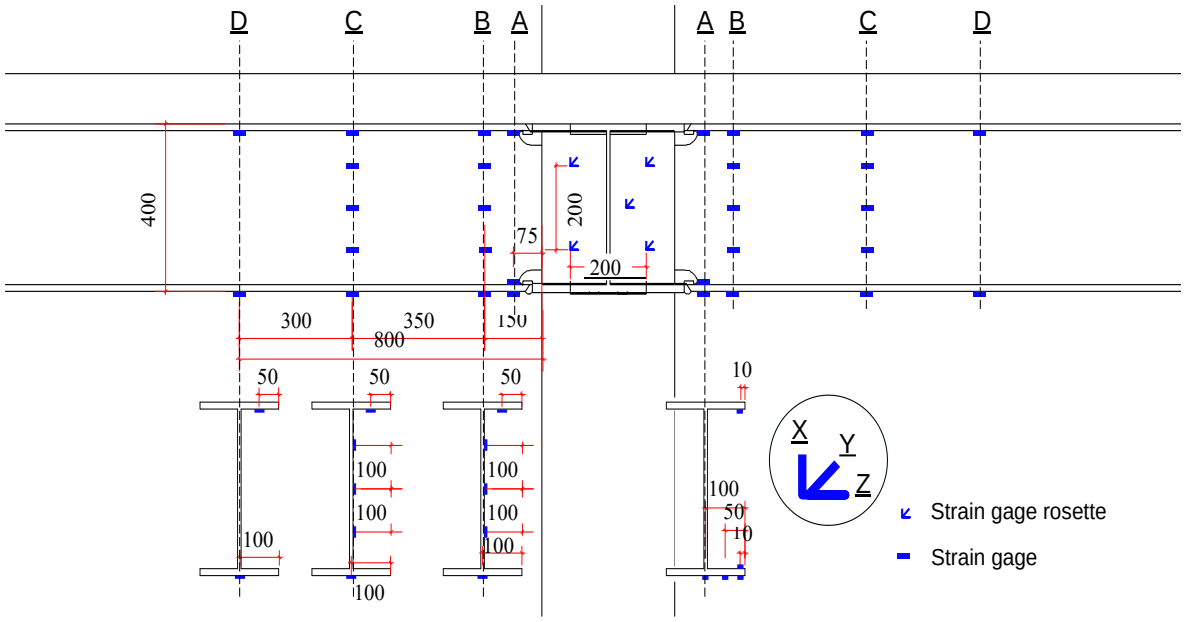

Figure 6.9 Locations of strain gauges

Figure 6.8 show the locations of displacement transducers and strain gauges. Thirteen linear variable differential transformer (LVDTs) were used to measure the displacements at various locations. In-plane displacement LVDT (D1 in Figure 6.8) measured the deflection at the top of the column. The deformation of the base beam were measured by LVDTs D2 to D5, which monitoredg

the movement of the pin of the beam struts or the column. The beam rotation relative to the column was measured using two LVTDs that are placed near the top flange and bottom flange. Two LVDTs (D10 to D11) were oriented to measure changes in displacement relative to the corner of panel zone between the two through diaphragms (Figure 6.8). Strain gauges were also attached to support struts (g1to g8 in Figure 6.8) so that the load applied to the beams can be calculated based on the strain measurement.

Figure 6.9 shows the measurement detail of strain gauges on steel beam. Strain gauges were glued at four representative beam sections. Section A is the section where the toe of the weld access hole locates, which are reported as the most likely fracture location in the past research; Section B is the section where the stud most close to column face is installed; Section C is the section closed to the section of an expected plastic hinge (one time of beam depth from column face); Section D is the section expected to remain elastic during the loading.

6.2.4 *Test Results*

General behavior and failure mode

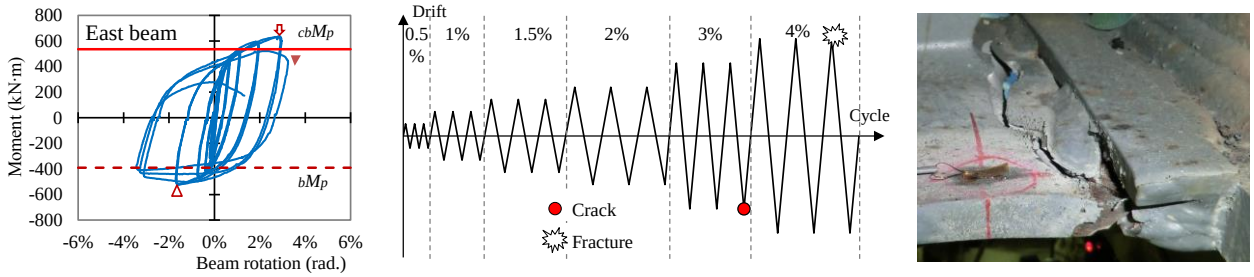

(a) (b) (c)

Figure 6.10 Test results of the original connection 'OC-1': (a) Moment and rotation relationship; (b) Loading history; (c) Fracture situation

The original connections following the post-Kobe earthquake design show good performance, the brittle fracture of the welded joints did not occur, but a mode of ductile fracture was observed. Local buckling was first observed in the lower portion of the beam web during the 3% SDR cycles.

The bending moment versus rotation relationship of east beam of specimens 'OC-1' are shown in Figure 6.10(a). The rotation represents the rotation angle between the beam end to the pin support. In Figure 6.10(a), ${}_bM_p$ is the full plastic moment of the bare beam (396 kN·m). ${}_{cb}M_p$ is the full plastic moment of the composite connection which is estimated as 0.85 times the compressive strength of the concrete ($0.85F_c$) and taking the effective width of the slab equal to the column width (350mm) (Matsumiya et al. 2005). The hysteretic behavior shows stable loops until the third cyclic of 3% SDR loading (the beam rotation of about 0.015). A crack extended from the toe of the weld access hole in the third positive cycle of the 4% SDR, with the beam rotation of 0.30 rad (Figure 6.10(b)). The crack leaded to a fracture of the bottom flange in the next positive bending and made the resistance reduced significantly. Figure 6.10(c) shows a close-up of the fracture. Most the fracture surface was in the base metal of the flange.

Damage pattern

Figure 6.11 shows that damage pattern of the composite connection after the test. Within the zone of about one time the beam depth (D_b), the bottom flange and web suffered significant buckling as shown in Figure 6.11(a). As for the RC slab, the portion around the column severely cracked and crushed in the vicinity of the column face as shown in Figure 6.11(b); and the most dominant damage was the fracture at the bottom flange as shown in Figure 6.11(c), which made the significant reduction on the connection's resistance.

(a)

(b)

(c)

Figure 6.11 Damage pattern of composite connection: (a) Bottom flange buckling and web buckling; (b) RC slab crack and crush; (c) Bottom flange fracture

6.3 Repair scheme and design

6.3.1 *Determination of stud number, repair steel plate, and steel rebar*

The sketch of the rehabilitated connection was shown in Figure 6.3. Widened steel plates are used to replace the bottom flange, and SFRCC slab was used to replace the damaged concrete floor slab portion.

Strength demand based on assumed failure mechanism

As shown in Figure 6.12, a plastic hinge is assumed to be located at the end of the steel plate and SFRCC slab. The moment at the column face, determined by projecting the moment capacity ${}_bM_{pr}$ at the plastic hinge section, is

$$ {}_bM_{pr} = \beta\ {}_bM_p = 1.2 \times 396 = 475\ \text{kN} \cdot \text{m} \tag{6.1} $$

The coefficient β accounts for strain hardening (FEMA-350 2000), $\beta = (\sigma_y + \sigma_u)/(2\sigma_y)$.

Based on the moment relationship, when the L_s is equal to the beam depth, the strength demands

of the critical section at column face M_{dem} is

$$M_{dem} = \frac{L_b - D_c/2}{L_b - D_c/2 - L_s} \, {}_bM_{pr} = 553 \text{ kN} \cdot \text{m} = 1.4 \, {}_bM_p \tag{6.2}$$

Where, L_b is the distance from column face to the point of inflection; D_c is the depth of the square tube column; L_s is the distance from column face to the edge where the SFRCC slab terminated. In the practical rehabilitation, the length of L_s should be determined according to the actual damage pattern of the connection.

The moment demand M_{dem} is 1.4 times of the full plastic moment capacity bare steel ${}_bM_p$. Therefore, the moment resistance of the composite beam ${}_{cb}M_p$ should be designed to larger enough than moment demand M_{dem}.

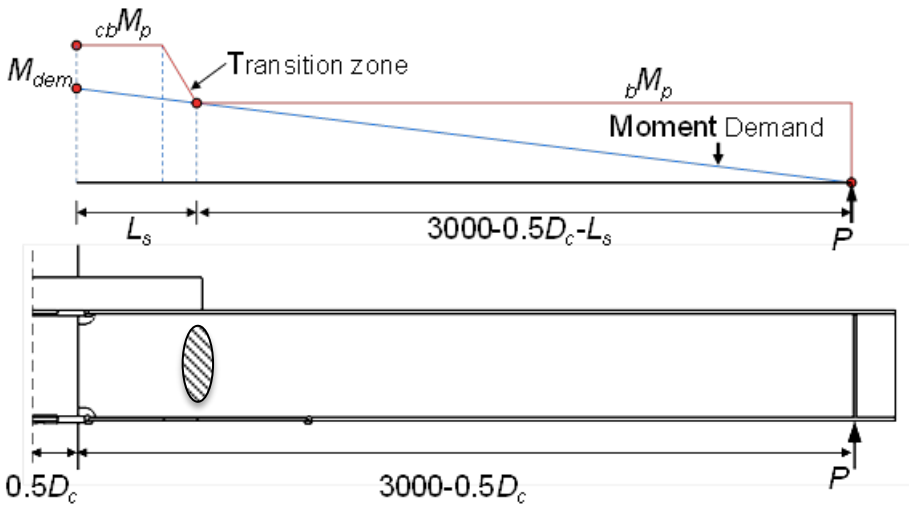

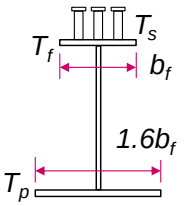

Figure 6.12 Moment schematic

Determination of the repairing steel plate

The composite beam section with bottom flange replaced by widened steel plate and SFRCC slab connecting to the top flange through headed studs.

The same thickness to the original bottom flange was adopted for the repairing steel plate. Therefor, the design parameter is the width of the steel plate b_s.

The size of the repair steel plate was determined by the force equilibrium between the tensile yield strength of the steel plate T_p and the sum of the tensile yield strength of the top flange T_f and the shear transferred by stud clusters T_s.

$$T_p = T_s + T_f \tag{6.3}$$

$$_{cb}M_p = T_p \cdot D \tag{6.4}$$

In the preliminary design, the b_s is designed to be 1.6 time of the width of original bottom flange

to achieve a moment resistance larger than the moment demand which is about 1.4 ${}_bM_p$.

$$T_p = 1.6\ T_f \tag{6.5}$$

Where, T_p is the tensile yield strength of the repairing steel plate; T_f is the tensile yield strength of the original bottom flange; and D is the depth of the steel beam.

Determination of the headed studs

After the determination of the repairing steel flange to replace the damaged bottom flange, the SFRCC slab and headed studs on the top flange should be properly designed to ensure the moment capacity of the composite beam section. The shear force achieved by the headed stud on the top flange, which is the counterpart of the difference of tensile strength between the top flange and the widened steel plate. The headed stud is determined by the following equation.

$$n \cdot q_s = T_s \tag{6.6}$$

Where, q_s is the per stud strength calculated according to the AIJ design code (Architectural Institute of Japan 2001); n is the stud number in each side of SPRCC slab; T_s is the design force acting on SFRCC slab and transferred through headed stud cluster.

6.3.2 *Design of the SFRCC slab*

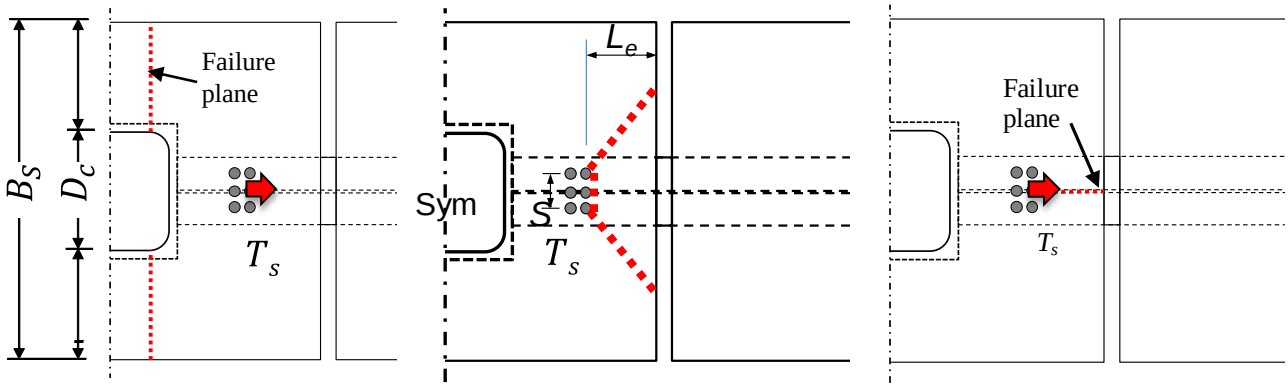

(a) (b) (c)

Figure 6.13 Failure modes of slab: (a) Tensile failure; (b) Breakout failure; (c) Split failure

The SFRCC slab without steel reinforcement was designed to sustain the unbalance force of the tensile yield strength of the widened bottom steel plate and top flange.

Three failure modes were assumed for the SFRCC slab and under negative bending, as illustrated in Figure 6.13. It includes the tensile failure that occurs at the section on the beam side (Figure 6.13(a)), the breakout failure that the slab block is push out by the stud cluster, and the split failure propagating from the stud cluster to slab free. The failure lines are marked by black and white dotted line as shown in Figure 6.13(a), (b) and (c), respectively. Based on these assumptions, the SFRCC

slab was designed to ensure the slab strength.

As shown in Figure 6.13(a), the tensile force transferred through the stud cluster is resisted by the normal tensile stress of the abrupt-changed section.

$$h_s \cdot (B_s - D_c) \cdot f_t \cdot \gamma > T_s \tag{6.7}$$

where

h_s = Thickness of SFRCC slab, mm.

B_s = Width of the SFRCC slab, mm.

D_c = Width of the abrupt changed SFRCC slab section at two side of column, mm.

f_t = tensile strength of SFRCC, MPa.

γ = Sectional uniformity coefficient to consider the uniform strain distribution on the critical section, here $\gamma = 0.5$ is used.

T_s = Assumed tensile force transferred through stud cluster, N.

As shown in Figure 6.13(b), the tensile force transferred through the stud cluster is resisted by the normal tensile stress within the projected area of the break out slab block. The strength of the break out failure is estimated based on the ACI 318-10 design code (ACI Committee 2008 318), the equation is given as follow,

$$h_s \cdot (3l_e + S) \cdot f_t > T_s \tag{6.8}$$

where

l_e = Distance from stud cluster to slab free edge, mm.

S = Width of the stud cluster, mm.

D_c = Width of the abrupt changed SFRCC slab section at two side of column, mm.

The split failure mode is assumed as shown in Figure 6.13(c). Strength evaluation equation proposed by Oehlers (Oehlers 1989) was adopted to estimate the resistance of the slab. The equation is given as follow,

$$\frac{0.6 b_c h_a f_t \pi}{\left(1 - \frac{d}{b_c}\right)^2} \cdot n_c > T_s \tag{6.9}$$

where

b_c = Effective bearing width of slab block, b_c=0.5 l_e , mm.

d = Diameter of headed stud, mm.

h_a = Effective height of headed stud, mm.

n_c = Number of studs along the slab width direction.

6.3.3 *Repair Scheme*

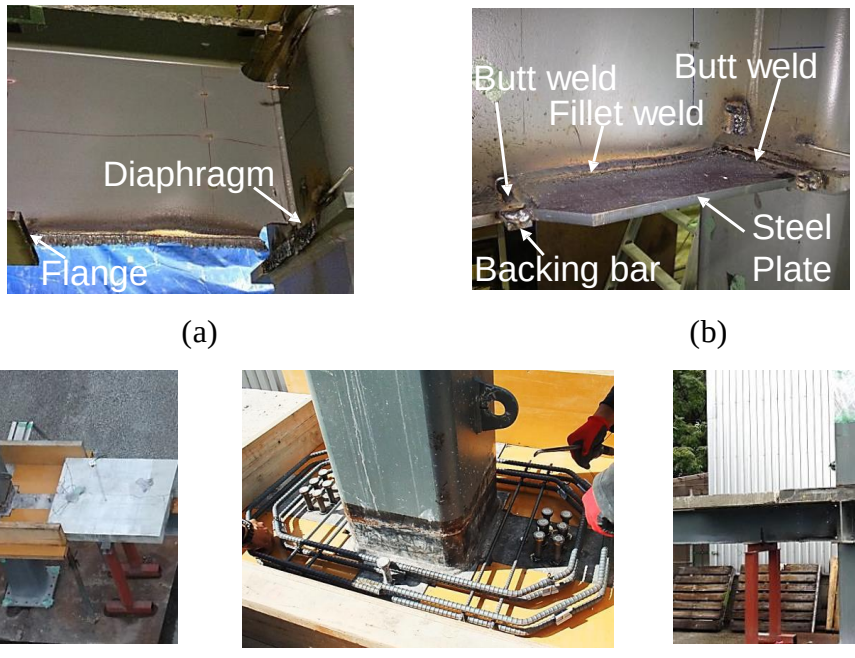

Figure 6.14 Repairing procedure: (a) Removal of damaged bottom flange by flame cut; (b) Replacement of steel plate by welding; (c) Removal of severely damaged slab portion; (d) Placing steel reinforcement and welding headed stud; (e) SFRCC slab cast

The repair consisted of the following steps, as shown in Figure 6.14: (1) First, the fractured and buckled bottom flange was removed by torch cut, and then a steel plate with a length equal to the depth of the beam was used to replace the removed bottom flange by welding to the through diaphragm, web, and bottom flange. The seriously damaged slab portion around the column was first separated from the rest of floor slab by concrete cutter, and then was broken and removed by rotary hammer, along with the reinforcement and headed stud. Rings of steel reinforcement were placed on the upper flange and around the column, and stud clusters were installed on the upper flange of each beam. Finally, SFRCC with fiber volume ratio of 6% was used to cast the floor slab. 50 mm width gaps between the SFRCC slab and rest RC floor slab were made when the SFRCC slab was cast.

6.4 Member test for the repaired connection

Two specimens ‘RC-1’ and ‘RC-2’ were tested after the repair is applied to the two damaged original connection ‘OC-1’ and ‘OC-2’. Figure 6.15 show the global dimensions of the repaired connection. Since the specimens were horizontally symmetric about the centerline of the steel tube column, the configuration of two repaired connection specimens are shown together in Figure 6.15. In Figure 6.15, the left side represents the configuration of the specimens RC-1, while the right side

showed that of the specimens RC-2. The SFRCC slab was the same for both specimens. The same slab width of 1000 mm and thickness of 120 mm used for the RC slab in the original specimens were adopted for SFRCC slab. The length of the SFRCC slab was 1250 mm, which is the sum of the column width and the 450 mm extension from the column face at the two sides. A gap of 50 mm in width was made between the SFRCC slab and remained RC slab on each beam. In practical applications, the gaps will be filled with epoxide material, in the test the gaps were remained without filling since the presence of the epoxide material was expected to having no effect on the specimen behavior.

Figure 6.16 shows the arrangement of the headed stud connector in SFRCC slab. The headed stud connectors welded on the top flange within the newly cast SFRCC slab region were removed, six supplemental studs arranged in the two rows three column pattern, were installed among the removed intrinsic studs on the top flange of each beam as shown in Figure 6.16. The center-to-center distance between the adjacent studs was 50 mm, which is the minimum spacing possible to install the studs with stud gun. The same type of stud was used for the supplemental studs and original studs. The stud arrangement was same for the two repaired connection RC-1 and RC-2.

In the proposed repair method, the SFRCC slab is cast without steel reinforcement. But in the experimental study, because the strain in SFRCC slab could not be measured directly, steel rebar was placed to serve as the strain indicator at critical locations for SFRCC slab. To verify the possibility of using SFRCC without steel reinforcement for the repair, the amount of steel reinforcement was determined as one of the parameters. In specimen RC-1, two layers of eight D16 rebar were placed around the studs cluster and column as shown in Figure 6.19. The top layer of rebar was located 46 mm below the top surface of the slab. The details of the two specimens RC-1 and RC-2 were the same except the amount of steel reinforcement in SFRCC slab. In Specimens RC-2, only the bottom layer of ring rebar was placed in the SFRCC slab.

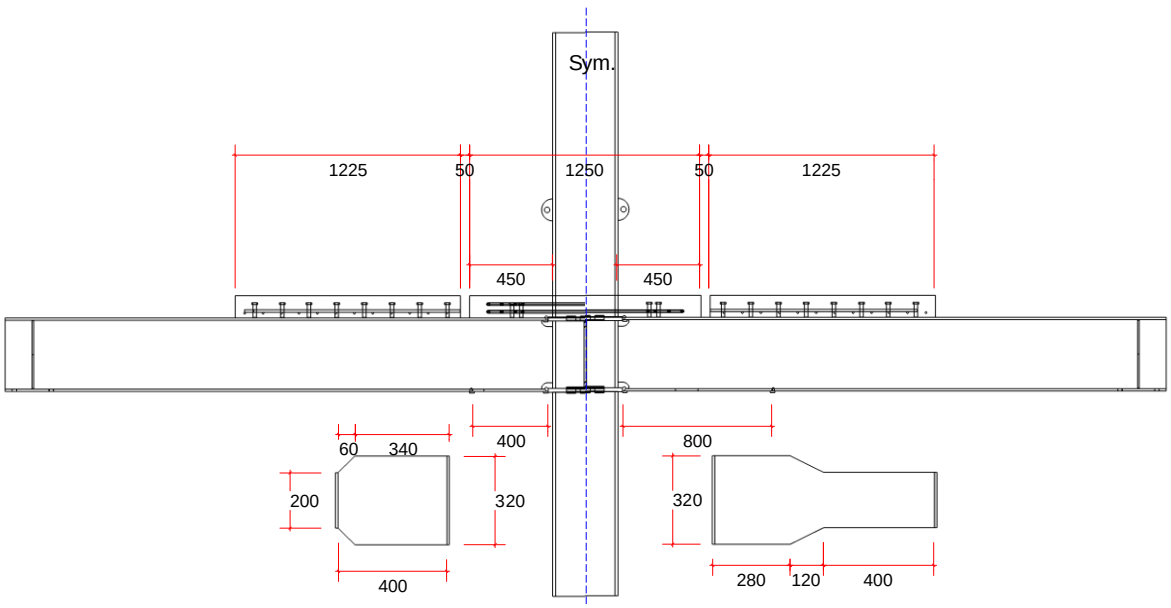

(a)

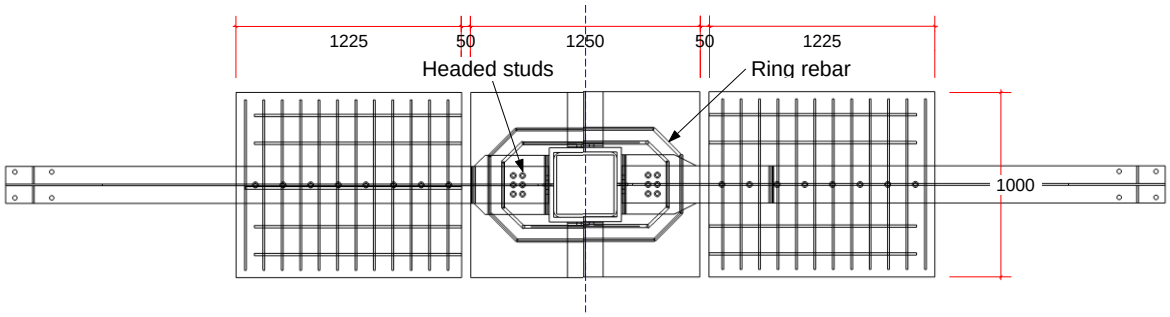

(b)

Figure 6.15 Global view of repaired connection: (a) Front view; (b) Plane view (unit: mm)

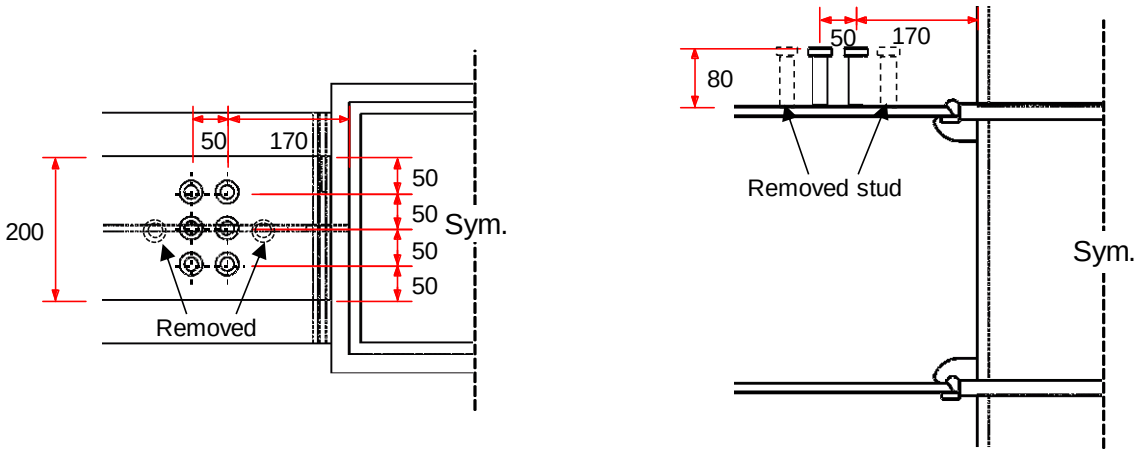

(a) (b)

Figure 6.16 Studs in SFRCC slab: (a) Plane view; (b) side elevation (unit: mm)

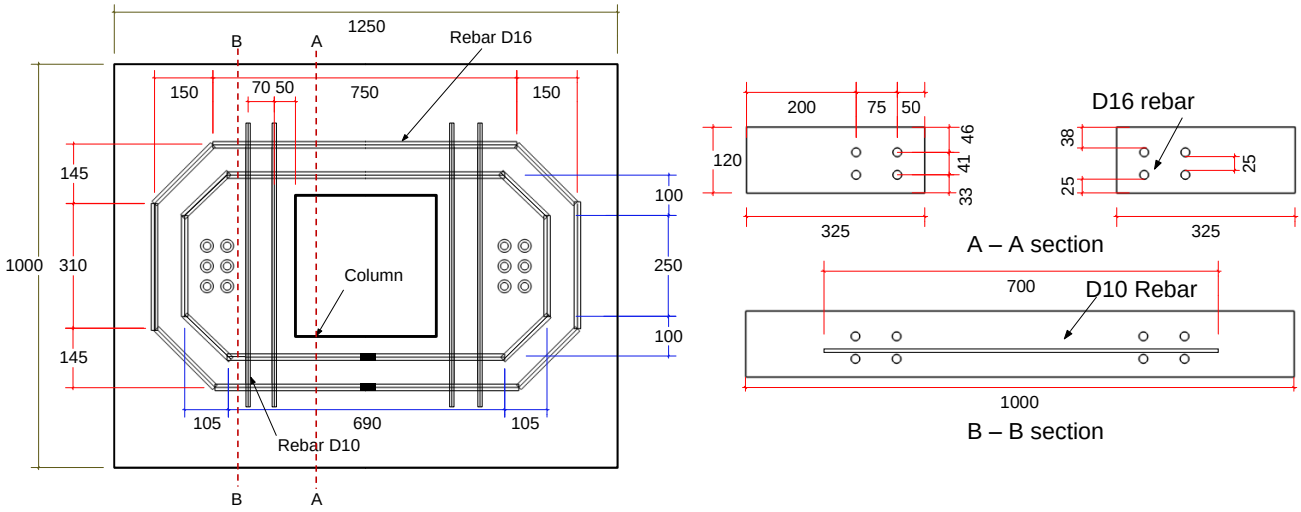

(a) (b)

Figure 6.17 Details for slab and rebar in Specimens ‘RC-1’:
(a) Plane views of SFRCC slab; (b) Section view of the SFRCC slab

The material properties of the steel and SFRCC used to repair the damaged original connections were obtained form the associated material tests and are summarized in Table 6.2. The mixture design

of SFRCC is shown in Table 6.3. Densit cement was used to mix the SFRCC paste with the water ratio of 17.5% (in weight) and the fiber ratio was 6% in volume.

Table 6.2 Material properties (Steel and SFRCC)

	Yield strength σ_y (MPa)	Tensile strength σ_u (MPa)
Steel plate (SS400)	315	459
Rebar (SD295)	375	512

	Compressive strength f_c' (MPa)	Split strength f_{sp}' (MPa)
SFRCC	112.6	15.2

Table 6.3 Compositions for 1 m^3 SFRCC (unit: kg)

Densit cement	Fine aggregate	Steel fiber	Water
871	1179	444	152

6.4.1 *Test setup, loading history and measurement*

The test setup (Figure 6.6) and loading history (Figure 6.7) adopted in the Phase one test were used for the test of the repaired connection.

The specimen was equipped with displacement transducers and strain gauges to measure deformation contributions of different parts and measure strain distributions, respectively. As shown in Figure 6.18, strain gauge were placed on the flange and web to monitor the bending strain along the length of the beam, and rosette gauges were placed to monitor the strains in the panel zone. A rosette gauge was glued to the bottom of steel plane at the location near the column face.

The measured strain position on the beam was shown in Figure 6.18. Five sections, A, B, C, D and E that are respectively 75, 150, 270, 500 and 800 mm in distance measured from the column face were the positions for strain measurement. In particular, Section A was located in line of the toe of weld access hole; Section B and section C were the two section in front of and behind the stud cluster in SFRCC slab; section D was located at the gap between the SFRCC slab and remain RC slab; Section E was located twice the column width away from the column face, representing the original beam section.

A typical strain gauge layout on rebars is shown in Figure 6.19. The rebars of the SFRCC slab were instrumented to investigate the strain distribution in the SFRCC slab and the contribution of rebars. A grid was drawn on the slab and the cracks were marked for various peak displacements. At each level of the peak displacement, these cracks were used as a qualitative measure of the level of damage.

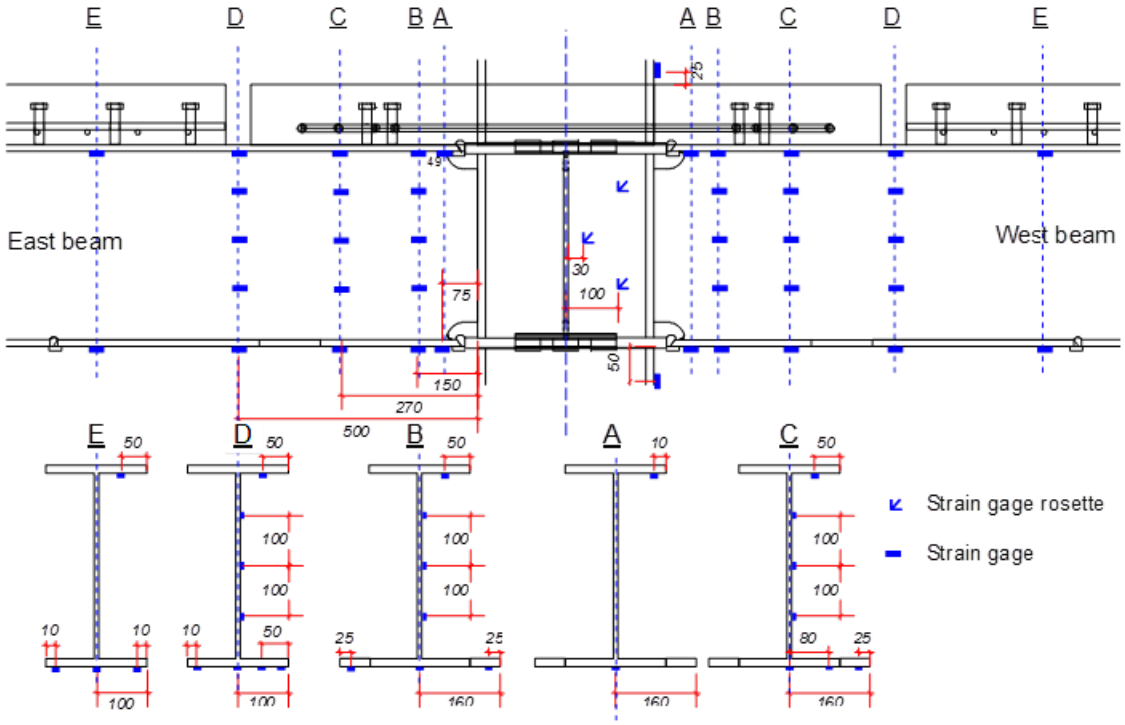

Figure 6.18 Measurement- locations of strain gauges

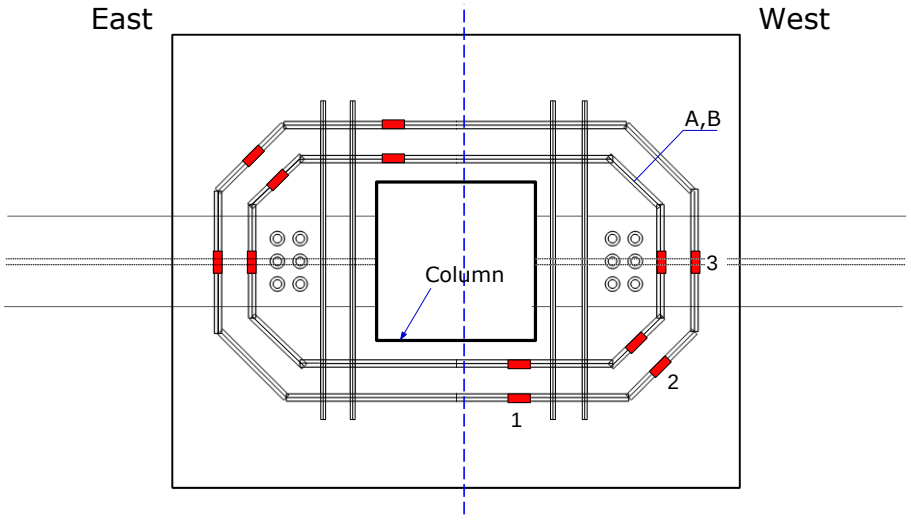

Figure 6.19 Layout of strain gauge on rebars (unit:mm)

6.5 Test results and discussions

6.5.1 *The repair performance*

Strength and stiffness

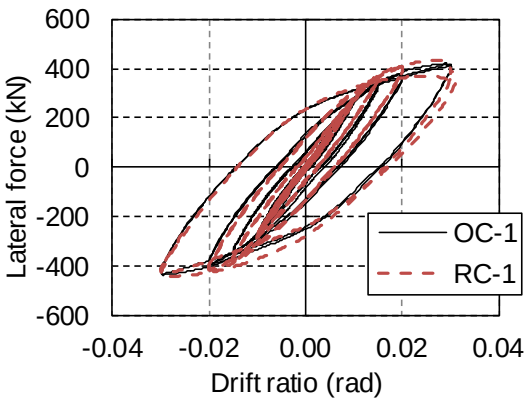

(a) Specimens OC-1 and RC-1

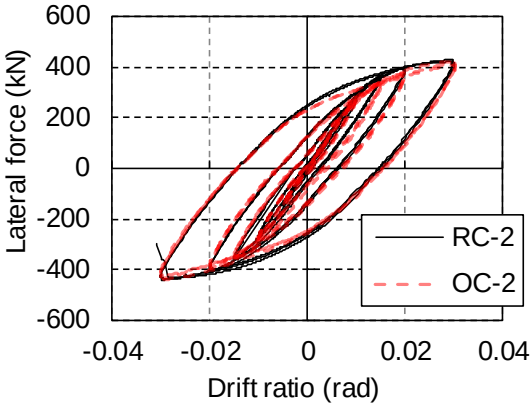

(b) Specimens OC-2 and RC-2

Figure 6.20 Comparison on load versus story drift rotation curves:

The column tip load versus SDR (story drift ratio) curves of the two pairs of original specimen and repaired specimen are compared in Figure 6.20. The SDR (story drift ratio) equals the lateral displacement at the loading point divided by the column height, 3000 mm. Both connections showed almost the same strength as well as the hysteretic behavior with the original connections till the SDR of 3%.

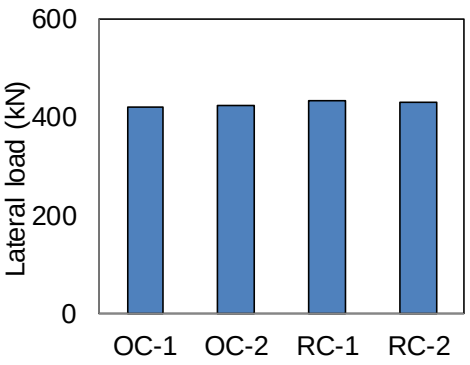

(a)

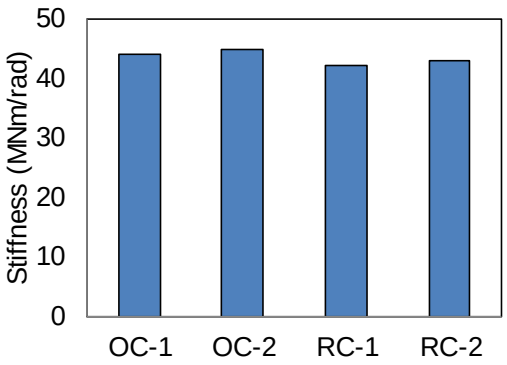

(b)

Figure 6.21 Comparison on strength and elastic stiffness: (a) Maximum moment strength; (b) Elastic stiffness

Figure 6.21 shows the maximum lateral load and elastic stiffness of the tested specimens. The elastic stiffness here is defined based on the lateral load versus SDR relationship curves. The elastic stiffness of the specimen is defined as the secant stiffness between the points at ±0.5% rad of the load versus story drift curves. From Figure 6.21, the repaired connection and the original connections showed almost the same elastic stiffness with the difference of 5%.

This indicates that the strength as well as the elastic stiffness of the connections can be restored to the original state by the repair with the proposed method.

Table 6.4 Test results

Spec.	M_{max}^{+} (kN·m)	M_{max}^{-} (kN·m)	K_c (kN/m)	Failure mode
OC-1	630.5	-654.3	43942.5	Bottom flange fracture
OC-2	633.3	-656.7	44762.2	Bottom flange fracture
RC-1	648.8	-660.3	42207.7	Beam yielded fracture
RC-2	644.4	-660.2	42929.1	Beam yielded fracture

Damage states and crack patterns

Figure 6.22 and Figure 6.23 show the test observations of the specimens at the instant when the SDR reach 3%. Figure 6.22(a) shows a close-up of the damages of the original connection. Local buckling occurred at the web and bottom flange. Cracks started from the toe of weld access hole and the welding boundary between the through diaphragm and flange mental. The initial ductile crack was located in the area between the weld fusion zone on the outside flange surface and the end of the access hole cut on the inside flange surface, which was similar to the damage which occurred observed in the Kobe earthquake. For the repaired connection, the plastic deformation was concentrated at the intentionally weakened bare steel section with the gap between SFRCC slab and remained RC slab. When the SDR reach 3%, as shown in Figure 6.22(b), the top flange yielded significantly and buckled at the bare steel section having the gap. An expected failure mechanism was achieved.

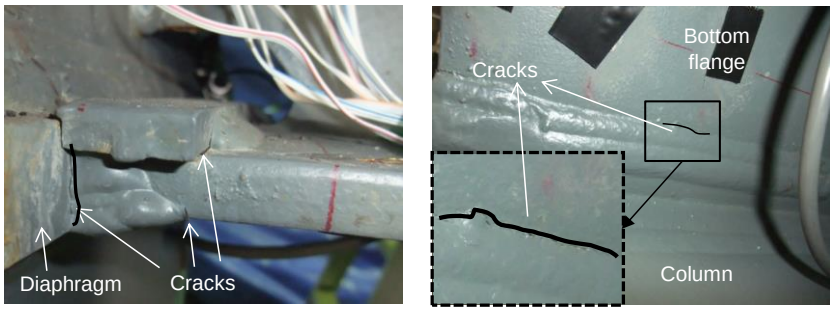

(a)

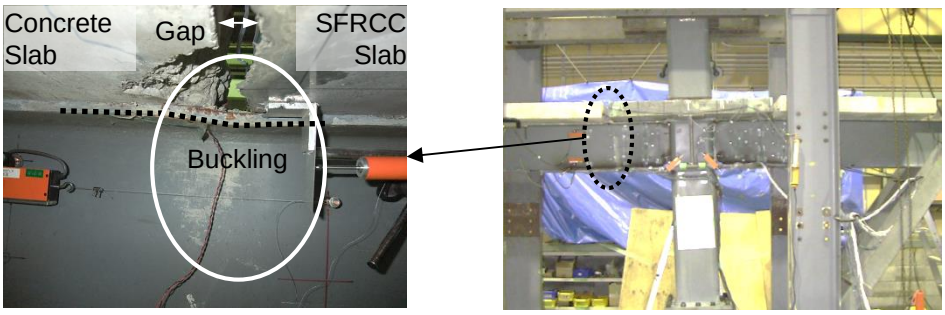

(b)

Figure 6.22 Test observation at 3% rad story drift: (a) OC-1; (b) RC-1.

Figure 6.23 shows comparison on the crack pattern between the original and repaired connections. For the original connection, the first crack in the slab initiated at the corner of the steel tube column,

extending transversely across the slab by the 0.5% SDR load cycle. In the 1% SDR load cycle, transverse cracks were formed at the minimum width section of slab (The section which the column passes through). In addition, a crack developed along the beam centerline (at the shear studs) from the column face and running half the length of the slab in the 1.5% SDR load cycle. This longitudinal crack extended to nearly the length of the slab in the 2% SDR load cycle. In the 3% SDR load cycle, the width of the main cracks running from the column corner to the edge of slab exceeded 5mm on the tension side. While at the compression side, slight crushing initiated at the column corner in the 1.5% SDR load cycle, and the crushing became substantially server at in the 3% SDR load cycle.

For the repaired connection, no cracks occurred in the load cycle of 0.5% and 1% SDR. The first crack was initiated from the column corner near the side of slab in tension (the side of beam under negative bending). Up to the load cycle of 3% SDR, cracks were developed as shown in Figure 6.23(c) and (d), but the maximum crack width was no greater than 0.2 mm. The crack distribution indicates that the most strained part on the slab is the section where the cross-section abruptly changed. Since the developed cracks on SFRCC slab in smaller than the allowable crack widths, the SFRCC slab can be considered almost undamaged.

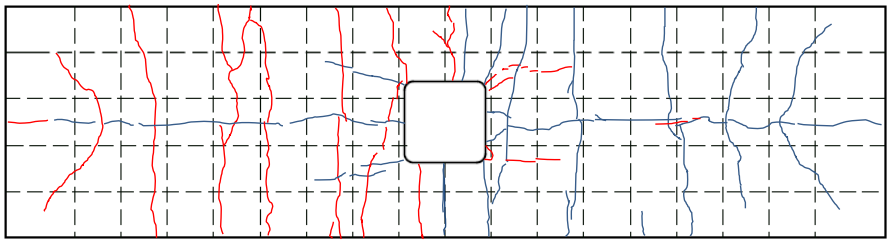

(a)

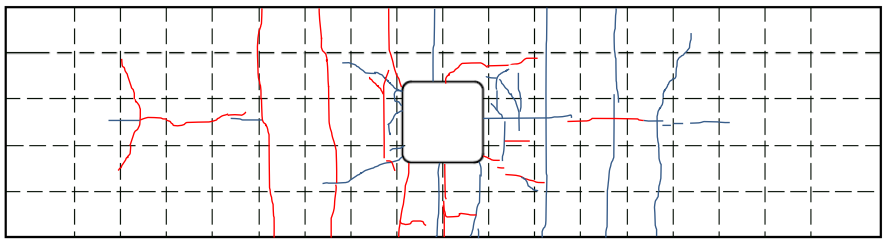

(b)

(c) (d)

Figure 6.23 Cracks of slab: (a) OC-1; (b) OC-2; (c) RC-1; (d) RC-2

Strain distribution

Figure 6.24 shows the strain values at different location along the beam length (see Figure 6.18)

for the bottom flange at the positive peak of the first cycle in each drift angle. At the beam section located of a 500 mm distance from the column face, which was the bare steel section with a floor slab gap on the upper flange, the strain was obviously larger than that in other locations after 1% SDR, as shown in Figure 6.24(a) and (b). This indicates that the plastic zone was formed at this intentionally weakened section instead of highly concentrated plastic zone near the welded access hold. When the specimens subjected to 3% SDR, strains at the location near the weld access hole increased dramatically, and several cracks were observed at the welding boundary between the bottom flange and through diaphragm of the column.

Figure 6.24 summarizes the strain of the centerline of bottom flange at each critical section as defined in Figure 6.18. The strain at the bottom flange of Section D on the east beam of the repaired connection exceeded 1.2% when subjected to the 2% SDR. The strain at the intentionally weakened bare steel section was significantly larger than those in other sections after the 1.5% drift angle.

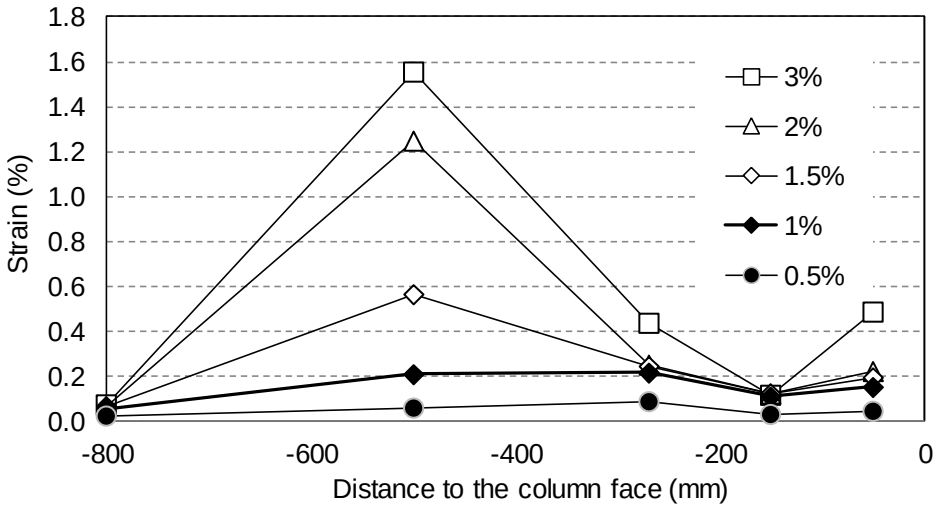

(a)

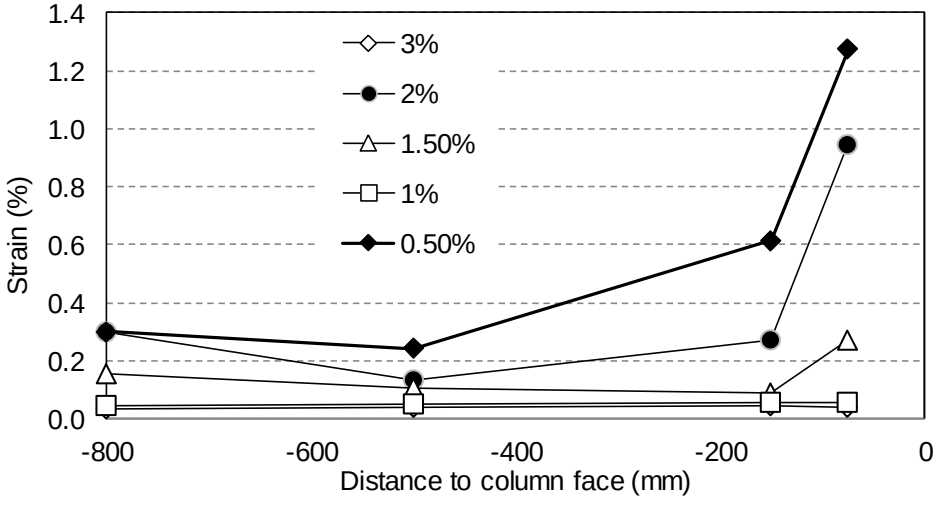

(b)

Figure 6.24 Strain at bottom flange: (a) RC-2; (b) OC-2

Although the SFRCC floor slab provided a strengthened zone in the vicinity of the connection that result in a lower level of stress/strain on the weld as shown in Figure 6.24, the proposed

connection scheme exhibited poor performance. As mentioned in the tests results, good workmanship and sound welding quality are required provide a reliable welded connection.

6.5.2 *Sectional bending stiffness*

Representative section were defined in Figure 6.18 and reviewed as shown in Figure 6.25 along with the strain gauge location. To investigate the bending performance of the beam section, moment versus curvature relationships of Section D, Section C, and Section B, was examined. The curvature was obtained from the gross sectional average strain of the top flange and bottom flange, while the moment was calculated by the force from the side-strut at the beam end times the distance from the section to the beam end. Based on the dimensions and sectional properties, the theoretical bending stiffness (namely the elastic moment of inertia) of the bare steel beam section and composite beam section were calculated. The bending directions (positive and negative) were defined as shown in Figure 6.26, positive bending was defined when the bottom flange sustains tensile force.

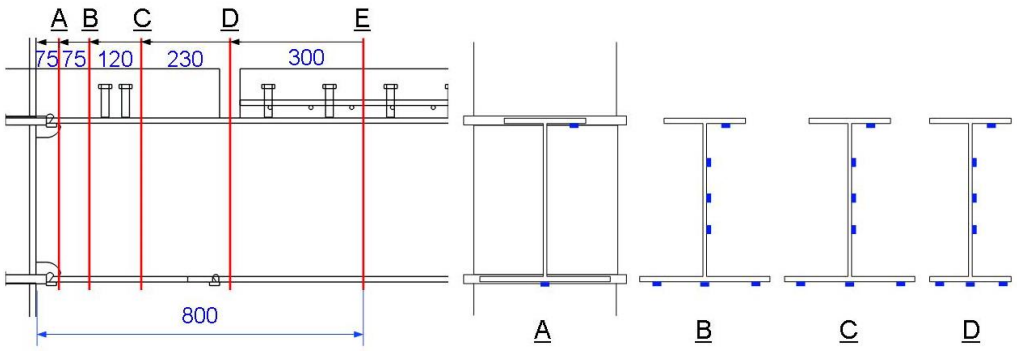

Figure 6.25 Locations of strain gauges and beam sections

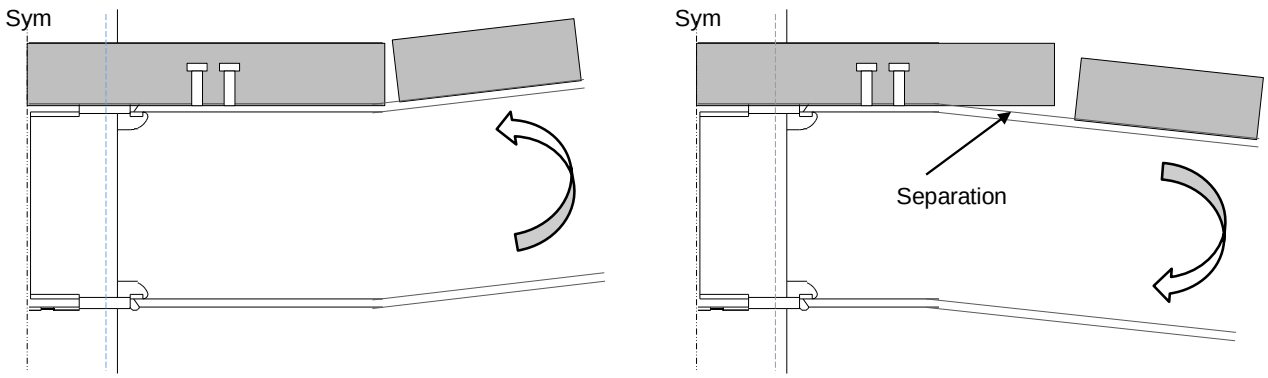

(a) (b)

Figure 6.26 Definition of loading direction: (a) Positive bending; (b) Negative bending

The skeleton curves of a curvature constructed from the moment versus curvature relationships at each section under positive and negative bending are shown in Figure 6.27 and compared to the corresponding calculated bending stiffness.

Section D was the bare steel section where the intentionally cut slab gap was located. The bending stiffness of Section D agree well with the calculated bending stiffness of the bare steel

section in both positive and negative bending as shown in Figure 6.27(a) and (b).

For Section C, in which the SFRCC slab extended from the stud cluster only overlays on steel beam without the headed stud connection. It can be seen from Figure 6.27(c) and (d) that, compared to the bending stiffness of the bare steel section, Section C showed about 10% larger bending stiffness under positive bending and developed similar initial flexural bending stiffness under negative bending. This indicated that the presence of SFRCC slab only affects the flexural stiffness under positive bending and the influence is not significant. Therefore, both the positive and negative bending stiffness of section C can be evaluated as the bare steel beam section.

Section B located between the stud cluster and the column face and was regarded as the composite bema section consisting of the steel beam section and SFRCC slab. When the composite beam subjected to positive bending, the section was compressed by the force transferred from the stud cluster. The compression force acting on the slab section contributed to the enhancement of the positive bending stiffness. Section B was defined as the partial composite beam section, its flexural stiffness is between that of fully composite beam section and that of bare steel section. According to AISC 360-10 (ANSI/AISC 360 2010), the elastic moment of inertia (initial bending stiffness) of partially composite beam can be approximated by Equation.(6.10)

$$I_{equiv} = I_s + \sqrt{(\Sigma Q_n / C_f)}(I_{tr} - I_s) \tag{6.10}$$

where

I_s = moment of inertia for the structural steel section, mm^4.

I_{tr} = moment of inertia for the fully composite uncracked transformed section, mm^4.

ΣQ_n = strength of steel anchors (headed stud) between the point of maximum positive moment and the point of zero moment to either side, N.

C_f = compression force in slab for fully composite beam; smaller of $A_s F_y$ and $0.85 A_c f_c'$, N.

A_c = area of concrete slab within the effective width, mm^2. Here, the effective width is determined as width of column, 350 mm.

The moment versus curvature relationship curve of Section B, and the lines representing the estimated bending stiffness of partially composite section and bare steel section were shown in Figure 6.27(e) and (f). Under positive bending, Section B have substantially larger flexural stiffness than that of bare steel section and had good agreement with the estimated initial stiffness of composite section. This indicates that the positive bending stiffness of the Section B can be approximated by Equation.(6.10). Under negative bending, the bending stiffness was about 15% larger than that of the bare steel section at negative bending but smaller than that of the composite beam. This is due to the longer deformation range when the SFRCC slab sustains tensile force under negative bending, it could not make the contribution as it did under positive bending.

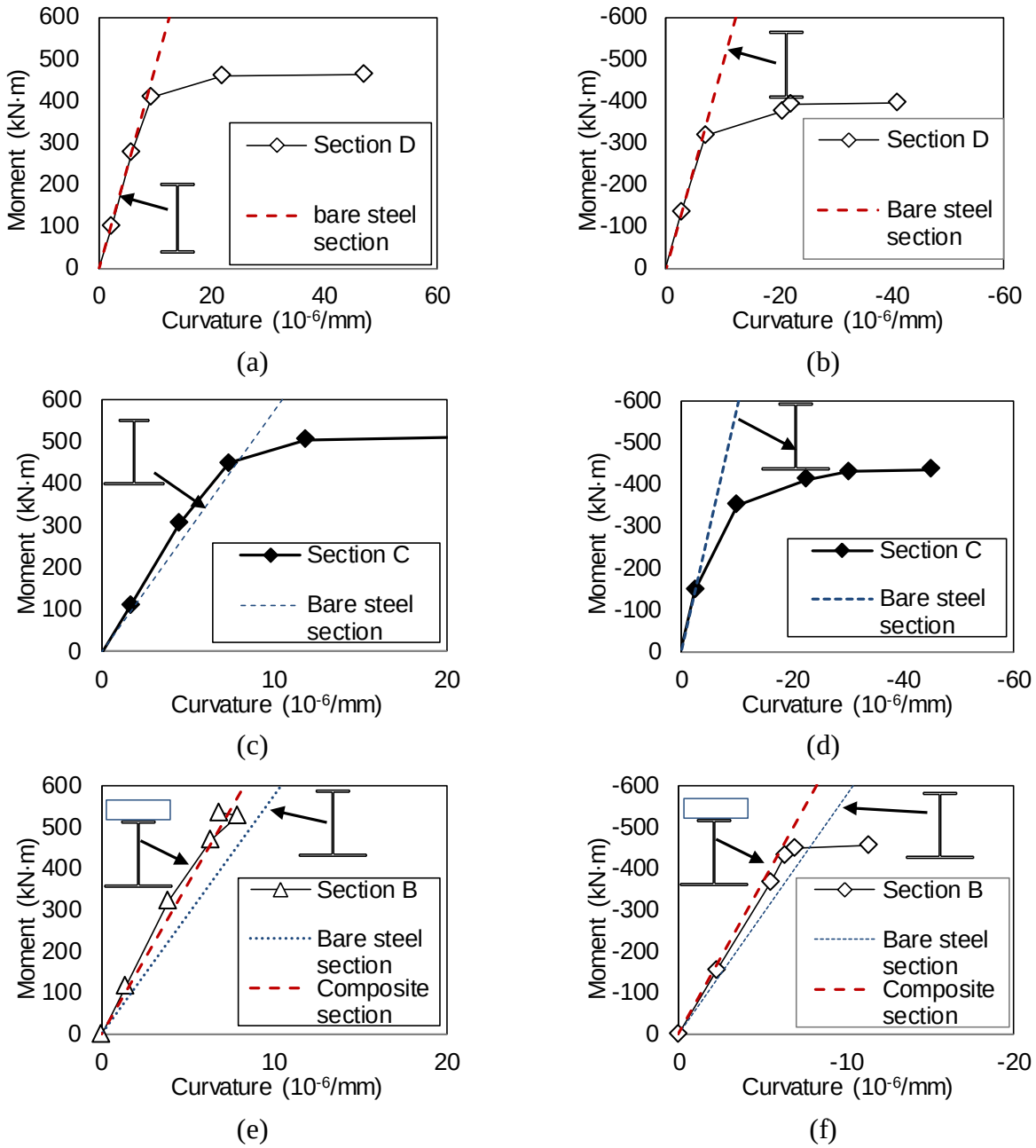

Figure 6.27 Moment-curvature relationship of: (a) Section D, positive bending; (b) Section D, negative bending; (c) Section C, positive bending; (d) Section C, negative bending; (e) Section B, positive bending; (f) Section B, negative bending

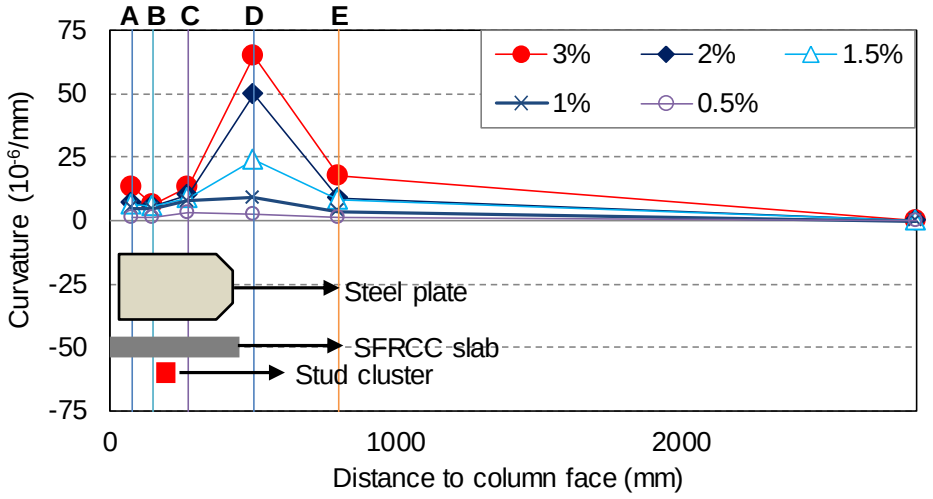

(a)

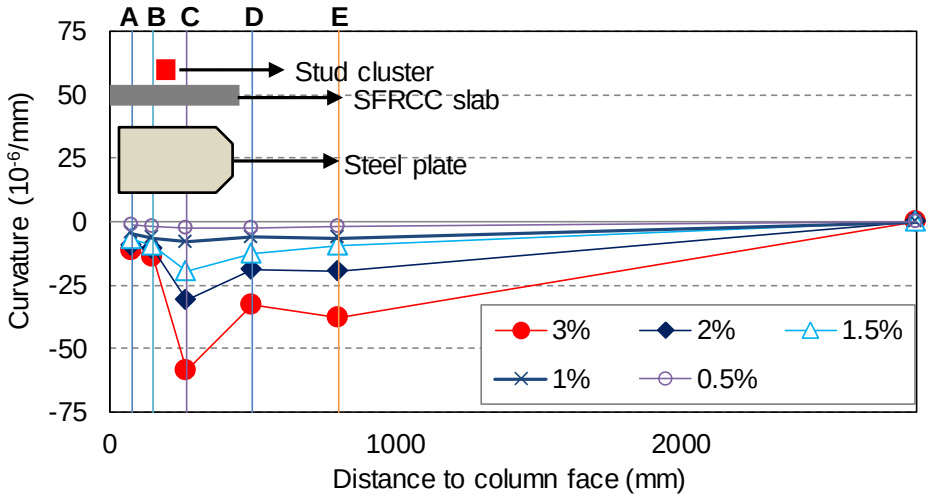

(b)

Figure 6.28 Distribution of curvature along beam length: (a) Positive bending; (b) Negative bending

Figure 6.28 shows the distributions of curvatures in the beam's longitudinal direction at each peak of the drift angle. Figure 6.28(a) shows the distribution of curvature when the beam was subjected to positive bending (bottom flange in tensile), it can be seen that Section D, which was the bare steel section located at the gap between SFRCC slab and RC slab, developed substantially larger curvatures than other sections. This indicates that when subjected to positive bending, the plastic zone was concentrated at the bare steel section with a gap; while under negative bending as shown in Figure 6.28(b), the largest curvature occurred, rather than at the bare steel section (Section D), but at the Section C, the section located at the external edge of the stud cluster.

6.5.3 *Force acting on slab*

During the test, it was difficult to directly measure how much force acting on the SFRCC slab sections. To quantify the section force on the SFRCC slab during the load, the measured strains at Section B, C and D (located 150, 270, and 500 mm away from the column face as shown in Figure 6.18) were used to evaluate the force acting at the slab section. Here, the distribution of the moment

resistance by the beam flange, the beam web, and the floor slab with respect to the total moment resistance were considered. Figure 6.29 shows the method to estimate the strength from the strain distribution at the section. By linearly connecting the strain values at different positions along the depth of the section, the location of the neutral axial was determined. In this test, the location was confirmed to be located in the web for all specimens. Then, the section force ${}_sF_1$ to ${}_sF_7$ were obtained as the product of the sectional area between the two strains, the average strain, and Young's modulus. Thus, the force acting at the slab section and the entire section moment can be determined by the following equations.

$$ {}_cF = \sum_{j=1}^{7} {}_sF_j \tag{6.11} $$

$$ {}_bM = \sum_{j=1}^{7} {}_sF_j \cdot d_j + {}_cd \cdot {}_cF \tag{6.12} $$

The beam section moment can also be obtained from the reaction force measured at the pin support at the end of the beam. Figure 6.30 shows the correlation between the section moment obtained from the measured beam section strains and that measured from the reaction force at section B. The difference between the two values become larger when the connection sustained deformation larger than 2% SDR (with the maximum error of about 20%). For the 1.5 % SDR and smaller deformation, the plots gathered along the 45 degree line (with the error not greater than 10 %). Thus, the estimate method was considered reasonable when loading was up to the 1.5% SDR.

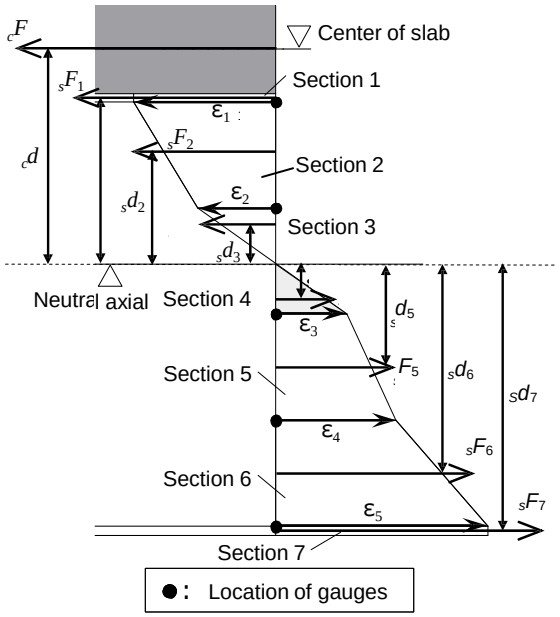

Figure 6.29 Section moment measure scheme.

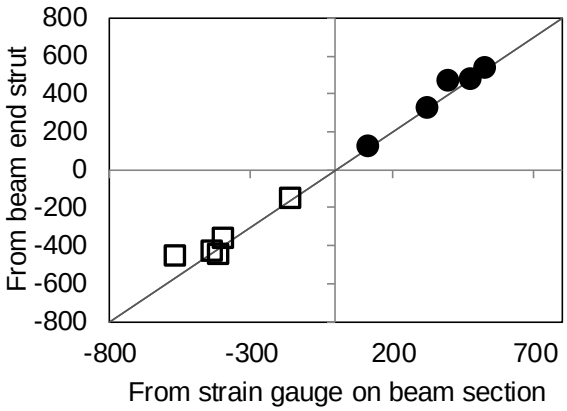

Figure 6.30 Section moment calculation at Section B

Using the method described above, the section force acting on Section B (see Figure 6.25) at the first cycle of each loading amplitude is obtained as shown in Figure 6.31. As described in 6.3.2, the design maximum force acting on the slab is the difference between the tensile yield strength of widened steel plate and the top flange. The design maximum force was shown together with the teted section force. Both the compression force induced under positive bending and the tensile force induced under negative bending reached their maximum value at the 1.5% SDR, it is corresponded to the yielding of the beam. It is also found that, when under positive bending the force acting on the maximum tensile force is about 60% of the maximum compression strength, it is because under negative bending the SFRCC slab has larger deform range.

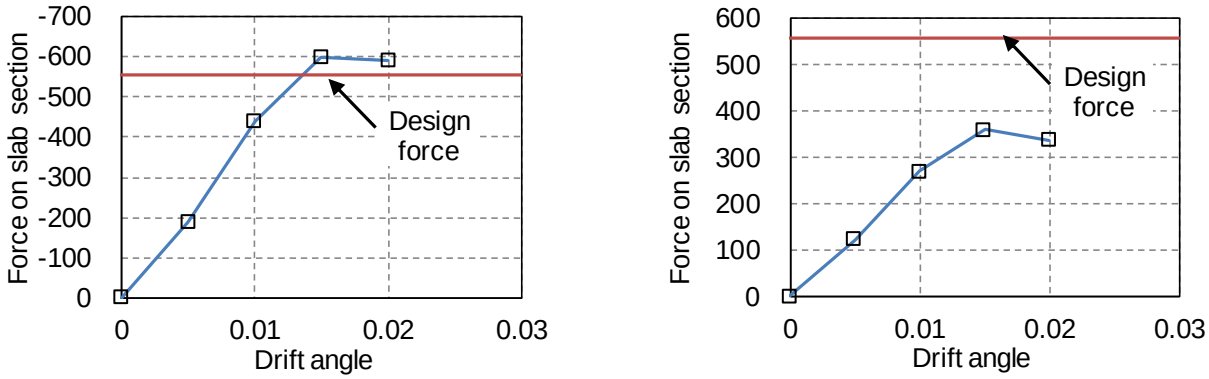

Figure 6.31 Force acting on SFRCC slab section B of specimen RC-1: (a) Compressive force under positive bending; (b) Tensile force under negative bending

6.5.4 *Effect of rebars*

The distribution of strains along one rebar and the difference in strain between the rebars of Specimens RC-1 and RC-2 are investigated. As described previously, the rebars of the SFRCC slab were instrumented with strain gauges as illustrated in Figure 6.19. Strains were measured at six locations on the rebars. The strain gauges were oriented so that strains were measured along the axis of the rebars. The nomenclature used to identify the strain gauges was based on the location of the

rebars. Two rebar rings in each layer were identified using the labels of "A and B" from the inner to outer. The three location on the rebars were classified using label of "1, 2, and 3" as shown in Figure 6.19. Specimen RC-1 had two layers of ring rebars. The strain gauges on the top layer of rebars were classified using the label of "U". In addition, each strain gauge label was classified based on its location on the specimen relative to the laboratory (East and West). For example, the strain gauges of "UAW1" was the strain gauge installed at Location 1 of the inner rebars of the upper layer on the west side.

The measured rebar strains at the location 1 to 3 (See Figure 6.19(b)) on the west side of Specimens RC-1 are plotted in Figure 6.32 for each positive load peak. The measured rebar strain was positive during the loading, which indicates that the rebars took the tensile force during the loading. Assuming that the steel rebars are compatible in strain with the surrounding SFRCC, the measured strain on rebars served as an indicator of the strain level of the surrounding SFRCC. Figure 6.32(a) shows comparison of strains on four rebar rings measured at Location 1 (See Figure 6.19(b)). It is notable the two outer rebars ('BW1' and 'UBW1') exhibited substantially small strains than those of the two inner rebar (('AW1' and 'UAW1'). In addition, the inner rebar of the upper layer (Labeled 'UAW1') showed the largest strain. The rebar strains measured at the Location 3 are compared in Figure 6.32(c). It was found that the rebar strains in the upper layer and lower layer were similar to each other when they had the same distance from the stud cluster; while the rebar strains on the outer rebar rings is larger than those on the inner rebar rings. The curve named '*BW3' is the predicted strain value at 'BW3' based on the measured strain at 'AW3'. The prediction was made by the assumption that transverse tensile strain linearly distributes from the root of stud cluster to edge of the SFRCC slab along the beam length. Comparing the predicted '*BW3' to the measured 'BW3', it was found that before the SDR of 1%, the two strain value are similar to each other, i.e., the inner rebar strain and outer rebar strain showed linear distribution. After the SDR of 1%, due to the stress redistribution caused by occurrence of micro cracks in the SFRCC slab, the linear strain distribution was no longer valid and the region close to the stud cluster became more stressed.

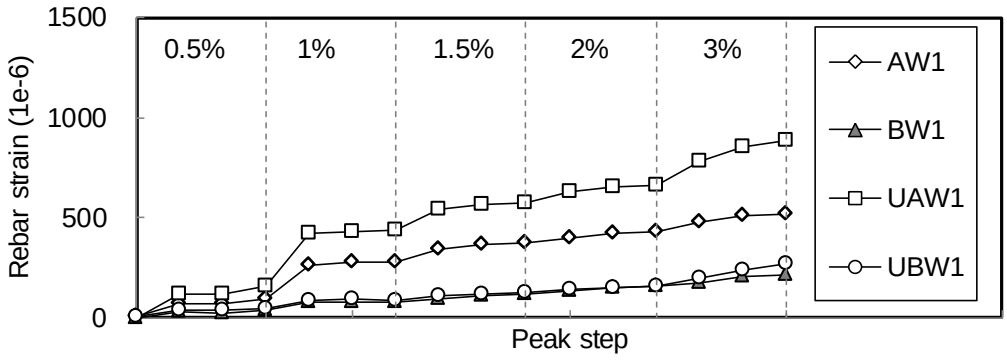

(a)

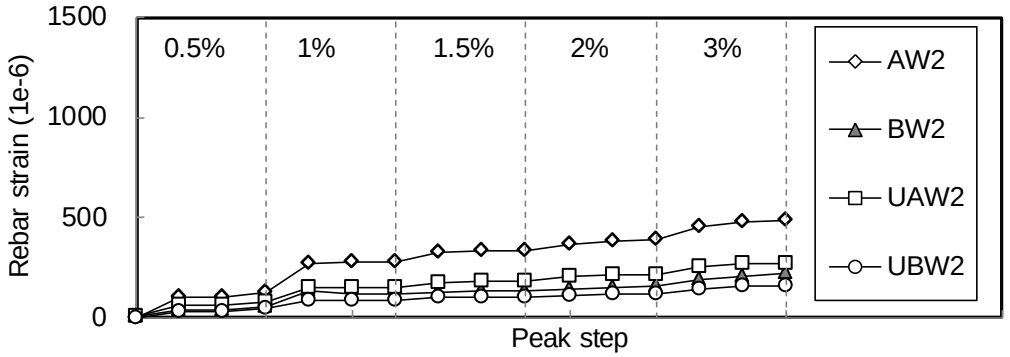

(b)

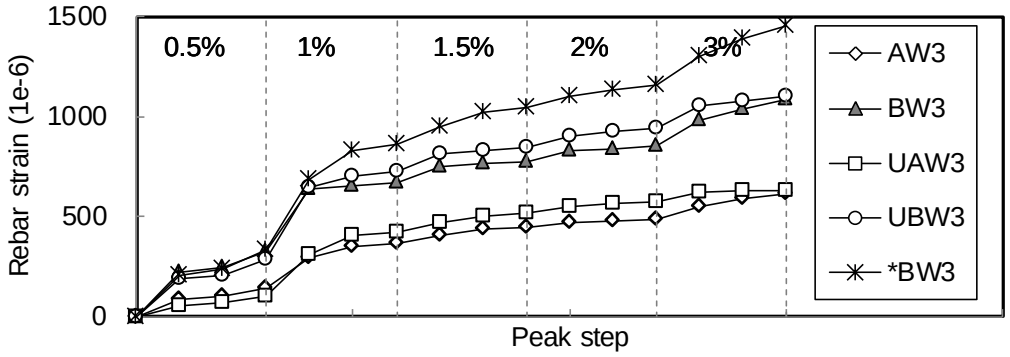

(c)

Figure 6.32 Rebars strains: (a) Set 1 of Specimen RC-1; (b) Set 2 of Specimen RC-1; (c) Set 3 of Specimen RC-1

The force sustained by SFRCC in Figure 6.33 was estimated by subtracting the rebar force from the total section force. In Specimens RC-1, in which two layers of steel rebar were used, the SFRCC burdened about 75% of the section tensile force. In Specimens RC-2, in which one layer of steel rebar was placed in the lower part of SFRCC slab, the SFRCC sustained about 90% of the section's tensile force. Since the presence of steel rebar only provided limited contribution to the section tensile resistance and nevertheless SFRCC slab remain undamaged up to 3% SDR, the SFRCC was regarded to be able to design without steel rebar.

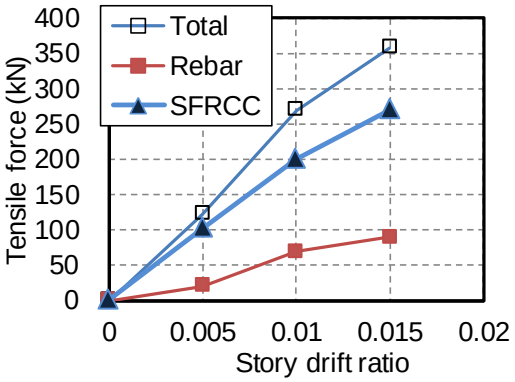

(a) RC-1

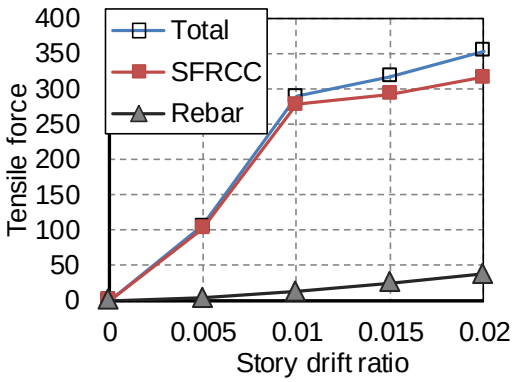

(b) RC-2

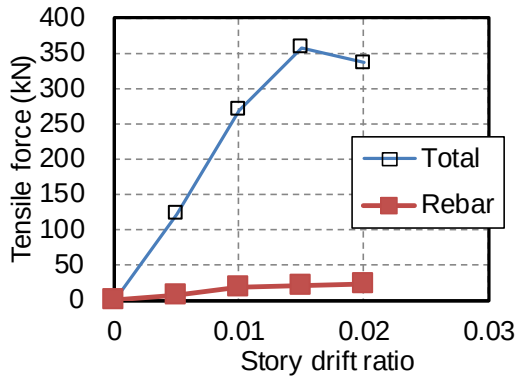

(c) RC-1

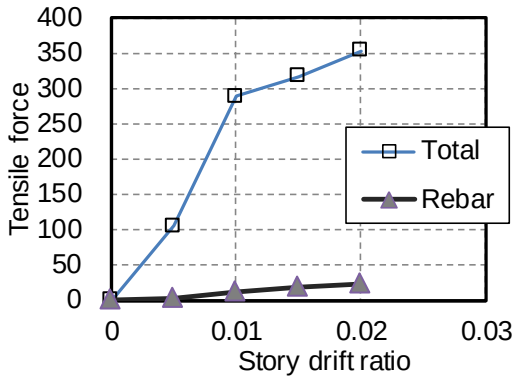

(d) RC-2

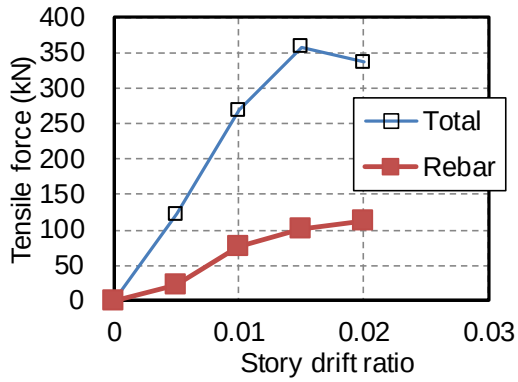

(e) RC-1

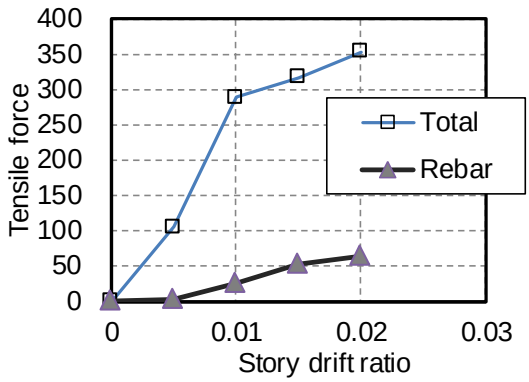

(f) RC-2

Fig.5 Comparison of rebar resisting force to section tensile force: (a) RC-1, location 1; (b) RC-2, location 1; (c) RC-1, location 2; (d) RC-2, location 2; (e) RC-1, location 3; (f) RC-2, location 3

6.5.5 *Numerical analysis*

To further examine the force transfer mechanism of SFRCC slab in the beam-to-column repaired by the proposed method, numerical analysis was conducted. The general-purpose finite element program ABAQUS version 6.10 (Systèmes 2010) was used to perform nonlinear three-dimensional (3-D) finite element simulations of the tested specimens.

The whole specimen was modeled, and the geometry and boundary conditions of the model conformed to the experimental conditions. The steel components were modeled by thick shell elements (S4R in ABAQUS element library). The RC floor slab and SFRCC slab portion were modeled using solid elements for the concrete and SFRCC, and truss elements for the steel reinforcement bars and assuming perfect bonding between the concrete and rebars. The slip between the solid floor slab and steel beam was modeled by a spring and rigid ties as shown in Figure 6.33(b).

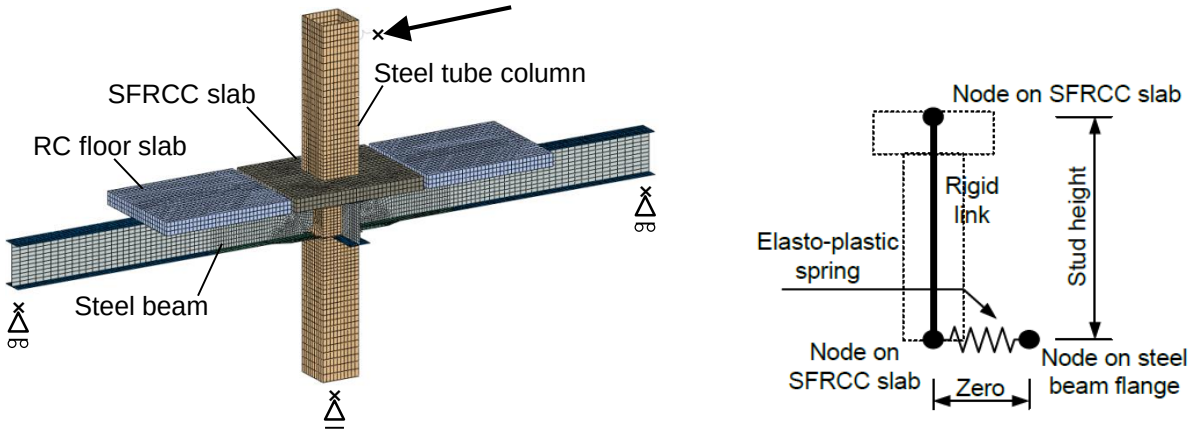

(a) (b)

Figure 6.33 Modeling of specimen: (a) Boundary condition, (b) Spring-rigid model for headed stud

Figure 6.34 compares the load-displacement relationship curves obtained from numerical analysis and from the testing of the original specimen OC-1 and repaired specimen RC-1. The figure shows good match between the numerical analysis and test up to the drift ratio of 3%. Because the numerical model did not possible fracture, the strength degradation following the fracture was not captured. The elastic stiffness was illustrated as the load-SDR relationship curves between the SDR of ±0.5% in Figure 6.35. The comparison shows that the elastic stiffness in FEM model had good agreement with the experimented elastic stiffness.

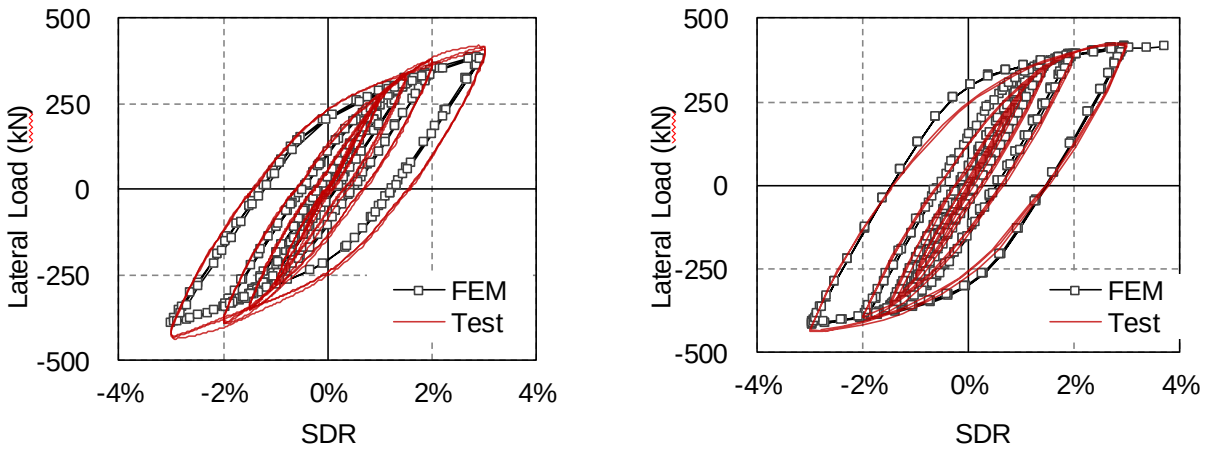

(a) (b)

Figure 6.34 Comparison on force-displacement relationship:
(a) Original connection ‘OC-1’; (b) Repaired connection ‘RC-2’

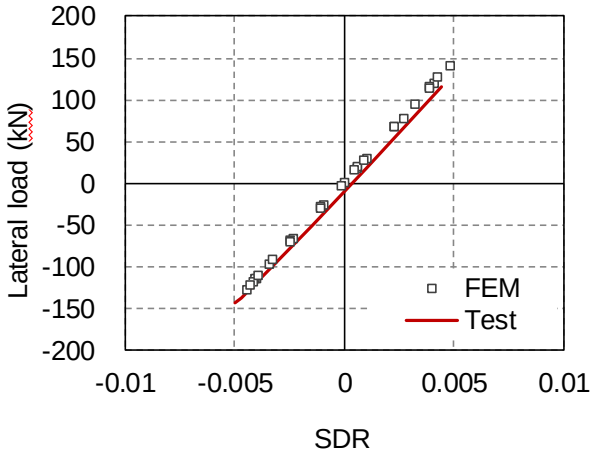

Figure 6.35 Comparison on elastic stiffness of specimen RC-1

The force acting on the slab were evaluated based on the section force equilibrium in the previous section. To further verify the FEM model and also the evaluation method of section force, the forces acting on the slab section obtained from FEM model and the corresponding value obtained from the evaluated method was compared in Figure 6.36. The section force in FEM was obtained by summing up the nodal force on the designated section. The comparison indicated that both results are generally in agreement with each other. It is revealed by both the test and numerical analysis that the compressive force on the slab developed under positive bending is 50% larger than the tensile force on the slab developed under negative bending. It is because of the difference, when the deformed region (from the reverse side of column face to stud cluster) when the SFRCC slab in tension is much larger than the deformed region (from the column face to stud cluster) when the SFRCC slab was compressed by stud cluster.

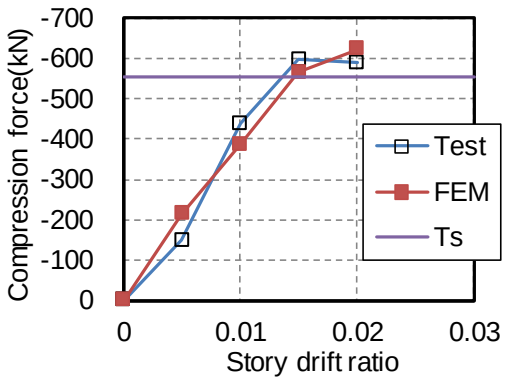

(a)

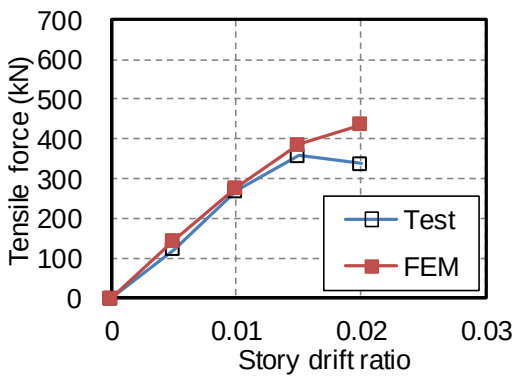

(b)

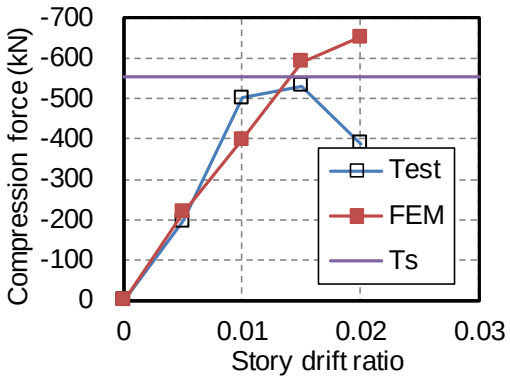

(c)

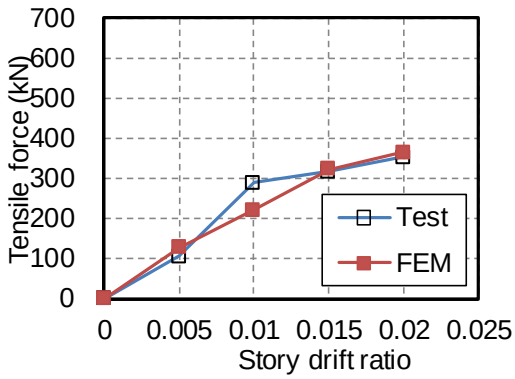

(d)

Figure 6.36 Section compression force obtained by strain data based calculation and FEM: (a) RC-1, positive; (b) RC-1, negative; (c) RC-2, positive; (d) RC-2, negative

Using the verified FEM model, the vector plots of the normal tensile strain on the SFRCC slab section given in plane view and side view are shown in Figure 6.37(a). It can be seen in the plane view that the strain on the abrupt-changed section presents a triangular distribution along the plane from inner edge to outer edge, while strain plot on the side view is looks like inverted trapezia along the section height. These stress distribution characteristic obtained from analysis results is consistent with test rebar strain distribution described in Figure 6.32.

Figure 6.37 shows the strain distribution along the height of the slab section A-A (see Figure 6.17(a)) at the first peak of each loading amplitude. At this section, four strain gauges were installed to two layers of steel rebar in Specimen RC-1. In Figure 6.37(b), the measured strain of the two strain gauges installed at same layer of rebar were taken average, and related to the section height the rebar located. By this approach, two average strain values can be obtained for the height of 33 mm and 74 mm from the bottom of the slab (see Figure 6.17(b)). The other two strain values for the top edge and bottom edge of the slab section was obtained by linear extrapolation, using the two average strain value from the top layer and bottom layer of the rebar and their respective height along the section.

For Specimens RC-2, since there was only one layer of the rebar pass through the section, the linear extrapolation method was not applicable. Therefore, the average strain taken from the single layer rebar at the corresponding to the section height was compared to the stress distribution for specimen RC-1 in Figure 6.37(b).

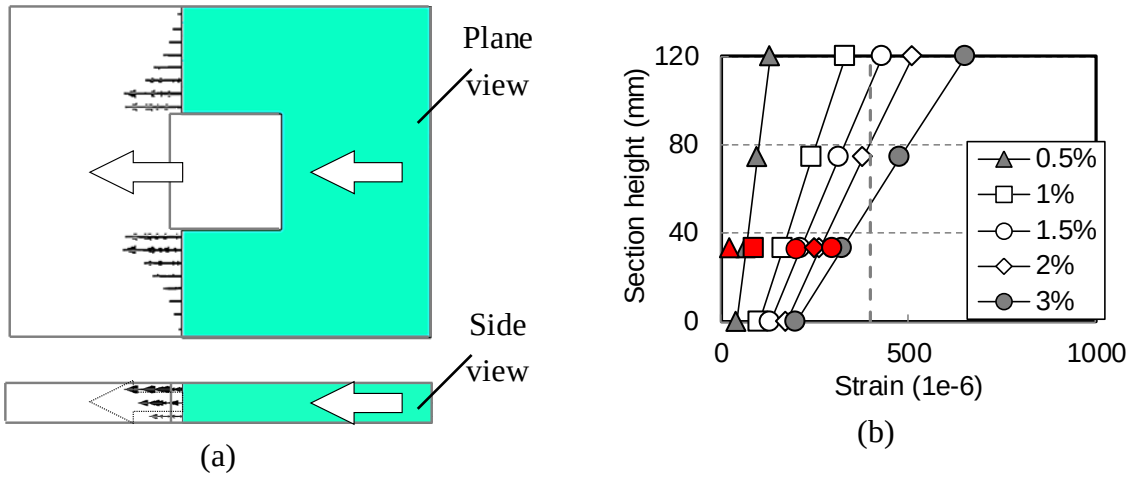

Figure 6.37 Stress distribution on critical section obtained from FEM

To derive a more reasonable and accurate evaluation method for the tensile failure on the abrupt changed section, the strain distributions along the design section should be considered. This study will be carried out in the future.

6.6 Conclusions

To examine the constructability, repair performance and force transfer mechanism of the new repair method using SFRCC for the damaged beam-to-column connections, two phases of full scale member test consisting of two cruciform connection specimens were tested under horizontal cyclic loading. According to the test results, the feasibility of the proposed repair method for beam-to-column was verified. Major findings obtained from the tests are as follows:

(1) Repaired by the proposed scheme, the damaged beam-to-column connection can restore not smaller strength and almost the same elastic stiffness to those of the original connections.

(2) The experimental results revealed that the proposed repair method has the potential to move the plastic hinge away from the column side to the designed section.

(3) The SFRCC slab was cast upon the top flange to serve as external diaphragm to transfer the force from top flange through stud cluster. Under positive bending, the SFRCC slab sustained compression force close to the difference of the tensile force between the widened bottom flange and original top flange as designed. Under negative bending, the tensile force sustained by the SFRCC slab is about 2/3 of that transferred at compression due to the longer deformation range.

(4) Under the negative bending, the tensile force transferred from stud clusters was almost resisted by the SFRCC material, and SFRCC slab remained almost undamaged up to 3% story drift ratio. It indicates that SFRCC slab can be applied without steel reinforcement to achieve desirable performance for the repaired beam-to-column connections.

Because only a limited number of variables/parameters were investigated, however, additional experimental and analytical data are needed to fully demonstrate the developed SFRCC-based rehabilitation method.

REFERENCES

Anderson, J. C., and Duan, X. (1998). "Repair/upgrade procedures for welded beam to column connections."

ANSI/AISC 360. (2010). *Specification for Structural Steel Buildings*. American Institute of Steel Construction, Chicago, Illinois.

Architectural Institute of Japan. (2001). *Recommendations for Design of Connections in Steel Structures*. Tokyo.

Architectural Institute of Japan (AIJ). (2010). *Design Recommendations for Composite Constructions*. Tokyo.

ACI Committee 318. (2008). *Building Code Requirements for Structural Concrete and Commentary*.

FEMA 351. (2000). *Recommended Seismic Evaluation and Upgrade Criteria for Existing Welded Steel Moment-Frame Buildings, prepared for the Federal Emergency Management Agency*. Federal Emergency Management Agency, Washington, DC.

FEMA 547. (2006). *Techniques for the Seismic Rehabilitation of Existing Buildings*. Federal Emergency Managment Agency, Washington, DC.

FEMA-350. (2000). *Recommended Seismic Design Criteria for New Steel Moment-Frame Buildings*. Federal Emergency Managment Agency, Washington, DC.

Matsumiya, T., Suita, K., Nakashima, M., Liu, D., Feng, Z., and Yuya, M. (2005). "Effect of RC Floor Slab on Hysteretic Characteristics of Steel Beams Subjected to Large Cyclic Loading-Test on Full-Scale Steel Frame with RC Floor Slab." *Journal of Structural and Construction Engineering(Transactions of AIJ)*.

Nakashima, M., Matsumiya, T., Suita, K., and Zhou, F. (2007). "Full-Scale Test of Composite Frame under Large Cyclic Loading." *Journal of Structural Engineering*, 133(2), 297–304.

Oehlers, D. J. (1989). "Splitting Induced by Shear Connectors in Composite Beams." *Journal of Structural Engineering*, 115(2), 341–362.

Systèmes, D. (2010). "Abaqus 6.10: Analysis User's Manual." *Providence, RI: Dassault Systèmes Simulia Corp*.

Takahashi, Y., Fujita, Y., and Sugimoto, H. (1996). *Retrofitting technique and modification practice for structural steel building damage during the Hyogo-Ken Nanbu earthquake*. Report of Obayashi Corporation Technical Research Institute Special Issue, 156–193.

Uang, C. M., Bondad, D., and Lee, C. H. (1998). "Cyclic performance of haunch repaired steel moment connections: experimental testing and analytical modeling." *Engineering Structures*, 20(4), 552–561.

CHAPTER 7

Summary and Conclusions

Summary and conclusions

Recently developed high performance fiber reinforced cementitious composites (FRCCs) exhibits a great potential for the applications in constructional engineering. FRCC is a cementitious material, which can be cast to fit any structural shape like concrete does, but also with many improved mechanical properties typically such as strength, toughness, and durability. FRCCs have been used on numerous applications, either as stand-alone or in combination with reinforcing bars and pretressing tendons, and also as a support material in repair and rehabilitation work. The steel moment resistant frame (SMRF) building structure has favorable seismic performance but still has much room for performance improvement. The beam-to-column connection is a key component of SMRF and welded connections are commonly used in seismic regions. During the 1994 Northridge earthquake and 1995 Hyogoken-Nanbu Kobe earthquakes significant weakness in steel moment-frame buildings was discovered. Various solutions have been suggested to ensure adequate plastic deformation capacity to the welded connection. Most of these solutions implement modification on the steel components but are accompanied by problems such as difficulty in welding quality control and necessity for in-site fire proof, among many others. To overcome such drawbacks, it may be better to develop alternative solutions implemented by using other construction materials outside of steel. The application of FRCCs is promising to offer such possibilities. Among various FRCCs, steel fiber reinforced cementitious composite (SFRCC) seems best suited for application in steel structures due to its remarkable high toughness and high strength. This study focuses on the development of a strong and compact stud-SFRCC shear connection and its applications to a weld-free beam-to-column connection system and a repair method for rehabilitation of damaged beam-to-column connection.

The headed stud-SFRCC shear connection is a structural element connecting the steel component with the SFRCC element to transfer the necessary force. It is a key element to achieve the cooperation between the steel and SFRCC component. Different from the conventional stud-concrete shear connection, the proposed stud-SFRCC is featured with densely arranged headed stud shear connectors and the elimination of steel reinforcement; therefore larger force can be transferred through the compact connection, and the fabrication work for steel reinforcement can be

reduced. The mechanical behavior of the stud-SFRCC shear connection was tested by a series of push-out tests. Effects of the stud dimension, stud spacing, number and arrangement of group arranged studs, and fiber volume ratio of SFRCC, and loading type on the strength and elastic stiffness, and failure modes were investigated. Numerical model was developed to generalize the behavior of the stud-SFRCC shear connection. Finally, strength evaluation procedures were developed as well.

The first proposed structural system using the proposed stud-SFRCC shear connection is a new beam-to-column connection. In the proposed weld-free beam-to-column connection, the floor slab portion around the column is cast in SFRCC, and the beam bottom flange is bolted to seat angles using high strength bolts, while a pair of post-tensioned steel bars is used to connect the seat angles located at both sides of the column. To achieve such a connection, a densely arranged stud cluster and heavily reinforced SFRCC slab are used to transfer the required forces. In this connection, the beam hinge is expected to form at the end of the SFRCC slab. In the study, a series of cyclic loading tests were conducted to investigate the feasibility of the new beam-to-column connection and the effect of number of studs, slab length, and arrangement of main steel reinforcement on the maximum strength, elastic stiffness, and energy dissipation of the connection.

The second application is the repair method using SFRCC to repair damaged beam-to-column connections. In this method, widened steel plates are used to replace the fractured and buckled bottom flange, and SFRCC slab without steel reinforcement is used to replace the damaged concrete floor slab portion in the vicinity of the column. A stud cluster is welded to the top flange and embedded in the SFRCC slab. SFRCC slab serves as a cover-plate to transfer the force from the top flange through the stud cluster. Gaps are made between the SFRCC slab and the remained RC slab to move the plastic hinge away from the column face. A two-phases full-scale member tests were conducted to verify the feasibility of the proposed methods and examine the performance of the repaired connection. The tests were divided into two phases. Phase 1 was the quasi-static cyclic loading test to two identical full-scale composite beam-column connections. The specimens were tested to fail under specified loading pattern. In phase 2, the proposed repair methods were applied to the damaged original connections. The repaired connections were tested under identical loading history used in the phase 1 test. Based on the test results, the repaired performances such as the elastic stiffness, maximum strength and energy dissipate capacity are examined. The mechanism of force transfer in SFRCC slab and the stud cluster are also investigated.

This dissertation consists of seven chapters. Chapter 1 is the background of this study, and Chapter 7 is the summary and future problems. Chapters 2 to 6 constitute the main part of the dissertation summaries and notable findings of representative chapters are as follows.

Summary for literature survey on SFRCC

In this chapter, a brief look at the history and classifications of FRCCs were given. The background and history of development of SFRCC was introduced, and the SFRCC mechanical properties important for structural applications were presented.

SFRCC is a new, advanced fiber reinforced cementitious material of elaborated composition,

with remarkably superior mechanical strengths and toughness in comparison to concrete. The compressive strength of SFRCC is higher than 120 MPa, and tensile strength in the range of 20 MPa is characterized by significant ultimate strain (more than 3 %) and the excellent corporation with dense main reinforcement due to much-improved bonding performance.

The combination of these properties postulates more advanced structural application:

(1) The high tensile and shear strength suggest that in many structural applications the reinforcement can be omitted and the tensile or shear stresses are carried by the fiber reinforced matrix alone.

(2) Good bond characteristics between the SFRCC and the reinforcement bars and the toughness of SFRCC suggest that main reinforcement can be embedded in SFRCC to transfer forces through a compact structural element.

Summary for push-out test of stud-SFRCC shear connection

In this chapter, the possibility of achieving strong and compact connections in steel-concrete composite components using SFRCC and steel headed studs was examined. As the initial step of this research, a total of nine push-out tests were conducted for studs embedded in SFRCC. The diameter of studs, number of studs, pitch length, gauge length, and the fiber volume ratio were chosen as the test variables. Major findings are summarized below.

(1) Without reinforcing steel bars, the slab cast with SFRCC can achieve the failure mode of stud fracture with a shear capacity not smaller than that stipulated in design codes for reinforced concrete. This shows that using SFRCC is possible to avoid the cumbersome placement of shear and confinement reinforcement.

(2) When embedded in SFRCC, the studs arranged densely with a pitch length 3.5 times the stud diameter can still possess a shear strength (per-stud) not smaller than 90% of the shear strength of a single stud, while in conventional concrete, a pitch length of 6 times of the stud diameter is required to achieve the same strength.

(3) Even if the gauge length is reduced from 6.9 times of stud diameter (a code specified minimum) to 2.3 times of stud diameter (the minimum spacing allowed for stud installation), no reduction was found in the shear strength carried by the stud.

(4) Within an area of 6.9d x 4.6d mm, which is close to the minimum area stipulated in current design codes, only four studs are permitted to place for reinforced concrete, but for SFRCC, it is possible to place nine studs. Although the per-stud strength decreases as the pitch length decreases, but as the number of studs in the limited area increases, the total of transferred shear force increases to more than twice what can be achieved in reinforced concrete.

(5) The test results indicate that when the fiber volume fraction was reduced from 6% to 2%, the fiber volume does not affect shear strength but did have a significant impact mainly on the ductility and damage tolerance of the connection.

Supplemental push-out tests were conducted to investigate the effect cyclic loading on the strength and mechanical behavior of the stud-SFRCC shear connection.

(1) Comparison on the specimens subjected to reverse cyclic loading and monotonic loading

show that reverse cyclic shear reduced the maximum strength by 16% and ultimate slippage to one third of those subjected to monotonic shear.

(2) Under reserved cyclic loading, specimens showed 7% to 16% strength degradation from corresponding monotonic cases with changing the failure mode. In this type of loading, none of the specimens could withstand more than two cycles at 90% of its monotonic capacity.

Summary of strength evaluation for stud-SFRCC shear connection

In this chapter, comprehensive investigations on strength of stud-SFRCC shear connection were conducted. The nonlinear three-dimensional finite element model was developed to reproduce the experimental behavior of stud-SFRCC connection specimens presented in the Chapter 3.

(1) By adopting the contact interaction between the headed stud and surrounding slab, the FEM models were found to be able to trace the experimental behavior of the push-out test specimens reasonably, in terms of the maximum strength and failure mode.

(2) The numerical analysis indicated that the presence of welded collar has substantial contribution to the shear strength of the headed stud when it is embedded in SFRCC. The contribution of welded collar was found related to the dimension of welded collar and compression strength of SFRCC. Parametric study was conducted to generalize the relationship between the strength contribution of welded collar and the influencing factors. An empirical equation to evaluate the welded collar contribution was adopted and updated by modifying an empirical factor based on the parametric analysis results to make it to suitable for headed stud embedded in SFRCC.

(3) The strength reduction mechanism due to small spacing between studs was studied. Investigation into the shear force of each stud in the group arranged studs revealed that the interaction between closely arranged studs weakens the confining effect on studs and thus the studs sustained less shear force comparing to those with large stud spacing. In addition, studs placed in different position sustain different shear forces. Such difference becomes more significant when the stud spacing becomes smaller.

(4) Formulas to evaluate the reduction for per stud strength of group arranged studs were derived by generalizing the parametric numerical analysis results. The stud spacing in the loading direction and number of studs are considered as the two primary parameters affecting the per stud strength reduction.

(5) The resistance for slab failure of the stud-SFRCC connection needs to be checked to avoid the slab failure. An evaluation method for the strength of slab proposed in the past was introduced, and the derivation process was illustrated.

Tests on Beam-to-column connection using SFRCC

A series of tests were conducted for the proposed beam-to-column connection. A numerical study was also carried out to reproduce the experimental results and to examine the effects of design parameters such as the number of studs, SFRCC slab size, and amount of rebars, on the elastic stiffness and maximum strength. Major findings are summarized as follows.

(1) The beam-to-column connection using SFRCC slab was found to be a promising alternative

for the design of ductile steel moment frames. Beam plastic rotations appeared at the end of SFRCC slab for specimens with proper arrangements of studs and rebars. The specimens showed stable hysteresis till 0.06 rad story drift angle and had the moment resistance capacity similar to that of the corresponding bare steel beam-to-column connection. The energy dissipation of the specimen was notably smaller than what can be achieved by traditional beam-to-column connections. This was primarily because of local damage of the SFRCC around the root of studs. Anchorage of rebars was found to control the strength, and it was secured by the use of rebar rings.

(2) The elastic stiffness of the proposed beam-to-column connection is controlled by the steel beam, SFRCC slab, and studs. The stiffness increases with the increase of the number of studs, and length or thickness of SFRCC slab. The rebars have a minimal effect on the elastic stiffness.

(3) Among the various failure modes that characterize the maximum strength of the proposed beam-to-column connection, the beam yielding at the end of SFRCC slab was considered as the preferred failure mode. A preliminary numerical analysis was conducted to examine the effect of design variables associated with the SFRCC slab on the strength of the proposed connection. The number of studs, slab thickness, and amount of rebars were chosen as variables, and their effects on the strength were found rather minimal within the ranges considered in the analysis.

(4) As observed from the experimental and numerical studies, the proposed beam-to-column connection with SFRCC slab has a potential to attain the structural performance that can be expected for conventional beam-to-column connections using welds. Dimensions of the SFRCC slab and the arrangement of studs and rebars in the slab were the primary factors that control the performance of this connection.

Tests on repairing damaged beam-to-column connection using SFRCC

In this chapter, to examine the constructability, repair performance and force transfer mechanism of the new repair method using SFRCC for the damaged beam-to-column connections, two phases of full scale member tests consisting of two cruciform connection specimens were conducted under horizontal cyclic loading. According to the test results, the feasibility of the proposed repair method for beam-to-column was verified. Major findings are as follows:

(1) Repaired by the proposed scheme, the damaged beam-to-column connection can restore almost the same maximum strength and elastic stiffness to those of the original connections.

(2) The experimental results revealed that the proposed repair method has a potential to move the plastic hinge away from the column side to the designed section.

(3) The SFRCC slab was cast upon the top flange to serve as an external diaphragm to transfer the force from the top flange through the stud cluster. Under positive bending, the SFRCC slab sustained compression force close to the difference of the tensile force between the widened bottom flange and original top flange. Under negative bending, the tensile force sustained by the SFRCC slab was about 2/3 of that transferred at compression due to a longer deformation range.

(4) Under the negative bending, the tensile force transferred from stud clusters was resisted primarily by the SFRCC material, and SFRCC slab remained almost undamaged up to 3% story drift ratio. It indicated that SFRCC slab can be applied without steel reinforcement to achieve desirable

performance for the repaired beam-to-column connections.

ACKNOWLEDGEMENT

First, I would like to express my gratitude to my advisor, Professor Masayoshi Nakashima. Throughout the past four years of study, his profound knowledge, encouragement and patience always provide me clear objectives, and more importantly, confidence, especially when I met with difficulties. He also teaches me how to be a scholar: to find a problem, to solve the problem, and to present the findings. His rigorous scholarship to his work and his kindness to his students are always worthwhile for me to keep in mind and take as my guideline. I have been fortunate to have such a kind, and also intelligent person as my advisor.

Great thanks are due to Professor Hitoshi Tanaka and Professor Yoshio Kaneko for their kindness to be the members of the dissertation committee, and for their thorough reviews and inspiring comments for this dissertation.

Very special thanks to Prof. Gang Wu in Southeast University for his guidance and encouraging me to study in Japanese. A special appreciation is to Prof. Zhishen Wu, Prof. Hanbin Ge, Dr. Chunlin Wang in Southeast University for their encouragement and kindness over many years.

I would also like to show my thankfulness to my group members, Dr. Kazuhiro Hayashi, Dr. Yao Cui, Dr. Kazuaki Hoki, Mr. Toru Tai, and Mr. Shuhai Song, for their great assistance on preparing and conducting physical experiments.

I am also grateful to Professor Masahiro Kurata and my other colleagues, Dr. Ryuta Enokida, Dr. Sachi Furukawa, Dr. Mai Ito, Dr. Xuchuan Lin, Dr. Zhenyun Tang, Dr. Po-Chien Hsiao, Dr. Tracy Backer, Mr. Yundong Shi, Mr. Liusheng He, Mr. Xiaohua Li, Mr. Mayako Yamaguchi, Mr. Ryosuke Nishi, Mrs. Kaede Minegishi, Mr. Takuya Togo and other colleagues from Nakashima Lab, for their kindness to help me with the difficulties I have met in Japan.

I am grateful to Mrs. Chisato Gamou, Mrs. Youko Shiono, Misuko Motohashi for their kind assistance regarding office matters.

Grateful acknowledgement is given to the Ministry of Education, Science, and Culture, Government of Japan (Monbusho) for granting me the scholarship which made this study possible.

Finally, I would like to show my sincere gratitude to my families for their continuous understanding and selfless support, especially to my parents and Ms. Xiwei Sun, for their continuous understanding and selfless support for these years, and for their in-time consolation when I met with frustrations. Therefore, I would like to share my happiness with them.